ABSTRACT

Title of dissertation: ADVANCED ANALYTICAL MICROSCOPY
AT THE NANOSCALE: APPLICATIONS IN
WIDE BANDGAP AND SOLID OXIDE
FUEL CELL MATERIALS

Joshua Aaron Taillon, Doctor of Philosophy, 2016

Dissertation directed by: Professor Lourdes Salamanca-Riba
Department of Materials Science and Engineering

The atomic-level structure and chemistry of materials ultimately dictate their observed macroscopic properties and behavior. As such, an intimate understanding of these characteristics allows for better materials engineering and improvements in the resulting devices. In this thesis, two material systems were investigated using advanced electron and ion microscopy techniques, relating the measured nanoscale traits to overall device performance.

First, transmission electron microscopy and electron energy loss spectroscopy (TEM-EELS) were used to analyze interfacial states at the semiconductor/oxide interface in wide bandgap SiC microelectronics. This interface contains defects that significantly diminish SiC device performance, and their fundamental nature remains generally unresolved. The impacts of various microfabrication techniques were explored, examining both current commercial and next-generation processing strategies. In further investigations, machine learning techniques were applied to the EELS data, revealing previously hidden Si, C, and O bonding states at the

interface, which help explain the origins of mobility enhancement in SiC devices. Finally, the impacts of SiC bias temperature stressing on the interfacial region were explored.

In the second system, focused ion beam/scanning electron microscopy (FIB/SEM) was used to reconstruct 3D models of solid oxide fuel cell (SOFC) cathodes. Since the specific degradation mechanisms of SOFC cathodes are poorly understood, FIB/SEM and TEM were used to analyze and quantify changes in the microstructure during performance degradation. Novel strategies for microstructure calculation from FIB-*nanotomography* data were developed and applied to LSM-YSZ and LSCF-GDC composite cathodes, aged with environmental contaminants to promote degradation. In LSM-YSZ, migration of both La and Mn cations to the grain boundaries of YSZ was observed using TEM-EELS. Few substantial changes however, were observed in the overall microstructure of the cells, correlating with a lack of performance degradation induced by the H_2O. Similar results were obtained for LSCF-GDC, aged in H_2O, CO_2, and Cr-vapor environments. FIB/SEM analysis revealed considerable formation of secondary phases within these cathodes, and quantifiable modifications of the microstructure. In particular, Cr-poisoning was observed to cause substantial byproduct formation, which was correlated with drastic reductions in cell performance.

ADVANCED ANALYTICAL MICROSCOPY AT THE NANOSCALE:
APPLICATIONS IN WIDE BANDGAP AND SOLID OXIDE FUEL CELL MATERIALS

by

Joshua Aaron Taillon

Dissertation submitted to the Faculty of the Graduate School of the
University of Maryland, College Park in partial fulfillment
of the requirements for the degree of
Doctor of Philosophy
2016

Advisory Committee:
Professor Lourdes G. Salamanca-Riba, *Chair/Advisor*
Associate Professor John Cumings
Professor Neil Goldsman, *Dean's Representative*
Professor Eric D. Wachsman
Dr. Tsvetanka S. Zheleva

Dedication

To Dad.
For nights at the telescope watching Hale-Bopp,
teaching me to always be learning,
and encouraging me to wonder.

Acknowledgments

There is most certainly no way a person could complete a graduate degree and a project such as this alone. Numerous people have given me personal and professional assistance, both prior to and during my time at Maryland, to whom I owe a great deal of thanks.

First, I would like to thank my advisor Dr. Lourdes Salamanca-Riba. Your passion for research, commitment to teaching others, and drive for discovery is obvious to all who work with you, and I sincerely thank you for your constant support and sharing your extensive knowledge (about TEM and everything else). During the course of my degree, you provided consistent direction while allowing me a great deal of independence and encouraging me to explore areas of personal interest, for which I am deeply grateful. There are many that do not have such a positive working and personal relationship with their advisor and mentor, and I consider myself blessed to have both in spades.

I would also like to thank our collaborators in the range of projects on which we have worked. To Drs. Tsvetanka Zheleva (ARL), Aivars Lelis (ARL), Len Feldman (Rutgers), and Sarit Dhar (Auburn) and the many past and present graduate students in these groups, thank you for providing us the materials for our SiC work, and for the many fruitful discussions over the years helping us to understand our results. Truly, without your assistance this thesis would not have been possible. To Dr. Eric Wachsman, thank you for involving us in your SOFC characterization efforts. The SECA project pushed me to learn more about FIB/SEM than I ever would have otherwise, and has inspired my future research interests. To my SECA collaborators, Chris Pellegrinelli and Yilin Huang, thank you for the samples, the laughs, and humoring my many naïve electrochemistry questions. I also thank Dr.

John Hagedorn and his ITL colleagues at NIST for helping us with some of the more in-depth programming in this work.

To those who have tutored, taught, and supported me in learning the experimental techniques of this work, thank you. Especially, Dr. Joshua Schumacher at NIST; your expertise, discussion, and granola bars kept me going during my time on the FIB diet, so thank you. I look forward to working with you more over the next few years. To Valery Ray, спасибо for your unwavering support of my (and everyone else's) projects and sharing your incredible FIB expertise during your time at Maryland. You taught me more about the workings of FIBs than I think I wanted to know, and for that I am truly grateful.

To Dr. Kathleen Hart, thank you for taking care of things behind the scenes, and navigating the many intricacies of the UMD Graduate School so we don't have to; your support is greatly appreciated. Also, to all the Materials Science business support staff, especially Ginette Villeneuve, Michael McNicholas, Kay Morris, and Jenna Bishop, thank you for making sure that we all get paid, purchases are ordered, and the innumerable other hidden things that have to happen get done.

Finally, to the family and friends for which there is not enough space to list, I thank you for your support, friendship, and encouragement throughout the years. Dad, Chris, and Marcel, thank you for your love and never-ending reassurances. To Stacey and Khuan, thank you for making me part of your family and always encouraging my studies. To Raina, thank you for your patience, comfort, and belief in me over the past five years, and especially the past few months. I absolutely could not have done this without you by my side.

Contents

List of Tables

List of Figures

List of Abbreviations and Symbols

α	Convergence semi-angle (in TEM)
ARXPS	Angle resolved X-ray photoelectron spectroscopy
β	Collection semi-angle (in TEM)
BF	Bright field
BSS	Blind source separation
DF	Dark field
D_{it}	Density of interfacial trap states
ε	Dielectric constant
EDS	X-ray energy dispersive spectroscopy
EELS	Electron energy loss spectroscopy
ELNES	Energy-loss near-edge structure
E_g	Bandgap
E_p	Plasmon energy
FEG	Field-emission gun
FIB	Focused ion beam
FIB-nt	Focused ion beam nanotomography
$f_{a,\mathrm{TPB}}$	Active fraction of TPB boundaries
$f_{i,\mathrm{TPB}}$	Inactive fraction of TPB boundaries
GIF	Gatan imaging filter
GDC	$(Gd_2O_3)_{0.2}\,(CeO_2)_{0.8}$
HAADF	High-angle annular dark field
HRTEM	High-resolution transmission electron microscopy
ICA	Independent component analysis
ICP	Inductively coupled plasma
$\overline{L}$	Average topological length
L_{cum}	Cumulative graph length of phase network
$\mathcal{L}_i$	Individual graph lengths (within a phase skeleton network)
LMIS	Liquid metal ion source
L_p	Plasmon mean free path
LSCF	$(La_{0.6}Sr_{0.4})_{0.95}\,(Co_{0.2}Fe_{0.8})\,O_{3-\delta}$
LSM	$(La_{0.8}Sr_{0.2})_{0.95}MnO_{3+\delta}$
L_{TPB}	Triple phase boundary length
μ_{FE}	Field-effect mobility
MEIS	Medium-energy ion scattering
MOS	Metal-oxide-semiconductor
MOSFET	Metal-oxide-semiconductor field-effect transistor
MVA/MSA	Multivariate statistical analysis
NMF	Non-negative matrix factorization
PCA	Principal component analysis
POA	Post-oxidation anneal
ρ_{TPB}	Triple phase boundary density
SEM	Scanning electron microscopy
SI	Spectrum image

SOFC	Solid oxide fuel cell
STEM	Scanning transmission electron microscopy
SVD	Singular value decomposition
τ	Phase tortuosity
T_d	Debye temperature
TEM	Transmission electron microscopy
TL	Transition layer
θ	Thermal conductivity
TPB	Triple phase boundary
V_{th}	MOSFET threshold voltage
WBG	Wide bandgap
w_{TL}	Transition layer width
ξ_c	Critical field
XPS	X-ray photoelectron spectroscopy
YSZ	$(\mathrm{Y_2O_3})_{0.08}(\mathrm{ZrO_2})_{0.92}$

Chapter 1:   Introduction

At its very core, microscopy of all forms deals with revealing the unseen. Whether with light, ions, or electrons, microscopes enable the study of physical and chemical processes at ever improving resolutions. Modern electron and ion microscopes allow for the direct observation (and modification) of microstructure at the atomic scale. Furthermore, information about the chemical and electronic structure of the materials under observations can be obtained through concurrent spectroscopic analysis. While these techniques can be (and are) applied in many fields, materials science provides ample opportunity for novel discovery in the detailed investigation of nano- and microstructures. In this work, advanced electron and ion microscopy techniques (transmission electron microscopy and focused ion beam microscopy) have been applied to two distinct systems, providing innovative insights into the material properties of each.

In the first portion of the work (Section 1.1 and Chapter 3), analytical TEM techniques were applied to the silicon carbide material system to investigate the atomic-scale characteristics of the interfaces in SiC microelectronics. In particular, this work has focused on characterization of the distinct transition layer (TL) that exists between $4H$-SiC and SiO_2 in MOS devices made from the wide bandgap

1

material. In addition to imaging in both HRTEM and STEM modalities, detailed multivariate analysis of electron energy loss spectroscopy measurements has revealed direct evidence of electronic states at the interface between SiC and SiO_2 that have never previously been observed. The impacts of variations in the oxidation process and changes in the crystallographic orientation of the SiC substrate on the nature of the TL have been examined in detail as well.

The second primary research effort in this dissertation (Section 1.2 and Chapter 4) focuses on characterizing the microstructural degradation of solid oxide fuel cell (SOFC) cathodes upon exposure to various environmental contaminants. In addition to TEM and EELS analyses (similar to the SiC studies), this body of work makes extensive use of the focused ion beam as a characterization tool, through a process known as *FIB nanotomography* (FIB-*nt*), which enables direct three dimensional reconstructions of the cathodes' microstructures at nanometer resolution. Significant developments have been made in the quantification of a number of important microstructural parameters, and are described in this work. These techniques have been applied to two composite cathode materials, and the impacts of H_2O, CO_2, and Cr contamination have been investigated and quantified.

In the remainder of the thesis, Chapter 2 provides a detailed introduction and description of the experimental methods used in this work, while Chapter 5 serves as a conclusion and provides discussion of potential avenues for future research.

1.1 Silicon carbide as a wide bandgap semiconductor

1.1.1 Importance of wide bandgap semiconductors

Global industrialization has resulted in worldwide energy demands that are growing exponentially, doubling approximately every 40 years [1]. While the development of clean and renewable energy sources is of obvious importance, it is equally critical to consider ways in which consumption (or at least its rate of growth) can be curbed. Since total demand can not be expected to decrease, the primary avenue for these reductions will be through overall improvements in system efficiencies, which can be partially achieved through the use of wide bandgap (WBG) materials. WBG materials are semiconductors with energy bandgaps significantly larger than that of typical electronic materials, such as Si, Ge or GaAs. Practically, this includes materials with bandgaps larger than $\sim 3\,\mathrm{eV}$, including SiC, GaN, and ZnO, amongst others [2].

The benefit of WBG materials comes from their unique properties that make them much more suitable than Si for industrial-scale power electronics and energy technologies. These materials are much more efficient in both AC-to-DC and DC-to-AC electricity conversion, reducing losses up to 90% compared to traditional Si devices. They can handle voltages more than 10 times those of silicon before breaking down, enhancing high-power performance greatly. Devices made from WBG materials have temperature ratings over twice those of Si, leading to better reliability, reduced cooling costs (and enhanced efficiency), and opportunities for novel

uses. WBG materials are being developed for a wide range of applications, including industrial motors, high-power, high-frequency, and high-temperature electronics, grid-scale power inversion, electric vehicles, defense, geothermal, and lighting. Because of their promise to transform multiple markets, these materials have been identified as a *foundational technology* by the U.S. Department of Energy [2], as well as a critical area of research by the Department of Defense [3].

Fig. 1.1 schematically demonstrates the benefits of a WBG material like silicon carbide, as compared to silicon (the typical electronic device material). This figure shows the field-effect transistor (FET) efficiency as a function of the designed blocking voltage. In lower voltage applications (such as logic circuits), there is little or no benefit in energy consumption, making Si the obvious choice. At blocking voltages greater than $100\,\mathrm{V}$ (where the performance of Si devices is severely degraded), the reductions in energy consumption for SiC devices far outweigh the added material costs, positioning SiC as an extremely promising choice in these applications. As an example, consider a residential photovoltaic (PV) power inverter. Inverters convert the DC current generated from PV cells to AC current that can be fed into the power grid. Replacing Si components of the inverter with SiC diodes and power MOSFETs can cut losses by 50%, yielding savings of about $100 a year per household, solely from efficiency gains. Additionally, SiC components can withstand higher temperatures, further reducing system costs and packaging volumes [1, 4]. It is simple to envision how similar gains in system efficiency could drastically transform device performance and costs in additional sectors.
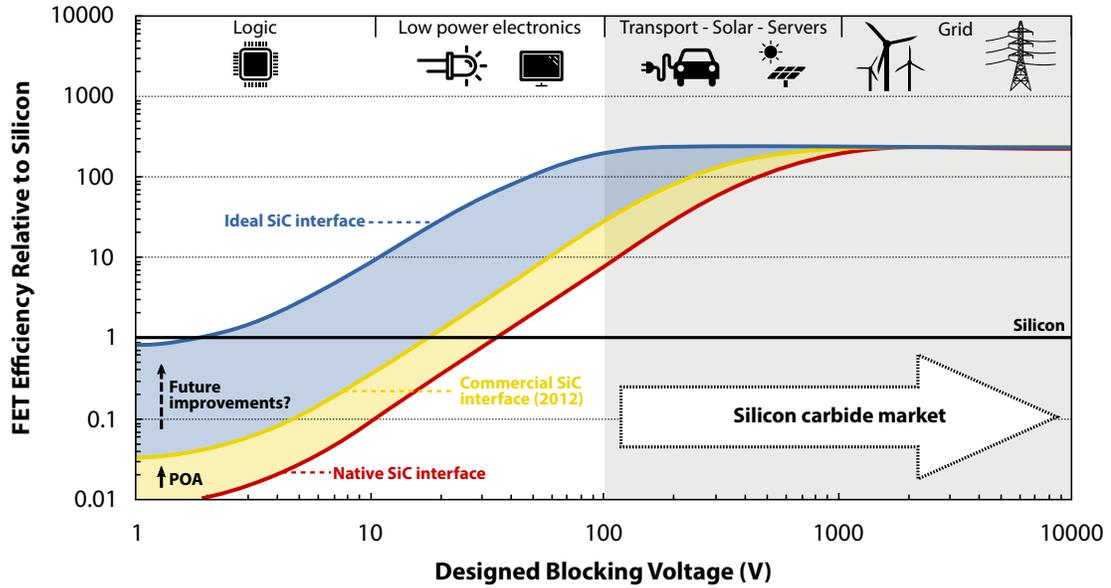
Figure 1.1: Comparison of SiC-based FET efficiency compared to typical Si devices as a function of intended voltage. Native (red), current (yellow), and ideal (blue) SiC devices are shown, with typical applications displayed at the top of the plot. At higher voltages (the SiC market), the gains in efficiency from SiC's material properties outweigh the added material costs. Figure adapted from Rozen [5, 6].

1.1.2 Material properties of silicon carbide

Silicon carbide in particular is a very promising wide bandgap (WBG) semiconductor for high power and high temperature applications. Its native oxide is SiO_2, meaning it can be easily used as a drop-in replacement for Si in a number of existing device fabrication processes (such as thermal oxidation, reducing processing costs). SiC also has high thermal conductivity and relatively high bulk electron mobility [7], allowing for improved thermal management, device stability, and suitable electronic performance. The SiC crystal is comprised of equal stoichiometric parts silicon and carbon, where each species is bonded in a tetrahedral configuration to four nearest neighbors of the opposite species [8]. While over 250 polytypes (distinct

crystallographic structures) have been identified for SiC [9], the most relevant for electronic device fabrication is the *4H* polytype. The *4H* hexagonal structure (shown in Fig. 1.2) follows a bilayer stacking sequence with four repetitions. Each bilayer consists of tetrahedra with four C covalently bonded to each Si, and *vice versa*. The stacking and relative offsets of these bilayers ultimately determine the polytype. In the *4H* (and *6H*) SiC polytypes, the surface may additionally be terminated by either a layer of Si atoms or C atoms creating two possible crystal polarities, referred to as the (0001) Si-face and (000$\bar{1}$) C-face orientations, respectively [10]. These polarities give rise to differences in behaviors such as the oxidation rate, with the C-face having a rate 5 times that of the Si-face [11].

Ultimately, it is the electronic properties of SiC that make it a useful WBG material, and these are summarized for the *4H* polytype (and compared to Si and GaN) in Table 1.1. In power electronics, it is crucial to have a large critical field (ξ_c). ξ_c is the upper limit of the electric field that a semiconductor can withstand before undergoing avalanche breakdown (the uncontrolled multiplication of electron-hole pairs) that will cause device failure. Thus, ξ_c is directly related to the amount of voltage that can be blocked by a power device in its "off" state.

As shown in Table 1.1, SiC has a significantly higher ξ_c than Si. Specifically, it is the high Debye temperature (T_d) and large bandgap (E_g) that give rise to the large critical field, and illustrate why SiC is such a useful material in high-power applications. The higher T_d corresponds to higher energy vibrational (phonon) modes within SiC than in Si. These phonon modes will dissipate a portion of the kinetic energy of the electrons within the solid through a process known as thermalization.
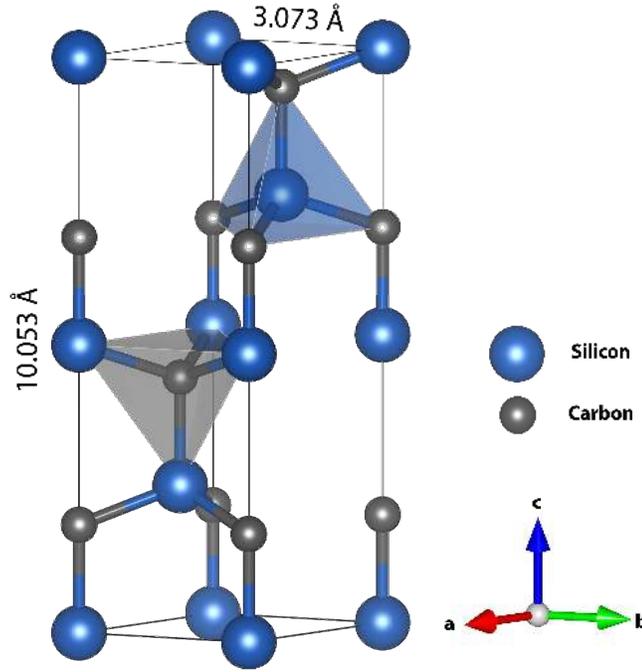
Figure 1.2: Model of the *4H*-SiC crystal structure. This hexagonal polytype of SiC (space group No. 186 - *P6₃mc*) contains 4 stoichiometric units per unit cell (total of 8 atoms), and follows an ...ABCB ...stacking sequence. At $300\,$K, the lattice parameters are $a = b = 3.073\,$Å and $c = 10.053\,$Å [12]. The bonding tetrahedra for both Si and C are indicated for clarity.

Since the phonon modes are at higher energies in SiC, carriers will continue to be thermalized (preventing runaway carrier generation) at higher fields, leading to a higher ξ_c [16].

Similarly, the wide bandgap of SiC correlates with a higher critical field, and in a first-order approximation, the carriers need to reach a kinetic energy of at least $3/2\ E_g$ to induce breakdown [1]. The larger bandgap in SiC arises from stronger electronic interactions between the silicon and carbon atoms than between the atoms in Si (illustrated by the shorter bond length of $1.89\,$Å in SiC compared with $2.35\,$Å in Si). The reduction in interatomic distances in SiC causes larger splitting of

7

Table 1.1: Overview of *4H*-SiC properties, compared to GaN (another promising WBG material), and silicon; while the values reported are for $T = 300K$, temperature and doping levels can cause significant variations. Data compiled from Refs. [1, 13–15]

Property	*4H*-SiC	GaN	Silicon
Crystal structure	Wurtzite	Wurtzite	Diamond
Space group (number)	$P6_3mc$ (186)	$P6_3mc$ (186)	$Fd\bar{3}m$ (227)
Lattice constant(s) (Å)	$a = 3.07$	$a = 3.19$	5.43
	$c = 10.05$	$c = 5.18$	
Density (g/cm^3)	3.211	6.15	2.329
Bandgap - E$_g$ (eV)	3.26	3.39	1.12
e^- mobility - μ_e ($cm^2/V.s$)	900	1600	1400
e^- effective mass - m^*/m_0	0.29/0.42†	0.20	0.98/0.19†
Critical field - ξ_c (MV/cm)	3 - 5	5	0.3
Dielectric constant - $\varepsilon/\varepsilon_0$	9.7/6.52††	8.9/5.35††	11.7
Debye temperature - T_d (K)	1300	600	640
Thermal conductivity - θ ($W/cm.K$)	3.7	1.3	1.3

† Longitudinal/transverse values

†† Under static/high-frequency operation

the bonding and antibonding states, which propagate as a wider bandgap in the bulk periodic crystal. Additionally, the larger E$_g$ increases the critical velocity of electrons in the material ($v_c = \sqrt{3E_g/m^*}$) meaning electrons can reach higher peak velocities in SiC without triggering avalanche device breakdown [1]. These properties enable WBG materials such as SiC to be used in very high-power and fast switching applications, substantially beyond the capabilities of Si.

While not investigated in this thesis, another very promising WBG material is GaN. This material is also hexagonal (although can also be made in the cubic zincblende structure), and has properties that are overall fairly similar to SiC, although with some differences. Its properties are also reported in Table 1.1. Compared with SiC, GaN has a higher electron mobility, making it more appropriate for fast switching applications, while SiC maintains its thermal conductivity advantage.

Thus, SiC is more appropriate for when higher power densities are desired.

1.1.3 Current state of and challenges for SiC in microelectronics

Intensive efforts over the past two decades have enabled the recent commercialization of SiC-based MOS devices, but performance (and reliability) of the devices is still limited by a low carrier mobility within the FET channel that is caused by electrically active defects at the semiconductor/oxide interface [7]. The following is a brief review of the basics of the recent progress and remaining challenges for SiC as a WBG electronic material.

1.1.3.1 SiC substrate processing

A SiC MOSFET device begins its life as a *4H*-SiC wafer substrate, and the production of these wafers has been a subject of intense research. The current state of the art commercial offering from Cree, Inc. is a six inch wafer, virtually free of extended defects such as micropipes (less than $1\,\mathrm{cm^{-2}}$ [17]). Material costs remain high however, with a three inch SiC wafer costing over \$2,000 (as of May 2016), compared to \$60 for an equivalent Si substrate [18]. For electronic devices, a high quality epitaxial layer is grown on top of this substrate by high-temperature chemical vapor deposition (CVD) using silane (SiH_4) and propane (C_3H_8) as Si and C sources, together with any desired dopants (N_2 or $(CH_3)_3Al$ for *n*- or *p*- type doping, respectively) [19].

Because of the very small energy difference between polytypes, it is common

for inclusions to occur during epitaxial growth if appropriate steps are not taken to prevent them. This will often lead to undesired sections of *3C*-SiC in the epilayer when *4H*- or *6H*-SiC is used as a substrate. The typical strategy used to eliminate this problem is to grow the epitaxial layer with a process known as *step-controlled epitaxy* [20]. A high density of atomic steps is created by intentionally lapping (or dicing) a SiC boule at a slight angle off from the [0001] *c*-axis (usually 4° in modern devices), leading to a series of parallel atomic steps in a predefined direction. The epilayer-forming gases are flowed along these steps, from which homoepitaxial growth proceeds laterally. This process results in extremely high-quality epilayers with very low defect densities, at the expense of added surface roughness and potential step bunching, which can have adverse effects for device performance [16, 17, 20].

1.1.3.2   SiO$_2$ gate oxide and its interface with SiC

It is generally accepted that the bulk oxide natively formed on SiC during thermal oxidation is stoichiometrically equivalent to that of SiO$_2$ grown on Si. The oxide has been found to have a density, refractive index, dielectric constant, and breakdown strength extremely close to that of SiO$_2$, to the point where most consider them to be functionally identical oxides [21]. The rate of oxidation of SiC is significantly slower than that of Si, and requires temperatures greater than 1000 °C [22]. When fabricated into a MOS device, the SiO$_2$ layer is a frequent source of performance degradation due to charge buildup within the oxide. This buildup occurs due

to carrier injection from the gate contact when the device is off, and from the SiC semiconductor when the device is on. The oxide charge buildup leads to threshold voltage instability, mobility degradation (from scattering), and eventual device failure [16]. Thus, it is important to have a thorough understanding of the oxide layer and how device processing strategies affect it.

While SiO$_2$ on SiC behaves identical to the Si system in the bulk, there are substantial differences in how it interacts with SiC at the interface of these MOS structures. Additionally, there is significant variation in the quality of the interface as a function of substrate orientation, which is manifested in the channel mobility (μ_{FE}) of resulting MOSFET devices. The differences in mobility arise from differences in scattering phenomena at the interface. The mobility of a carrier is defined as

$$\mu = \frac{q\tau}{m^*} \tag{1.1}$$

where q is the elementary charge of the electron or hole, τ is the mean scattering time of a given scattering process, and m^* is the carrier's effective mass. Since there will be a distinct τ_i for each scattering process, the mobilities will combine according to Matthiessen's rule:

$$\frac{1}{\mu_{tot}} = \sum_i \frac{1}{\mu_i} = \frac{1}{\mu_{ph}} + \frac{1}{\mu_{cs}} + \frac{1}{\mu_{lt}} + \frac{1}{\mu_{sr}} \tag{1.2}$$

where the contributing processes are (in order) carrier-phonon interactions, Coulomb scattering, carrier recombination, and surface/interface roughness scattering.

At the interface between SiC and SiO$_2$, defects and surface states lead to energy levels within the bandgap. During inversion of a MOSFET channel (the "on" state), these additional acceptor levels will be filled, reducing the number of free carriers by "trapping" electrons. This reduces the lifetime of carriers (reducing μ_{lt} from Eq. 1.2) and causes additional Coulomb scattering from the negatively charged center (reducing μ_{cs}). These processes cause a drastic reduction in the field-effect mobility (μ_{FE}) for SiC compared to its bulk mobility (μ_e). Indeed, typical devices produced from *4H*-SiC (without mobility enhancing treatments) have a μ_{FE} only about 1% the value of μ_e [23]. Compare this to the case of silicon, where the field-effect mobility reaches values of about 50% the bulk value.

As mentioned, the large band gap of *4H*-SiC makes it particularly sensitive to interfacial defect states. Many of the states that exist at the SiC interface also exist at the Si/SiO$_2$ interface, such as Si-dangling bonds [26] and oxygen vacancies [27], amongst others [28]. These defect states are at energy levels centered approximately 2.8 eV below the SiO$_2$ conduction band edge [28], and are observed in oxide layers on both Si and SiC substrates. In the case of Si/SiO$_2$ though, this energy level is well within the conduction band of Si, and as a result does not reduce carrier mobilities. In SiC, the larger bandgap means these states are active during inversion, causing a drastic reduction in mobility (see Fig. 1.3). As would be expected from the qualitative energy diagram in Fig. 1.3, *4H*-SiC has a lower μ_{FE} than *6H*-SiC for the same reason.

More quantitatively, the density of interface trap states (D_{it}) can be measured using a capacitance-voltage (CV) technique. Such measurements by Cooper *et al.* [7]
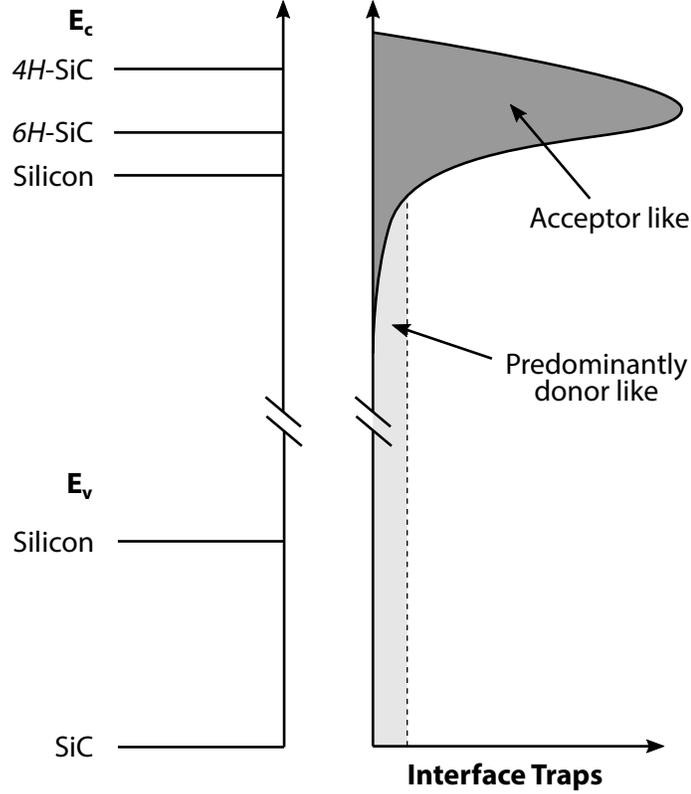
Figure 1.3: Qualitative schematic of the density of electron traps present at the oxide/semiconductor interface in SiC and Si. The relative positions of the valence and conduction band edges are indicated (E_v and E_c, respectively). Because of its larger bandgap, *4H*-SiC is susceptible to more trap states than *6H*-SiC and silicon. Figure adapted from Schörner *et al.* [24] and Rozen [25].

revealed significantly higher trap densities in *4H*-SiC near the conduction band edge when compared with *6H*-SiC, explaining the lower mobility values in those samples (see Fig. 1.4). μ_{FE} was also found to increase with temperature in *4H*-SiC samples, indicating that the main charge transport limiting process is Coulomb scattering.

In addition to the Si-related defects that affect both Si/SiO_2 and SiC/SiO_2, the added carbon species in SiC provide another potential source of mobility limiting defects. During the thermal oxidation process, carbon must be released from the substrate at the interface, and this is not always a perfect process. A number

13
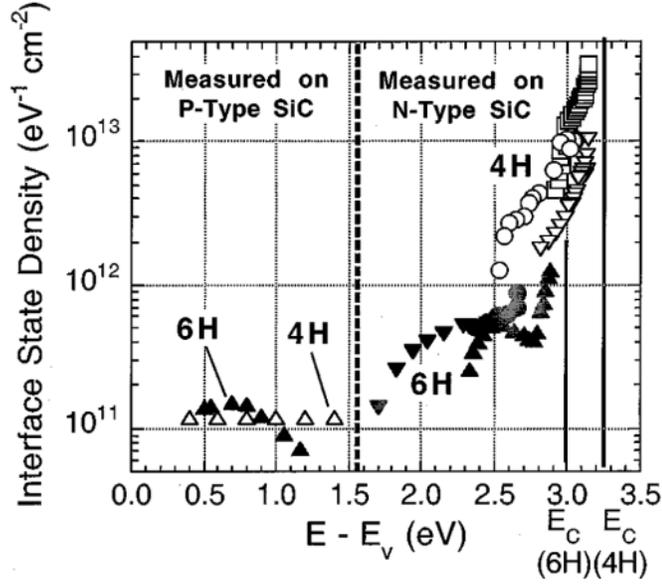
Figure 1.4: Quantitative measurement of interface trap density (D_{it}) as a function of energy within the bandgap of *4H-* (empty symbols) and *6H*-SiC (filled). Of particular interest is the significant number of states present just below the conduction band edge for *4H*-SiC compared to *6H*. Figure from Cooper *et al.* [7].

of previous works from the past two decades, using a variety of techniques such as Rutherford backscattering [29], XPS [30–33], TEM/EELS [34, 35], surface enhanced Raman spectroscopy [36], and spectroscopic ellipsometry [37] have all demonstrated the presence of excess carbon at the interface, which is posited to be contained in a Si_xC_yO transition layer, extending a few nm around the interface. Interestingly, more recent works have not observed an excess of C at the interface as seen in earlier studies, raising questions about the nature, extent, and even the existence of the transition layer [38–40].

Theoretical works have proposed the possibility of stable carbon defects in the form of carbon interstitials and carbon dimers at the interface [22]. Additionally, graphitic inclusions could explain the shape of the D_{it} curve throughout the lower

and middle ranges of the bandgap [41]. To this point however, there has been no direct evidence in either XPS or TEM of these "graphitic clusters," suggesting they are smaller than the resolution of current techniques, or they simply do not exist [25].

1.1.4 Existing device processing strategies

As explained above, the μ_{FE} measured for a typical *4H*-SiC MOSFET is significantly lower than the bulk mobility value due to the wide variety of defect states that are active within the bandgap of the semiconductor's electronic structure. A number of methods have been developed for improving the mobilities in fabricated SiC devices by removing or passivating these defects. Initial attempts at passivating the interface defects took inspiration from the processes used in Si device fabrication. One of the first attempts was the use of a hydrogen post-oxidation anneal (POA). This process is known to be very effective at passivating dangling Si- bonds at the Si/SiO_2 interface, and it has been found to lower D_{it} in the Si system by about an order of magnitude [42, 43]. Unfortunately, the same process applied to SiC only results in modest improvements, suggesting that dangling Si- bonds are likely not the primary mobility limiting defect [44, 45].

The commercialization of SiC as a device material would not have been possible without the revolutionary discovery of a high temperature (1100 °C) nitric oxide (NO) POA, first applied to *6H*-SiC by the Dimitrijev group in 1997 [46]. This work was extended to *4H*-SiC by Chung *et al.* [47], leading to a joint effort over the next decade between Auburn, Vanderbilt, and now Rutgers Universities, with the goal

of optimizing the *4H*-SiC/SiO$_2$ passivation process. Significant progress was made over this time, leading to order of magnitude gains in SiC device mobilities compared to the regular thermal oxidation process (see Fig. 1.5) [23, 48]. This success has enabled widespread commercialization to take hold, with numerous companies actively producing off-the-shelf SiC power components (*e.g.* Wolfspeed, Infineon, STMicroelectronics, Rohm, etc.). Production of SiC components and value-added products is in a ramp-up phase currently, and market analysts predict that SiC and next-generation power device revenues will increase 17-fold to \$2.5B by 2023 [49].
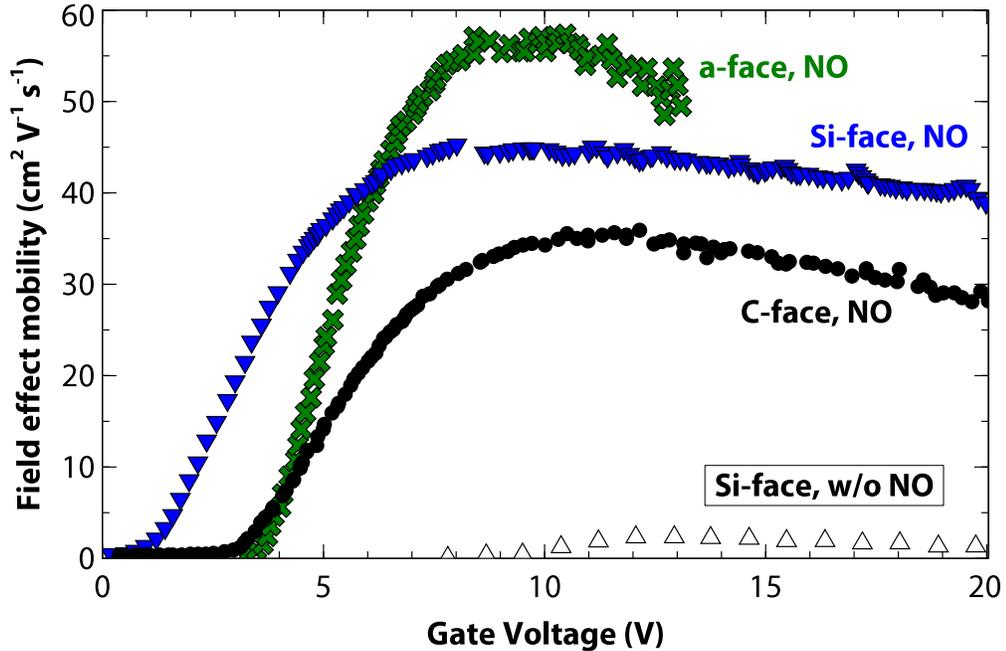
Figure 1.5: Field effect mobility values for NO-annealed MOSFET devices fabricated on various crystallographic faces of *4H*-SiC, together with the "raw" values for a device without an NO post-anneal. Figure recreated with data from Dhar *et al.* [48].

While the practical improvements gained from NO annealing are obvious, the mechanisms and atomic effects of nitrogen incorporation are yet to be fully understood, and are an active area of research within the SiC community. Generally,

the improvements from NO annealing are attributed to the presence and bonding of nitrogen at the SiC/SiO$_2$ interface, which has been confirmed by elemental profiles using XPS [30], medium energy ion scattering (MEIS) [11], secondary ion mass spectroscopy (SIMS) [50], and EELS [51], showing the nitrogen to be localized within a few nm of the interface. The areal density of N incorporation was found to be in the range of 10^{14} to 10^{15} atoms/cm^2. The NO anneal process has been observed to eliminate excess carbon at the SiC/SiO$_2$ interface, in addition to significantly reducing the atomic-scale roughness [52]. Theoretical studies have revealed that N atoms can passivate C interstitial defects (manifesting as carboxyl groups) through substitution [53] or by formation of isocyanate configurations [54]. The introduction of nitrogen however, will introduce additional states near the valence band edge (hole traps) due to extra lone pair of electrons. These states raise further concerns regarding device reliability [53, 55].

Beyond the NO post-anneal, many additional techniques have been demonstrated to improve the performance of SiC devices, but even less is known about the structural and chemical effects upon the interface than NO treatments. Incorporation of nitrogen via an N$_2$ plasma has been shown to supply greater N-coverage and lower interface trap densities, but does not enhance the field-effect mobility (μ_{FE}) greater than a standard NO process [56]. Phosphorus-based treatments have also been proposed, and have yielded a 2x improvement in μ_{FE} (compared to NO), at the expense of lower threshold voltages (V_{th}) and V_{th} instability (both of which adversely affect performance) [57]. Additionally, a boron passivation has been found to improve μ_{FE} similar to a P process, and although the mechanism by which this

group III acceptor can reduce D_{it} is not well understood, it is currently proposed that it does so through a physical change in the oxide layer, reducing stress at the interface [58]. Finally, altering the orientation of the SiC substrate (from the typical (0001) Si-face) in the MOSFETs has shown promising results as well, with the (11$\bar{2}$0) a-face and (000$\bar{1}$) C-face showing significant mobility enhancement (see Fig. 1.6 for a schematic of the relative orientations) [59, 60].
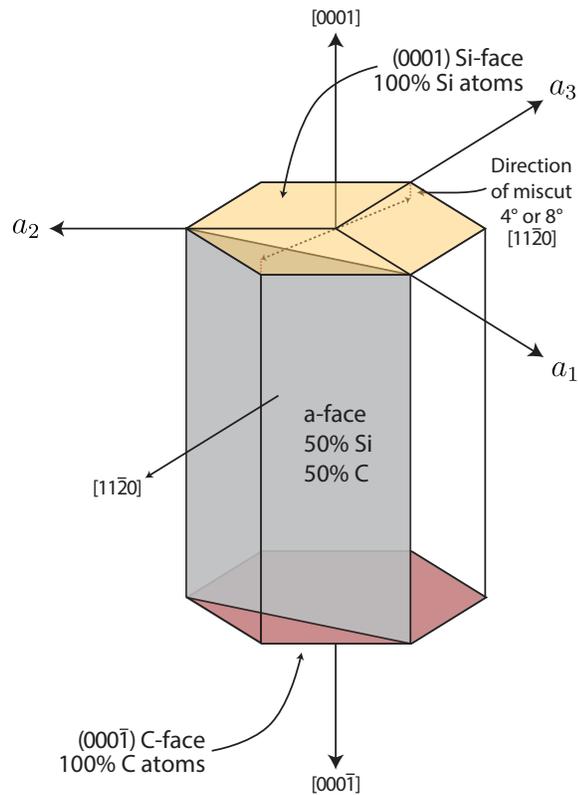
Figure 1.6: Schematic of *4H*-SiC crystal orientations showing three adjacent SiC unit cells. The atomic positions of Si and C are omitted for clarity. The three crystallographic faces used in fabrication are highlighted, with the (0001) Si-face being the most common face in commercial devices. The direction of the miscut orientation is highlighted as well. Figure adapted from Dhar [11].

1.1.5 Characterization of the SiC/SiO$_2$ interface

In addition to electronic device investigations, the *4H*-SiC/SiO$_2$ interface has been the subject of a great deal of atomic scale characterization, with the aim of directly observing the specific atomic configurations (and defects) that are present at the interface (as opposed to just their impacts on electrical performance). Unlike the Si/SiO$_2$ interface, which is known to be very sharp (transitioning to SiO$_2$ within 3 Å) [61], evidence has suggested that a distinct transition layer (TL) exists at the SiC-oxide interface, with a spatial extent ranging from a few to tens of nm.

A great deal of early work studying the SiC/SiO$_2$ interface via TEM-EELS was performed by K.C. Chang as part of Lisa Porter's group at Carnegie Mellon University [34, 35, 51, 62]. A particularly important contribution from this body of work were the elemental profiles measured using EELS in devices receiving an NO anneal. In these works, an excess of carbon species was clearly shown to be present at the interface, with a larger excess in C-face samples than Si-face ones. This excess carbon was not observed uniformly throughout the interface however, and in one study was observed in only 6 of 20 regions analyzed [51]. Additionally, nitrogen was observed to accumulate at the interface in Si-face samples at a concentration of approximately 0.35×10^{15} cm^{-2}, equivalent to about 1/3 monolayer of atoms. Detailed results of these experiments are shown in Fig. 1.7.

Following on this work was a combined HRTEM/HAADF-STEM/EELS study in 2007 by Zheleva *et al.* [63]. This work was one of the first to attempt a complete structural and compositional characterization of the SiC transition layer, analyzing a
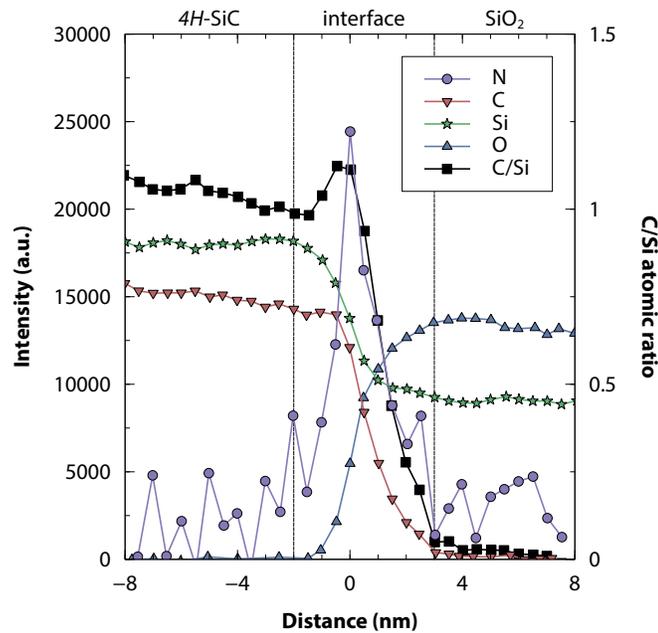
Figure 1.7: Distribution of elemental species at the interface between $4H$-SiC and SiO$_2$ on a C-face substrate. Intensity values were calculated by integrating the area under the EELS core-loss edge of interest. The N is shown to be localized within a few nm of the interface, and the C/Si ratio reveals an excess of carbon piled up at the interface. Figure recreated with data from [51].
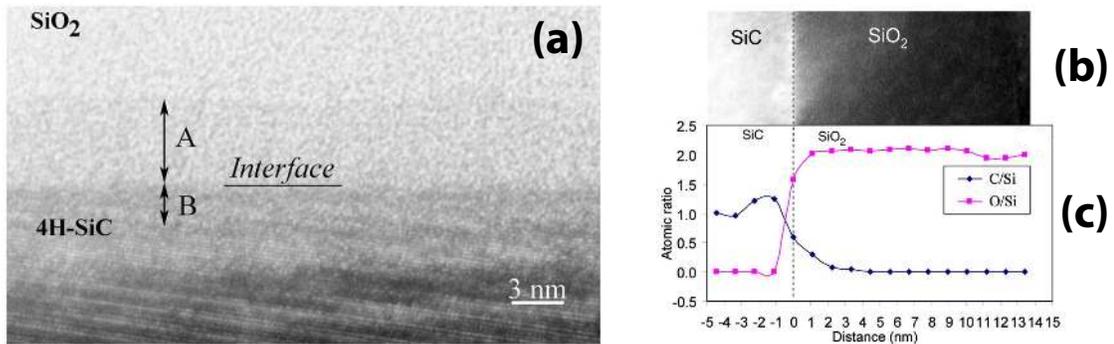
Figure 1.8: (a) HRTEM image of the $4H$-SiC/SiO$_2$ interface revealing asymmetric transition layers within both the SiC and SiO$_2$ of $3.3\,\text{nm}$ and $4.8\,\text{nm}$, respectively. (b) HAADF-STEM image of the SiC/SiO$_2$ interface. (c) Elemental profiles of the C/Si and O/Si atomic concentration ratios, measured using EELS. Figure from [63].

Si-face sample without NO annealing. As seen in Fig. 1.8(a), high resolution TEM

images revealed layers of distortion parallel to the interface in both the SiC and

SiO$_2$, which were interpreted as two distinct constituents of the overall transition layer, totaling about 8.2 nm. While HAADF-STEM images did not reveal similar interfacial characteristics (Fig. 1.8(b)), atomic ratios measured by EELS (Fig. 1.8(c)) showed a clear excess of approximately 30% extra carbon in the SiC. Since the intensity of HAADF-STEM images is proportional to the atomic mass being sampled (Z-contrast), the existence of the TL in HRTEM images (and not in the STEM images) suggests a modification at the interface that is primarily structural in nature, rather than chemical (with the exception of the excess C).

In a continuation of the work by Zheleva, Biggerstaff *et al.* [64] studied five different *4H*-SiC devices, some with and without NO anneal, as well as with or without an Al implantation (simulating another device processing step). The samples were imaged using Z-contrast STEM imaging, and transition layers in the SiC were observed as a dark band near to the interface. The widths of these TLs were measured (ranging from 5 to 20 nm), and compared to the peak μ_{FE} of the devices. An inverse linear trend was observed between TL width and μ_{FE}, providing the first evidence of a link between the structure of the interface and ultimate device performance. This study also revealed the presence of excess carbon within the SiC at the interface.

More recently, researchers at the University of Tennessee used an aberration corrected STEM to obtain atomic-resolution Z-contrast images of the *4H*-SiC/SiO$_2$ interface [38]. In this work, a TEM sample was prepared with its zone axis intentionally parallel to the direction of the miscut in the SiC substrate. By incrementally changing the STEM probe's focus by a small amount, information was measured

from subsequent planes of atoms within the material, enabling a three-dimensional interpretation of the STEM data (see Fig. 1.9). From this study, the authors concluded (in contradiction to previous works), that there was no distinct transition layer at the interface between SiC and SiO_2, instead attributing the modifications observed within 2nm of the interface to solely structural roughness. Additionally, no excess C beyond the expected 1:1 ratio of SiC was observed in EELS measurements.
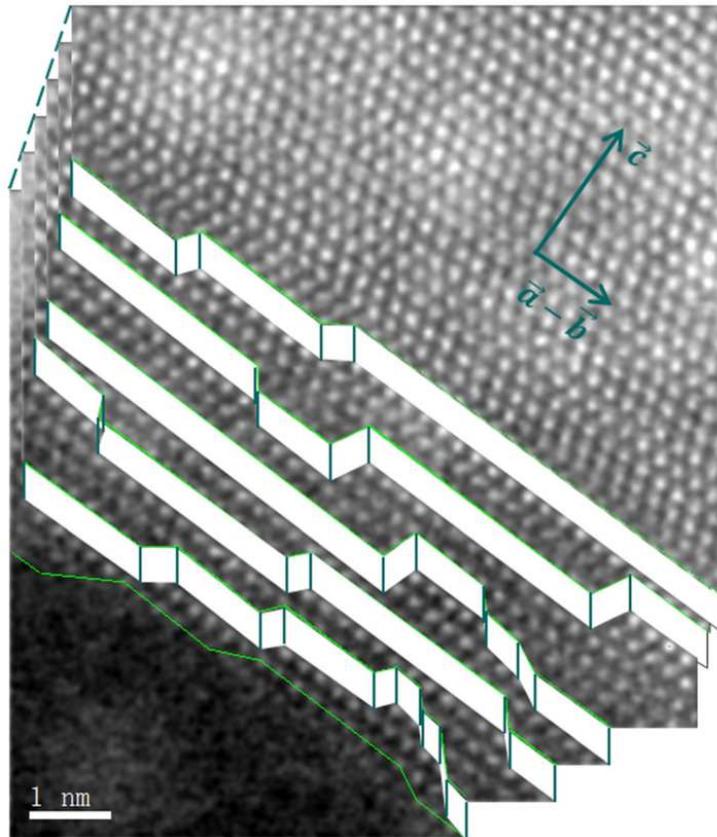
Figure 1.9: Through focal series Z-contrast images stack along the $[11\bar{2}0]$ zone axis with a focal increment of 40 Å. In each 40 Å defocus step, two additional monolayers of the SiC (0001) plane became visible. The boundaries of each atomic plane are outlined for clarity. Figure from Liu [65].

Finally, a very recent work from NC State University has also used aberration-corrected HAADF-STEM and EDS to analyze the transition region of NO-annealed

Si-face devices [66]. Atomic-resolution STEM images of the interface did not reveal any modifications indicative of a transition region. EDS analysis reveals the N to be primarily accumulated within 2 nm of the interface, similar to the original findings of Chang *et al.* [51]. Further detailed analysis of the STEM images enabled a precise measurement of the atomic strain at the interface, the results of which are shown in Fig. 1.10. On average, no strain was observed in the direction parallel to [11$\bar{2}$0], while a compressive strain of 0.34% was measured along the [0001] direction (perpendicular to the interface), localized within two lattice planes of the interface. This strain was attributed to the shorter bond length of Si-N bonding compared to Si-C, and suggests that in these samples, the SiC portion of the TL is limited to these few atomic planes (approximately 0.75 nm). No estimate of the transition extending into the SiO_2 is provided, but one could reasonably expect it to be on the same order as the distribution of N that was measured.
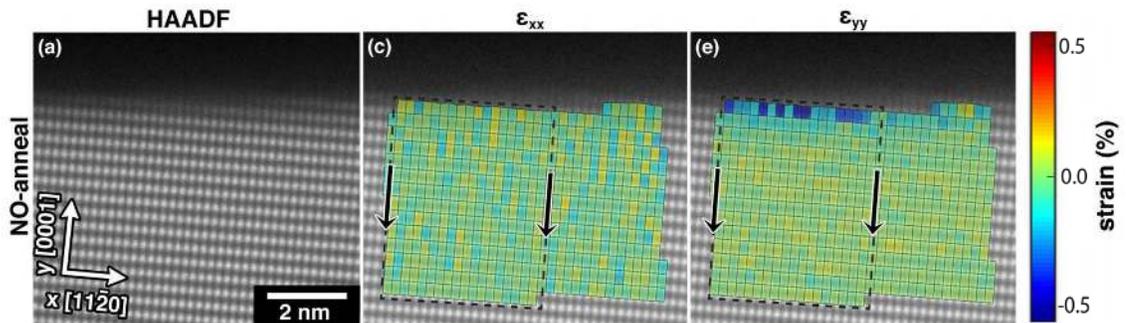
Figure 1.10: (*left*) Aberration-corrected HAADF-STEM image of a Si-face *4H*-SiC/SiO$_2$ interface subjected to an NO post-anneal. (*center, right*) ϵ_{xx} and ϵ_{yy} maps revealing the presence of compressive strain in the SiC at the interface in the [0001] direction. Figure adapted from [66].

1.1.6 Goals of this research

In summary, while there are many similarities between the prior works reviewed here, there are a number of important differences between them, leading to a somewhat unclear overall picture of the $4H$-SiC/SiO$_2$ interface. All of the TEM studies investigating NO-annealed devices agree that the nitrogen is incorporated primarily within approximately 2 nm of the interface, confirming the results obtained via surface science techniques [67–69]. Beyond this however, there is limited agreement (if any) as to the overall structure. Initial works repeatedly reported large (tens of nm) TL widths, with excessive amounts of carbon localized at the interface. More recent works however seem to indicate a much sharper interface, with no indication of excess carbon at all. Ultimately, the interface between $4H$-SiC and SiO$_2$ is still not fully understood, providing ample opportunity for this thesis to provide novel discoveries.

This work provides analysis of a variety of interfaces in $4H$-SiC devices subjected to a range of processing conditions and substrate orientations. TEM, HAADF imaging, EELS, and XPS are used to provide insights into the specific effects of NO annealing, as well as phosphorus and boron treatments. The impacts of SiC substrate orientation and interface roughness on the transition layer are investigated. Finally, a few samples receiving bias-temperature stressing were analyzed to provide insight onto how the interface changes under "real-world" application conditions.

24

1.2 Solid oxide fuel cell cathodes

With each passing year of warming global temperatures [70], ever growing pollution in major cities [71], and massive volatility in energy markets [72], it is becoming increasingly obvious that the world's dependence on fossil fuels has wide-ranging deleterious effects on the environment, health, and both individual and national economic security. The need for cost-effective and sustainable energy sources is greater than ever before, and fuel cells represent a promising technology capable of efficiently and cleanly converting fuel into electricity through electrochemical oxidation [73–75].

Solid oxide fuel cells (SOFCs) present an efficient, clean, and flexible means to convert hydrocarbon fuels to electricity through electrochemical oxidation, without combustion, leading to electrical efficiencies of up to 65%, and approaching 90% in combined heating and power applications [76–78]. SOFC devices operate at high temperatures ($> 650\,°C$), and as such are capable of using almost any hydrocarbon fuel source, including conventional fuels such as natural gas or gasoline, but also alternative fuels such as H_2, ethanol, or biodiesel [78]. Finally, SOFCs are fully solid-state devices, reducing the probability of mechanical failure modes.

SOFCs are constructed by sandwiching a dense solid ionic-conducting material between two porous electronic conducting materials, both of which can participate in electrochemical reactions, converting chemical potentials into electric ones. A qualitative schematic of a typical SOFC is shown in Fig. 1.11. An SOFC device's fundamental operation is governed by three processes: first, oxygen is reduced at

the cathode (air side) of cell, converting oxygen molecules into oxygen ions (O^{2-})
via the oxygen reduction reaction (ORR). Next, these ions are transported through
the ion-conducting electrolyte until they reach the anode (fuel side). Finally, on the
fuel side, the oxygen ions oxidize a hydrogen-containing fuel such as H_2 or methane
(CH_4). This last reaction releases electrons that give rise to the generated current
and produces water (and/or CO_2) as a byproduct.
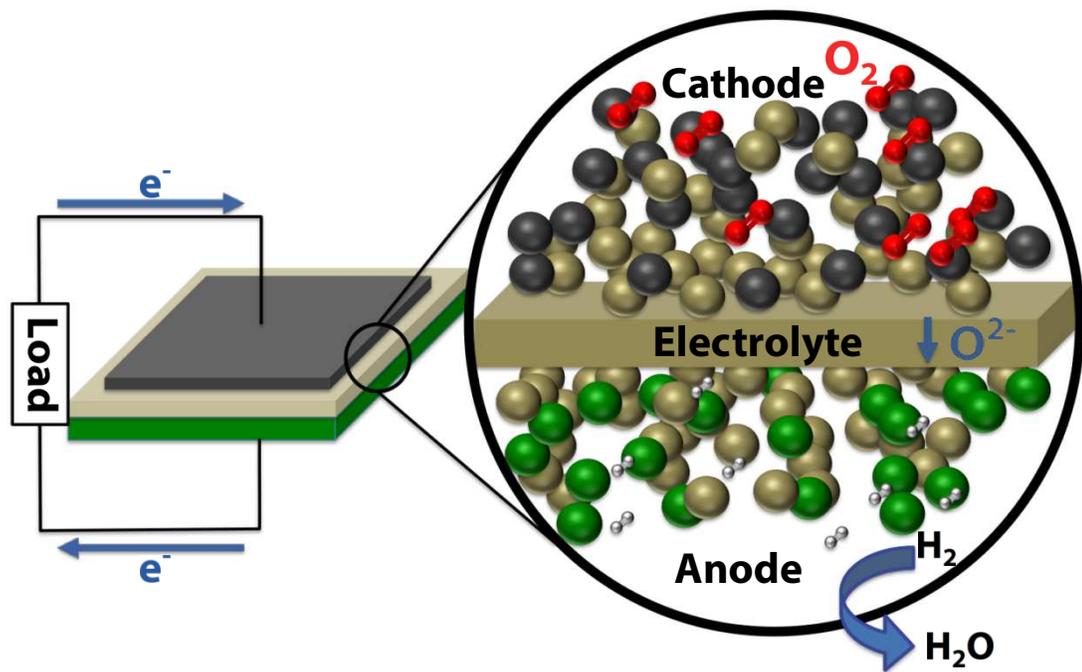
Figure 1.11: Schematic working principle of SOFC energy conversion devices. The fundamental mechanism of electricity generation is through electrochemical reactions that take place in the porous cathode (gray) and anode (green). On the cathode side, oxygen molecules are reduced into negatively charged oxygen ions (O^{2-}). The O^{2-} ions diffuse through the ion conducting solid electrolyte (tan) to the anode, where they oxidate hydrogen from a fuel source, producing electrons and H_2O as a byproduct. The free electrons are then accessible to perform useful work, after which they are returned to the cathode for further participation in the SOFC operation. Figure adapted from Huang [79].

The chemical reactions governing the operation of the cell are dependent on
the specific fuel supplied to the anode, but can be generally written as follows [80]:

Assuming H_2 fuel:

Cathode reaction (ORR):

$$\frac{1}{2}O_2 + 2e^- \rightarrow O^{2-} \tag{1.3}$$

Anode reaction:

$$H_2 + O^{2-} \rightarrow H_2O + 2e^- \tag{1.4}$$

Total cell reaction:

$$H_2 + \frac{1}{2}O_2 \rightarrow H_2O \tag{1.5}$$

Assuming CH_4 fuel:

Cathode reaction (ORR):

$$2O_2 + 8e^- \rightarrow 4O^{2-} \tag{1.6}$$

Anode reaction:

$$CH_4 + 4O^{2-} \rightarrow CO_2 + 2H_2O + 8e^- \tag{1.7}$$

Total cell reaction:

$$CH_4 + 2O_2 \rightarrow CO_2 + 2H_2O \tag{1.8}$$
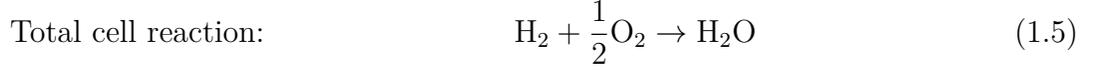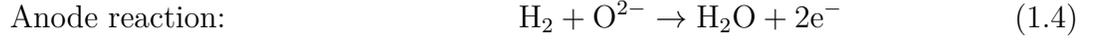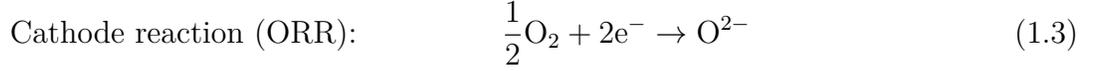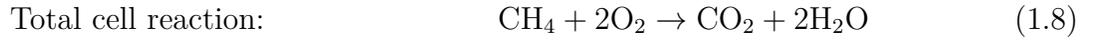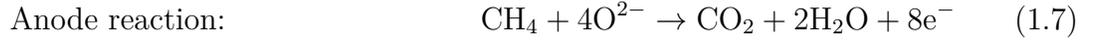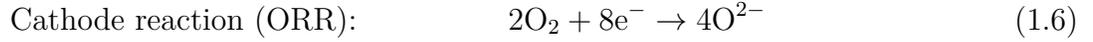
The balance of these reactions is controlled by the oxygen partial pressure at each electrode, and the open circuit voltage (V_{OC}) produced by the cell is ultimately determined by the Nernst equation:

$$V_{OC} = \frac{RT}{4F} \ln \left(\frac{pO_{2,anode}}{pO_{2,cathode}} \right) \tag{1.9}$$

where R is the gas constant, T is the operating temperature, F is the Faraday constant, and pO_2 is the oxygen partial pressure at the anode or cathode, respectively [81].

1.2.1 Origins of polarization loss

In a perfect electrochemical system, the entire V_{OC} potential produced by the SOFC would contribute to performing useful work. In reality however, each reaction driving the cell is subject to inefficiencies that will reduce the overall output voltage.

These drops in voltage, which are caused by various polarization resistances within the system, are referred to as polarization losses or overpotentials, and each has a specific origin in the cell: Ohmic losses (η_{ohmic}) arise from the Ohmic resistance that charge carriers face within the electrolyte and electrode materials, while concentration losses (η_{conc}) originate from the mass transfer process of gas diffusion in the porous electrodes. The most import polarization loss however, is that due to the activation energies that must be overcome during the participation of oxygen in the reactions described in Eq. 1.3 - 1.8 (η_{act}). This η_{act} has two primary components. Namely, losses from the kinetics associated with adsorption and dissociation of oxygen to/from the active sites, as well as from the charge transfer of active oxygen species at the triple phase boundaries within the cathode/anode. In a typical SOFC operating at intermediate temperatures ($\sim 700\,^{\circ}\text{C}$), the primary source of polarization losses is from the inefficiencies of the ORR at the cathode/electrolyte interface, and thus studies of the cathode layer are particularly important to understand the ways in which SOFCs can be improved.

1.2.2   SOFC cathode materials

On the air side of the SOFC, a cathode material is required to provide active sites for the ORR to take place. In Kröger-Vink notation, the ORR is described by the following defect reaction:

$$\frac{1}{2}\text{O}_2 + \text{V}_\text{O}^{\bullet\bullet} + 2e' \leftrightarrow \text{O}_\text{O}^\text{X} \tag{1.10}$$

necessitating that at the active sites in the cathode (or cathode/electrolyte interface), molecular oxygen, oxygen vacancies, and electrons must be available for reaction. Ideally, the material providing these sites should be stable, inexpensive, and efficient. Over the past three decades, the SOFC community has generally settled on materials with the perovskite structure as the preferred choice for the cathode layer, due to their high electronic conductivity (relative to other oxides), and their low cost compared to platinum (the previously used cathode material) [82]. Perovskites are a class of material defined by their crystal structure and with a stoichiometry of ABO_3, where A sites are filled by rare earth metals such as La or Sr, while the B sites are filled with transition metals such as Fe, Co, or Mn. The structure is shown for reference in Fig. 1.12.

In particular, two perovskite materials are most frequently used for SOFC cathodes: $(La_{0.8}Sr_{0.2})_{0.95}MnO_{3+\delta}$, known as LSM, and $(La_{0.6}Sr_{0.4})_{0.95}(Co_{0.2}Fe_{0.8})O_{3-\delta}$, known as LSCF. Both of these materials have high catalytic activity due to surface oxygen vacancies, as well as empty d states of the transition metal ion on the B site [83–86]. Also, the thermal coefficients of expansion of LSM and LSCF are well-matched to the common electrolyte materials yttria-stabilized zirconia (YSZ: $(Y_2O_3)_{0.08}(ZrO_2)_{0.92}$) and gadolinium-doped ceria (GDC: $(Gd_2O_3)_{0.2}(CeO_2)_{0.8}$), respectively. This match provides strength and reduces stresses in the cell during cycling and prevents premature mechanical failure. The following is a brief overview of each cathode material.
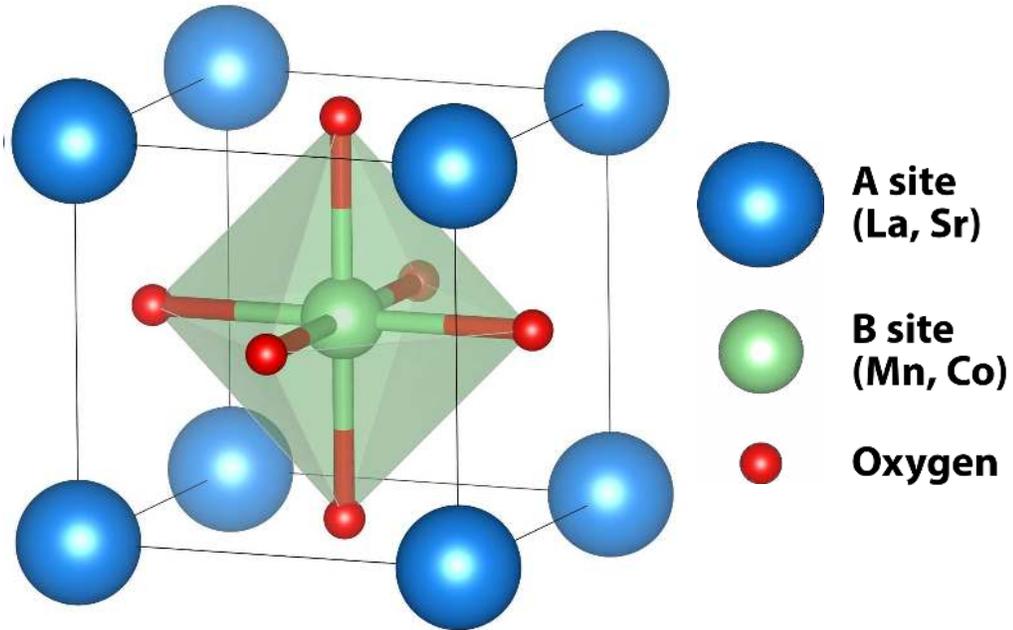
Figure 1.12: Generic cubic perovskite crystal structure, showing the relationship between the unequal A and B sites. The B site transition metal sits at the center of the unit cell in an octahedral site, with 6-fold coordination to the oxygen atoms on the face of the cell. The coordination polyhedron of the B site is shown for reference. The A site rare earth atoms are at the corners, in a 12-fold cuboctahedral coordination.

1.2.2.1   LSM: $(La_{0.8}Sr_{0.2})_{0.95}MnO_{3+\delta}$

Because of the high operation temperature of SOFCs (ranging from 600 °C to 1000 °C), few electrically conductive materials are even eligible candidates for use in systems such as these. Initially, noble metals such as platinum and silver were used, but these materials have high costs, and have limited stability due to coarsening, cracking, and evaporation [74]. High-temperature perovskite conducting oxides were initially proposed as an SOFC cathode material in 1966, in the form of $La_{1-x}Sr_xCoO_{3-\delta}$ (LSC) [87]. LSM soon thereafter became the favored cathode material due to its high electronic conductivity at SOFC operating temperatures [82].

As mentioned previously, LSM is an ABO_3 perovskite with La and Sr sharing the A-site and Mn occupying the B-site. It's electronic conductivity originates from a small polaron conducting mechanism, resulting in an electronic conductivity (σ_e) above $100\,S\,cm^{-1}$ at $950\,°C$ [88]. In SOFC systems, LSM is considered solely an electronic conductor (rather than a mixed conductor) due to it's low ionic conductivity (σ_i) of $10^{-7}\,S\,cm^{-1}$ (at $900\,°C$) [89].

A cathode with purely electronic conductivity such as LSM requires a triple phase boundary (TPB) for the reduction of oxygen via the ORR (Eq. 1.3 and 1.10). At the TPB, gaseous oxygen conducted through the pore structure is reduced, filling an oxygen vacancy within the electrolyte while consuming electrons from the cathode (LSM). LSM has good long-term stability and its thermal expansion is well matched to YSZ, but it is not truly an ideal choice for an SOFC cathode. It suffers from high polarization losses at intermediate temperatures, which are a critical application range for commercial SOFCs. Also, the active region is limited to the immediate vicinity of the TPBs, since those are the only locations where the three species of Eq. 1.10 are mutually present. Being able to extend this active region beyond the TPBs could significantly enhance cell efficiencies. Furthermore, environmental contaminants such as humidity in the air supply can accelerate degradation processes that cause additional losses in the SOFC performance [90–92].

1.2.2.2 LSCF: $(La_{0.6}Sr_{0.4})_{0.95}(Co_{0.2}Fe_{0.8})O_{3-\delta}$

Although they have a similar structure, LSM and LSCF have quite different properties when it comes to their use as SOFC cathodes. LSCF has fractional occupancies on both the A- and B-site leading to a highly nonstoichiometric crystal that can more easily generate oxygen vacancies. Because of these vacancies, LSCF has a reasonably high ionic conductivity, classifying it as a mixed ionic and electronic conductor (MIEC). Indeed, at $900\,°C$ its σ_i is $0.23\,S\,cm^{-1}$ (orders of magnitude larger than LSM), and its σ_e is $252\,S\,cm^{-1}$ (about double that of LSM) [93]. A MIEC such as LSCF has the added benefit of being able to conduct oxygen vacancies, and thus the active region for the ORR is expanded, due to the additional source of $V_O^{\bullet\bullet}$. Additionally, due to its higher overall conductivities, LSCF can be used at lower temperatures than LSM while still maintaining suitable performance, making it a preferred material for intermediate temperature (IT) SOFC applications [94].

Compared to LSM, LSCF suffers from more modes of degradation, and is incompatible with the widely used YSZ electrolyte material, due to interface reactions that negatively impact performance. Instead, GDC is typically used with LSCF as a solid electrolyte. Sr also easily diffuses out of LSCF, and when depleted from the cathode, degrades the perovskite structure and lowers performance [95]. Additionally, humidity in the air source has negative impacts on the ORR in LSCF cathodes, to an even greater degree than in LSM [96]. Furthermore, additional contaminants such as CO_2 and Cr vapor have been shown to limit both the durability and performance of SOFC cathodes by accelerating degradation processes [91, 97].

1.2.3 Durability of SOFC perovskite cathodes

One of the primary concerns hindering commercialization of SOFCs is the durability of the cathode layer in real-world working conditions [98–100]. In particular, the long-term performance of SOFCs has been found to degrade when exposed to various gaseous species during operation [91, 92, 97, 101–105]. When this degradation is irreversible, no amount of cell cycling or clever system design can recover the original material configuration. Chief among degradation concerns are effects of the contaminants on the microstructure of the system. Coarsening, decomposition, cation interdiffusion, and secondary phase formation are all possible mechanisms of cell degradation, and understanding their origins will enable engineering of the system to mitigate their occurrence, or at the very least, their negative effects.

Previous research has lent some insight into particular degradation modes in SOFC cathodes, although the fundamental mechanisms are still not totally clear. A range of different gases can induce undesired interactions with the cathode material, such as CO_2, H_2O, and Cr-vapor. CO_2 and H_2O are naturally occurring and difficult to avoid in real-world environments, so understanding under which conditions they are most reactive is critical. Previous studies suggest that H_2O exposure can cause reduction of LSM-YSZ contact area due to it causing degradation of the perovskite phase [92]. Conversely, CO_2 has been found to inhibit the dissociation of oxygen at the surface of LSM and LSCF, but no evidence has been presented to suggest irreversible microstructural decomposition [97]. Cr-vapor arises from the interconnect materials used within the SOFC system, and is a catalyst for the formation of

secondary phases [105], but with a better understanding of its reaction pathways, its usage can be engineered to reduce its impacts on cell performance.

1.2.4   Microstructure/performance relationships

As mentioned previously, the ORR in a composite cathode takes place at the boundary between the pore, electrolyte, and cathode phases (the TPB). Accordingly, the morphology and three-dimensional microstructure of the cathode will strongly affect the available sites at which the ORR can take place, which in turn will strongly affect the cathode polarization and performance. Indeed, a number of quantifiable microstructural parameters have previously been related to cell performance [106, 107]. As described in Sec. 1.2.3, many of the specific mechanisms of cathode degradation are still unclear, but it is known that the microstructure plays a critical role in cell performance [107]. The total polarization resistance experienced by the cathode (R_{cathode}) is an additive function of the various resistances (R_p) caused by distinct polarization processes (see Fig. 1.13) [108]. Ultimately, each R_p depends on particular microstructural parameters (and some on reaction kinetics), enabling correlation of performance degradation measurements with microstructural ones.

A significant amount of prior research aiming to characterize the microstructural parameters of SOFC cathodes (and anodes, as well) has been carried out. In recent years, the tool of choice for this characterization has been a dual beam focused ion beam/scanning electron microscope (FIB/SEM), used to perform a tomographic reconstruction of a cell (see Sec. 4.1). The proposal and initial refine-
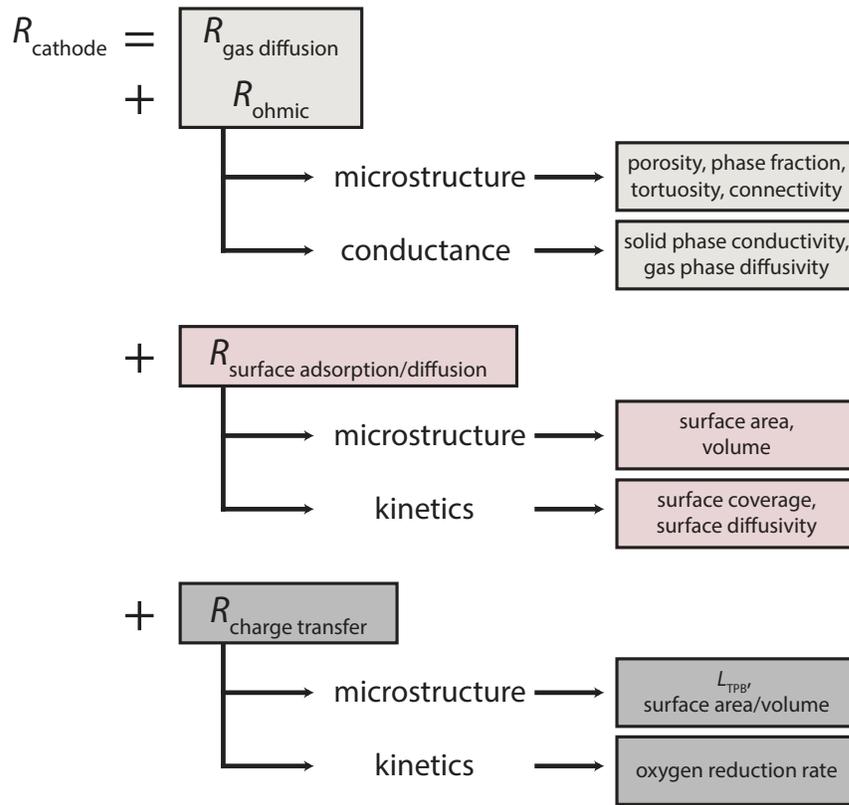
Figure 1.13: The total polarization resistance of the SOFC cathode (R_{cathode}) is comprised of multiple contributions (gas diffusion, ohmic, *etc.*), which are in turn controlled by various sample characteristics (microstructure, conductance, or kinetics). Each of these characteristics can be directly related to a quantifiable parameter (porosity, surface area, *etc.*).

ment of the FIB/SEM-nanotomography (FIB-*nt*) procedure was first reported in the early 2000s [109, 110]. Application of the technique to SOFC anodes and cathodes soon followed from the Barnett Group (Northwestern University) and the Wachsman Group (University of Florida) [111, 112]. These works pioneered the use of the FIB/SEM to quantify basic electrode layer parameters, such as porosity, phase surface area and volume, and particle size.

Analysis of phase and topological connectivity can also be accomplished with

the FIB/SEM, which reveals parameters expected to affect bulk transport [106, 113]. Tortuosity, another important microstructural parameter related to the effective diffusivity of a phase has been quantified in a myriad of ways, ranging from simple center of mass considerations to finite element modeling [106, 113, 114]. A natural extension of these nanotomographic methods is to examine the three dimensional interface between all phases, known as the triple phase boundary (TPB), and to quantify both the total triple phase boundary lengths (L_{TPB}), as well as the fraction of these that are expected to be electrochemically active or inactive [106, 111, 113, 115].

Ultimately, the microstructural parameters in question need to be related to cell performance in order to prove useful. Smith *et al.* [107] demonstrated this process in their work relating L_{TPB} and phase specific surface area to various measured polarization resistances (R_p), revealing the relationships shown in Fig. 1.14. In their work, electrochemical impedance spectra (EIS) of an SOFC with an LSM cathode and YSZ electrolyte (not composite) were measured. The constituent R_p values were extracted through equivalent circuit modeling and compared to L_{TPB} measurements derived from FIB/SEM observations on the same samples. The R_p values due to both adsorption of oxygen to the cathode surface and charge transfer of electrons to the cathode were found to have an inverse power-law correlation to the density of L_{TPB} within the cathode. This result was a direct observation of the effect that the number of available reaction sites for the ORR has on the specific polarization resistances.
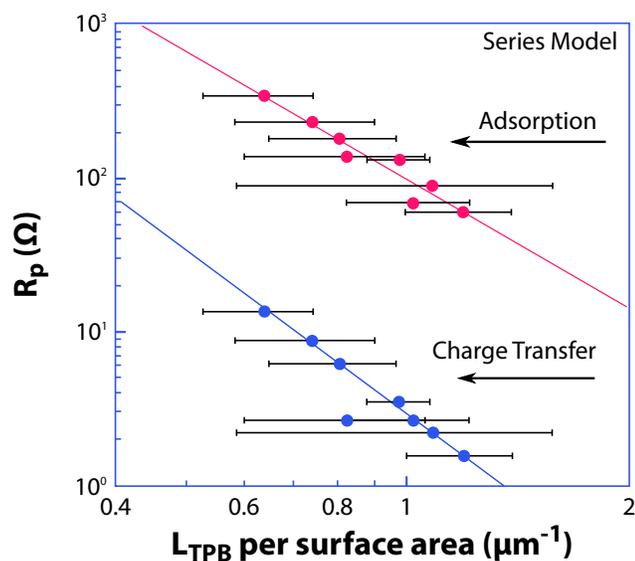
Figure 1.14: Charge transfer and adsorption resistances in relation to L_{TPB} measured in air at 800°C for an LSM on YSZ cathode. Electrochemical impedance spectroscopy data was fit with a series equivalent circuit model to extract R_p values. Figure recreated with data from [107].

1.2.5 Goals of this research

While promising, the performance of SOFCs is still well below what is required for wide spread commercial success due to the accelerated degradation of the cathode layer. The fundamental mechanisms of this degradation (and its effect on cathode microstructure) are unclear. With a better understanding of how (and why) the cathode degrades, improvements to cell fabrication and processing will be enabled, facilitating the introduction of higher performance SOFCs into the marketplace.

Additionally, while a substantial amount of development has been put into methods by which to quantify SOFC microstructure, few (if any) of these tools have been made publicly available. Every group uses its own codes to process

37

data and produce measurements of cell parameters (in particular, tortuosity and L_{TPB} calculations vary widely in implementation). This disparity precludes useful comparisons between results from different research groups because the changes cannot be specifically linked to physical alterations, as opposed to methodological differences. Comparisons between various techniques are needed, as well as an open framework through which to analyze FIB/SEM nanotomographic data.

This work contributes towards the solution of both problems. A significant portion of the work focuses on the development and description of techniques used both during the acquisition of FIB-nt data, as well as those used to filter, process, and measure the data. These methods are well documented have been distributed via a public software repository in order to facilitate collaborative improvements in FIB/SEM microstructural quantification amongst the community. Documentation of the modules developed in this work is available in Ref. [116].

Besides methodological contributions, this thesis provides a detailed study of the degradation of two SOFC cathode systems, presented in Chapter 4. In the first, the impacts of H_2O and polarization on LSM-YSZ composite cathodes are investigated. The microstructure of the cells is quantified via FIB-nt, and an analysis of the degradation products using TEM-EELS and EDS is provided. The second system analyzed is a series of LSCF-GDC composite cathode cells. For this material, the impacts of H_2O, CO_2, and Cr-vapor are all analyzed, and irreversible changes in the cathode microstructure are quantified and described. Like the LSM-YSZ system, compositional analysis of the degradation products is performed and a relationship between the microstructural parameters and cathode performance is described.

Chapter 2:   Introduction to experimental methodologies

2.1   Analytical transmission electron microscopy

A TEM is a unique instrument, in that it is the only tool capable of directly imaging the interior of a specimen with atomic level resolution. The TEM operates with a similar principle to a transmission light microscope, but using accelerated electrons as the illumination source, rather than visible light, and electromagnetic lenses instead of glass lenses. The greatest benefit of a TEM compared to a visible light microscope is the immense increase in resolution that can be achieved with electrons. A useful (if oversimplified) estimate of TEM resolution can be obtained through the use of the Rayleigh criterion, originally developed for resolving overlapping diffraction disks in optical experiments [117]. The criterion states that the smallest distance (δ) resolvable by a source of electromagnetic radiation (in the classical case, light) is proportional to the wavelength (λ) of the illumination source:

$$\delta = \frac{0.61\lambda}{\mu \sin \beta} \tag{2.1}$$

where μ is the refractive index of the viewing medium and β is the semi-angle of collection of the magnifying lens. In an electron microscope, δ will be a theoretical smallest resolvable distance due to practical limitations in lens design and the

presence of various apertures [118, 119]. Typically, $\mu \approx 1$ and $\beta \approx \frac{\pi}{2}$ (without a limiting aperture), such that the denominator of Eq. 2.1 can be approximated to unity. With a λ value of 2.5 pm, this results in a $\delta = 1.53$ pm. For comparison, state-of-the-art aberration corrected microscopes are capable of 55 pm resolution, illustrating the difference between theory and reality [120].

The wavelength of an accelerated electron can be calculated by utilizing the de Broglie wave-particle duality relationship between wavelength and momentum. Since electrons in a TEM travel at speeds comparable to c (speed of light), it is necessary to use a relativistic momentum when calculating λ:

$$\lambda = \frac{h}{p} = \frac{h}{\sqrt{2m_0 eV \left(1 + \frac{eV}{2m_0 c^2}\right)}} \qquad (2.2)$$

where h is Plank's constant, m_0 is the rest mass of an electron, e is the elementary charge of the electron, V is the accelerating voltage of the electron beam, and c is the speed of light. Using Eq. 2.2, it can be determined that at the energies used in a TEM (typically 80 to 300 keV), the wavelength of the electrons is approximately 2 to 4 pm, compared to ≈ 400 nm for visible light. Combining this result with Eq. 2.1, it is clear that this drastic reduction in wavelength corresponds to a dramatic improvement in resolving power, and as such, obtaining atomic-resolution images is commonplace, although aberrations arising from lens imperfections worsen the absolute resolution when compared to Eq. 2.1.

The microscope used primarily in this work is a JEOL *JEM-2100F* field emission TEM. In a field emission gun (FEG) TEM, electrons are extracted from a very sharp tungsten tip and accelerated to high energies (200 keV in this work),

providing good resolution with high brightness (current density). This TEM, located within the University of Maryland AIMLab, is equipped with scanning coils to operate in scanning (STEM) mode, as well as a Gatan *Tridiem 863* post-column electron energy loss spectrometer (EELS) and an *Oxford INCA 250* EDS system for spectroscopic analysis. Operating with a 200 kV voltage, the microscope has a point-to-point resolution of 0.19 nm in conventional mode, and 0.2 nm in STEM mode. As mentioned, when compared with the values obtained in Eq. 2.1 the resolution is significantly worse, due to the limitations imposed by the aberration coefficients of the electromagnetic lenses within the column [118, 119].

2.1.1 Conventional vs. scanning microscopy

Traditionally, a TEM is operated in conventional mode (as illustrated in Fig. 2.1), meaning that the sample is illuminated with a parallel beam of electrons, and the interactions of this beam with the specimen are viewed (in projection) on the fluorescent screen or CCD camera. This is the preferred mode of operation for high-resolution TEM (HRTEM), selected area diffraction (SAD), and bright/dark field (BF/DF) imaging. Conversely, the microscope can also form a highly focused probe, converging the beam to a single point on the sample (0.2 to 1.5 nm in diameter for the microscope used in this work). In this (scanning) mode, the STEM probe can be operated much like an SEM, but with the beam transmitting through the sample. The focused probe allows for very precise collection of bright and dark field imaging signals, as well as highly-localized analytical analysis, which is critical

for studies of interfaces and nano-sized features, as investigated in this work. For further details of the techniques, please refer to Refs. [118, 119, 121, 122].

2.1.2   Electron energy-loss spectroscopy (EELS)

The primary analytical TEM method used in this work is electron energy loss spectroscopy (EELS). In this technique, the energy distribution of the primary electron beam is analyzed after interacting with the thin lamella specimen. In much the same way a glass prism spreads light into its constituent wavelengths, the EELS spectrometer, located at the bottom of the TEM column, separates the electron beam by the energy of the electrons contained within. These electrons begin their path down the column with a definite energy (in this work, 200 keV). A proportion of the electrons in the beam interact with the sample through inelastic scattering events, causing them to lose a certain amount of energy that can be attributed to particular physical processes. These interactions appear at specific energies within the spectrum and can be clearly identified [124–126].

An example of a typical EEL spectrum is shown in Figure 2.2. At low energies, the spectrum is dominated by the *zero-loss* or *elastic* peak (ZLP). This peak represents the electrons that pass through the sample without measurable energy loss. This includes electrons that do not interact with the specimen, as well as those exciting phonon modes within the sample. At energies < 0.5 eV, these vibrational mode interactions are at too low an energy to be faithfully deconvolved from the non-interacting zero-loss peak in TEM-EELS, requiring methods such as reflection
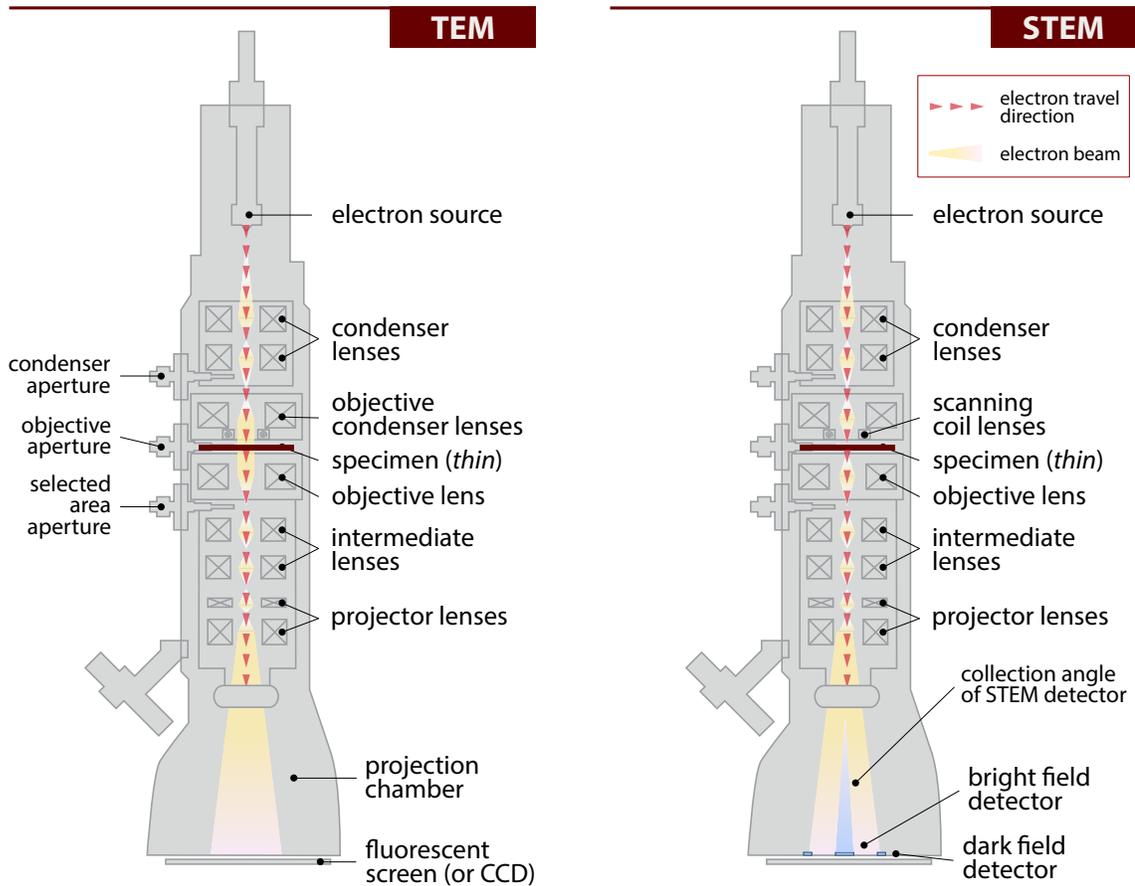
Figure 2.1: Representative schematic of a general TEM system design operating in conventional (CTEM) mode (*left*) and scanning (STEM) mode (*right*). In both cases, electrons originate from a high voltage source at the top of the column, and are condensed by a series of electromagnetic lenses into a collimated beam that interacts with the thin specimen. In CTEM, the transmitted electrons are formed into an approximately parallel beam of illumination before interacting with the sample, which is then formed into an image (or diffraction pattern) by the objective lens. The result is projected onto a phosphor screen (or CCD camera) by the intermediate and projector lenses. Apertures throughout the system allow selective use of different parts of the electron beam. In STEM mode, the behavior is much the same, except for an additional pre-specimen condenser lens that forms a highly localized probe on the sample. The scanning coils are used to steer the beam around the sample. Post-specimen projection of the beam is similar to CTEM, but rather than measuring an image, electron counts are measured on either a center (BF) or annular (DF) detector. Figure adapted from [123].
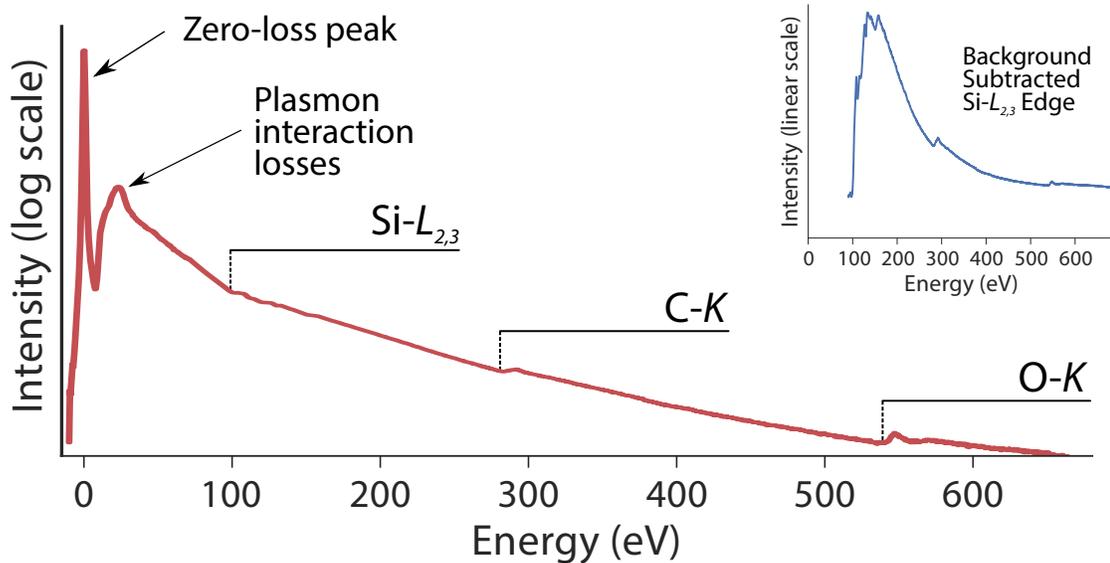
Figure 2.2: Example EEL spectrum plotted on a logarithmic scale. This spectrum, from the interface of SiC and SiO$_2$, shows all the expected features of the low- and core-loss energy ranges, as indicated on the plot. (*inset*) The data on a linear scale, after subtracting a power-law background fit to energies slightly lower than the Si-$L_{2,3}$ edge.

high-energy electron loss spectroscopy (RHEELS) or a highly specialized TEM to measure [127, 128]. The ZLP provides a convenient way to measure the energy resolution of the TEM, usually defined as the full width half-maximum (FWHM) of the ZLP. In the TEM used in this work, this resolution is typically on the order of 1.0 ± 0.1 eV.

The remainder of the spectrum ($\gtrsim 4$ eV) is due to the *inelastic* scattering of electrons. At the lower energies (within the first 50 eV or so), this is due to excitations of outer-shell (conduction or valence) electrons within the sample. This portion of the spectrum is typically dominated by energy losses arising from the collective excitations of the weakly-bound electrons in the sample. These excitations cause a collective oscillation of the charge density in the lamella along the electron's

trajectory, known as a *plasmon.* This interaction is the second most intense feature in an EELS spectrum (next to the ZLP), and evidenced by a peak centered at the plasmon energy $E_p = \hbar\omega_p$, where ω_p is the plasmon frequency of the material ($\omega_p \propto N_V$, where N_V is the valence electron density).

If the sample is sufficiently thin (thinner than the plasmon mean free path, L_p), there will be only one such plasmon peak. Otherwise, due to multiple scattering events, subsequent peaks will be evident at integer multiples of E_p. These peaks will interfere with signals of interest at higher energies, giving rise to an upper limit to the practical thickness of a specimen in EELS (dependent on the material's L_p). To ensure the measurement of single-scattering spectra in this work, samples were thinned to a thickness ranging from 25 to 80 nm (although usually below 50 nm), well below the estimated L_p for SiC and SiO_2 of ≈ 115 nm [129].

At higher energies ($\gtrsim 50$ eV), interactions with inner-shell electrons become measurable. These core-shell excitations appear within the spectrum as asymmetric "edges" (rather than peaks) due to the precise minimum energy required to induce the excitation of a core electron. Compared to other analytical techniques (such as XPS or EDS), the signal-to-background ratio for a core-loss EELS edge is generally quite low, due to the superposition of the edge on a slowly-decaying background signal of the lower energy-loss excitations. This background can usually be suitably modeled by a power-law function, and is typically removed prior to quantitative analysis of the spectrum (see the inset of Fig. 2.2) [124]. The core-level excitation raises a tightly bound electron from its relaxed state into an unoccupied state within the conduction band (CB) of the sample. For each atomic orbital (and each element),

45

a minimum ionization energy is required to promote an electron into the conduction band, and thus a sharp rise in intensity takes place at the *ionization threshold*, which is roughly equivalent to the binding energy (BE) of the specific atomic orbital in question. For example, the Si-$L_{2,3}$ edge (in silicon) has its onset at $99\,\mathrm{eV}$, which corresponds to the approximate BE of the Si $2p^{1/2}$ and $2p^{3/2}$ orbitals.

A number of practical quantifications and electronic structure information can be inferred from an EELS spectrum. The integrated intensity of each element's signal can be used to obtain relative (and sometimes absolute) atomic concentrations from the spectrum, allowing for elemental quantification (see Sec. 2.1.2.1) [125].

Furthermore, due to the band structure of a material (its electronic configuration), there are many final states into which a core-level electron can be excited. This means that the intensity profile of an EELS edge contains *fine structure*, or variations in intensity within about $50\,\mathrm{eV}$ of the ionization threshold. Alternatively, this fine structure is referred to as the energy-loss near-edge structure (ELNES) of the edge [125]. These variations are intimately related to the unoccupied density of states of a material (into which the electrons are excited), and can be used to directly probe the electronic structure of a specimen [130]. In fact, the ELNES of an edge can be modeled and compared to experiment by calculating the *symmetry-projected* density of states at a given energy. This calculation is then convolved with Lorentzian functions to account for energy broadening arising from the finite initial and final state carrier lifetimes (plus another to account for the instrumental broadening measured at the ZLP) [124]. Fig. 2.3 demonstrates how the fine structure (as well as the precise edge onset energy) of the Si-$L_{2,3}$ EELS edge changes

significantly depending on the bonding configuration of the Si atoms within different materials [131]. In this thesis, the fine structure of the Si-$L_{2,3}$ edge (as well as the C-K and O-K edges) will be used extensively to characterize the bonding of Si at SiC/SiO$_2$ interfaces.

2.1.2.1 Elemental quantification

Because each ionization edge occurs at an energy specific to a particular element, one can obtain quantitative information regarding the elemental concentrations by integrating the intensity of each element's core-loss edge. To do this, the background is removed by fitting a power law function: AE^{-r} to the spectrum in the pre-edge energy range and subtracting it from the signal. The resulting intensity is then integrated over an energy range Δ. Assuming $\Delta > 50\,\text{eV}$, the variations in the ELNES typically average out, but if a spectrum has two closely spaced overlapping edges, it is extremely difficult to obtain an accurate quantification due to the significant contribution of the ELNES over a limited Δ.

An example of the quantification procedure is shown in Fig. 2.4. After fitting and subtracting of the background, the integrated quantity I_c represents the amount of the element independent of its atomic environment. It is important to note that I_c is a function of both the integration window Δ (selected by the user), and the collection semi-angle β, defined by the final limiting aperture of the EELS system (limiting the angle of scattered electrons that are admitted to the spectrometer). With the I_c integral calculated, the *areal density* of the element (in units of atoms
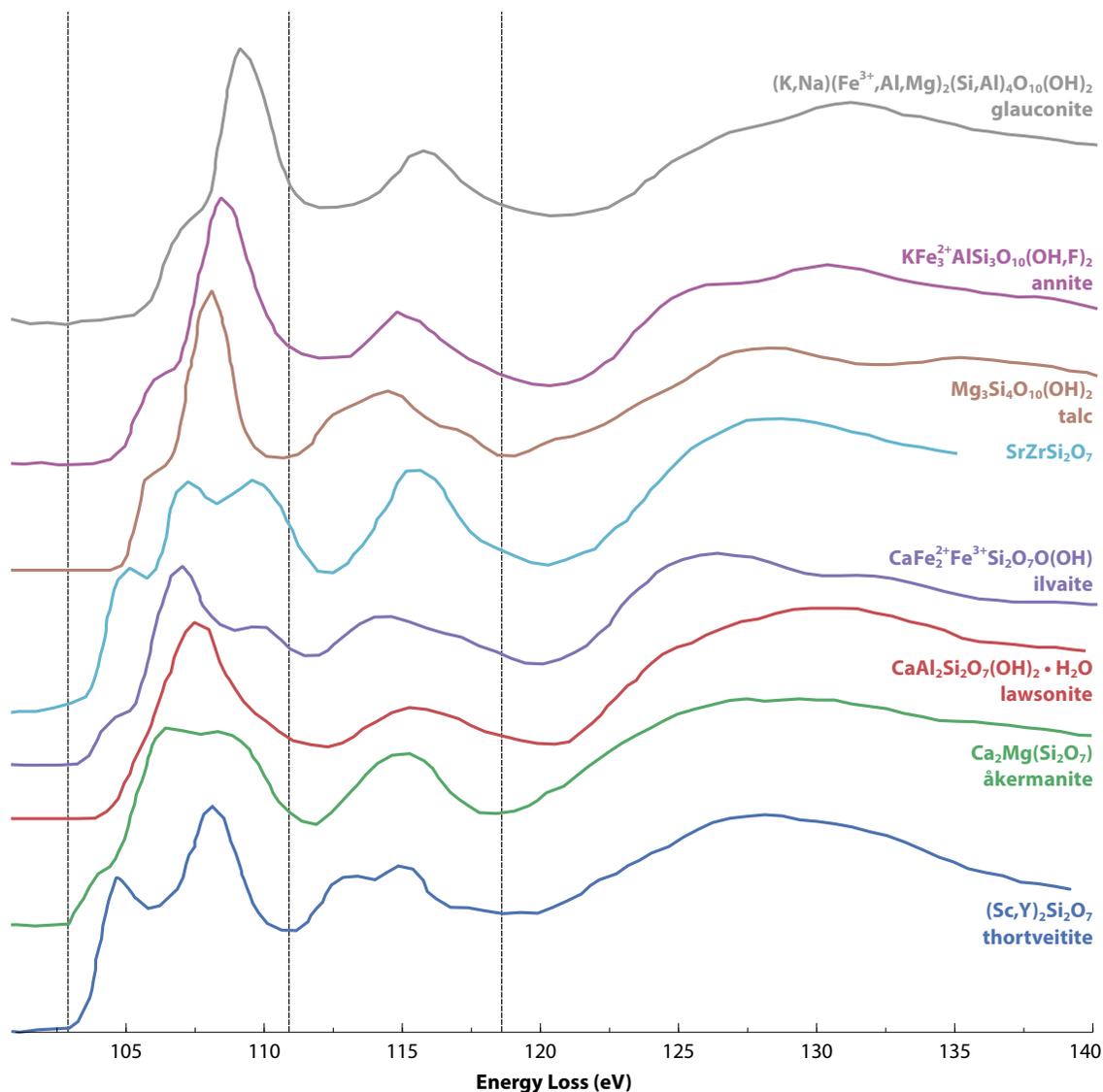
Figure 2.3: Comparison of the Si-$L_{2,3}$ edges for various types of silicate minerals. The specific mineral for each edge is indicated in the figure. The dashed vertical lines are aligned to the features of the thortveitite edge, clearly illustrating how the spectral features vary throughout the edges. In particular, the edge onset energy and the position of the various peaks change significantly depending on the material. The differences in the ELNES of the Si edge reflect the differences in the electronic structure of Si in each of the minerals. Figure recreated with data from Garvie *et al.* [131].
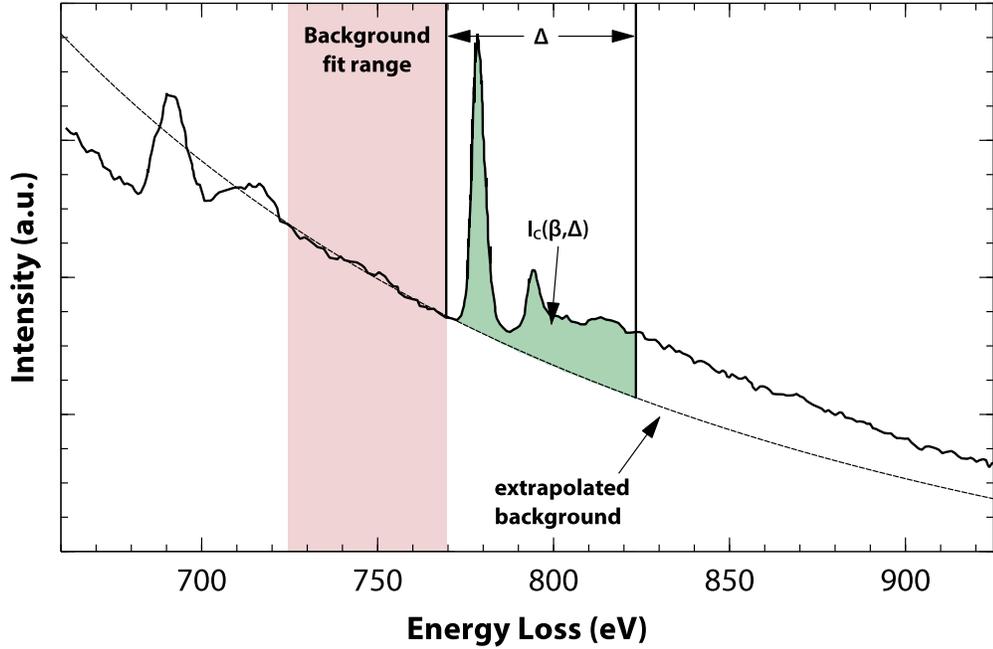
Figure 2.4: Procedure for elemental quantification (using the Co-$L_{2,3}$ edges as an example). A power law function is fit to the background in the area preceding the edge of interest, and the intensity of the EELS edge is integrated over a window Δ to give $I_c(\beta, \Delta)$. Figure adapted from Egerton [124].

per unit area) N, can be estimated as:

$$N \approx \frac{I_c(\beta, \Delta)}{I_l(\beta, \Delta)} \; \sigma_c(\beta, \Delta) \tag{2.3}$$

In Eq. 2.3, $\sigma_c(\beta, \Delta)$ is a partial scattering cross section for the element in question, which can be determined from Hartree-Slater calculations [132]. The other integral in the equation, $I_l(\beta, \Delta)$, represents an integral of the low-loss spectrum up to an energy-loss Δ, including the ZLP. Thus, Eq. 2.3 provides a method to obtain absolute quantification of an element, so long as the ZLP can be obtained simultaneously. If the thickness (t) is known, the total concentration n can be obtained by dividing the area density by the thickness ($n = N/t$). The primary source of error in these calculations arises from σ, the calculated cross sections,

and from the selection of the pre-edge background, giving a practical error in the quantification of about 10% [133].

Typically, it is more useful to find the elemental ratios within a sample, which can be calculated using Eq. 2.3. Collecting a spectrum containing two elements (A and B), figuring each element's areal density and then dividing them gives the following:

$$\frac{n^{\mathrm{A}}}{n^{\mathrm{B}}} = \frac{N^{\mathrm{A}}}{N^{\mathrm{B}}} = \frac{I_{\mathrm{c}}^{\mathrm{A}}(\beta, \Delta)}{I_{\mathrm{c}}^{\mathrm{B}}(\beta, \Delta)} \frac{\sigma_{\mathrm{c}}^{\mathrm{B}}(\beta, \Delta)}{\sigma_{\mathrm{c}}^{\mathrm{A}}(\beta, \Delta)}. \tag{2.4}$$

It follows from Eq. 2.4 that neither the sample thickness nor the low-loss spectrum is needed to calculate elemental ratios in a spectrum, providing a simple yet powerful means of quantifying elemental composition from EELS spectra. When combined with STEM spectrum imaging, this technique also allows for easy calculation of compositional maps [124, 125].

2.1.2.2 Multivariate data analysis

Besides the quantification methods described in Sec. 2.1.2.1, there are a number of newer and more advanced techniques that allow for one to gain a deeper understanding of the EELS data that is collected. In a typical EELS experiment, data is collected in a spectrum imaging mode. In such a mode, the beam is scanned across an area of interest, collecting an EELS spectrum at each point. This can result in large datasets (300 MB of raw data for a 200 x 200 x 2048 dataset), and while they do not precisely qualify as "big data" per se, some of the data analysis methods from that field are indeed useful when processing spectrum images (SI).

Of particular interest (in this work and others), is the analysis of mixtures within a spectrum image. While it is fairly simple to analyze a specimen of uniform composition, it becomes significantly more difficult to detect small changes in the signal at features such as interfaces, inclusions, etc. In such a sample, the EELS signal is dominated by the overall matrix (bulk) component, making it difficult to accurately determine (and quantify) the unknown weaker component. This is directly relevant to the SiC/SiO_2 system investigated in this thesis, as there is great uncertainty regarding the presence of distinct atomic structures and/or electronic states at the interface. A technique that could resolve and quantify both the known and unknown components at this interface would indeed prove incredibly useful.

Initially, the predominant technique used for this sort of problem was one called the multiple linear least-squares (MLLS) fitting method [134]. In this technique, one or more reference spectra are used as linear components, and are scaled linearly to best fit the collected data at each point in the spectrum image. If the residual is close to zero at all points, then the data is simply a linear combination of the reference spectra. Where there is a worse fit, it is likely that another component is present. While looking at the residual between the model and fit can give some indication as to the nature of the unknown component, the MLLS method does not do well at separating multiple unknowns, and the results are extremely sensitive to the choice of reference spectra, and is clearly not of particular use when reference spectra are unavailable.

A more advanced class of methods, known as multivariate statistical analysis (MVA or MSA) [135], become very useful when trying to identify unknown signals

51

within an large dataset such as an EELS SI. These techniques aim to describe the data as a function of multiple known or unknown variables, where each variable represents a specific physical spectrum source within the sample. The algorithms operate by finding statistical correlations in the distribution of data, and as such, become more powerful (and more sensitive) as more data is collected. Thus, they are particularly well-suited to the analysis of larger datasets collected as a line of spectra or a 2D spectrum image. The improvement compared to traditional analyses arises from treating the dataset as an ensemble, and analyzing the data globally by projecting the data from a high-dimensionality space onto one of reduced dimension [136]. The benefits of this approach, rather than analyzing an SI spectrum-by-spectrum will become clear throughout this work.

Specifically, the class of MVA algorithms that are of interest for EELS SI analysis are known as unsupervised or blind algorithms, which are able to extract constituent phase information from the hyperspectral mixtures acquired in an SI. An algorithm is blind if it operates based on the output observations only (the measured data), meaning that no biased *a priori* assumptions are made about what results should be found in the data (this is decidedly not the case in MLLS, where a user-supplied reference spectrum is required). Generally, the problem of identifying signal sources within data such as an EELS SI is a problem referred to as "spectral unmixing," and is an active area of research in the computer science field, with applications far beyond just EELS analysis [137, 138]. Indeed, these types of algorithms have found utility in geological remote sensing [139], X-ray absorption spectroscopy [140], scanning probe microscopy [141], and only recently, electron

microscopy [136, 142–150], as briefly reviewed in the following section.

2.1.2.3   MVA for EELS spectrum imaging

Principal component analysis

One of the simplest, and perhaps most widely used MVA techniques is principal component analysis (PCA) [136, 142, 144]. The goal of PCA is to reduce the dimensionality of the collected data while retaining its important internal characteristics, with the goal of removing the parts of the data that do not contribute to the overall information content (i.e. noise). In an areal spectrum image, this is done by storing the spectral data (E) for the two spatial dimensions (x, y) in a matrix $\mathbf{D}_{(x,y),E}$. $\mathbf{D}_{(x,y),E}$ can then be decomposed as

$$\mathbf{D}_{(x,y),E} = \mathbf{S}_{(x,y),n} \times \mathbf{L}^{\mathrm{T}}_{(E,n)} \tag{2.5}$$

where $\mathbf{S}_{(x,y),n}$ is known as the *score* matrix, and $\mathbf{L}^{\mathrm{T}}_{E,n}$ the *loading* matrix. In the context of EELS SI, each row of $\mathbf{L}^{\mathrm{T}}$ contains a spectral signature that is uncorrelated to the other rows. In typical linear algebra parlance, the rows of $\mathbf{L}^{\mathrm{T}}$ would be known as eigenvalues. In spectroscopic analysis, they are correspondingly referred to as eigenspectra. Conversely, each column of $\mathbf{S}$ is a description of the spatial amplitude of each eigenspectrum from $\mathbf{L}^{\mathrm{T}}$, illustrating where within the SI that component is the strongest. The products of each row of $\mathbf{L}^{\mathrm{T}}$ and each column of $\mathbf{S}$ are known as the principal components (hence the origin of the name PCA).

Practically, the decomposition in Eq. 2.5 can be accomplished through eigenanalysis or singular value decomposition (SVD) [151]. Each eigenspectrum of the

decomposition will be orthonormal to all the others, and $\mathbf{L^T}$ can be intuitively thought of as a transformed set of basis vectors for the data, such that the new axes point along the directions of highest signal variance. The relative magnitude of each eigenspectrum describes how much of the variance (of the overall data) is explained by each component, and by sorting the principal components in order of decreasing intensity, an idea of which components are most important (as opposed to just noise) can be obtained.

An example of this sort of analysis is shown in Fig. 2.5, taken from the work of Peña *et al.* [146]. In this example, an EELS spectrum image was acquired from a TiO_2-SnO_2 solid solution (nominally $Sn_{0.5}Ti_{0.5}O_2$), which has been spinodally decomposed. Their ultimate goal was to characterize the chemical composition of the decomposed phases at high resolution. PCA was applied to the EELS data, resulting in 15 principal components. Sorting the components by magnitude and plotting their explained variance in a *scree plot* provides useful insights into the statistical distribution of the data. As can be seen in Fig. 2.5a, the first three components contain the vast majority (98.3%) of the variance. Typically, an analysis is performed including only the components that do not lie on a straight line towards the higher-index end of the scree plot. Since the eigenvalues of the purely noise-containing components decrease exponentially, they are expected to lie on a straight line in the logarithmic scree plot, as is observed [144].

While the three components shown in Fig. 2.5(b-d) are the most important, it is clear from their spectral shapes that they cannot be directly interpreted as EELS spectra. Each of the three components contains signal variation from all of the
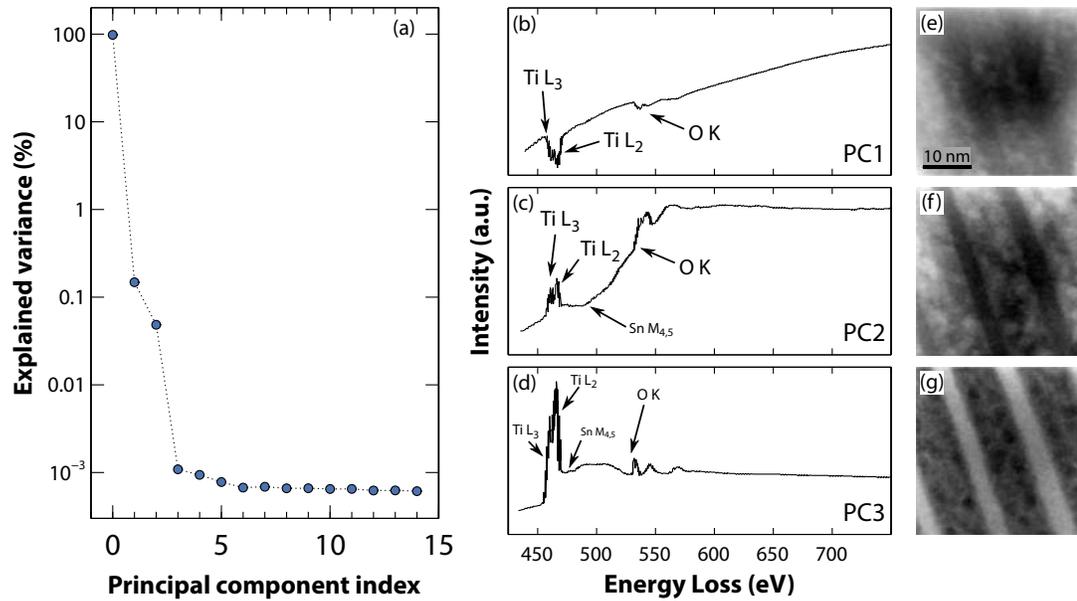
Figure 2.5: Example of a PCA decomposition analysis of an EELS SI dataset collected from a $Sn_{0.5}Ti_{0.5}O_2$ ceramic. (a) Scree plot showing how much variance in the data is explained by each principal component. (b-d) The first three principal components (eigenspectra), which collectively describe 98.3% of the overall data variance; (e-g) their corresponding loading maps (distributions). Figure adapted from Peña *et al.* [146].

relevant edges, making it difficult to interpret the distribution maps. Indeed, this is a well-documented problem with PCA [136], which arises from the assumption of orthogonality between components. This is strictly untrue in EELS data, as the constituent spectra are often highly correlated (as they share a common background and perhaps chemical composition). This assumption makes PCA rather unfit for detailed compositional analysis of EELS data. Nevertheless, it is an extremely useful method to denoise data (by discarding those components explaining little total variance) and to provide an initial insight into the areas of the spectra exhibiting the most variation. For compositional analysis, more advanced techniques are needed to extract physically interpretable components.

Independent component analysis

As mentioned, PCA allows for qualitative interpretation of the dataset (and improving signal-to-noise ratio), but it is not particularly useful at describing new or unknown spectra due to the orthogonality assumption. Another class of algorithms, known as independent component analysis (ICA) [152], are concerned with transforming the principal components to maximize the degree of independence between them (n.b. depending on the author, ICA is sometimes referred to as blind source separation (BSS), given its unbiased nature) [153]. This can be envisioned as a rotation of the axes from an *orthogonal* representation of the data to an *independent* one. Choosing the correct function to maximize independence between components (the "contrast function") is a difficult problem and an active area of research [152]. Various algorithms using different contrast functions have been implemented, and have varying degrees of success in separating EELS signals [154]. One of the most commonly used (and the one used in this work) is the FastICA algorithm [155], which minimizes the mutual information between components through a fixed-point iteration scheme by maximizing the non-Gaussianity, which functions as an estimate of independence. It should be noted that while ICA often leads to more interpretable results than PCA alone, the assumption of independence between components within a sample is not always valid, meaning that ICA components can often contain unphysical features (such as negative peaks) that require careful interpretation.

A practical example of ICA applied to EELS data is shown in Fig. 2.6. This data is a continuation of the analysis from Fig. 2.5 by Peña *et al.* [146]. By applying
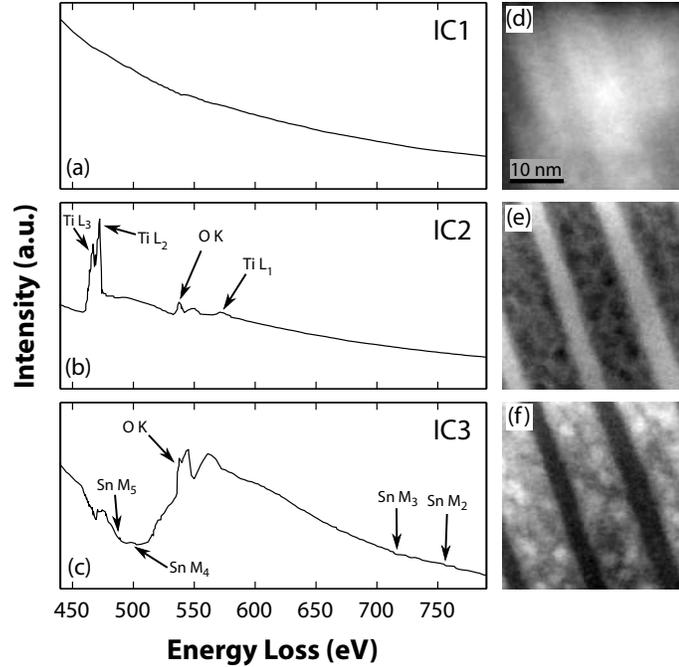
Figure 2.6: Example of an ICA decomposition analysis of an EELS SI dataset collected from a $Sn_{0.5}Ti_{0.5}O_2$ ceramic. (a-c) The first three independent components, which still collectively describe 98.3% of the overall data variance; (d-f) their corresponding loading maps (distributions). Figure adapted from Peña *et al.* [146].

an ICA algorithm to the three principal components previously obtained, a more physical representation of the data was obtained. The first component (IC1) closely resembles the background that is observed in all EELS spectra, which is usually modeled to the first order by an inverse power-law function. The intensity of this background component will be a function of the specimen thickness, as well as the degree of carbon contamination (since the area investigated is at energies higher than that of the C-K edge at $284\,eV$). The second component (IC2) is very similar to the expected spectrum for rutile TIO_2, and its distribution map reveals that the TiO_2 is localized in Ti-rich layers typical for spinodal compounds. The final component (IC3) reveals a spectrum that was not observed at all in the raw data, due to the

57

strong overlap of the Ti and Sn EELS edges and the weak nature of the Sn-*M* edge compared to the sharp Ti spectral features. This signal contains variations indicative of SnO_2, with stronger intensity in the Ti-deficient layers. Interestingly, the Sn signal does not appear uniform between the Ti layers, but instead is clustered into nm-sized Sn-rich grains.

This sort of analysis demonstrates the added qualitative insight that can be obtained through the use of PCA + ICA, compared to traditional EELS SI mapping methods. Unfortunately however, the MVA methods preclude direct quantification of elemental composition, because the components have arbitrary scales and scores arising from the matrix decomposition (PCA) and transformation (ICA). Relative variations in the component weights however, do contain real information that can be used to infer about the phase distributions. Likewise, if a standard quantification is possible, its results can be used to normalize the independent components and their weights [146].

Non-negative matrix factorization

While the lack of assumptions used in blind unmixing is very useful in preventing biased data analysis, it can sometimes result in less than ideal separation of components, leading to (for example) negative spectral intensities that are clearly unphysical [154]. The introduction of select prior assumptions (where appropriately valid) can drastically enhance the resulting unmixed components by reducing the complexity of the problem and limiting the size of the potential solution space. One such criterion that is particularly useful in EELS unmixing is the enforcement of a positivity constraint. Since the collection of an EELS spectrum is a Poisson process

by definition there can be no negative values. Non-negative matrix factorization (NMF) is a matrix decomposition technique introduced in 1999 that can be used as an alternative to SVD [156]. Thus, the challenge is the same as for PCA. Namely, a decomposition of the matrix $\mathbf{D}_{(x,y),E}$ into a basis set and its corresponding weights, as shown in Eq. 2.5.

The primary difference between NMF and PCA arises from the differing constraints placed on the matrix factors $\mathbf{S}$ and $\mathbf{L}$. For PCA, the columns of $\mathbf{S}$ must be orthonormal and the rows of $\mathbf{L}$ must be orthogonal, leading to eigenspectra like those found in Fig. 2.5, which are intuitive statistically (i.e. they have maximal intensity in the directions of largest variance), but are clearly unphysical in nature. By contrast, NMF prohibits negative values in $\mathbf{S}$ and $\mathbf{L}$, leading to positively-valued components that describe the observed data in an additive fashion, meaning they are compatible with the intuitive interpretation of combining parts of a signal to create a holistic representation of the overall data. It is this characteristic that makes the result of an NMF unmixing a *parts-based* representation of the data [156].

NMF has been used for EELS SI data, but only recently and only on a very limited scale (e.g. a June 2016 Google Scholar search for papers published after 1999 with the terms "'transmission electron microscopy' 'EELS' 'NMF' 'non-negative matrix factorization' " returned fewer than 10 relevant results, with the vast majority originating from the Midgley group at the University of Cambridge) [147, 150, 157–161]. This nascent technique however, shows great promise for the simple interpretation of unmixed EELS spectrum images.

An example NMF unmixing of EELS data is shown in Fig. 2.7 from a study

59
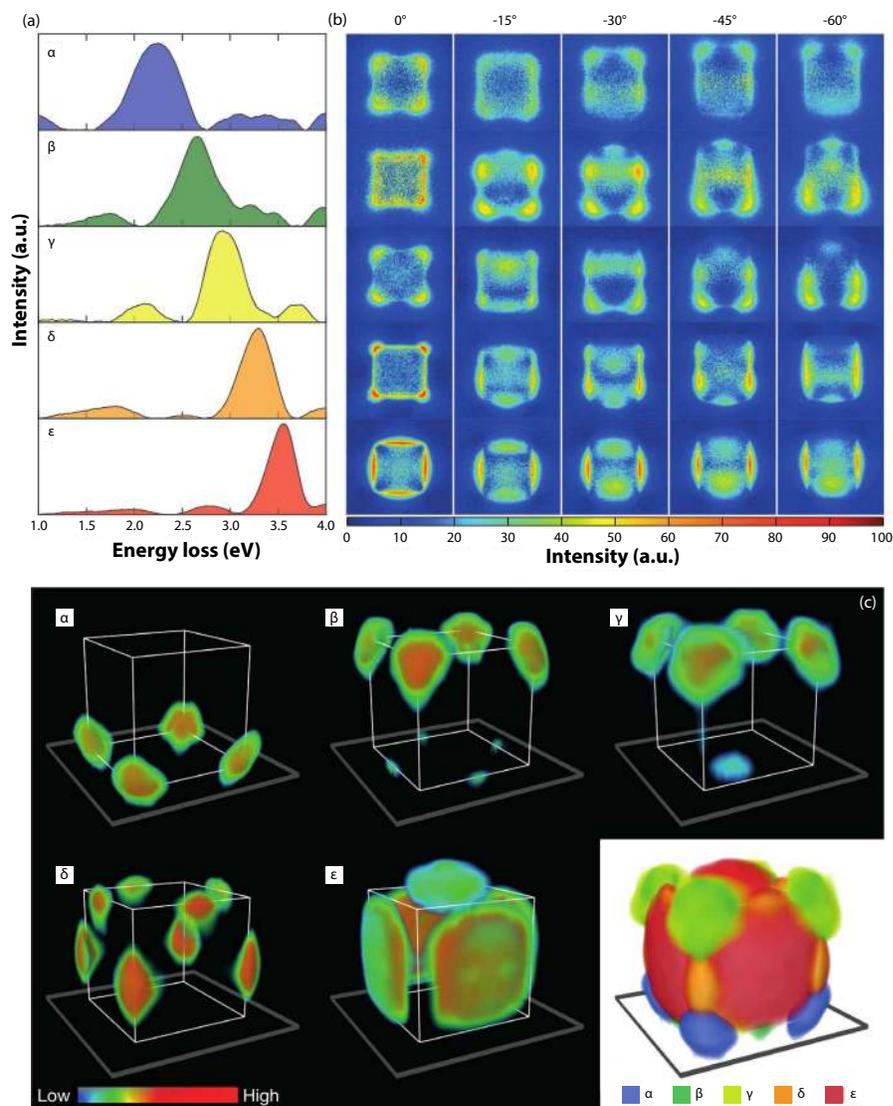
Figure 2.7: Example of NMF spectral unmixing applied to a low-loss EELS spectrum image, combined with TEM tilt tomography. In (a), five spectral components were extracted with NMF, and their corresponding loadings (distributions) are shown in (b) at each tilt angle. Each row is one component, and each column is a different tilt value. (c) Three-dimensional tilt reconstructions of the five plasmon modes, illustrating how the different modes can be extracted, even when they are severely overlapping. Figure adapted from Nicoletti *et al.* [148].

performed by Nicoletti *et al.* [148]. In this work, the authors measured the low-loss plasmon region of a silver nanoparticle (NP) to investigate the energy and distribution of the localized surface plasmon resonances (LSPRs). These modes involve shifts of the surface plasmon peak of only a couple eV, and due to the very small dimensions of the NP, the modes are almost always overlapping in a TEM measurement. By acquiring a series of EELS SI at a range of various tilts, the two-dimensional images can be extrapolated into three through a process known as electron tomography (n.b. while electron tilt-tomography is a very interesting technique, it is not used in the present thesis, so the reader is referred to Ref. [162] for a recent review of the topic).

After acquisition of the tilt data, the SI were decomposed using NMF. It was clear that there were five distinct components with primary plasmon resonances at discrete energy levels (Fig. 2.7a). The loading maps of the decomposition revealed that each of these components were localized around different areas of the NP surface (Fig. 2.7b), and when combined into three dimensions (Fig. 2.7c), a powerful and insightful representation of the various plasmon modes was obtained. Due to the asymmetry and strong overlap (spatial and energetic) of the identified components, traditional techniques such as Gaussian fitting, MLLS, etc. would have had immense difficulty obtaining a result such as this. Similarly, PCA and ICA would have likely identified components with negative spectral features, complicating interpretation of the results. It is the additive nature of NMF that makes it a very powerful technique for EELS signal unmixing, and is thus the primary algorithm of choice for this work.

2.1.2.4   A note on software

Although the techniques reviewed above are remarkably powerful, they are remarkably underutilized in the electron microscopy community. It is the author's opinion that this is primarily due to the lack of a suitable commercial solution (at reasonable cost), as well as general lack of awareness of the methods. Where commercial software has lagged however, open-source implementations have flourished, providing easily accessible and free frameworks for many of these advanced analysis schemes.

In particular, `HyperSpy` is a mature software package built in the *Python* programming environment that enables simple access to both the standard EELS quantification routines as well as advanced model-based and multivariate statistical analysis [163]. It provides a facile means by which to manipulate hyperspectral data (unlike the commercial offerings), with the added power of the entire scientific *Python* ecosystem available through simple imports. This thesis makes significant use of this software not only as a user, but as a contributing developer. As an open-source software, `HyperSpy`'s development is driven by the needs of its users, and the methodological developments in this work will be contributed automatically to the greater scientific community through their inclusion in the upstream software.

2.2   Focused ion beam techniques

A focused ion beam microscope (FIB) operates very similarly to a scanning electron microscope (SEM), with the distinct difference that the primary beam is
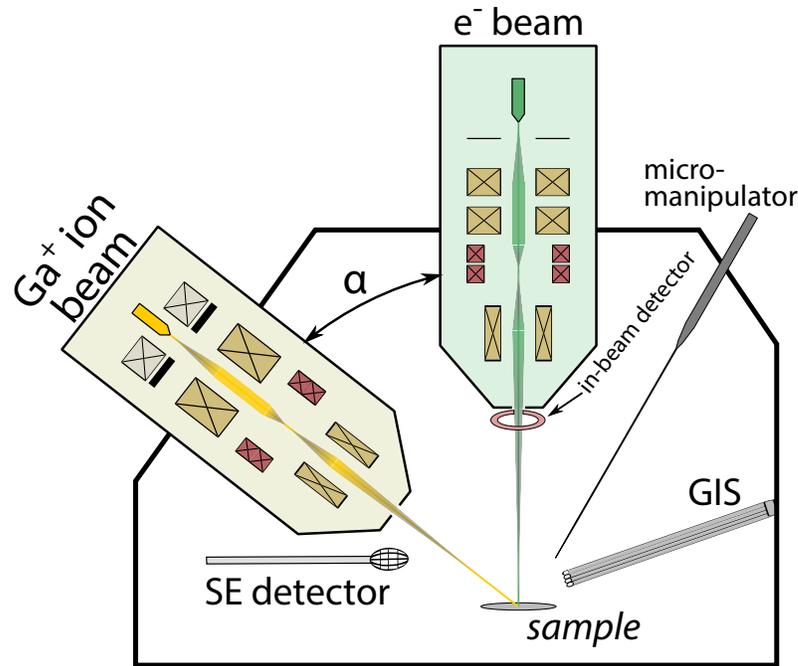
Figure 2.8: Representative schematic of a dual-beam FIB/SEM system (not to scale). The electron and ion columns are at a fixed offset angle of α and are coincident at the surface of the sample. Multiple electron detectors are typically present, as well as analytical capabilities such as EDS and EBSD (*not shown*). A gas injection system (GIS) for material deposition and a micro-manipulator for TEM lamella preparation or electrical probing are also common parts of a dual-beam FIB/SEM.

formed from massive ions (positive, usually) rather than electrons [164]. This mass means that when accelerated by high voltages (2 to $30\,\text{kV}$), the ions can sputter material from a sample, providing an *in situ* means of both observing and modifying a specimen. In modern systems, a FIB is typically combined in the same chamber as an SEM in a dual-beam configuration, that allows for independent computerized control of both the ion and electron beams (a FIB/SEM). A prototypical schematic of a FIB/SEM is shown in Figure 2.8. The beams are placed at a fixed angle (typically between 52 and 55°), coincident on a point approximately $5\,\text{mm}$ below the entrance to the SEM column [165]. In this configuration, the FIB/SEM serves as one of the most versatile characterization tools currently in existence, with site-specific
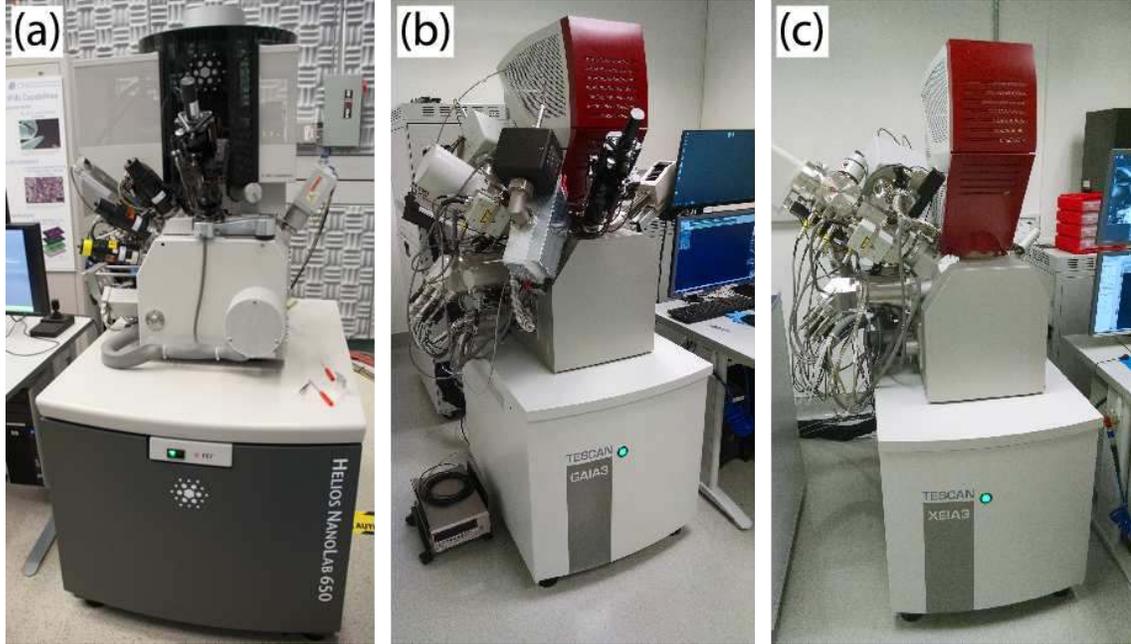
Figure 2.9: Image of FIB/SEM tools used in this work. (a) FEI *Helios Nanolab 650* at CNST/NIST; (b) Tescan *Gaia* Ga^+ LMIS FIB/SEM at the UMD AIMLab; (c) Tescan *Xeia* Xe^+ ICP FIB/SEM at the UMD AIMLab.

imaging (electron and ion), sectioning, material deposition, analytical analysis, and micro-probing capabilities readily available.

Three different FIB/SEM systems have been used in this research, and are shown in Fig. 2.9. For the initial portion of the thesis, FIB/SEM work was performed on a FEI *Helios Nanolab 650* dual-beam FIB system within the Center for Nanoscale Science and Technology (CNST) at the National Institute of Standards and Technology (NIST) in Gaithersburg, MD. This FIB has a liquid metal ion source (LMIS), providing a primary beam of positively charged Ga^+ ions. In October 2015, the University of Maryland AIMLab acquired two dual-beam FIB/SEM systems manufactured by Tescan, and after this point, all work was performed at UMD. The first (the *Gaia*), is a Ga^+ LMIS source system, comparable in perfor-

mance and capability to the FEI *Helios.* The second (the *Xeia*), is a relatively new type of dual-beam FIB that is equipped with an inductively coupled plasma (ICP) source that produces a beam of Xe^+ ions. The ICP source is capable of much higher ion beam currents than the LMIS (at the expense of resolution), meaning this tool can be used for efficient milling of large volumes, but is not well-suited for delicate work. While the OEM manufacturers of the tools may differ, their fundamental capabilities are nearly identical, meaning they can be easily interchanged in this work. Both tools were used extensively for TEM sample preparation, and while reconstructions of the LSM-YSZ cathodes (Sec. 4.2) were achieved using the Helios, LSCF-GDC reconstructions (Sec. 4.3) were completed on the Gaia. The following sections give a brief overview of how these tools have been used specifically within this thesis.

2.2.1 FIB/SEM for TEM sample preparation

One of the primary uses for a FIB/SEM system is as a sample preparation tool for TEM. Compared to traditional techniques, FIB sample preparation allows for unmatched precision when locating a sample site, specifying lamella orientation, and determining final lamella thickness. The *in situ* preparation method (reviewed in Fig. 2.10) is the state-of-the-art means by which to fabricate TEM lamellae, allowing artifact-free preparation of samples at thicknesses regularly lower than 50 nm [166]. In this process, an area of interest is located on the sample (Fig. 2.10a), after which a layer of protective metal is deposited with the gas injection system to prevent
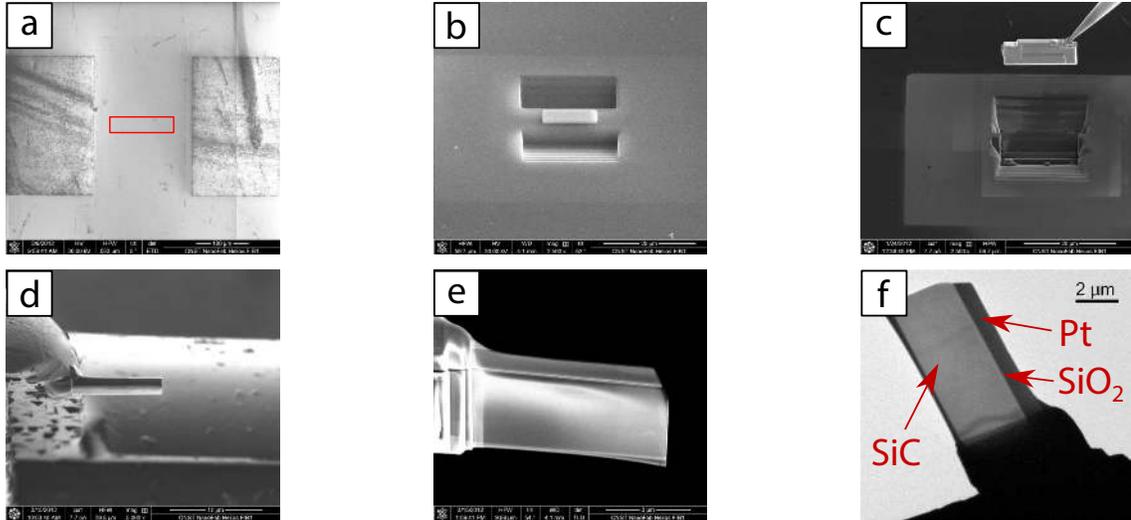
Figure 2.10: Example of TEM sample preparation with the FIB/SEM. (a) Precise location of area of interest (*scale bar:* 100 μm); (b) Rough trenching of lamella using FIB after deposition of a protective Pt layer over the area of interest (*scale bar:* 20 μm); (c) Lift out of thick lamella using micromanipulator (*scale bar:* 20 μm); (d) Attachment of lamella to special TEM half-grid (*scale bar:* 10 μm); (e) SEM image of lamella after final thinning to ≈ 50 nm (*scale bar:* 3 μm); (f) Low magnification TEM image of lamella showing SiC MOSFET gate region in cross section.

undesired irradiation by the ion beam at the feature of interest. Rough trenches are milled on either side to expose a lamella (Fig. 2.10b), which is extracted from the sample *in situ* using a tungsten micromanipulator needle (Fig. 2.10c). The lamella is brought to an open 3 mm grid, where it is attached with deposited metal and the probe is cut free (Fig. 2.10d). The lamella is then milled with successively lower ion beam currents and voltages to thin the sample as much as possible. Finally, the specimen is polished at a low ion beam accelerating voltage, to remove the amorphization at the sample surfaces that arises from using a 30 kV beam (Fig. 2.10e) [167, 168]. After this, the sample is ready for inspection in the TEM (Fig. 2.10f). For the thinnest samples with high quality, typical preparation times are on the order of 5 h, depending on the material, operator experience, and many other factors.

2.2.2 As a characterization tool

Beyond its use for sample preparation, the FIB/SEM can be used for a great deal of characterization in its own right. The FIB/SEM can (by definition) be used for all the same sorts of characterization as a typical SEM, including imaging of secondary and backscattered electrons. Imaging can also be performed with the ion beam, which while destructive, has a much shallower interaction volume and can give complementary information compared to an electron beam image. In addition to the typical electron detectors, most modern systems are further equipped with a complement of analytical tools. Some examples include energy dispersive spectroscopy (EDS), electron backscatter diffraction (EBSD), electrical probing capabilities, time of flight secondary ion mass spectroscopy (ToF-SIMS), transmission electron detectors (STEM-in-SEM), atomic force microscopy (AFM), and others. In combination with the *in situ* modification made available by the ion beam, a dual-beam FIB/SEM offers nearly unparalleled capabilities in nano- and micro-scale characterization.

2.2.3 FIB nanotomography

As reviewed in Sec. 1.2.4, FIB/SEM nanotomography (FIB-*nt*) presents a uniquely appropriate means to quantify the microstructure of SOFC cathodes. The FIB-*nt* process is an automated procedure by which the FIB/SEM serially mills thin slices of the sample, followed by imaging by the electron beam. In this manner, a series (often hundreds or thousands) of images is obtained, at equally spaced depths

(a) 2D Image Slices   (b) 3D Image Cube   (c) 3D Segmented volume   (d) 3D Connected pore network
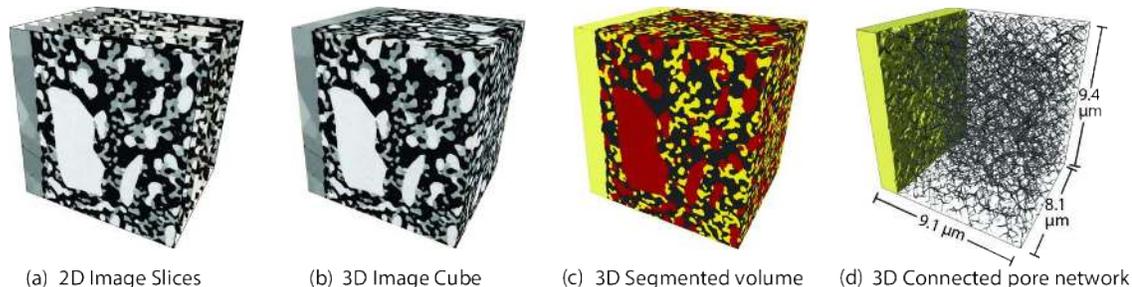
Figure 2.11: Example of FIB/SEM nanotomography. (a) A series of electron images is acquired using serial slicing and imaging in the FIB/SEM (this example is of an LSM-YSZ composite cathode). (b) The stack of images is aligned and filtered, and converted to a 3D image volume; (c) Once post-processed and segmented, this three-dimensional volume can be interrogated for various microstructural quantifications (LSM - red, YSZ - yellow, Pore - black). (d) An example of phase connectivity analysis, showing the skeletonization of the pore network.

throughout the sample. In this work, a slicing depth of $20 - 30$ nm has been used in order to allow sufficient precision in the reconstruction of smaller particles. Once this series is obtained, it can be processed as shown in Figure 2.11. The image slices are aligned and filtered, and then segmented into distinct phases to form a labeled volume. This labeled volume forms the basic dataset of analysis, allowing quantification of parameters such as surface area, volume, particle size, phase identification, and phase connectivity within software programs such as *ImageJ* or FEI's *Avizo Fire.*

Beyond these simple quantifications however, there is room for significant improvement in the measurement of more complex parameters. A primary example of this is the measurement of phase tortuosity (τ). τ is generally a poorly specified parameter, frequently being specifically defined for the particular case in question. [169]. Within the FIB-*nt* SOFC reconstruction literature, almost every research group uses its own definition of τ and means of calculation (see Refs. [106,

111, 115, 170, 171]). Comparing the results between groups is extremely difficult, and a careful critique of the methods presently used in the literature is direly needed. Similarly, a multitude of methods have been used to calculate triple phase boundary length (L_{TPB}). Some of these include phase change analysis, [107] stereology, [172] voxel edge-counting, [113] and the volume expansion method. [115] Careful consideration of each method's strengths and potential artifacts is needed, and due to a lack of software tools available for this purpose a suitable technique must be developed "in-house," offering the opportunity to improve upon the established methodology.

In this work, the process of three-dimensional slicing an imaging was implemented using FEI's *Auto Slice and View G3* software when using the Helios FIB/SEM. On the Gaia machine, Tescan's *3D Acquisition Wizard* software extension was used. Both packages allow for definition of a volume to be sampled, control of the slicing current and resolution, and drift compensation of the ion and electron beams. Typical total acquisition times were on the order of 15 h on the FEI tool and 50 h on the Tescan machine (due to greater stability and easier local access). Reconstructions were calculated using a combination of softwares, including *Avizo Fire*, *ImageJ*, and a collection of external processing algorithms primarily implemented in Python (and described in Sec. 4.1 and the documentation of Ref. [116]). In the spirit of open scientific collaboration and to aid in the reproducibility of results, the FIB-*nt* methods implemented in this thesis have been made publically available for use and adaptation by other researchers [116].

2.3 X-ray photoelectron spectroscopy (XPS)

In addition to the other techniques, a portion of the SiC/SiO_2 investigation utilized X-ray photoelectron spectroscopy (XPS). XPS is a characterization technique for analyzing the surface chemistry of a material, and since it is not a primary focus of this thesis, only a brief introduction to the relevant portions of the theory is presented here. For further details, the reader is referred to Refs. [173–176].

XPS makes use of the photoelectric effect by measuring the kinetic energy of electrons that are emitted from a surface during irradiation by an X-ray source. The physical phenomenon behind the XPS process is the photoelectric effect, causing the excitation of electrons at the surface of a material due to the energy absorbed during an X-ray scattering event. This process is shown schematically in Fig. 2.12. A radiation source (in this case, X-rays) with a certain energy ($h\nu$) causes the excitation of a core-level electron to an energy above the vacuum level. This electron can be detected and its kinetic energy (E_{kin}) measured. Due to the conservation of energy, the original binding energy of the analyzed photoelectron can be determined to be:

$$E_{B} = h\nu - E_{kin} - \Phi \qquad (2.6)$$

where Φ is the work function of the spectrometer. In an XPS experiment, the Fermi levels of the sample and spectrometer are aligned, meaning that knowledge of the work function for the specific sample (which is less than that of the spectrometer) is not required. Practically, this means Φ is a constant value for a particular spectrometer, and does not need to be adjusted during analysis.

70
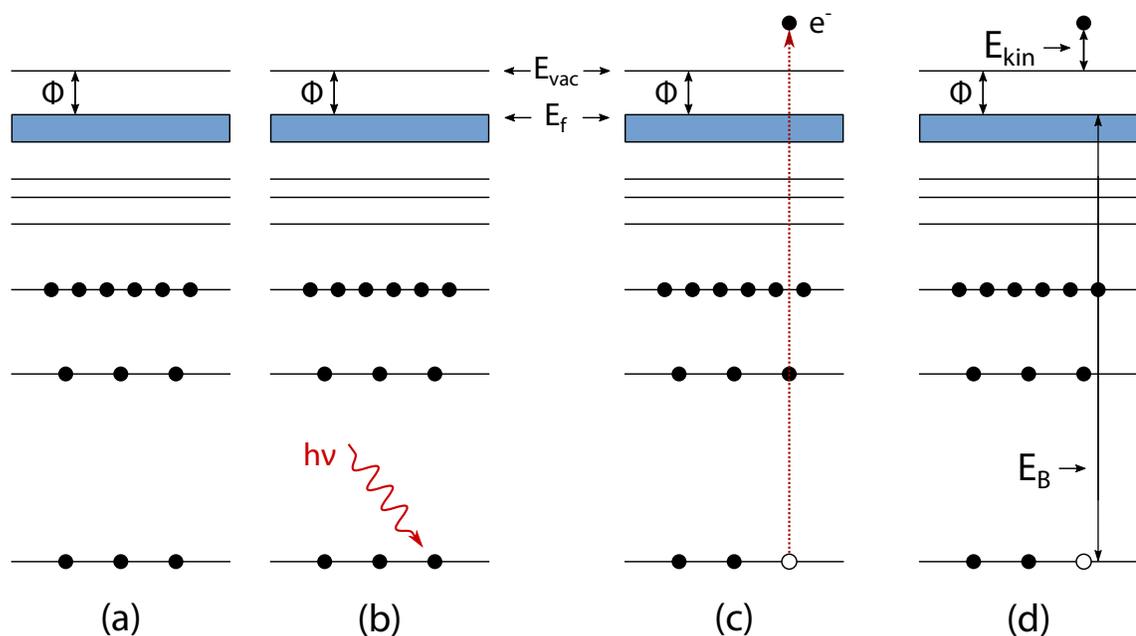
Figure 2.12: Simplified energy level schematic of the photoelectric interaction that enables XPS analysis. (a) The initial electronic state of a material surface. (b) A radiation source with energy of $h\nu$ interacts with a core-level electron. (c) The core electron is excited above the vacuum level and escapes the surface, leaving behind a core hole. (d) A schematic representation of the energies involved in the excitation. Figure adapted from [177].

Through this process of excitation and measurement, a spectrum of electron counts as a function of binding energy can be obtained from the sample surface. With the fine energy resolution of modern XPS systems, this spectrum provides information about not only the element that emitted the photoelectron, but also its orbital and its chemical environment (i.e. a C–O bond would result in a different spectral signature than C=O). The depth of analysis in XPS is approximately 10 nm, and is limited not by the primary X-ray beam, but instead by the escape depth of the emitted photoelectrons, which have a mean free path that is dependent on the material being analyzed.

The XPS performed in this thesis was collected with a Kratos *Axis 165*, located

within the Surface Analysis Center in the University of Maryland Department of Chemistry and Biochemistry. This system has a monochromated Al X-ray source, an analytical spot size of approximately 30 µm, and an ultimate energy resolution of about 0.45 eV. Measurements were taken in the *angle resolved* mode, where the sample is tilted prior to each measurement. By modifying the tilt angle, the effective electron escape depth can be modified, and measurements can be made with high surface sensitivity. This enables one to measure the thickness of certain signals within the data, as reported for SiC in Sec. 3.2.3.

Chapter 3:   Atomic characterization of SiC MOS interfaces

As described in Sec. 1.1, there are still a number of unresolved questions regarding the nature of the interface between SiC and SiO_2 (even though initial commercialization has been achieved). To gain a better understanding of this interface and the atomic-scale effects of modern device processing strategies, a series of TEM experiments (and one XPS investigation) were devised. The results of these five experiments are presented in the following sections: In Sec. 3.1, a TEM-EELS investigation of SiC/SiO_2 transition layer width in NO-annealed devices is presented. Sec. 3.2 reports the XPS study of interfacial states at the interface, while Sec. 3.3 investigates these states more deeply with an MVA study of TEM-EELS data. Sec. 3.4 measures the impacts of post-annealing strategies beyond the typically used NO process, and finally, Sec. 3.5 reports initial results from a TEM study of the impacts of bias and temperature stressing on SiC MOSFET devices.

3.1   Measuring transition layer widths in NO-annealed SiC devices

As discussed, progress in developing *4H*-SiC metal-oxide-semiconductor field effect transistors (MOSFETs) has been hampered by low carrier mobilities in the FET channel introduced by electrically active defects at the oxide interface. The

energy of these defects is within the band gap of *4H*-SiC [24], with most around an energy 2.9 eV above the valence band edge, leading to mobility reduction during inversion of the channel by field termination, carrier trapping, and Coulomb scattering [47]. Possible defects present at the interface include accumulated interfacial carbon [62, 178], threefold-coordinated O and C interstitials [179], Si vacancies [180], and dangling Si and C bonds [47]. Distinct transition layers at the SiC/SiO$_2$ interface have been associated with these defects [63, 64].

In recent years, a number of groups have found that the incorporation of N at the interface between *4H*-SiC and SiO$_2$ can improve the inversion mobility of SiC MOSFETs by reducing the density of electrically active defects [23, 44, 47, 181–184]. Biggerstaff *et al.* [64] have also reported that the width of the transition layer observed between SiC and SiO$_2$ is inversely correlated with effective channel mobility in samples that have been post-annealed in nitric oxide. There are no studies, however, that systematically characterize this transition layer as a function of post-annealing time, as is the primary goal of this experiment. Initial EELS experiments suggested an excess of C in the transition region [51, 62–64], although recent theoretical [178], X-ray photoelectron spectroscopy (XPS) [67], medium-energy ion scattering (MEIS) [69], and further EELS [39] investigations have raised doubts about this possibility. The present work attempts to further resolve this question.

3.1.1   Experimental Methods

A total of six SiC MOSFET samples were manufactured by collaborators at Auburn University fo this study. The 150 μm n-channel MOSFET devices were fabricated on an epitaxial layer (dopant density $N \approx 5 \times 10^{15}/\mathrm{cm}^3$) grown on the (0001) Si-face of 4° miscut $4H$-SiC wafers available commercially from Cree, Inc. The samples were thermally oxidized in dry O_2 at 1150 °C, resulting in 55 nm oxides, and post-annealed in NO at 1175 °C for up to 240 minutes. Further sample and process details, as well as peak field-effect mobility, N density, and interface trap density measurements are available in Refs. [23, 182, 184].

The samples were analyzed using HRTEM, Z-contrast HAADF-STEM, and EELS using the field emission TEM at the UMD AIMLab. The Mo MOSFET gate metalization was removed using a 30% H_2O_2 solution (VWR) to facilitate TEM specimen preparation. Cross-section specimens were prepared from the region under the gate contact using FIB techniques (Fig. 2.10). The specimens' foil normals were [1$\bar{1}$00], perpendicular to the [11$\bar{2}$0] miscut direction on the Cree SiC wafers. This ensures that TEM images will be taken perpendicular to, rather than through the miscut, and prevents the atomic steps of the miscut from artificially inflating the transition layer width (w_{TL}) when viewed in projection. A layer of Pt (or C, if not available) was deposited to minimize FIB ion damage to the SiC/oxide interface. After thinning, the specimens were polished in the FIB at low voltages to remove surface amorphization and Ga contamination. Final "flag" specimens had thicknesses < 80 nm, with minimal ion damage. Electron diffraction patterns and

high resolution lattice images were obtained in TEM mode, and the sample was tilted to the $[1\bar{1}00]$ zone axis to ensure the interface was parallel to the electron beam.

EELS data were collected as spectrum images (SI) at 200kV in STEM mode, allowing for simultaneous HAADF-STEM imaging. while utilizing the microscope's spectrum imaging (SI) capabilities [185]. Typical SI were taken from a rectangular area extending approximately 20 nm into each material and 50+ nm along the interface. By summing the resulting spectra parallel to the interface, a very high signal/noise (S/N) ratio could be obtained with a short dwell time (typically < 0.01 s). SI were collected with a spot size of 0.5 nm and a dispersion of 0.3 eV/channel. Data from a few of the samples were collected with line SI under similar experimental conditions. Elemental quantification of the EELS data was performed using Hartree-Slater ionization cross sections and inverse power-law background fitting [125], implemented within the Gatan DigitalMicrograph (DM) software.

3.1.2   Results and Discussion

A typical HRTEM image of the SiC/SiO_2 interface in the NO-annealed MOSFET devices is shown in Fig. 3.1. The atomic columns are clearly visible in the SiC region, together with an amorphous oxide. The images reveal a smooth interface free from obvious voids or structural defects. Initial visual inspection reveals transition regions narrower than those in prior works [63], in better agreement with more recent studies [186]. HRTEM analysis reveals minimal interfacial roughness in these
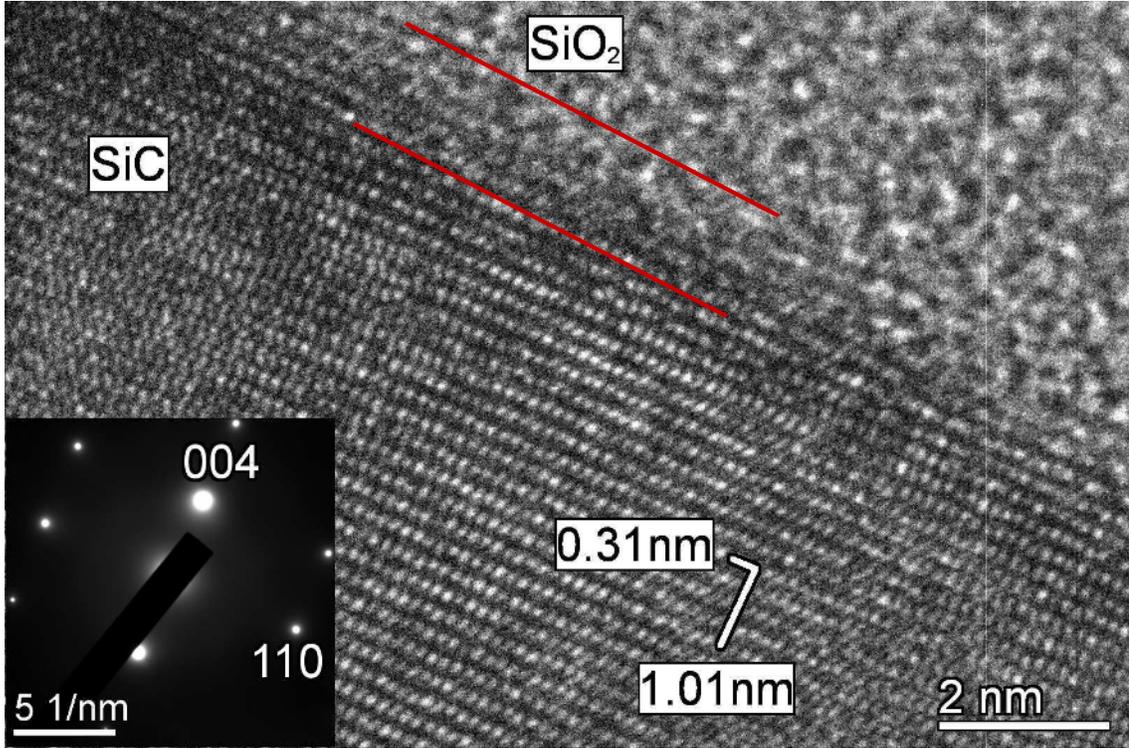
Figure 3.1: $[1\bar{1}00]$ HRTEM image and electron diffraction pattern of the NO-annealed (*60 min*) *4H*-SiC/SiO$_2$ interface. Contrast variations near the interface suggest a structurally-evident transition region of a few nm, but diffraction effects at the interface make it difficult to obtain quantitative measurements from these HRTEM images. A rough estimate of the structural extent of the TL is indicated by the red lines, indicating a structural w_{TL} of $\approx$ 1.2 nm

NO-annealed samples aside from that inherent from the miscut of the substrates (agreeing with Ref. [52]). While a large degree of interfacial roughness could lead to a possible overestimation of w_{TL}, a simple calculation reveals that the small degree of roughness present in our samples will have a negligible effect. With a 4° miscut and an average roughness of a single monolayer (0.2514 nm) in the $\langle 0001 \rangle$ direction of *4H*-SiC, the expected roughness perpendicular to the interface will be only 0.2507 nm. This is substantially lower than the w_{TL} values found with every measurement method (as shown below), and thus interfacial roughness is not expected

to artificially inflate the transition layer thickness. It remains difficult however, to quantitatively measure the interface width from these HRTEM images alone, but chemical w_{TL} measurements using EELS indicate a transition region extending beyond that observed in the high-resolution images, indicating the need for deeper chemical analysis to fully describe the TL.

To perform this chemical analysis, and to quantify w_{TL}, the chemical shift of the Si-$L_{2,3}$ EELS edge onset energy was measured across the interface. This parameter reveals information about the local bonding state of Si throughout the transition region [187]. The results from this measure were compared to the common EELS profiling methods that have been used in previous works. These involved performing EELS quantification across the interface and taking profiles of (*i*) the C/Si and O/Si atomic concentration ratios (normalized to 1:1 and 2:1 in the bulk SiC and SiO$_2$, respectively) [62–64]. Using the tails of these ratios, (*ii*) the relative contributions to w_{TL} of C in SiO$_2$ and O in SiC were determined. These tails were measured from the point where the ratio profiles crossed to the point where the derivative of the C or O signal was 2% of its maximum intensity. Using atomic ratios helps to eliminate systematic quantification errors due to possible specimen thickness variations and diffraction contrast [188]. Finally, w_{TL} was measured by (*iii*) HAADF intensity profiles [64] in order to reveal contrast from differences in atomic composition. w_{TL} was correlated with peak field-effect mobility of devices made from the same samples as reported in Ref. [23]. Results from each method are discussed below, and tabulated in Table 3.1 (pg. 86).

Fig. 3.2 depicts a typical EELS analysis performed on each sample. The

78

HAADF-STEM image in (b) was used to locate an EELS SI, collected from the area enclosed by the green box shown in (c). Typical SiC (A), SiO_2 (C), and interface (B) spectra are shown in (a). These spectra illustrate the chemical changes that occur across the interface, including a shift of the Si-$L_{2,3}$ edge onset from ~100 eV to ~104 eV, as well as the emergence of the O-K edge (540 eV) and suppression of the C-K edge (283 eV) as the beam passes from SiC to SiO_2. These phenomena can be used to systematically determine w_{TL} at the interface.
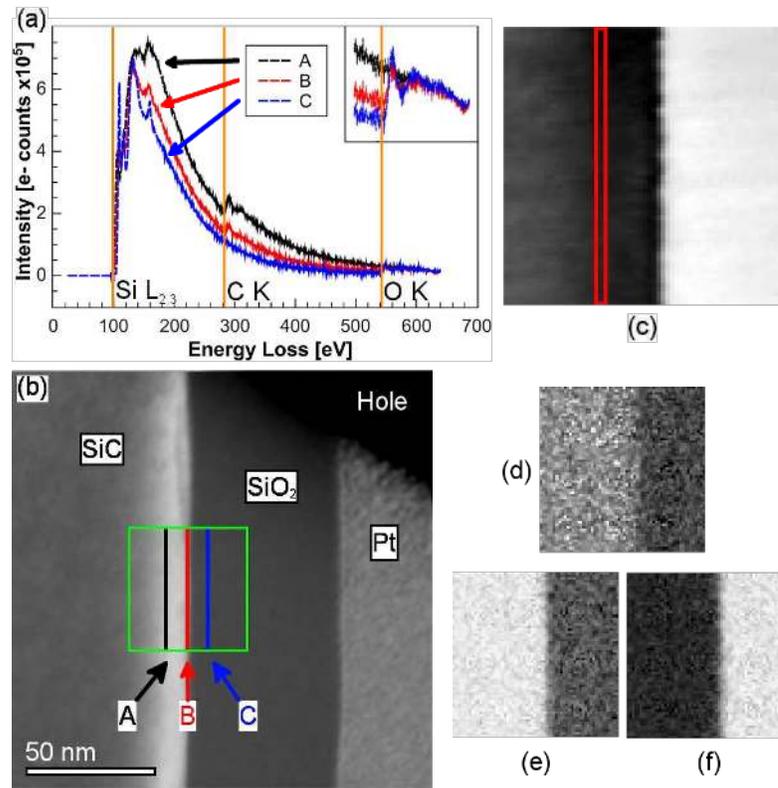
Figure 3.2: (a) Typical background-subtracted core-loss EELS spectra at three locations across the *4H*-SiC/SiO_2 interface (*60 min. NO-anneal*). Inset shows detail of O-K edge. (b) HAADF-STEM image highlighting SI location. (c) SI across interface; each pixel contains a full core-loss EEL spectrum and these are summed parallel to the interface (as shown) to increase S/N ratio. Quantification allows calculation of relative composition maps of (d) Si, (e) C, and (f) O.

3.1.2.1 Si-$L_{2,3}$ chemical shift

The primary method used to determine w_{TL} was a measurement of the chemical shift of the Si-$L_{2,3}$ edge (Fig. 3.3). As the local bonding configuration of Si changes across the interface, the core-electron levels and conduction band edge shift with respect to the Fermi level [189]. This leads to a chemical shift of the core-level EEL spectrum onset, representing a change in the local bonding and cohesive energy of the element as the material transitions from semiconducting (SiC) to insulating (SiO$_2$), as in Fig. 3.3a [187]. This energy is most reproducibly traced by the inflection point of the edge onset, rather than the absolute energy of the onset [190]. Since this method probes Si bonding and depends on relative energy shifts, many sources of systematic error cancel, including thickness variations, sample contamination, and spectrometer energy shifts. This leads to very precise values for w_{TL}, as are shown in Fig. 3.4(b).

Figure 3.3 depicts the details of the chemical shift method used to measure w_{TL}. In Fig. 3.3(a), the Si-$L_{2,3}$ near-edge structure is shown for SiC and SiO$_2$, as well as spectra from sequential points within the transition region. These spectra are separated spatially by 0.7 nm, giving a w_{TL} value of 4.0 nm for the 60 min NO-anneal sample shown in the figure. The spectral changes in the transition region are primarily characterized by a shift of the edge onset to higher energy, as discussed above. Due to spectral noise, accurately determining the absolute edge onset energy can prove difficult, but the inflection point of the onset can be easily found. This point is a reliable means by which to determine edge onset position [190], and pro-
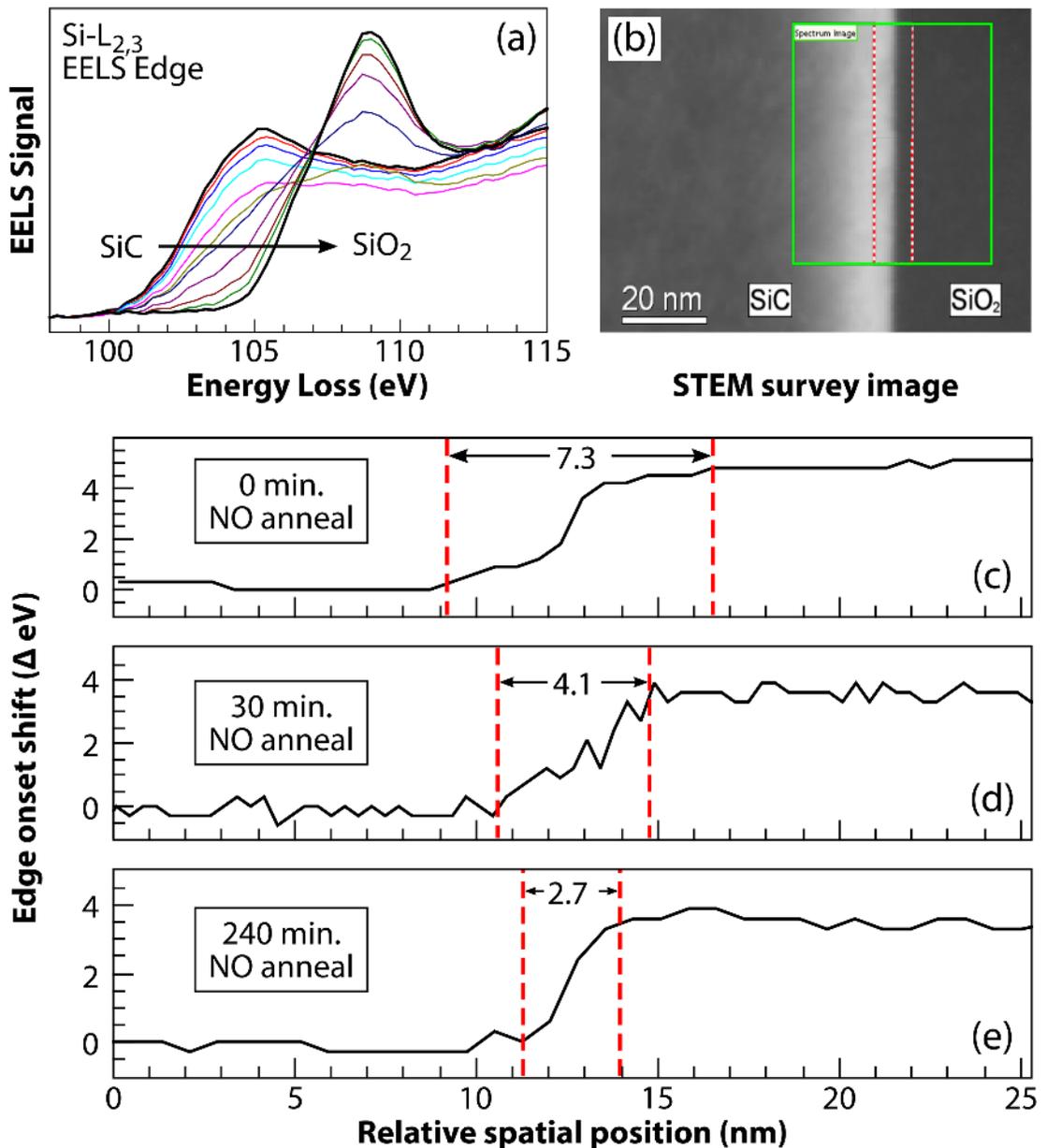
Figure 3.3: Overview of chemical shift w_{TL} measurement method. (a) Typical high energy-resolution view of the core-loss EELS spectra across the interface from SiC to SiO$_2$ (*60 min. NO-anneal*); only the Si-$L_{2,3}$ edge is shown. The two thick black spectra with peaks on the left and right depict the edge in fully SiC and SiO$_2$ regions, respectively. (b) Cropped HAADF-STEM survey image from Fig. 3.2(b). The solid green box shows the location of the SI; the dotted red box indicates the region from which the spectra in (a) were taken. (c-e) Three examples of the chemical shift as a function of position for unannealed, 15 min. NO-anneal, and 240 min. NO-annealed samples, respectively, showing clear monotonic shifts in each case. Chemical shift was measured by tracking the inflection point of the spectra in (a); w_{TL} is indicated by dashed lines.

vides a convenient way to determine the boundaries of the transition layer. Plotting

the energy of the inflection point as a function of position (as in Fig. 3.3(c-e)) reveals

a clear transition region that was uniform in character among all samples examined.

The limits of w_{TL} were determined using a rise time analysis (borrowed from the

signal processing community [191]), measuring the width of the region contained

between the 2% and 98% points of the edge onset profile (see further discussion of

this point in Sec. 3.1.2.2).
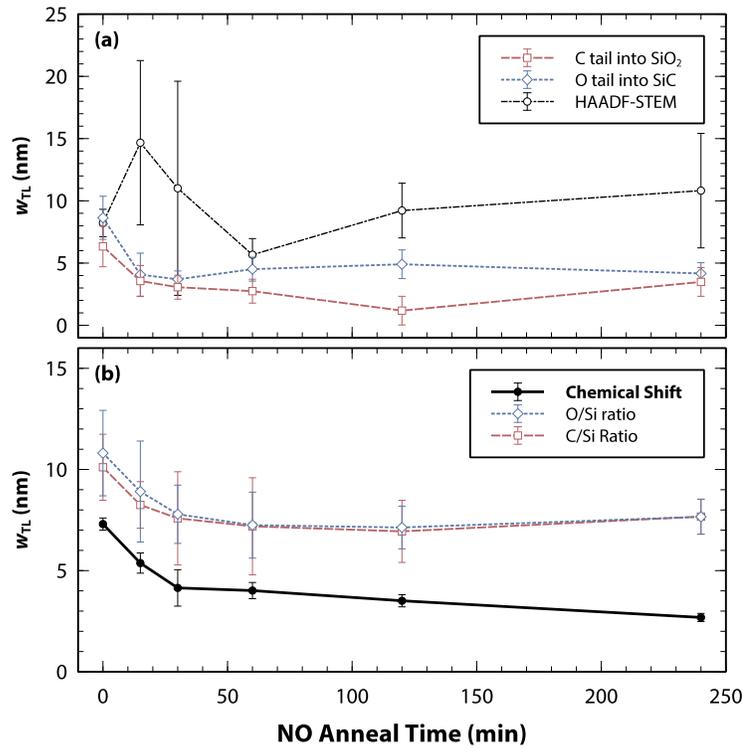
Figure 3.4: w_{TL} vs. NO-anneal time for all methods investigated. Methods in (a) were less reliable and had larger errors than those in (b). Errors are reported as the standard deviation of multiple measurements for each method. The chemical shift measure (in bold) had the least error and proved most reliable.

Measuring w_{TL} with the Si-$L_{2,3}$ chemical shift method revealed a clear down-

ward trend in w_{TL} with respect to NO-annealing time (see Fig. 3.4(b)). The energy

of the Si-$L_{2,3}$ edge for all samples increased from SiC to SiO$_2$ monotonically, indicating a gradual progression in the character of Si bonding across the interface. If a layer containing a unique configuration were present (such as Si-Si), it would manifest as an anomaly in the progression of the chemical shift. The absence of such anomalies suggests a mix of Si-C and Si-O bonding in the transition region [44], but the presence of other configurations at concentrations lower than the detectable limit cannot be categorically excluded. The narrowest w_{TL} was measured for the 240 min anneal at 2.7 nm, which is significantly larger than the "few atomic layers" as has been suggested by recent XPS measurements [67]. The reasons for this discrepancy are not immediately obvious, but since this prior work did not include XPS depth profiles, it is difficult to make a direct comparison to the present results. Our results indicate w_{TL} values on the same order (a few nm) as a number of previous profiling methods, including secondary ion mass spectrometry (SIMS) [52], XPS [192], and EELS composition profiles [39, 40, 63, 64, 193]. The Si-$L_{2,3}$ edge shift method provides a direct observation of a defined transition region in Si bonding character, and its width correlates with decreased mobility (see Sec. 3.1.2.4), suggesting that the local bond structure of Si has a pronounced effect on the electronic properties of SiC MOSFETs.

3.1.2.2 Atomic composition ratios and elemental "tails"

To further evaluate this chemical shift method, it was compared to various other measurement methods used in the literature. Standard quantification proce-

dures [125] were used to calculate the relative concentration of each element, using the relationship described in Eq. 2.4. Quantifying each pixel of the SI yields relative composition maps (Fig. 3.2 (d)-(f)), which were divided to give atomic composition ratio maps (Fig. 3.5a). From these maps, a single row of the SI can be selected as a profile (Fig. 3.5b), and summed parallel to the interface, increasing the S/N ratio (Fig. 3.5c). In this experiment, w_{TL} was defined as the the rise time of the profile from the 2% to the 98% level of the profile. Using 2/98% provides an estimate for the profile as measured by 90% of the electrons contained in the beam (the full-width tenth-max of a Gaussian beam), consistent with the accepted definitions for STEM probe resolution [194]. Fig. 3.5 (e) shows how w_{TL}, as determined by the EELS composition ratios, extends much farther than expected from the HRTEM images alone.

An excess C signal (with a minimum sensitivity of 2.5% above the expected stoichiometric value) was not observed for any of the NO-annealed samples, agreeing with a number of recent works [39, 69, 178]. w_{TL} was found to decrease nonlinearly as the annealing time increases, suggesting a limit to the gains from the NO-anneal, as previously seen [55]. The O/Si ratio indicated a (very) slightly larger contribution to w_{TL} than the C/Si ratio (Fig. 3.4(b)). Likewise, the O signal "tail" extended farther into SiC than the C signal "tail" into SiO_2 (see Fig. 3.4(a)). A few possibilities could explain this difference. During oxidation, any ejected C is very efficiently removed from the interface via formation of CO [179], leaving a small C concentration tail in the SiO_2. Also, the solubility of O in SiC is very low [179], meaning that even the limited incorporation of O in the SiC lattice will force O atoms farther from the
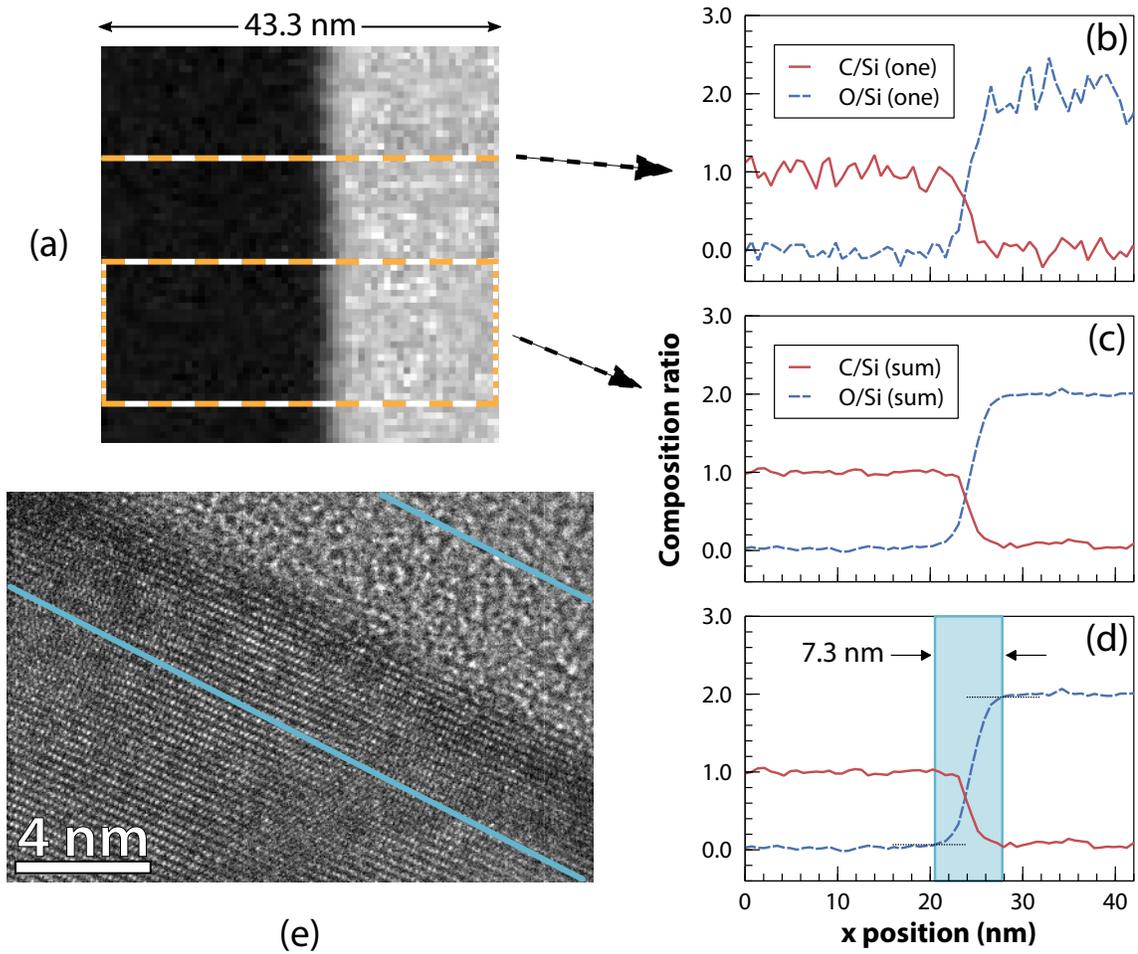
Figure 3.5: (a) O/Si composition ratio map calculated from Fig. 3.2 (d and f); (b) Profiles from one row of map in (a); (c) Profiles summed from all rows of map in (a); note the pronounced improvement in signal to noise ratio. (d) Demonstration of 2/98% rise time calculation used to determine w_{TL}, using the profiles from (d); the thin dashed lines are the 2 and 98% levels of the profiles. (e) Comparison of chemically derived w_{TL} (in blue) with HRTEM from Fig. 3.1.

Table 3.1: Summary of w_{TL} measurements (in nm) by all methods (as plotted in Fig. 3.4). The chemical shift method (in bold) was found to be the most accurate and reliable method by which to measure w_{TL}.

NO-anneal time (minutes)	C/Si Ratio	O/Si Ratio	HAADF Intensity	**Si-L$_{2,3}$ Shift**	Interdiffusion C	O	Mobility $(\text{cm}^2/\text{V}\cdot\text{s})$ [23]
0	10.1	10.8	8.2	**7.3**	6.3	8.6	5 ± 3
15	8.2	8.9	14.7	**5.4**	3.6	4.1	24 ± 2
30	7.6	7.8	11.0	**4.1**	3.1	3.7	36 ± 3
60	7.2	7.2	5.7	**4.0**	2.7	4.5	42 ± 4
120	6.9	7.1	9.2	**3.5**	1.2	4.9	43 ± 4
240	7.7	7.7	10.8	**2.7**	3.5	4.2	48 ± 5

interface. It is important to note that the C and O elemental "tail" measurements are not explicitly measures of w_{TL}, but rather of the relative contribution of each element. As such, the values reported in Fig. 3.4(a) cannot be directly compared with those from the chemical shift and ratio methods in Fig. 3.4(b).

3.1.2.3 HAADF-STEM imaging

Although previous work [64] has characterized w_{TL} by identifying a transition in the intensity profile of HAADF-STEM images, this method proved unreliable in the present investigation. Attempting to maintain consistency with Ref. [64], w_{TL} was defined as the distance between the inflection point and the maximum in the intensity profile of the SiC HAADF image (see Fig. 3.6(b)). The HAADF method uniformly yielded w_{TL} values larger than those obtained through EELS (Fig. 3.4(a)) measurements. The method also did not display as clear a downward trend and appears subject to greater error from external factors such as experimental conditions, thickness variations near the interface (originating from preferential thinning of the
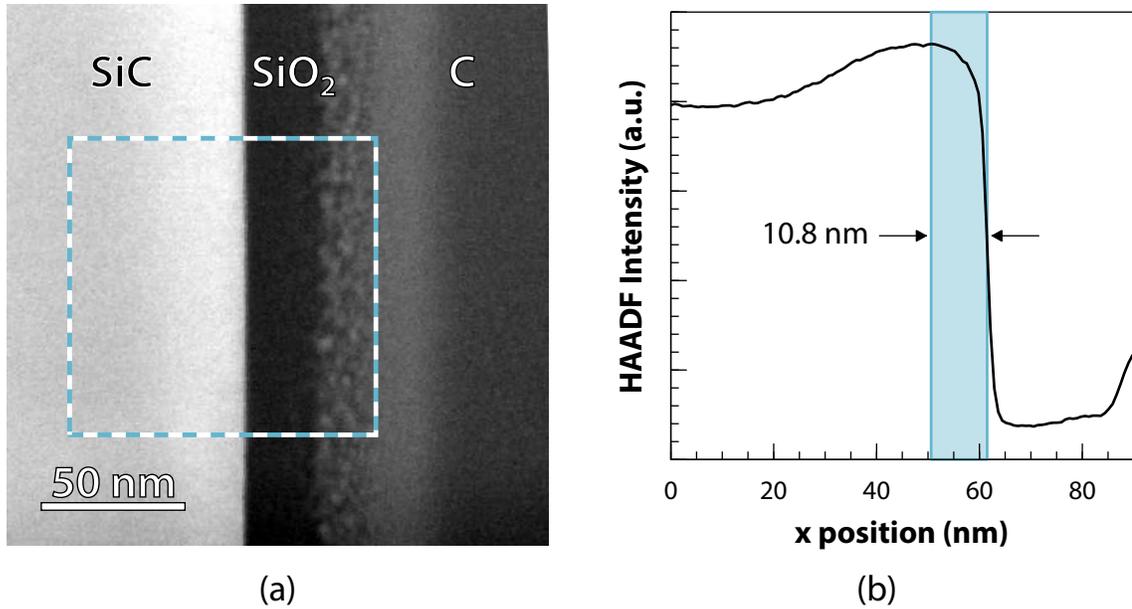
Figure 3.6: (a) HAADF-STEM image with highlighted region showing area from which the intensity profile in (b) was taken (*240 min. NO-anneal*). w_{TL} was defined as the width between the intensity peak and inflection point, as shown.

oxide during FIB milling), or possible surface contamination. Additionally, since C was observed in its expected stoichiometric ratios, the bright region present in the SiC (see Fig. 3.6(a)) could not be correlated to excess C, as was reported by Zheleva *et al.* [63]. w_{TL} could not be reliably characterized using HAADF-STEM intensities, and thus the chemical shift method was found to be the most appropriate means to do so.

3.1.2.4 Correlation with electrical measurements

Fig. 3.7 shows a clear correlation between w_{TL} (as measured from the Si-$L_{2,3}$ edge chemical shift) and peak field-effect mobility, and both characteristics improve with longer NO-anneal times, but with reduced gains for anneals longer than 1 hour. These results correlate further with decreased interface trap density
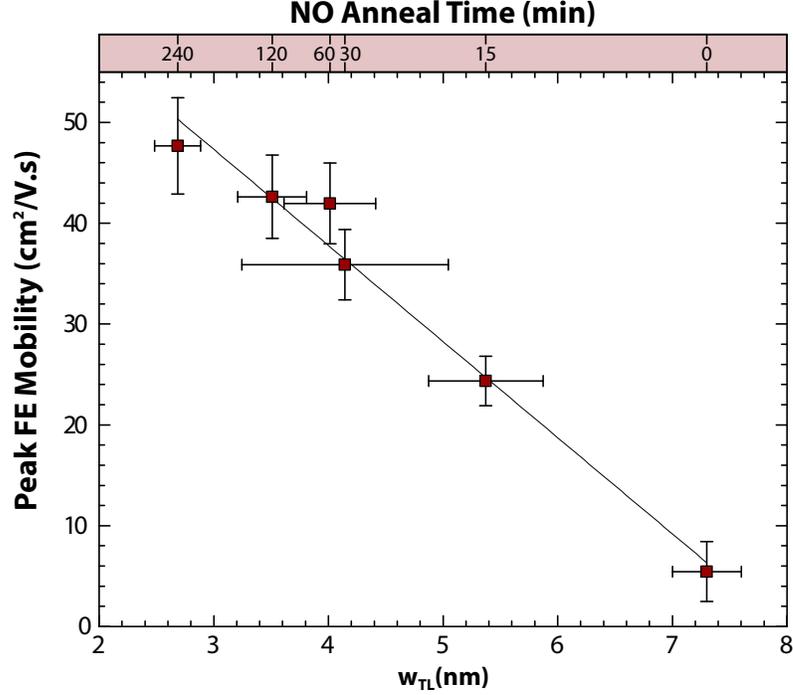
Figure 3.7: Comparison of NO-anneal time, w_{TL} (as measured by chemical shift), and peak field-effect mobility, as measured in Ref. [23].

and increased N density at the interface (as measured by SIMS in Ref. [23]). The narrowing of w_{TL} observed with longer NO-anneal times suggests that in addition to passivating dangling bonds at the interface [44], the anneal process (including the incorporation of N) can help clean the interface by actively removing C and reducing extraneous bonding configurations, which has been previously observed by XPS [30]. EELS results did not reveal any significant N-K edge signal at 401 eV near the interface, likely due to the very dilute concentrations and brief collection times used for the $\approx 80\,\text{nm}$ thick samples. The results nevertheless suggest that the presence of N introduced by an NO-anneal significantly narrows the SiC/SiO$_2$ interface and enhances the MOSFET electrical properties.

3.1.3 Conclusions

Aside from the HAADF intensity, all w_{TL} measurement methods reveal the same trend of decreasing w_{TL} with increased NO-anneal time. Each of these measurements probes a different physical phenomenon, and their agreement enhances the validity of the methods and results used in this work. The effect correlates very well with increased peak field-effect mobility, decreased interface trap density, and increased N density, as reported in Ref. [23]. A declining trade-off was observed between annealing time and mobility improvement (i.e. the first 15 min of annealing improves w_{TL} as much as the last 3 h).

The chemical shift method presented in Sec. 3.1.2.1 was the most reliable means used for measuring w_{TL}. This technique had the least error and every sample analyzed exhibited the same gradual shift in edge onset energy, which is measured easily by the inflection point of the edge. This method directly probes changes in the electronic structure of the transition region and is thus particularly suited to measurement of w_{TL}. Since the electrical performance of SiC MOSFETs is adversely affected by defects in the transition layer and is what needs improvement, the chemical shift technique is proposed as the most appropriate measurement method.

In summary, the results of this study reveal a clear transition layer at the *4H*-SiC/SiO$_2$ interface of NO-annealed samples at different annealing times and suggest a nonlinear inverse relationship between transition layer width and NO-anneal time. A clear, objective, and repeatable method to determine w_{TL} using the Si-$L_{2,3}$ EELS edge shift has been presented, which confirms (using a systematic sample set) the

inverse linear relationship between w_{TL} and peak field-effect mobility first observed by Biggerstaff *et al.* [64]. The observed chemical shift of the Si-$L_{2,3}$ edge indicates a gradual modification of the local Si configuration near the interface. Finally, no excess C was observed at the interface (with a noise threshold of 2.5% above the expected stoichiometric ratio) on either side of the interface of these NO-annealed Si-face samples.

3.2 XPS analysis of the NO-annealed SiC/SiO$_2$ interface

As described in Sec. 2.3, XPS is a surface characterization technique that utilizes spectroscopy of photoelectrons to measure the binding energy of elements within a sample. In contrast to prior EELS studies (and the results of Sec. 3.1), XPS and MEIS reports of the SiC/SiO$_2$ interface have described a "near-perfect interface dominated by Si–O bonds" [67] that is "not only chemically abrupt but structurally nondistorted within the surface plane" [69]. To investigate these discrepancies, an XPS analysis of samples like those used in Sec 3.1 was performed.

3.2.1 XPS depth-profiling

The goal of this experiment was to gain insight into the presence of any distinct atomic configurations at the interface between SiC and SiO$_2$, as well as their spatial distribution (to be compared to w_{TL} from EELS measurements). Various techniques are available for profiling states as a function of depth with XPS, each with advantages and potential negative consequences, which must be carefully considered.

The standard means of profiling a structure in XPS is through the use of an argon ion sputtering process [195]. In this method, a prescribed dose of Ar$^+$ ions bombards the sample surface, sputtering material away prior to an XPS measurement. The process is repeated until a suitable depth is reached. This provides a profile of XPS signal as a function of depth through the sample, and is relatively simple to perform. While applicable for some situations, this technique suffers from a

number of shortcomings that limit its use in detailed chemical analyses of multilayer structures.

First, the sputter yield (the amount of material removed per Ar^+ ion) is highly dependent on specific material properties. This means that as a profile proceeds through an interface, the yield may change substantially, preventing a simple conversion from sputtering time to sputtering depth during the subsequent analysis. Furthermore, sputtering via physical bombardment will not only remove material, but create an amorphous damage layer in the material. As such, each XPS measurement will be collected from a damaged region, rather than a pristine surface. While the overall stoichiometry may not change significantly, this damaged region is likely to have a substantially modified chemical signature, making precise measurement of fine interfacial states close to impossible with this technique.

Another common technique for measuring interfacial states is to perform a complete chemical etch of the covering oxide layer, allowing for an XPS measurement from the substrate [196]. Again, this is a fairly simple technique to implement, but has the obvious shortcoming of removing the entire oxide layer prior to measurement. Any chemical states present in a configuration susceptible to attack by HF (or another etchant) will be removed, and will not be present in the resulting measurement. Also, chemical processes such as these can alter the surface bond termination, which may adversely affect the measurement.

3.2.2 Spin-etch depth profiling methodology

To alleviate many of the above concerns, a technique referred to as "spin-etching" was implemented to carefully profile close to the SiC/SiO_2 interface. This method involves introducing an etchant solution in very small quantities to a spinning substrate, allowing for very careful control of the etching amount, with minimal damage and residue on the sample surface. The technique was originally developed in the 1970s during XPS investigations of the Si/SiO_2 interface by Grunthaner *et al.* [197]. Further refinement of the technique demonstrated its utility for very clean etching of oxide layers, leaving an order of magnitude less chemical residue at the surface compared to Ar^+-ion sputtering and traditional dip etching [198–202]. The method has not previously been used to investigate SiC/SiO_2 oxide layers, perhaps due to the potentially hazardous nature of the etch process.

In this work, an adaptation of the Grunthaner spin-etch process was implemented to etch the oxide to a very thin layer on SiC/SiO_2 samples. A spin coating system (Laurell Technologies), equipped with a polytetrafluoroethylene (PTFE) process chamber was used as an etching system in the following manner: Small ($10 \times 5\,mm$) SiC/SiO_2 samples were placed onto the vacuum chuck of the spin coater, where they were spun at 3000 rpm and rinsed with ethanol and H_2O prior to etching. Using a repeating pipette with its tip positioned $1\,cm$ from the sample, the etchant solution was introduced in steps of $125\,\mu L$, consisting of 5 drops of $25\,\mu L$ each, after which the sample was quickly dried using a clean N_2 bench-top blow gun. The samples were spun continuously during this time.

Prior to etching of the SiC/SiO$_2$ samples (which are expensive and limited), refinement of the etch process was performed using Si/SiO$_2$ samples of similar shape, where the oxide was grown via thermal oxidation. The etchant solution used in this work is that recommended by Fenner *et al.* [202]: a 10:1:1 ratio of EtOH:H$_2$O:49.5% HF. All chemicals used were high-performance liquid chromatography (HPLC) grade, to ensure minimal contamination of the sample surface. In order to gain a full control of the etching process, the effects of various process parameters on the etching yield were investigated. The thickness of the oxide layer was measured before and after each experiment at multiple points across the sample surface using a variable angle spectroscopic ellipsometer (J. A. Woollam Co.), providing an extremely precise measurement of the amount of oxide removed in each step.

Number of etching steps (n_{etch})

The first control investigated was varying the number of repetitions of the etch process, effectively changing the total amount of etchant delivered to the sample surface. Each step consisted of delivering five 25 μL drops of etchant at a rate of 1 drop per second. The total amount of oxide etched was determined by ellipsometry, and the results of two different experiments are shown in Fig. 3.8. As expected, a linear relationship was found between the oxide etch amount and the volume of etchant delivered. Interestingly, the etch amount was found to be dependent on not only the number of etch steps, but also the length of time the sample was dried with N$_2$ between steps. Fig. 3.8 shows two repeated experiments, with the time of drying varied. Indeed, the etch magnitude was found to be significantly higher for 15 s of

drying, compared to 2 s, with identical volumes of etchant used (0.8 vs. 0.5 nm/step, respectively).
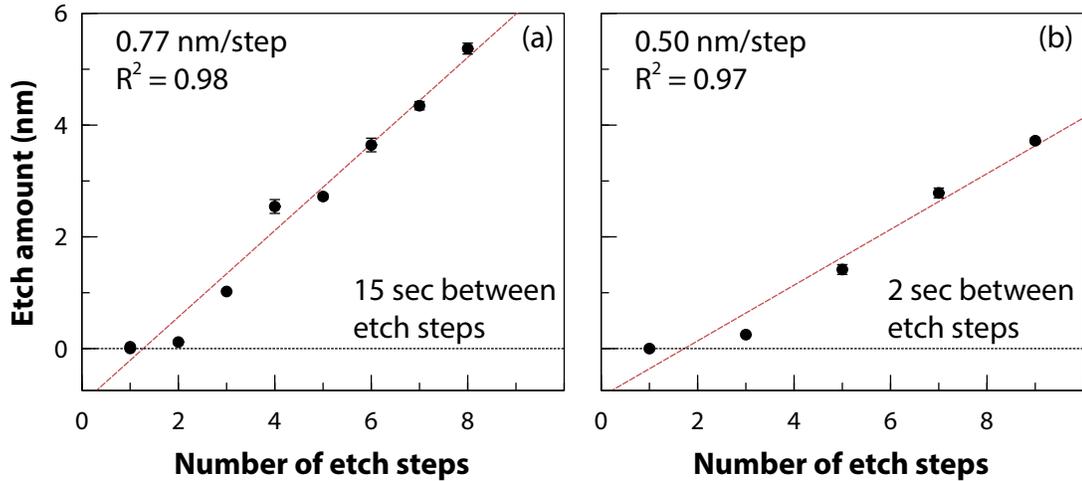
Figure 3.8: Results of two experiments measuring the amount of oxide etched as a function of the number of etching steps performed. In the first experiment (a), the spinning sample was dried for 15 s between etch step. In the second (b), this time was shortened to 2 s. Error bars reflect the standard deviation of the etch over the length of the sample.

Time between etch steps (t_{step})

To further investigate this time dependence, two subsequent experiments were performed, varying the timing of the process rather than the total amount of etchant used. The first experiment (Fig. 3.9a) varied the length of time that the sample was dried with N_2 between etching steps, attempting to gather a better understanding of the phenomenon observed in Fig. 3.8. For each sample, nine etch steps were performed with a drying time of 2, 5, or 15 s. The 15 s sample was repeated two times to ensure adequate control of the process. The drying time was observed to be an important controlling parameter, with an etch effect of 0.2 nm per second of
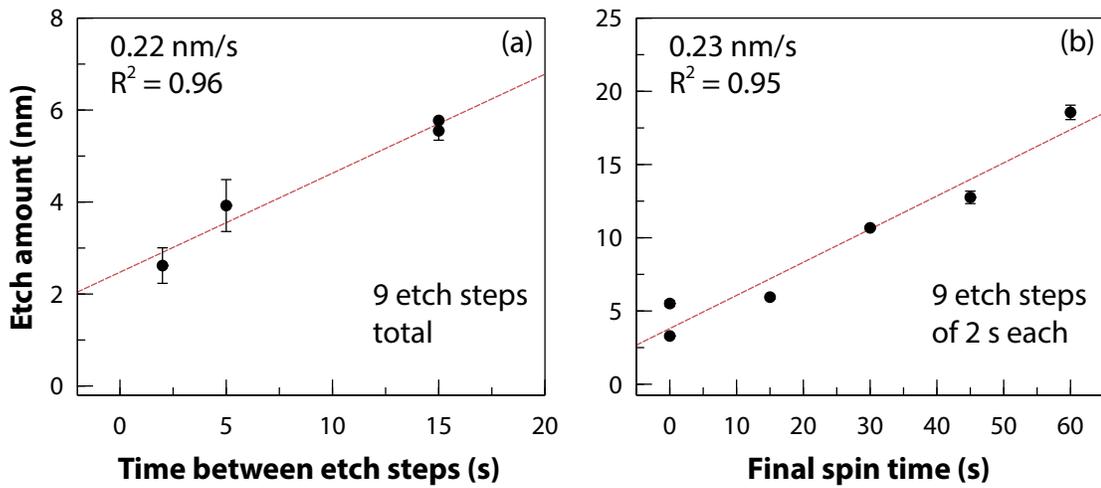
Figure 3.9: Results of two experiments measuring the amount of oxide etched as a function of process timing. (a) Etch amount vs. drying time between steps; (b) Etch amount vs. the length of time the sample was left spinning on the chuck after 9 etch steps (with 2 s of drying between each step). Error bars reflect the standard deviation of the etch over the length of the sample.

drying time. As demonstrated by the identical magnitude of etching for the two 15 s samples (and the good fit of the trend line), this effect was extremely reproducible.

Time left in spin chamber (t_{end})

The second timing experiment (Fig. 3.9b) was similar, but instead of varying the time between steps, the drying time was held fixed at 2 s. The time varied was the length of time the sample was allowed to spin in the process chamber at the end of nine etch steps (without the N_2 gun blowing). As shown in the results of Fig. 3.9b, the extra spinning time had a pronounced effect on the amount of oxide removed, even though no additional etchant was used. This result confirmed that both the volume of etchant and the timing of the process are critical predictors of total etch amount.

The proposed mechanism for this additional etching is through a secondary vapor phase etch, arising from the vapor pressure of etchant that evaporates from the side walls of the process chamber. While the use of the N_2 blow gun efficiently dries the sample surface of liquid phase etchant, it likely assists in evaporating waste etchant and delivering it to the sample. Prior research has determined vapor etching with HF to be an order of magnitude slower than wet etching, while still being capable of removing up to $15\,\text{nm}$ of thermal SiO_2 per minute [203]. Thus, any parameter that affects the vapor pressure of HF within the chamber (such as chamber size, temperature, efficiency of waste removal, etc.) should be expected to have an impact on etch results, and should be controlled for carefully.

Etch uniformity

By measuring the oxide thickness as a profile along the length of the sample, the uniformity and spatial characteristics of the etch process can be evaluated. The results of a single etch performed on two SiC/SiO_2 samples is shown in Fig. 3.10. The average etch amounts were $(1.0 \pm 0.1)\,\text{nm}$ and $(1.2 \pm 0.2)\,\text{nm}$ for the oxidized and NO-annealed samples, respectively. As can be observed in the profiles, the etch uniformity is generally very good, given the roughness in the initial oxide profile. The spin-etch procedure was often found to smooth roughness in the oxide, and the standard deviation (σ) of the etch values across the samples were generally $0.2\,\text{nm}$ or less.
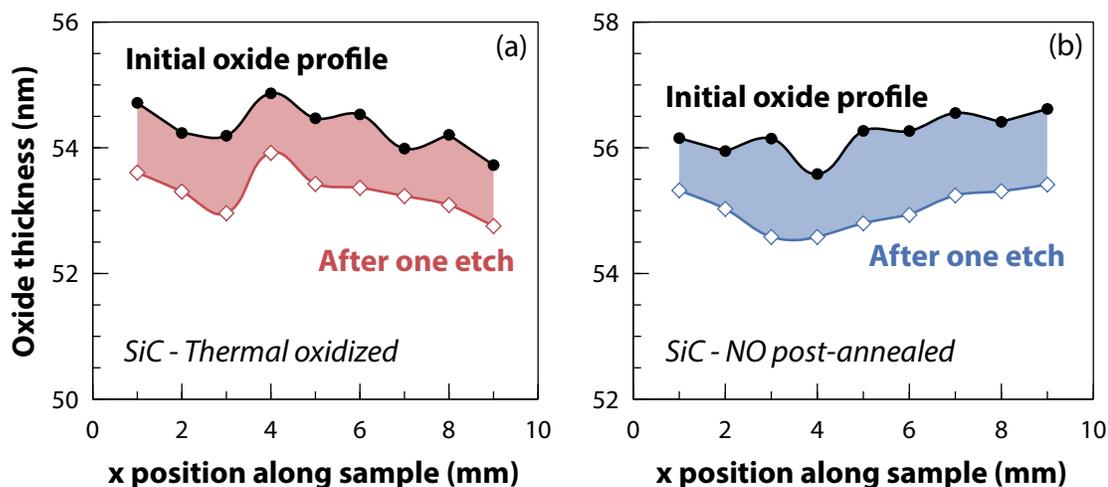
Figure 3.10: Oxide thickness profiles measured by ellipsometry before and after a single etch process of 2 steps (as defined previously). The filled area represents the amount of oxide removed during the etch. Two samples are shown: (a) SiO_2 on SiC grown via thermal oxidation (with no other treatment), and (b) SiO_2 on SiC receiving an additional NO post-anneal. The etch was found to be very uniform, and the overall oxide profile is retained (although smoothed somewhat) after the single etch.

3.2.3 Angle resolved XPS measurements

To gather further insight regarding the nature and extent of the bonding configurations at the SiC/SiO_2 interface, angle resolved XPS measurements were performed on a set of four interfaces. All of the samples were prepared in a manner similar to those in Sec. 3.1, with two of the four receiving a 2 h NO post-anneal. Besides the NO process, the four samples were identical. Multiple samples were used to allow comparison between different levels of etching during a single XPS session. Throughout the text, the terms *oxidized* and *NO-annealed* will be used to refer to samples that did not and did receive the NO POA, respectively.

3.2.3.1 Etch process artifacts

Prior to fully commencing the etch experiment, an analysis of the etch process's surface effects was performed. Each sample was cleaned using HPLC-grade ethanol and H_2O (as described in Sec. 3.2.2). Following this, one of both the oxidized and NO-annealed samples was etched a slight amount, leaving more than 50 nm of remaining oxide (see Fig. 3.10 for precise oxide profiles). Both high-resolution and survey XPS spectra were then acquired from all four of the samples, allowing for a detailed comparison between pre- and post-etching signals. The scans were taken at a high angle of 70° between the sample normal and the photoelectron detector, in order to promote detection of excitations originating from the very surface of the sample, rather than within it's bulk. Generally speaking, higher angles of detection (relative to the sample normal) are more surface sensitive, while lower angles probe deeper into the substrate.

The results of the survey scans (for the two NO-annealed samples) are shown in Figure 3.11. These scans cover a wide range of binding energies, allowing a quantification of the various elemental species present within the sample. As expected, the predominant signal arises from oxygen and silicon interactions. A strong carbon signal is also apparent due to the presence of adventitious hydrocarbon that inevitably forms on the sample surface under exposure to atmosphere [204]. In the NO annealed samples, a very faint fluorine signal was detected at the energies indicated in Fig. 3.11, but did not appear to change significantly after etching. The oxidized samples (not shown) had a slightly stronger fluorine signal both before and
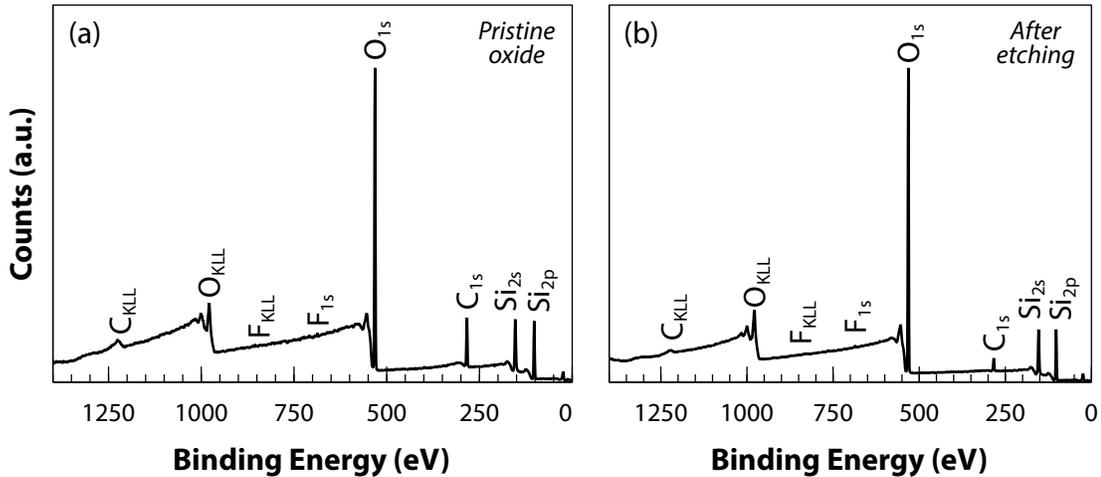
Figure 3.11: XPS survey scan ($\theta = 70°$) showing all the elements present in a measurement of a thick ($\approx 55\,\text{nm}$) SiO_2 oxide on a SiC substrate. No effects from the SiC substrate are apparent at such high thicknesses. (a) Survey scan of the NO-annealed oxide as-received, after cleaning with ethanol and H_2O; (b) survey scan of the second NO-annealed oxide, receiving the same cleaning as (a), but with a single spin-etch, removing $\approx 1\,\text{nm}$ of the oxide layer. Core-level excitations are identified by their shell (*1s*, *2p*, etc.), while Auger peaks are indicated by their transition pathway (e.g. *KLL*).

after etching, suggesting surface contamination that existed prior to the spin-etch

process.

Table 3.2: Quantification of elemental composition (atomic %) for four SiC/SiO_2 samples using XPS. The concentration of fluorine does not appear to grow significantly upon etching.

	Oxidized		NO-annealed	
Element	*Pristine*	*Etched*	*Pristine*	*Etched*
O	44.8 ± 0.2	53.2 ± 0.2	44.3 ± 0.3	49.1 ± 0.3
Si	30.5 ± 0.2	33.5 ± 0.2	33.0 ± 0.3	31.4 ± 0.3
C	20.0 ± 0.3	8.9 ± 0.3	22.5 ± 0.3	18.9 ± 0.3
F	4.7 ± 0.1	4.4 ± 0.1	0.2 ± 0.1	0.6 ± 0.1

In XPS, the relative stoichiometry of various components can be obtained by

calculating the ratios between the integrated peak intensities (after background re-

moval). In this work, this process was accomplished using the *Casa XPS* software package. Detailed elemental quantifications of the four samples (before and after etching) are presented in Table 3.2. The results do not show the expected composition of SiO_2 due to the presence of contamination layers on the surface of the sample, but changes in the concentrations after etching can be analyzed.

The most important consideration is the presence of fluorine, as this would be the primary source of residue arising from the HF spin-etch. As shown in the table, the concentration of F changes very slightly as a result of the etching, decreasing a small amount for the oxidized sample, while increasing for the NO-annealed. This is not assumed to be an effect of the NO annealing process, and is thought to be due to individual variation between samples. Regardless, the amount of F residue left behind by the spin-etch process is nearly insignificant compared to individual sample variation, indicating this process is suitable for the purposes of this work. For a more detailed analysis of spin-etch residue considerations, see Ref. [202].

Furthermore, high energy resolution analysis of the Si-2p regime revealed a silicon signal that matched exactly to bulk SiO_2 at an energy of $103.5\,eV$. This was the case both for all four specimens, both with and without etching, This fact provides further confidence that the spin-etch technique will not artificially impact the binding energy measurements when the interface is probed, or introduce unexpected states that may be confused for an interfacial state.

3.2.3.2 SiC/SiO$_2$ interfacial states

Using the spin-etch process, the four SiC/SiO$_2$ samples described above were etched to varying oxide thicknesses. Two of the samples (one oxidized and one NO-annealed) were etched completely to the substrate, in order to provide comparison to the methods used in prior studies by Xu *et al.* [196]. The remaining two samples were etched to very thin oxide layers using the spin-etch technique, with final thicknesses determined by ellipsometry as given in Table 3.3. With oxide thicknesses under 5 nm, the entire oxide and the substrate can be probed by XPS in one measurement, providing a complete picture of the interfacial area without the need for further etching or sputtering. Depth sensitive information can be obtained by comparing successive XPS measurements at different angles (i.e. angle-resolved experiments).

Table 3.3: SiO$_2$ thicknesses prior to XPS analysis, as measured by ellipsometry

	Complete etch	Thin oxide
Oxidized	$(1.0 \pm 0.1)\,\mathrm{nm}$	$(4.5 \pm 0.8)\,\mathrm{nm}$
NO-annealed	$(0.9 \pm 0.0)\,\mathrm{nm}$	$(2.0 \pm 0.4)\,\mathrm{nm}$

In this experiment, high energy resolution measurements were taken for each element (Si, C, N, and O) at three different angles – 0°, 50°, and 70° relative to the sample normal. The 0° measurement will probe the deepest depth, with the 70° the most surface sensitive. The signals from each element were analyzed for differences between the completely etched and thin oxide layer samples, as well as between the oxidized and NO-annealed samples.

Si-2p analysis

The results of the Si-2p analysis for the two thin oxide samples are shown in Fig. 3.12. In each of these spectra, the total 2p signal was well-fit by the summing of three distinct contributions, each comprised of two spin-orbit split components ($2p_{1/2}$ and $2p_{3/2}$). The degeneracy of the 2p energy levels requires the ratio of the split components to be 2:1 (4 e^- in the 3/2 level compared to 2 in the 1/2 level) [174]. Furthermore, the energy difference between the two levels is fixed, requiring a separation of $0.63\,\mathrm{eV}$ for silicon [205]. These physical constraints must be included in the fit in order to produce a valid interpretation of the data. Fitting the data with these requirements resulted in three components for each sample, which are attributed to Si in a SiC, interfacial, and oxide configuration (in order of increasing binding energy).

As shown in Fig. 3.12, only one interfacial "sub-oxide" component was required for valid fitting, in contrast to the three interfacial states reported in a recent synchrotron XPS work [67], agreeing instead with a few slightly older studies investigating SiO_2 grown on SiC *in situ* during the XPS measurement [68, 206, 207]. The binding energies of each of these components are shown in Table 3.4 for all four samples. The energy of the primary interfacial component is consistent with that of the Si^{+1} oxidation state reported by Johansson *et al.* [68]. Regardless of etching or NO-annealing, the bulk SiC and interfacial components remain at a uniform energy. The oxide component reveals an interesting phenomenon however. While the binding energy does not change with NO annealing, the completely etched samples have their "oxide" component at an energy consistently $-0.5\,\mathrm{eV}$ lower than those
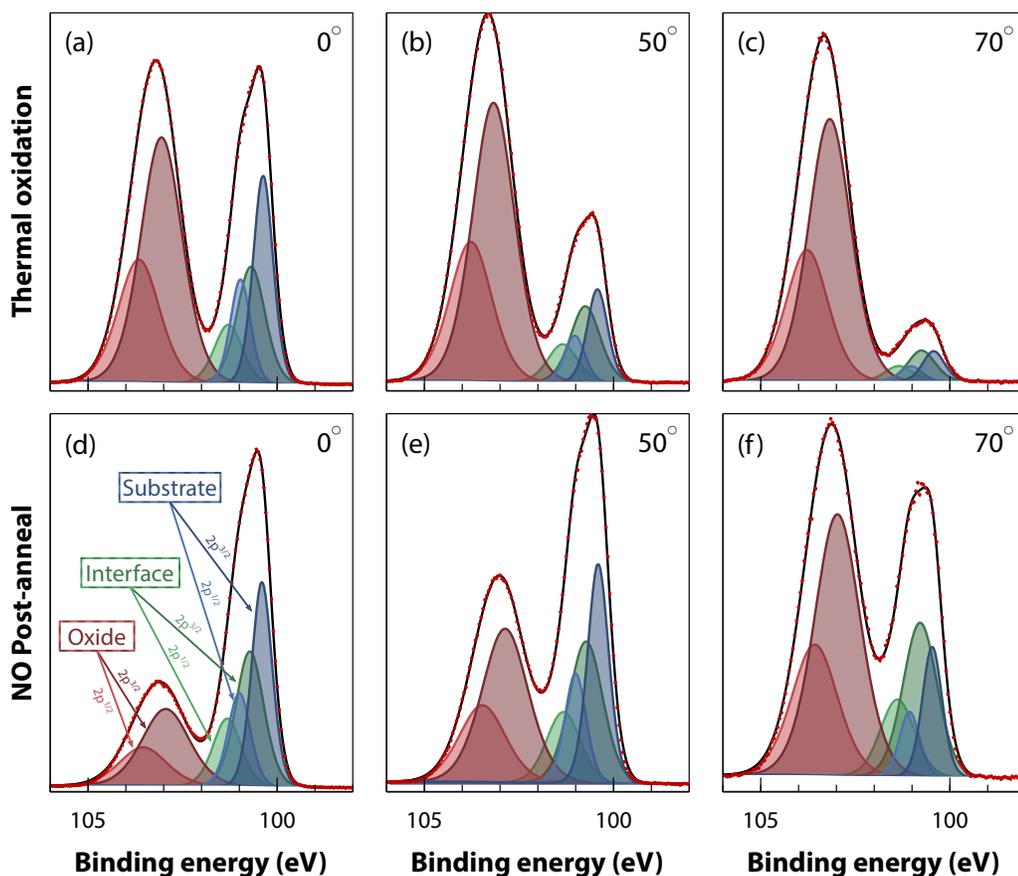
Figure 3.12: Angle-resolved high resolution XPS spectra from the "thin oxide" samples in the Si-2p energy regime. (a-c) Oxidized sample measurements at angles ranging from normal (a) to highly surface sensitive (c). (d-f) NO-annealed sample at the same angles. The spectra are fit by three spin-orbit split Gaussian components as described in the text. The raw data is shown as red dots, and the various colored peaks are the fitting components. For each color, the dark peak is the $2p_{3/2}$ peak and the lighter peak is the $2p_{1/2}$. The black line matching the raw data is the total envelope function obtained by summing the individual components.

samples retaining a thin SiO_2 layer.

Two possible mechanisms could explain this phenomenon. First, it is commonly accepted that upon NO annealing, the nitrogen forms a layer containing $Si-N$ bonds localized to within approximately one monolayer of the SiC/SiO_2 interface. This layer has been found to be resistant to etching, as evidenced by the quantification of nitrogen in XPS and MEIS signals after complete etching [196]. It has been proposed that this lower energy component may be evidence of this nitridated layer that remains after etching in HF [208]. This interpretation is unlikely correct however, due primarily to the fact that the reduced energy peak is observed at nearly identical energy in both the oxidized and NO-annealed sample. Were it to be a surface state attributable to nitrogen, its presence would not be expected in the sample not receiving an NO POA.

Table 3.4: Binding energies (in eV) of the Si-2$p_{3/2}$ peak for each fit component for four SiC/SiO_2 oxides, measured by XPS at a 70° angle of incidence.

Sample	SiC	Interface	Oxide
Thin oxide – Ox.	100.4	100.7	103.1
Thin oxide – NO	100.5	100.8	103.0
Etched – Ox.	100.5	100.9	102.6
Etched – NO	100.5	100.9	102.5

Rather, it is proposed that lower energy peaks observed in the completely etched samples arise from the formation of a native surface oxide complex with a binding energy slightly lower than that of fully complemented SiO_2 (a "sub-oxide"). As the samples are exposed to air after etching, this oxide has ample opportunity to form at room temperatures. Evidence for such a state at the SiC surface upon

exposure to air has been previously reported as a mixture of SiO_xC_y species, with binding energies of $+0.2$ to $2.1\,eV$ above that of SiC [209] (note that comparing relative binding energies is more appropriate than absolute values due to differences in energy calibration between experiments). The thickness of the sub-oxide was determined to be approximately $0.7\,nm$ by angle-resolved measurements. Such a value is similar to that measured for the completely etched samples using ellipsometry ($0.9\,nm$), further validating this interpretation. It is important to note that this "native oxide" state is entirely distinct from the "interfacial" state identified at $\approx 100.8\,eV$, which does not appear to be drastically modified by etching or the NO-anneal process.

Interestingly, in both the completely etched and thin-oxide samples, the NO-annealed sample had its oxide (or sub-oxide) peak at a binding energy consistently $-0.1\,eV$ below that of the corresponding oxidized sample. The chemical shift was not significant enough to justify an additional fitting component in the model (likely due to low overall N concentrations), but suggests a subtle modification of the surface state due to nitrogen at the interface. Owing to nitrogen's lower electronegativity, the Si−N bond is lower in energy than Si−O ($+1.7$ and $+3.0\,eV$ above Si−C, respectively [210]), meaning the presence of N atoms could very well lower the energy of this peak.

N-1s analysis

Further insight into the effects of nitrogen at the SiC/SiO_2 interface can be gained by careful analysis of the N-1s XPS signal. The results for each measure-

ment of the N signal in the NO-annealed devices is shown in Fig 3.13. Measuring this energy regime on the oxidized sample did not show any significant nitrogen contribution (not shown), meaning the entire signal can be considered to originate from the NO annealing process. Due to the lower degeneracy of the 1s core level, no spin-orbit splitting is required when fitting components to the signal, meaning it can be directly fit by a sequence of Gaussian peaks, each one representing a unique configuration of the N atoms within the sampled volume.
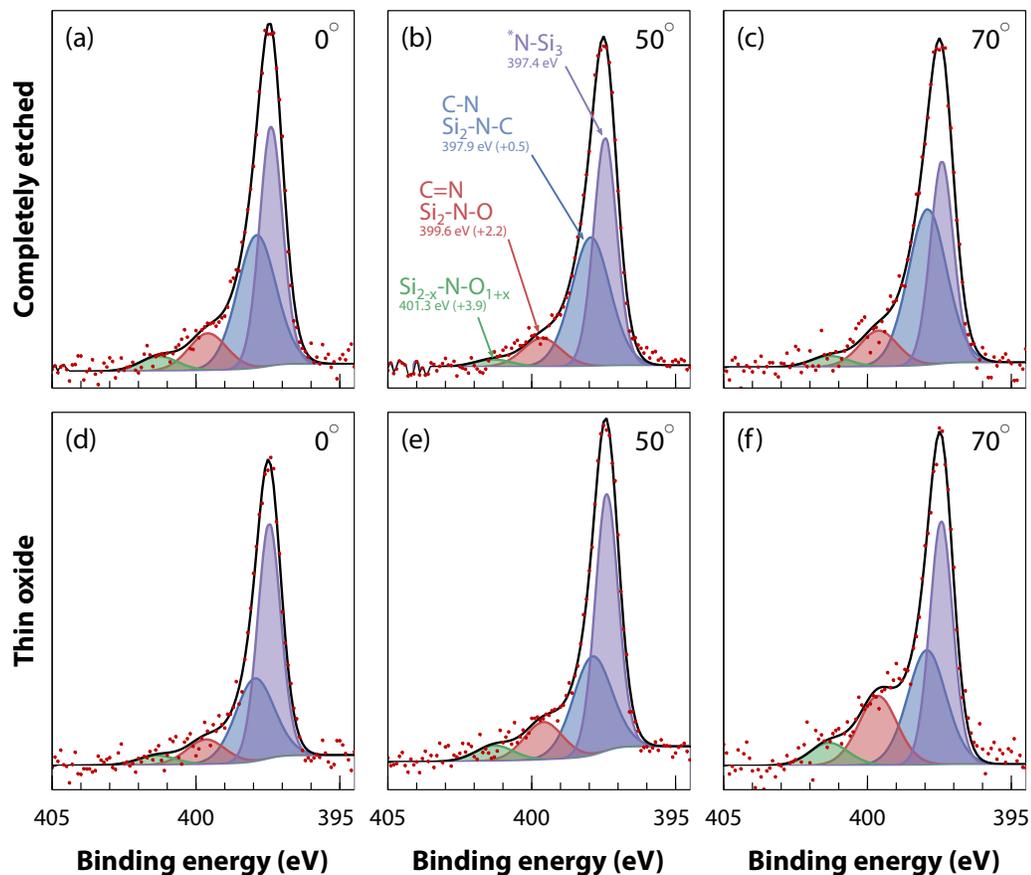
Figure 3.13: Angle-resolved high resolution XPS spectra from the two NO-annealed samples in the N-1s energy regime. (a-c) "Completely etched" NO-annealed sample measurements at angles ranging from normal (a) to highly surface sensitive (c). (d-f) Thin oxide NO-annealed sample at the same angles. The spectra are fit by four Gaussian components as described in the text, shown in various colors. The raw data is represented by the red dots, and the envelope function of the fitted components is shown in black.

The N-1s signals are shown in Fig. 3.13 for the two NO-annealed samples. The corresponding fit components are highlighted in the figure as well. In all measurements, four distinct components were required to model the experimental data. The primary peak in each measurement was located at a binding energy of $397.4\,\mathrm{eV}$, consistent with the literature value for N in a 3-fold coordination with Si ($\mathrm{N-Si_3}$ configuration, like observed in $\mathrm{Si_3N_4}$) [210]. Interestingly, the energy of the peaks was not significantly different between the completely etched and thin oxide samples, confirming as previously argued [196] that the HF etching process does not significantly affect the states of the nitridated layer at the interface. There is however, a decrease in the relative intensity of the higher energy components (red and green, relative to purple) in the completely etched sample compared to the thin oxide (compare Fig. 3.13c and 3.13f), suggesting that while the etch process does not appreciably alter the nitrogen states, it does remove some of them. This indicates (intuitively) that completely removing the oxide changes the interface from its typical configuration, and extreme caution must be taken when extrapolating the meaning of measurements from such an etched interface to real devices.

Aside from the primary $\mathrm{N-Si_3}$ peak (purple in Fig. 3.13) in the N-1s signal, the three remaining peaks at higher energies represent the bonding of nitrogen to successively more electronegative elements, such as carbon or oxygen. Due to the significant overlap in energies of the various possible bonding configurations, it is unlikely that a definitive attribution can be accurately made to each peak, but analyzing prior works on these materials provides some possible candidates. Again, since spectrometer calibrations can vary significantly between experiments, com-

parisons are made by relative energetic offsets (compared to the $N-Si_3$ peak), as opposed to absolute binding energy measurements. The first peak (blue), located $+0.5\,eV$ above $N-Si_3$, is most likely due to the substitution of N for C within the SiC structure at the interface, giving rise to a Si_2-N-C configuration [196]. Another possible candidate for this peak is the $C-N$ bond [210], but it is less likely that nitrogen would not be involved in silicon bonding, making the former configuration more probable.

The next component (red, $+2.2\,eV$ above $N-Si_3$) appears most likely to be an oxynitride state with a configuration of Si_2-N-O [211, 212]. Since oxygen is more electronegative than carbon, this state has a higher binding energy than the previous one. Alternatively, this peak could arise from imine-like double bonds between carbon and nitrogen ($C{=}N$) [210], although as above, the former configuration is more likely due to the presence of silicon. Finally, the most energetic nitrogen configuration was found at an energy $+3.9\,eV$ above that of $N-Si_3$ (green). A direct match for this state could not be found in the literature, The other silicon oxynitride configuration ($Si-N-O_2$) and direct $N-O$ bonds are expected at higher offsets of $+5.3$ and $+5.1\,eV$, respectively [210, 212]. Thus, the observed state could be a mix of these and perhaps other C-containing configurations, or perhaps a $Si_{2-x}-N-O_{1+x}$ -like state where the nitrogen is not fully coordinated with oxygen atoms. More investigation of the state is needed, especially since this fourth component has not been previously observed at nitridated SiC/SiO_2 interfaces [196].

Composition of nitridated interfacial layers

Besides the bonding state analysis, the high energy resolution scans of each element can provide a precise measurement of elemental composition (similar to that performed with the survey scans in Sec. 3.2.3.1). Of particular interest is the distribution of nitrogen at the interface. As described in Sec. 1.1.5, most prior literature has found the N to be localized very close to the SiC/SiO_2 interface, and the results of the present XPS experiment confirm this fact as well. Quantification of the relative atomic composition of the two NO-annealed samples is given in Table 3.5.

Table 3.5: Relative elemental composition of the two NO-annealed surfaces (atomic %), measured from the relative integrated intensity of the high-resolution XPS signals. Note the increase in N content for both samples as the measurements become more surface sensitive.

Sample	Angle	C-1s	N-1s	O-1s	Si-2p
Thin oxide	0°	29.9	1.0	21.8	47.3
	50°	33.6	1.4	29.4	35.6
	70°	36.3	1.5	33.5	28.7
Etched	0°	40.9	1.7	9.6	47.8
	50°	41.4	2.6	16.5	39.5
	70°	41.2	2.7	20.6	35.5

Absolute differences in composition cannot be directly compared between the two samples due to the oxide overlayer present in the thin oxide specimen (causing the N content to appear lower). Changes in the signal intensities with angle reveal information about the depth distribution of the components, however. For both samples, the measurement at more glancing angles (surface sensitive) indicates significantly higher N content compared to the measurement at normal incidence (probing deeper into the sample). This clearly indicates that the nitrogen is indeed preferentially located at the surface (or interface), as opposed to evenly distributed

throughout the substrate or oxide.

3.2.3.3 w_{TL} from XPS measurements

The final piece of information that can be gleaned from the angle-resolved XPS measurements concerns a quantitative measure of the thickness of the interfacial state identified in the Si-2p signal. A common means to measure the thickness of signals in XPS is to analyze the variation in peak intensities as a function of measurement angle, making use of the additional signal attenuation that occurs as a result of a longer path length through the sample [213].

Assuming a layer of SiO_2 with thickness d_{SiO_2} on top of a layer of sub-oxide interface of thickness d_{int}, both on top of a bulk SiC substrate, the layer attenuation model predicts the ratios of integrated peak intensities as:

$$\frac{I_{SiO_2}}{I_{SiC}} = \frac{c_{SiO_2}}{c_{SiC}} e^{\frac{d_{\mathrm{int}}}{\lambda \cos\theta}} \left(e^{\frac{d_{SiO_2}}{\lambda \cos\theta}} - 1 \right) \tag{3.1}$$

$$\frac{I_{\mathrm{int}}}{I_{SiC}} = \frac{c_{\mathrm{int}}}{c_{SiC}} \left(e^{\frac{d_{\mathrm{int}}}{\lambda \cos\theta}} - 1 \right) \tag{3.2}$$

where c_i is the atomic concentration of Si in the relevant species (i.e. 0.5 in SiC, 0.33 in SiO_2, and assumed to be 0.66 in the interface (in a configuration similar to Si_2O)) [68]. λ is the effective attenuation length through the sample for Si-2p electrons, calculated as an average value of $3.2\,\mathrm{nm}$ using the NIST standard reference data [214]. By plotting the calculated integrated intensity ratios for each component as a function of electron emission angle, the values for d_{int} and d_{SiO_2} can be fit according to Eq. 3.1 and 3.2 to obtain a measure of the thickness of the layer creating the signal.
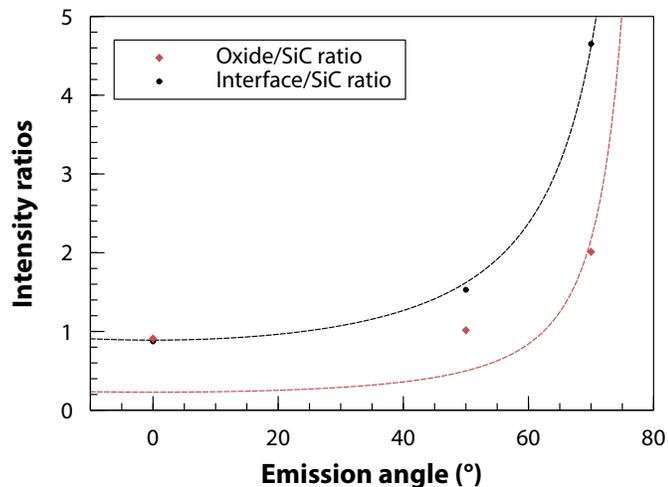
Figure 3.14: Determining layer thicknesses for the NO-annealed thin oxide sample using a layer attenuation model. Integrated XPS intensity ratios are plotted as a function of measurement angle to obtain the values of d_{int} and d_{SiO_2}. The dashed lines are the result of fitting Eq. 3.1 and 3.2 to the data.

The intensity ratios for both the oxide and interface component are shown for the NO-annealed thin oxide sample in Fig 3.14. The layer thickness equations were fit to these data points (using a non-linear model fit in the *Mathematica* software), and the results are shown as dashed lines in the figure. For this sample, the interface component was fit very well (meaning d_{int} will be an accurate value), while the oxide fit was less ideal. This is attributed to to thickness variations in the SiO_2 overlayer, which cause varying ratio calculations at different angles. The results from this fitting for the four samples investigated in this work are provided in Table 3.6.

Generally speaking, the total overlayer thickness (interface + oxide) measured by XPS agrees very well with the original ellipsometry measurements reported in Table 3.3, providing confidence in both techniques. Interestingly, the completely etched samples have d_{int} values significantly lower than the thin oxide results, further

Table 3.6: Interface and oxide layer thicknesses, calculated with a layer attenuation model from angle-resolved XPS data. Thicknesses are given in nm, and the R^2 value of the fit is provided in parentheses after each value.

Sample	d_{int}	d_{SiO_2}	d_{total}
Thin oxide – Ox.	2.9 (0.99)	0.2 (0.60)	3.1
Thin oxide – NO	1.6 (1.00)	0.6 (0.87)	2.2
Etched – Ox.	0.3 (0.94)	0.7 (0.76)	1.0
Etched – NO	0.2 (0.96)	0.8 (0.83)	1.0

confirming that the HF etch does indeed have significant impacts on the interfacial states, even if the majority of the N content is retained (similar to the implications of the N-1s measurements in Sec. 3.2.3.2).

The thin oxide values of d_{int} provide insight into the modification of interfacial states by NO annealing. There is a clear reduction in d_{int} upon NO annealing, agreeing with the reduction in w_{TL} observed via TEM in Sec. 3.1. The values of d_{int} obtained by XPS however, are only approximately half those measured for w_{TL} for devices under similar conditions. It is likely that the conservative definition of w_{TL} used in the TEM experiments (and the finite Gaussian beam size) may artificially inflate the TL widths relative to XPS measurements. Regardless, both TEM and XPS experiments confirm the presence of an interfacial layer extending over multiple SiC unit cells and greater than 1 nm in thickness, which is well over atomic-scale roughness. Furthermore, these results find that the interface is certainly not "chemically abrupt" as some prior works have posited [69].

3.2.4 Conclusions

The XPS experiments performed as part of this work provide an important perspective of the SiC/SiO$_2$ interface that is complementary to that obtained from TEM-EELS measurements. Using a carefully refined spin-etch process, oxidized and NO post-annealed SiC samples were etched in varying degrees, providing insights into the effects of the etch process, as well as the undisturbed SiC/SiO$_2$ interface in the "thin oxide" samples. This is the first study to carefully etch close to, but not all the way through to the interface, allowing for a unique measurement of the bonding configurations present. Analysis of the Si-2p signal revealed one primary interfacial Si bonding state that changes very slightly in binding energy upon NO annealing, while fitting of the N-1s signal uncovered at least four distinct N configurations at the interface. Finally, angle resolved XPS measurements determined the Si interfacial state to have a finite thickness on the order of 2 to 3 nm, comparable to the w_{TL} value measured by TEM-EELS.

3.3 Impacts of SiC substrate orientation on the transition layer

Commercialization of SiC MOS devices has been achieved primarily due to improvements in substrate fabrication methods and the NO post-annealing process that enables practical μ_{FE} values in fabricated SiC/SiO$_2$ components. While understanding the fundamental mechanisms behind this mobility enhancement is an interesting academic question, it is equally important to look towards future advancements in device performance in order to spur SiC (and other WBG materials) to full market saturation. One of the more promising avenues of research has been the modification of the SiC substrate's crystallographic orientation. In particular, the $\left(11\bar{2}0\right)$ face of the SiC unit cell (known as the *a*-face) has shown great promise with very desirable device properties, such as high mobility and low threshold voltage [48, 60, 215–218] (see Fig. 1.6 for a depiction of the SiC orientations). Indeed, as shown in Fig. 1.5, performance gains of 50% (compared to equitable Si-face devices) have been observed when combining the *a*-face with the NO-anneal process [48].

While the *a*-face performance gains are obvious, the physical origins of the improvements remain to be suitably described. There are three primary differences in *a*-face interfaces compared with the corresponding Si-face:

1. *a*-face interfaces are inherently flatter than Si-face ones in practical devices, due to the 4° or 8° miscut that is used in the fabrication of Si-face epilayers. This miscut is not required in *a*-face devices, allowing for smoother interfaces that may reduce surface roughness scattering of free carriers (and improving mobility as a result) [60].

2. The *a*-face has been shown to have higher reactivity than the Si-face [219], suggesting that the N introduced by the NO anneal may more easily become electrically active, contributing to a higher number of free carriers within the channel region (improving mobility).

3. The *a*-face has a significantly different surface bonding termination than the Si-face (50% each Si- and C- termination, compared to 100% Si- for the Si-face). Potentially related to the reactivity described above, this unique surface structure will almost definitely lead to different bonding configurations at the interface with SiO_2, potentially creating additional donor or acceptor states that could help improve mobility.

To investigate these differences, a TEM-EELS experiment was devised to carefully test each particular effect. A total of six SiC samples (two of each orientation) were fabricated by collaborators at Rutgers University with three different substrate orientations. The first was a typical Si-face substrate miscut at the standard 4° from the *c*-axis. The second was a Si-face on-axis wafer (i.e. without any miscut), chosen to help investigate difference in Si-face interfaces as a function of roughness. The last substrate was an *a*-face wafer (again with no miscut), chosen in hopes of better understanding the origins of this orientation's higher mobilities. The six samples received the industry-standard thermal oxidation, resulting in $\approx 60\,nm$ SiO_2 layers. One sample of each orientation additionally received a $2\,h$ NO POA, to investigate differences in N incorporation as a function of orientation. TEM lamellae were extracted from each of the samples following the procedures of Sec. 2.2.1 and 3.1.1.

Throughout this section, the samples will be referenced by their orientation and treatment (e.g. "Si- on-axis NO" for the Si-face on-axis sample receiving an NO POA).

3.3.1   HRTEM investigation of various orientations

Initial inspections of the various orientations began with high resolution TEM imaging. The results of this measurement for each sample are shown in Fig. 3.15, and clearly illustrate the differences in atomic structure of the SiC substrates.

In the Si-miscut samples (Fig. 3.15a and d), the atomic scale terraces arising from the miscut are clearly visible, with monolayer steps appearing every 2 to 5 nm. Large bunches of steps were rarely observed, indicating a relatively uniform roughness in the direction of steps of only about a monolayer (2.5 Å). Since TEM measurements are projected through the thickness of the lamella, the atomic-scale roughness in the direction of the beam can be estimated by the extent of mixing of the amorphous SiO_2 and crystalline SiC signal at the interface (assuming an atomically sharp interface, which may or may not be a valid assumption). This mixing of signals rarely extends further than one monolayer perpendicular to the interface, again suggesting an upper limit on the atomic scale roughness of approximately 2.5 Å. It is important to note however, that this measurement will not capture larger scale variations in surface roughness, as it only accounts for a distance equal to the thickness of the sample (in this case, $\approx$50 nm). While TEM is a less-than-ideal technique for measuring roughness (due to the projection issue, as well

117

as electron wavefunction delocalization), these results are generally consistent with AFM studies, which have revealed an average roughness of $1.2\,\text{Å}$ at NO-annealed Si-face interfaces [52]. Interestingly, the oxidized sample did not appear to have significantly more roughness at the interface than the NO-annealed one.
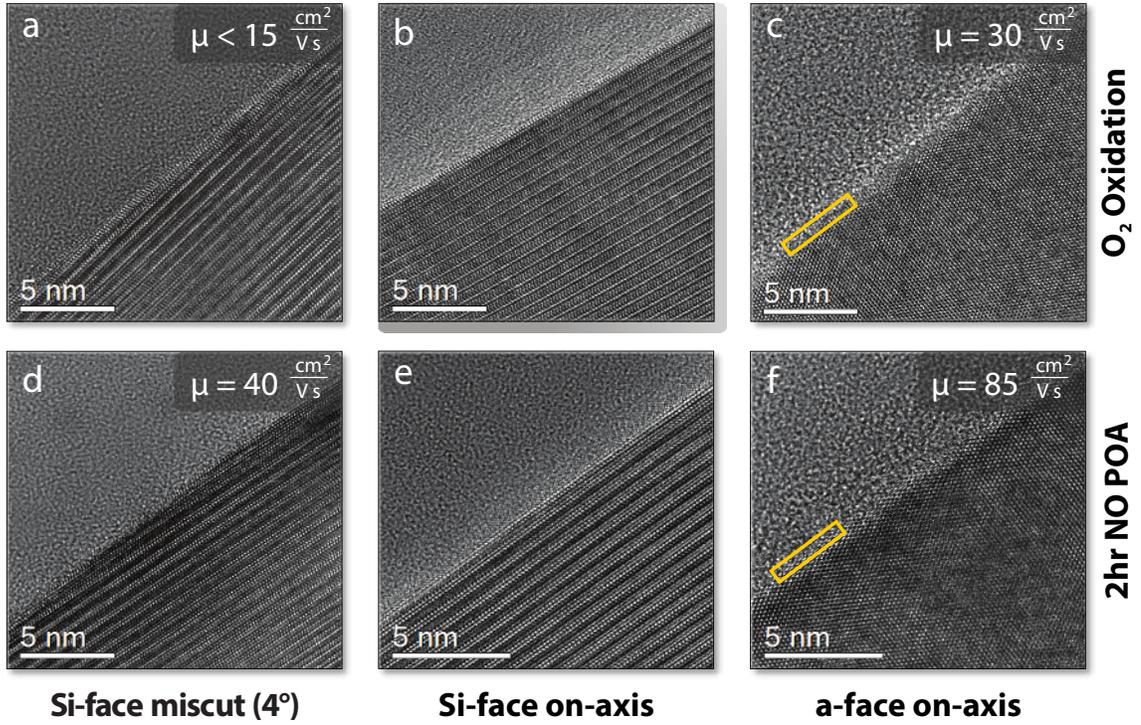
Figure 3.15: High-resolution TEM images of each substrate orientation. (a-c) Thermally oxidized samples; (d-f) NO post-annealed samples. Where measured, the mobility of devices fabricated for each orientation is indicated. Zone axes are $[1\bar{2}10]$ for the Si-face samples (with the miscut in the substrate visible), and $[0001]$ for the *a*-face. The yellow boxes highlight apparent structural modifications to the SiC crystal structure at the interface.

The on-axis Si-face samples (Fig. 3.15b and e) appear very similar to the miscut ones within the substrate and oxide, with the only variation appearing near the interface. As expected, these on-axis samples to not exhibit any systematic atomic steps or terraces as observed for the miscut samples (Fig. 3.15a and d). This results in significantly lower roughness in the $[11\bar{2}0]$ direction parallel to the

interface, with only rarely any steps visible in an image. In the direction of the beam, again the roughness appears to be no more than one (or perhaps two) monolayers. Differences between the NO annealed and oxidized samples are not immediately obvious from the HRTEM images, as their interfacial characteristics appear very similar.

The *a*-face samples (Fig. 3.15c and f) appear significantly different to the Si-face images, primarily due to their different zone axis (the direction the electron beam travels through the sample). While the Si-face images are taken with the beam parallel to the basal plane of the structure, the *a*-face have the zone axis parallel to the *c*-axis of the crystal structure. As with the Si on-axis samples, the *a*-face substrates have interfaces that are very smooth, with very limited roughness. Both samples appear to have a modification of the usual SiC crystal structure within about 5 Å of the interface, highlighted within the yellow boxes of Fig. 3.15.

In the oxidized sample, there is a distinct region of 4 atomic layers with a periodicity of 1.5 Å (perpendicular to the interface), compared to nearly twice that in the bulk SiC. While unclear from the HRTEM images alone, this could be either a chemically distinct layer, or perhaps a compressive strain along the $[11\bar{2}0]$ direction. In the NO-annealed *a*-face sample, there is a similar modification, once again extending for approximately 4 atomic layers. In this sample, the layer appears less uniform however, suggesting a potential effect of the NO annealing process on this interfacial state.

While discussion of the differences between sample images is useful, care must be taken not to infer too much about the structure in this region from HRTEM im-

ages alone however, due to a multitude of factors that can affect such experiments. In a high-resolution image, the structure of the sample is not directly measured. Instead, the interference pattern of many transmitted and diffracted electrons gives rise to the intensity patterns observed in an image. With ideal experimental conditions, this image represents only the shift in phase of the electron beam wavefunction introduced by the sample, which is proportional to the electrostatic potential at the exit surface of the specimen.

In practice however, thick specimens and imperfections of the objective lens cause a mixing of the wavefunction's phase and amplitude, meaning a direct interpretation is rarely possible from a single image. Additionally, Fresnel (near-field) diffraction at interfaces can give rise to "fringes" of intensity parallel to the interface, often masquerading as legitimate features [118]. The appearance of such features will change greatly depending on specific lens defocus settings. Great care has been taken in this work to ensure images are taken with similar experimental conditions, but this caveat is provided to prevent the reader from inferring too much from the HRTEM images alone. For more definitive results, reconstruction of the exit-plane wavefunction should be performed, which allows for the extraction of the pure phase without the convoluting affects of defocus [220].

3.3.2 w_{TL} as a function of crystallographic orientation

While the HRTEM results show some interesting differences between the various orientations, they ultimately give only limited structural information related to
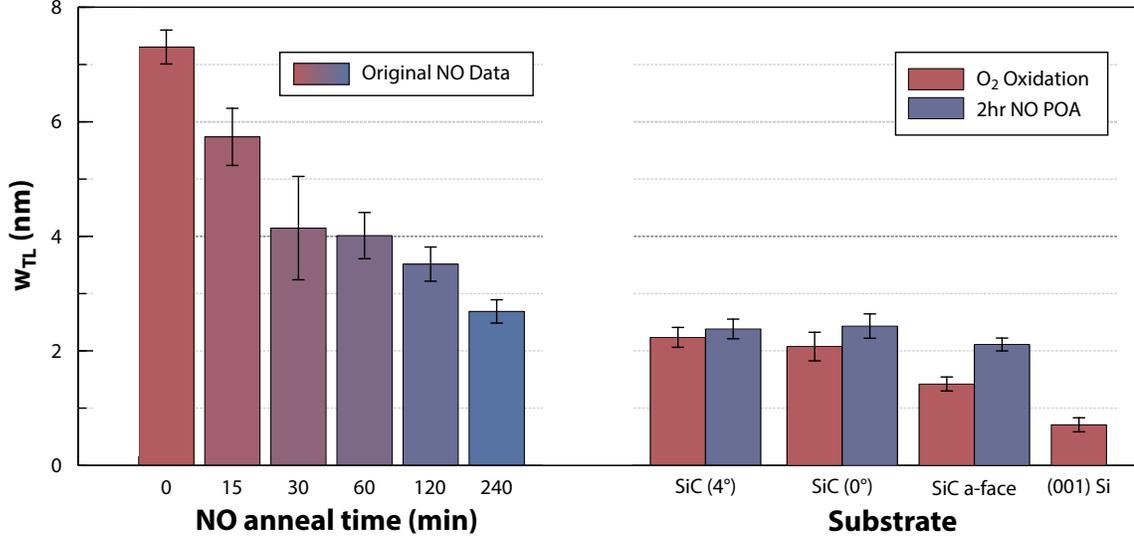
Figure 3.16: Comparison of w_{TL} for the various crystallographic orientations. (left) Original NO-anneal time series data from Sec. 3.1 reproduced for reference. (right) w_{TL} measurements for the three SiC orientations presented in this section (Si-4°, Si-0°, and a-face), together with a reference measurement from a (001) Si/SiO$_2$ interface. The previously measured NO-anneal/w_{TL} relationship is not observed on these samples, as all SiC samples had a w_{TL} around 2 nm. The sharper w_{TL} measured for the Si/SiO$_2$ (< 1 nm) indicates the data is not limited by the resolution of the measurement technique.

the periodicity of the electron density in the sample. Techniques such as EELS reveal more information about the chemical nature of the samples, providing a better overall understanding of the interfaces in question. A procedure very similar to that of Sec. 3.1.2.1 was used to measure the w_{TL} for each of the samples using the chemical shift method. For control (and comparison), an additional sample (thermally grown oxide on a (001) Si wafer) was measured. The Si/SiO$_2$ is known to be nearly perfect, and such a measurement provides a useful comparison to the SiC samples.

The results of these w_{TL} measurements are shown in the right half of Fig. 3.16. The left portion of the figure is a reproduction of the data from Sec. 3.1 for facile comparison. The error bars of the data represent the 95% confidence intervals for the mean of many line scans taken across each interface. Interestingly, the results from

the present set of samples were found to be in direct contrast with expectations derived from the previous NO time-series experiments. Namely, all of the w_{TL} values measured for each orientation were nearly identical, even when comparing the oxidized samples to those receiving a 2 h NO post-oxidation anneal.

The present w_{TL} values indicate a TL on the order of about 2 nm, significantly smaller than the range of values observed previously in this thesis (2.7 to 7.5 nm). This suggests that even for samples not receiving an NO treatment, the quality of the interface has improved substantially. It is thought that this difference may be due to the significant improvements made by commercial suppliers (Cree, Inc.) in the quality of SiC substrates and the resulting epilayers. The wafers used for the NO time-series experiment were purchased from Cree circa 2008, while those for the present data are substantially newer (2014). Furthermore, it is proposed that this may help explain the improvement observed in SiC/SiO$_2$ interfaces over time. Recent studies have shown significantly smaller TL widths (2 nm presently vs. 20 nm [64]) and the complete lack of excess carbon at the interface [221] compared to its regular detection in prior works [35, 62–64].

The fact that all measurements from this sample set were very similar (and smaller than all previous samples) led to some concern that the results were being influenced by a resolution limit inherent to the w_{TL} measurement technique. To investigate this possibility, a lamella was fabricated from a thermally oxidized Si substrate. The thermal Si/SiO$_2$ interface has been previously shown to have a chemical thickness in the range of 3 to 7 Å [222], meaning a measurement higher than this with the methods used in this work would suggest a resolution limit. As

shown in the right-most bar of Fig. 3.16, w_{TL} for the Si sample was measured at 7 Å, in close agreement with the value obtained by Muller *et al.* [222]. This result confirms that the SiC measurements are indeed valid, and not limited by spatial resolution.

Aside from their unexpected nature, two results from the w_{TL} measurements are particularly interesting. First, the results for the on-axis vs. miscut Si-face samples were nearly identical for both the oxidized and NO-annealed cases. This indicates that the interfacial roughness added by the miscut does not substantially affect the TL on the atomic scale (although it is possible that it could still adversely affect mobilities). Second, the present w_{TL} results contradict the relationship between TL width and μ_{FE}, observed in Sec. 3.1 and in prior research [64]. Recent results have shown marked improvements in μ_{FE} for *a*-face samples between oxidized and NO-annealed devices [60], but in the present findings w_{TL} was in fact larger for the NO-annealed sample. This fact suggests that other interfacial parameters are likely ultimately responsible for improvements in μ_{FE}, and the w_{TL} relationship was merely a correlation.

3.3.3 Hyperspectral decomposition at the SiC/SiO$_2$ interface

To better probe the specific interfacial states in this work, the hyperspectral decomposition (or unmixing) techniques introduced in Sec. 2.1.2.2 were used. The goal of this process was to observe how the chemical states at the interface vary with and without NO annealing, as well as with changes in substrate orientation.

Subtle differences in the ELNES of each element (Si, C, and O) reveal information regarding the bonding configurations of that element throughout the sampled area.

In the following sections, results from the unmixing of EELS spectrum images for each element are presented. Spectral decomposition was accomplished using the `HyperSpy` software package [163], using non-negative matrix factorization after background subtraction. Multiple SI were acquired from each sample, and the results presented here are qualitatively representative of all the measurements taken. It is important to note that in its current form, the spectral unmixing process is inherently a qualitative technique rather than a quantitative one, due to the lack of a physical basis for the resulting output (although this may improve with better algorithms and understanding of the impacts on data statistics [136, 145]). Regardless, it provides a very useful method by which to explore dilute and unknown signals in a collection of data, as will be shown.

Generally, the process of spectral unmixing was accomplished with the following steps. First, the experimental data was treated to remove common artifacts typical in acquisition. This included aligning the EELS data to a flat interface (using the simultaneously collected STEM signal) to correct for spatial drift that inevitably occurred during acquisition. Drift of the beam energy over the course of collection was also corrected by aligning the energy of the edge onset to a constant value in the first column of acquired data (see Ref. [116] for the specific implementation). This technique, while less than perfect, approximates the benefits of collecting the zero-loss EELS signal at the same time as the core-loss, which was not experimentally possible with the equipment used in this work. Significant spikes in

124

the data arising from spurious x-rays sensed by the detector were removed though linear interpolation of the signal in the spike region (with random Poissonian noise added). Finally, for lower energy edges such as Si-$L_{2,3}$ and C-K, the background intensity was typically removed through the use of a power-law fit. This process was of limited utility for the lower intensity O-K edge, however.

Once processed, an initial PCA decomposition was performed to generate a scree plot (as shown in Fig. 2.5a). An initial choice for the number of components (n) to include in the analysis was determined by finding the "elbow" in the scree plot by inspection. For most of the signals investigated in this work, n ranged from 2 to 4. n indicates the minimal number of components necessary to describe the majority of variance within the data. With this value for n, an analysis of the independent components followed using the NMF algorithm for unmixing. The positivity assumption inherent in NMF typically provided more interpretable results than the ICA algorithms, although these were performed as well, for comparison. The results provided in the ensuing sections were obtained using NMF. Since it is possible that a weak signal source within the data could have a variance similar to that of the higher-order noise components, the unmixing process was always repeated with a larger number of components to ensure that significant contributions to the data were not being missed.

In this manner, the Si-$L_{2,3}$, C-K, and O-K edges were analyzed to find their constituent components, with the results presented in the following sections. Unfortunately, the concentrations of N were too low for reliable detection of the N-K edge, precluding it from hyperspectral analysis.

3.3.3.1 Si-$L_{2,3}$ EELS SI unmixing

Given that w_{TL} has been measured with the chemical shift of the Si-$L_{2,3}$ edge, initial decomposition investigations used this signal as well, for direct comparison. The results of the NMF decomposition of the Si-$L_{2,3}$ edge for each of the three oxidized samples are shown in Fig. 3.17. For each sample, the identified spectral components are shown in the bottom half of the figure, with their respective loading maps reflecting the spatial distribution of the components' intensity displayed above. Due to slight differences in spectrometer offset calibration between samples, the components are plotted on a relative energy-loss scale, aligned to the edge onset of the SiC component in each case, which is expected to be located at $100\,\mathrm{eV}$. For all of the oxidized samples, three components were suitable to fully describe the collected data.

The first component, present in varying amounts everywhere throughout the sample reflects (to a first order) the ionization cross section of the Si atom, absent of any ELNES features. Given the energy of the edge onset and the overall lack of fine structure in this component, it is clear that it originates from excitations of the Si-2p electrons, but does not include the final state or bonding effects that give rise to the oscillations of intensity observed in the ELNES. At higher energies, it is likely this component additionally includes background intensity that was not effectively removed by the power-law fit subtraction, which may explain why the background component varies slightly in different samples. Its overall intensity throughout the sampled area is expected to be proportional to the number of Si atoms present

(scattering probability), explaining why the component is typically stronger in the SiC than SiO_2. FIB lamella preparation generally results in a slightly thinner oxide than SiC due to its higher susceptibility to ion sputtering, and in SiC the Si atomic percentage is higher than in SiO_2 (50% vs. 33%), meaning there are more overall opportunities for Si interactions in SiC than in SiO_2.

The two remaining components are clearly localized within the SiC and SiO_2 halves of the interface, respectively. As described in Sec. 2.1.2.2, the NMF algorithm results in additive components, such that the total signal at each point in the data can be represented by the sum of all three components, weighted by their relative intensities (as shown in the loading maps). As such, each additional component includes only the features of the ELNES unique to the particular material. As expected, the onset of the SiC component is approximately $5\,\mathrm{eV}$ below that of the SiO_2 component. The overall spectral signatures of the SiC and SiO_2 components do not appear to be significantly altered by the substrate orientation, indicating little change in Si bonding character between the samples.

Interestingly, there were no additional components observed to be localized near the interface in the oxidized samples, suggesting that (with respect to Si) the TL may indeed be a linear combination of SiC and SiO_2-like bonding. The presence of the interfacial state observed via XPS (Sec. 3.2.3) is not evidenced in the data, suggesting that the present technique may not be as sensitive to subtle changes in oxidation state as XPS.
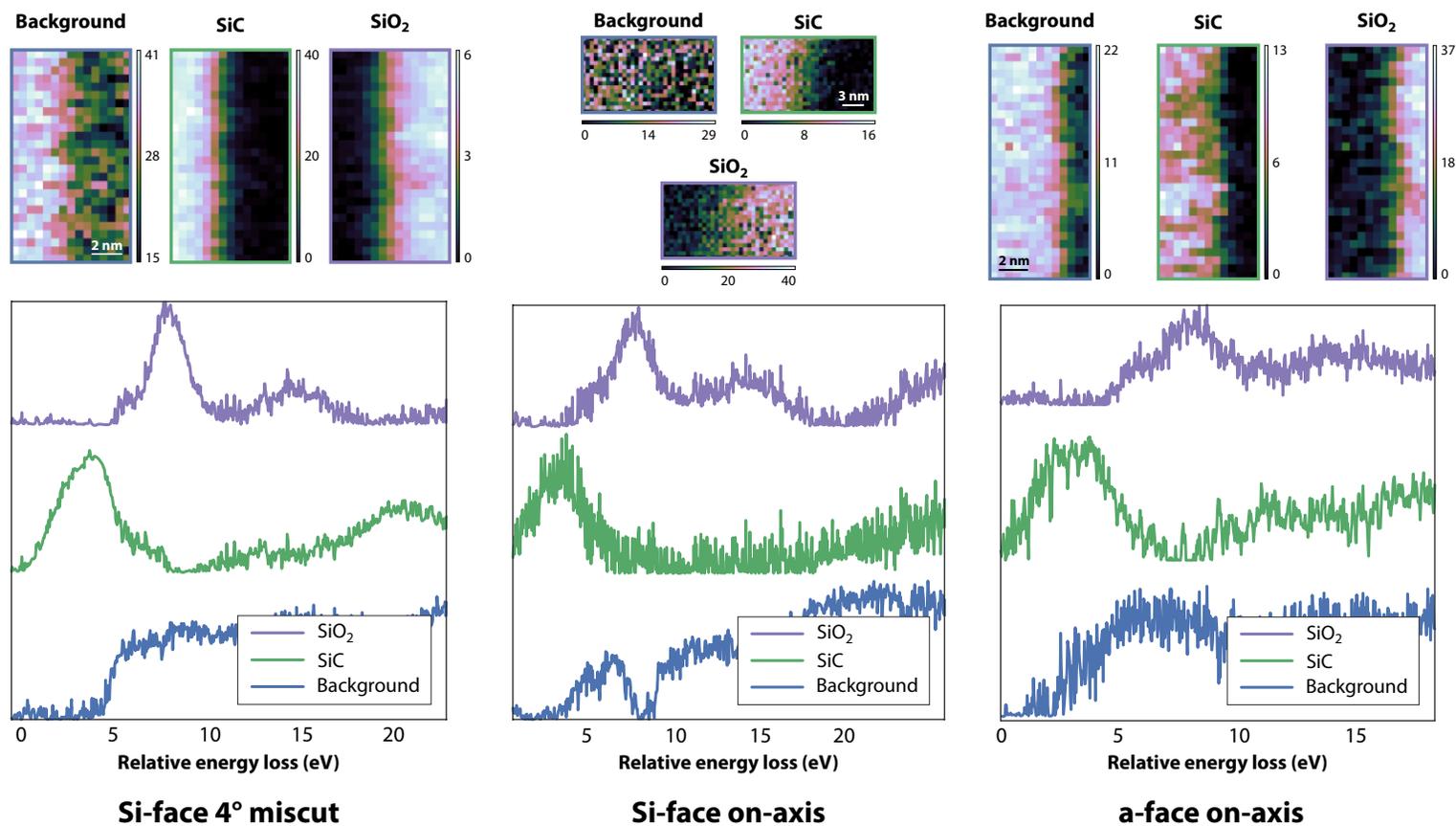
Figure 3.17: Spectral decomposition (unmixing) of Si-$L_{2,3}$ edge for the three oxidized samples. Images at the top are the loading maps of the decomposed components displayed below. The energy axis is relative, aligned to the edge onset of the SiC component. Substrate orientation is indicated at the bottom for each panel. Each oxidized sample required only three components for a full representation of the collected data, unlike the four required for the NO-annealed samples. No significant interfacial components were identified at the Si-$L_{2,3}$ edge for any of the oxidized samples.

In contrast to the oxidized samples, the decomposition of the Si-$L_{2,3}$ signal in NO-annealed devices showed particularly interesting characteristics related to the interface. The results of the NMF decomposition of these samples are displayed in Fig. 3.18. Much like for the oxidized samples, distinct background, SiC, and SiO_2 components are clearly visible with expected spectral shapes and locations within the sample. For each of the NO-annealed samples however, an additional component (above the noise) was apparent, and generally was localized near the interface. This component is a direct observation of a silicon state chemically distinct from both SiC and SiO_2, and to the author's knowledge, the first direct TEM measurement of such a state.

In all three NO samples, the interfacial state has a similar structure, comprised of two peaks (a doublet) located at an energy between that of SiC and SiO_2, suggesting a binding energy for the origin of the signal between the Si$-$C and Si$-$O bonds. Given the known presence of nitrogen in these samples, and the location of N between C and O in the periodic table, it is reasonable to assume that this extra component is evidence of Si$-$N bonding at the interface. Upon searching the relevant literature, multiple works by Skiff *et al.* [223] and Auchterlonie *et al.* [224] appear to validate this supposition. In these studies, density functional theory calculations and experimental measurements were used to investigate the ELNES of various Si$-$x compounds, including Si_3N_4 and SiC. Their results indicated a doublet peak structure in the Si_3N_4 spectra, with the first peak at an energy approximately $1\,\mathrm{eV}$ above that of SiC, in almost exact agreement with the components identified in the present work.
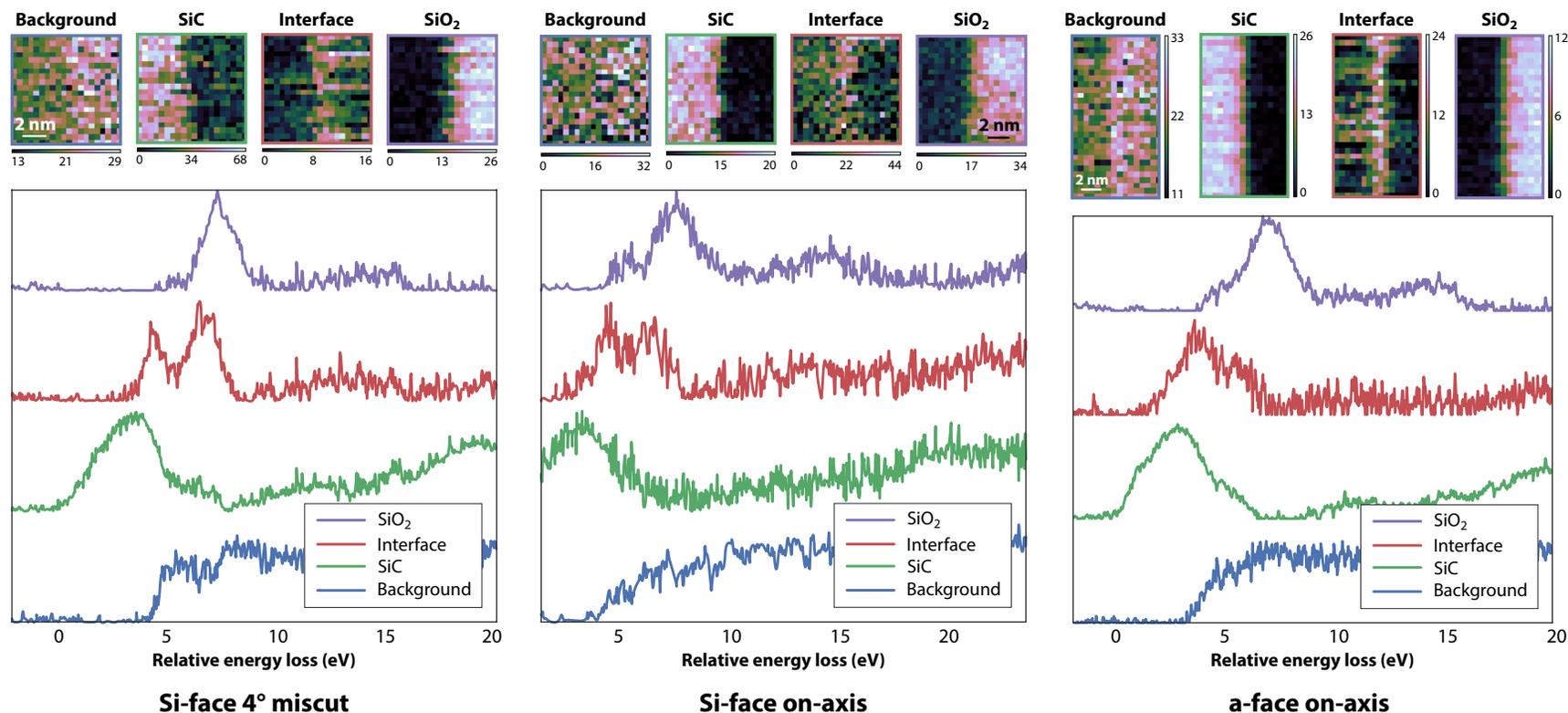
Figure 3.18: Spectral decomposition (unmixing) of the Si-$L_{2,3}$ edge for the three NO-annealed samples. Images at the top are the loading maps of the decomposed components displayed below. The energy axis is relative, aligned to the edge onset of the SiC component. Substrate orientation is indicated at the bottom for each sample. Each NO-annealed sample had a decomposition component localized preferentially at the interface, which had an edge onset energy between that expected for the Si-$L_{2,3}$ edge in SiC and SiO$_2$, attributed to Si$-$N bonding.

To further confirm the identity of the unknown component, additional EELS measurements at the Si-$L_{2,3}$ edge were obtained from a $100\,\mathrm{nm}$ thick Si_3N_4 thin film. The results of this measurement (compared to the NMF components) are shown in Fig. 3.19. The doublet peaks were not resolved in the film measurement, but the overall structure of the spectrum agrees well with the interfacial components identified in the Si-face samples. It is important to note that this single Si_3N_4 measurement cannot separate the contribution of the Si ionization cross section (usually isolated into the background component of the spectrum image decompositions), which explains the additional intensity in the [0-20] eV range, and likely explains why the doublet peaks are not resolved.

While the Si_3N_4 edge shape matches fairly well to all three NMF components, the onset energy matches almost exactly to the Si-face data. The *a*-face component however, has a lower onset by about $1.5\,\mathrm{eV}$, and is not as well matched to the measured Si_3N_4 result, most likely due to the additional bonding contribution of carbon which would serve to lower the overall binding energy of Si. This reveals an important fact about the bonding between Si- and *a*-face samples: the mixed termination of the *a*-face fundamentally alters the available bonding configurations for N (and Si) at the interface, which should be expected to affect overall device performance.
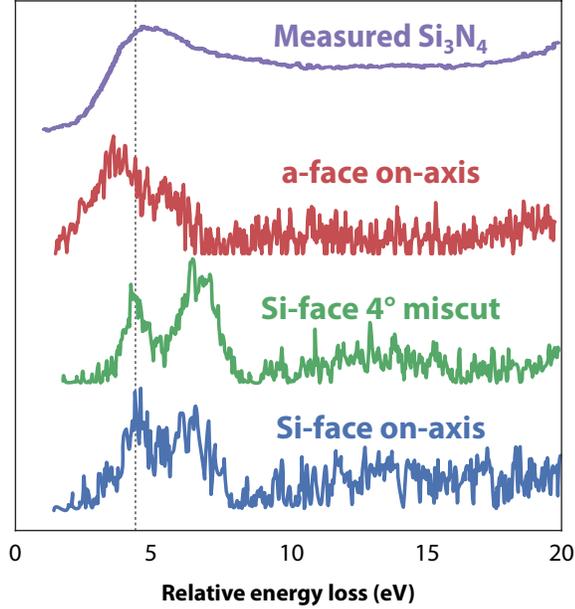
Figure 3.19: Comparison of the Si-$L_{2,3}$ interfacial components identified through NMF (Fig. 3.18) to a measured Si_3N_4 thin film. The two Si-face components match fairly well to the film, while the *a*-face has a lower edge onset energy, likely due to additional C-bonding. The dashed line provides a reference for the first doublet peak position in the Si-face on-axis sample.

3.3.3.2 C-K EELS SI unmixing

Besides the Si-$L_{2,3}$ edge, the C-K edge also provides interesting information concerning the chemical configuration of carbon within the sample. In particular, this edge is often used to determine the relative fraction of sp^3 to sp^2 type bonding [225]. sp^2-type bonding is characterized by a lower edge onset energy, typical of $1s \to \pi^*$ transitions, while the higher energy sp^3 peak represents $1s \to \sigma^*$ excitation events. Bearing this in mind, unmixing of the C-K edge signals from the six samples was performed. The results of this process for the NO-annealed samples are shown in Fig. 3.20.
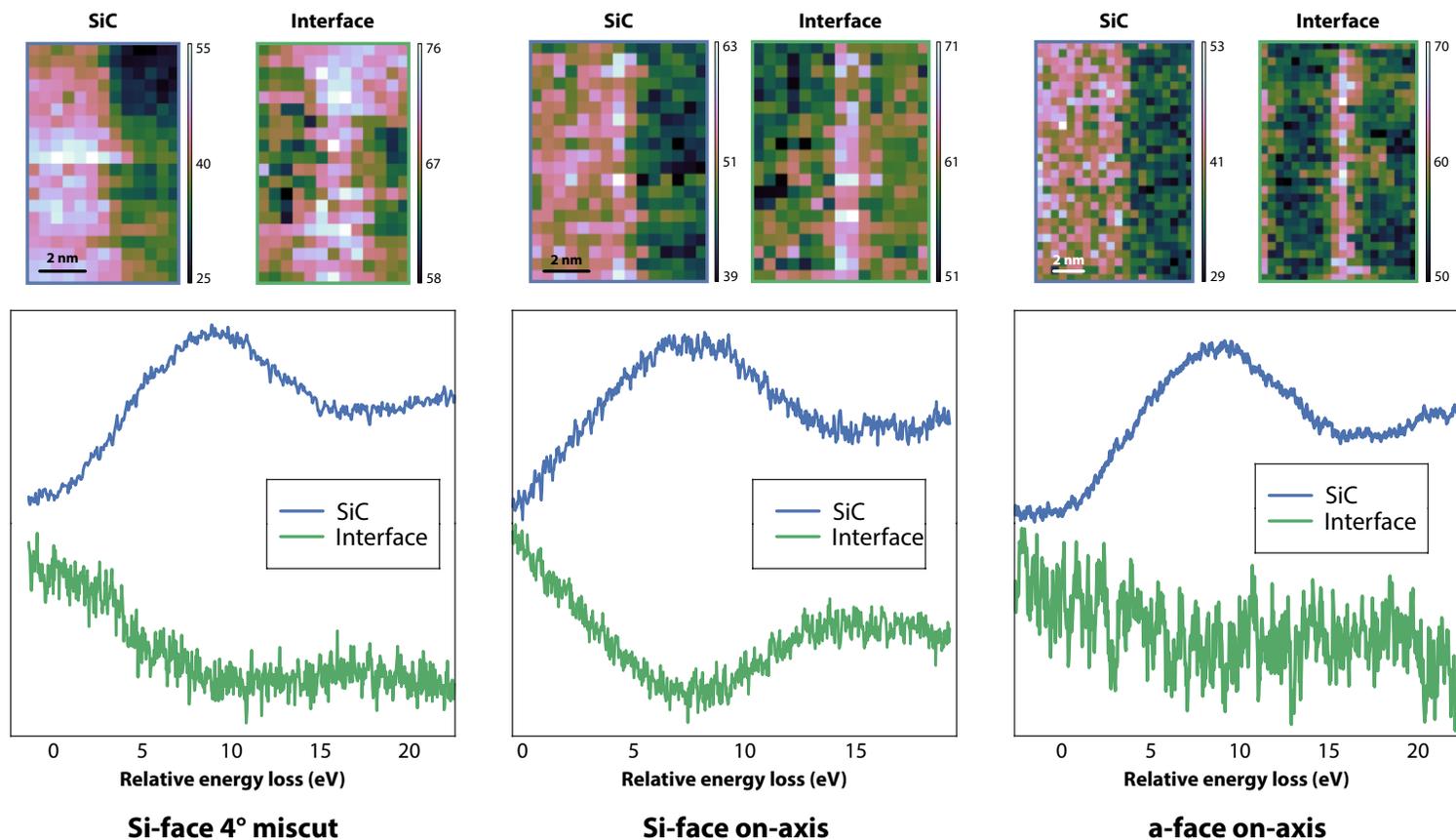
Figure 3.20: Spectral decomposition (unmixing) of the C-K edge for the three NO-annealed samples. Images at the top are the loading maps of the decomposed components displayed below. The energy axis is relative, aligned to the edge onset of the SiC component. Substrate orientation is indicated at the bottom for each sample. Each NO-annealed sample required two components for a full representation of the collected data. In each case, the second component was localized near the interface, and had spectral intensity in the pre-edge region of the C-K edge, indicating more sp^2-like character in the C- bonds in these areas, attributable to the presence of N at the interface.

In each NO sample, two components were needed to fully describe the data. The first was a C-K edge signal located chiefly within the SiC side of the image, with a spectral signature typical of C in a SiC configuration with mostly sp^3-type bonding. The second component was a clearly an interfacial state in each case. Generally, this interfacial component is characterized by additional intensity in the pre-edge region when compared to the SiC signal. While not strong enough to create a distinct peak, it is more likely than not that this additional intensity arises from the development of sp^2 bonding character that is typical in carbon nitride samples [226], demonstrating the presence of C−N bonding at the interface in all three samples.

Between orientations, there is little difference between the spectral shape of the interface components. The primary difference is evident in the loading maps, which show the interfacial state to be more highly localized in the *a*-face sample, compared to more diffuse distributions in the two Si-face samples. This can be intuitively understood by considering the relative availability of carbon atoms for bonding at the interface in the two samples. The *a*-face is 50% terminated with C- bonds, providing ample opportunity for nitrogen bonding directly to carbon. Contrast this with the Si face, which is 100% terminated by silicon atoms, meaning to bond with C, N atoms must either diffuse at least through the Si surface, or be limited to second nearest-neighbor configurations. This explanation also explains the reduced edge onset of the interfacial component of the *a*-face Si-$L_{2,3}$ edge observed in Fig. 3.19.

In contrast to the NO samples, the C-K signals from the oxidized samples

134

were well described by a signal component, typical of the SiC contribution. Regardless, the decomposition was performed with two components to allow for direct comparison to the NO results. The second component was always found to describe either noise (the case for the Si-miscut and *a*-face samples) or the presence of hydrocarbon contamination attracted to the surface by the electron beam (observed in the Si-face on-axis sample). The loading maps for each of the components are shown in Fig. 3.21. As in the Si-$L_{2,3}$ data, the lack of a distinct interfacial state again suggests a smooth transition in the C- bonding across the interface. Finally, as has come to be expected for recent samples, no excess carbon contribution was observed at the interface. In the *a*-face sample, the noise component had a slight apparent enrichment at the interface. Closer inspection reveals an enrichment also within parts of the SiC, meaning that this second component was correlated with the presence of SiC. Indeed, the spectral component (not shown) appeared to be a noisier version of the first component, indicative of an "over-decomposition" (only one component was really necessary to describe the data).

3.3.3.3   O-*K* EELS SI unmixing

The final signal analyzed for these samples was the O-*K* edge, which provides valuable information related to the oxygen configuration within the sample. O-*K* edges are frequently used to obtain information regarding vacancies or to "fingerprint" oxides by their unique spectral signatures [227]. They can also provide information about the band gap of oxide materials, as demonstrated by Muller *et*

135
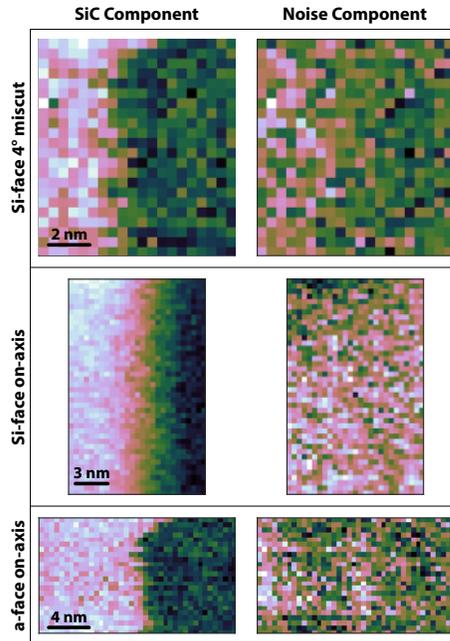
Figure 3.21: Loading maps from the spectral decomposition (unmixing) of the C-*K* edge for the three NO oxidized samples (spectral components not shown). In each case, only one component was needed to describe the variation in the overall EELS signal, while the second component was solely a noise contribution. No interfacial component was observed for any of the oxidized samples measured. A map of the second component for each sample is included for comparison to Fig. 3.20.

al. [222].

Results of the O-*K* edge decomposition for the Si-miscut NO-annealed sample are presented in Fig. 3.22, and this result was typical for all samples observed, with the exception of the *a*-face NO-annealed. Generally, the oxygen edge was well described by single component, typical of the O-*K* edge within SiO_2. In some cases (such as that shown in Fig. 3.22), an additional component was identified, but inspection revealed it to be a signal with spectral shape opposite to that of SiO_2, with a distribution strongest in the SiC. In other cases, the second component was simply noise. The origins of this opposite component are not currently well-understood, but given its clearly non-physical nature, it is considered an artifact
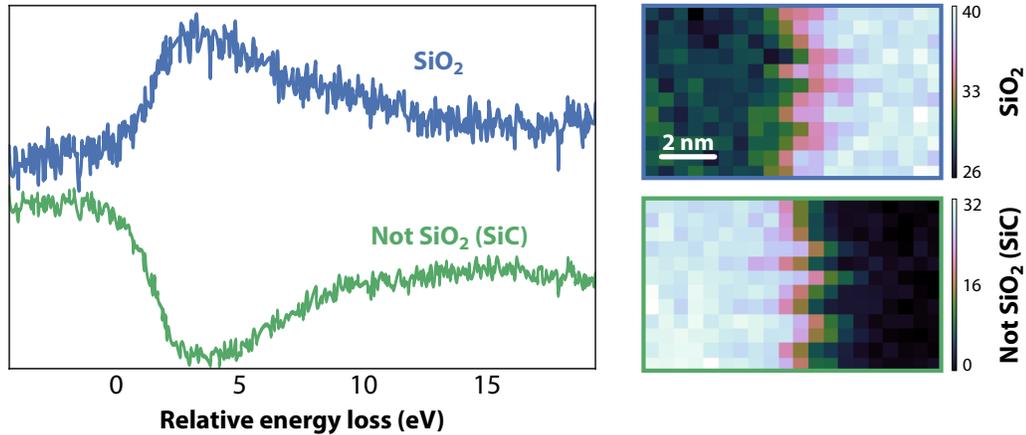
Figure 3.22: Results of the O-K edge decomposition for the NO-annealed Si-face miscut sample. The energy axis is relative, aligned to the edge onset of the SiO$_2$ component. The first component represents the O-K edge in SiO$_2$, while the second component is nearly the complete opposite of the first, and is present everywhere the SiO$_2$ is not. This result was typical of all the samples other than the a-face NO-annealed (the results of which are shown in Fig. 3.23).

from over separation of the data, rather than a true sample effect, and can be safely disregarded.

In contrast to the other five samples, the a-face NO sample showed a clear and particularly interesting interfacial component, as shown in Fig. 3.23. The primary component in this decomposition was the typical SiO$_2$ signal, located solely within the oxide area of the spectrum image. The interfacial component however, has an edge onset 2 to 3 eV below that of SiO$_2$, and peaks right as the SiO$_2$ begins to rise. This reduced onset energy indicates a distinctly unique oxygen coordination at the interface in this sample that was not observed in any other specimen.

Interpretation of this feature is greatly assisted by the volume of work undertaken to understand the Si/SiO$_2$ interface in the 1980s and 90s. In particular, Muller et $al.$ [222] performed a detailed analysis of the O-K edge at the Si interface that
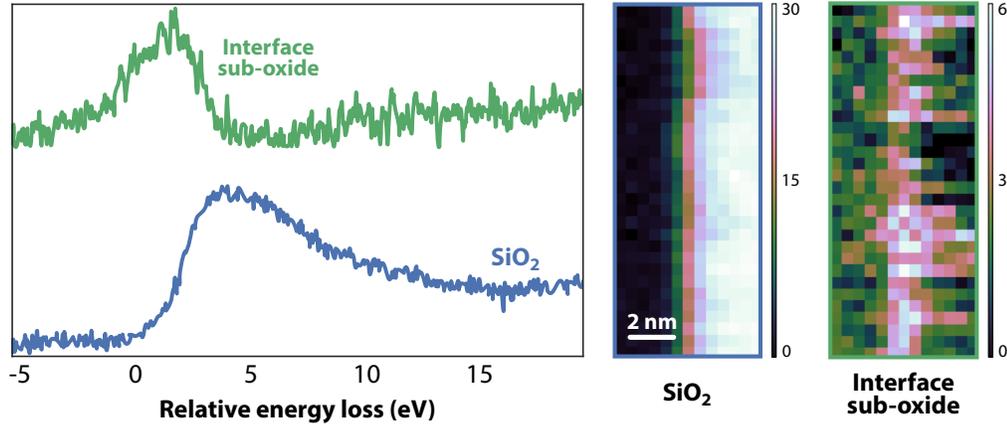
Figure 3.23: Results of the O-K edge decomposition for the NO-annealed a-face sample. The energy axis is relative, aligned to the edge onset of the SiO_2 component. This was the only sample that showed a significant interfacial component in the O-K edge (the second component, in green). This interfacial component has an edge onset at lower energy than SiO_2, which suggests a localized reduction in the bandgap [222].

provides some relevant insights. They observed a $3\,eV$ reduction in the O-K edge onset at the interface between Si and SiO_2, strikingly similar to the component reported in Fig. 3.23. The O-K edge represents the portion of the conduction band (the unoccupied states) projected onto the measured oxygen atom, meaning that a reduction in the edge onset energy correlates to a reduction in the band gap (although this is not a 1:1 relationship [189]). By the Moss-relation, this further suggests an increase the in the local dielectric constant close to the interface [228].

These observations provide hints as to the origins of the drastically enhanced mobilities measured for NO-anneal a-face devices [229]. It appears that in addition to the defect passivation [50] and counter-doping [230] within the SiC, the NO anneal has significant impacts in the oxide layer close to the interface. In the a-face sample measured in this work, the decomposition results suggest a silicon oxynitride layer of approximately $1.5\,nm$ with a reduced band gap and higher dielectric constant,

which would be expected to give rise to higher mobilities.

3.3.4   Conclusions

In this portion of the thesis, the impacts of substrate orientation and miscut on the transition layer were investigated. HRTEM images revealed structurally sharp interfaces, with roughness apparently limited to 1-2 monolayers. The *a*-face samples appeared to have a distortion of the crystal lattice at the interface extending approximately 4 monolayers. Detailed reconstruction of the exit-surface wavefunction would allow for a more precise determination of structural modifications at this interface.

w_{TL} was measured using the previously described methods for each of the variously oriented substrate samples. The results revealed little impact of the NO anneal on the w_{TL} value, in contrast to the NO time-series results. This contradiction is attributed to the vast improvements made in the quality of SiC substrates and epilayer growth within the past decade.

To more deeply investigate the differences between orientations and the effects of NO annealing, spectral decomposition was performed for each element in the system (excluding N). Generally, little to no differences were observed between the on-axis and miscut Si-face samples. In the case of the Si-$L_{2,3}$ edge, the NO anneal gave rise to a significant interfacial layer due to Si$-$N bonding. In the Si-face samples, this is attributed primarily to Si_3N_4-like configurations, while for the *a*-face, the contributions of carbon cause the interfacial state to be shifted to lower

energies. In the C-K edge, a significant interfacial state was again observed in the NO-annealed samples, with substantial sp^2-like characteristics. This state was more highly localized to the interface in the a-face sample due to the added availability of C for bonding in this orientation. Finally, the O-K edge revealed a distinct interfacial layer for the a-face NO-annealed sample, indicating an oxynitride layer with a reduced bandgap that is proposed to help explain the improved mobilities observed in such devices.

3.4 Beyond NO: novel processing techniques and their effects

Besides altering the crystallographic orientation of the substrate, changing the passivation process used during the fabrication of SiC MOSFETs can have drastic impacts on the resulting device performance. Within the past five years, significant "channel engineering" research has led to the development of a number of protocols beyond the standard NO annealing. Liu *et al.* [231] provide a recent review of such efforts, describing the present status of the "beyond NO" treatments and highlighting important remaining questions surrounding these next-generation processing techniques.

In this section, two specific processes were analyzed, and their effects on the interface and oxide layer explored using TEM and EELS. The samples were fabricated by collaborators at Auburn University, using standard thermal oxidation processes. Following this oxidation, introduction of either phosphorus or boron was achieved through the use of diffusion sources during subsequent anneals. Further details of each process are provided in the following sections. In both cases, the introduction of the dopant element converts the oxide layer into either phosphosilicate or borosilicate glass, respectively, with remarkably different properties than the native SiO_2 thermal oxide. The mechanisms of incorporation for these two processes was found to be markedly different, and provides insights into how each glass layer impacts device performance. These results however, represent only an initial investigation into the effects of such treatments, providing ample incentive for additional studies of their properties.

3.4.1 Phosphorus passivation

Introduction

The first alternative post-oxidation annealing scheme investigated was one using phosphorus instead of nitrogen as a passivating agent. Following a typical thermal oxidation process on an *n*-type epilayer, the SiC samples were subjected to a further anneal at $1000\,°C$ for $15\,min$ in a gas mixture of $POCl_3$, O_2, and N_2. Phosphorus was introduced by N_2 gas passing through a $POCl_3$ bubbler at $15\,°C$ [232]. The sample was further annealed in pure N_2 for $30\,min$ in a "drive-in" annealing step, with the goal of homogenizing the oxide layer. Prior results using secondary ion mass spectroscopy (SIMS) have indicated that this anneal converts the SiO_2 film into a phosphosilicate glass (PSG), with a relatively uniform concentration. XPS measurements from the PSG layer indicate a bulk P concentration of approximately 5 at.%, and that the phosphorus uptake into the oxide film is consistent with the liquidus curve of the $P_2O_5-SiO_2$ phase diagram [232].

With regards to device performance, the conversion of SiO_2 to PSG has two primary effects. The first is a significant enhancement of mobility (approximately double that of NO-annealed devices), originating from an order of magnitude decrease in interface trap density (D_{it}), combined with interfacial counter doping. P is an n-type donor in SiC, and small amounts may be be incorporated into the substrate, increasing the number of available carriers near the interface, and improving device performance during inversion [57, 60]. Besides the μ_{FE} enhancement however, P-anneals have been shown to give rise to positive polarization charge at the

interface under bias and temperature stress. This is due to the polar nature of PSG, and the charge at the interface negatively impacts device performance by lowering the threshold voltage, increasing the leakage current in the OFF state, and limiting the effectiveness of the device in power electronics [57, 233].

To date, only one TEM study of the SiC/PSG interface has been reported [234]. In that work, EDS was used to determine that phosphorus was "almost homogeneously distributed within the insulating layer." EDS has a limited spatial resolution however, owing to the larger interaction volume for X-ray generation in a sample, which may preclude reliable detection of nanoscale features (for which EELS is more appropriate). Thus, almost any additional contribution in this area is likely to assist in better understanding of the phosphorus passivation process.

TEM imaging results

A TEM lamella was fabricated from the PSG sample following the procedures of Sec. 2.2.1 and 3.1.1. Because the sample had no metal gate contact layer and a thin oxide layer (60 nm), a thin conductive polymer (AquaSAVE) was spun onto the sample surface prior to deposition of additional protective material within the FIB, to ensure the integrity of the oxide film and SiC/PSG interface. High-resolution and HAADF-STEM images of the SiC/PSG interface are shown in Fig. 3.24. A number of interesting differences (compared to the native SiO_2) are noticeable in the images, even without chemical analysis.

First, compared to NO-annealed oxides, the PSG layer appears to be much less conformal. As seen in Fig. 3.24a and b, there is a long-range roughness in
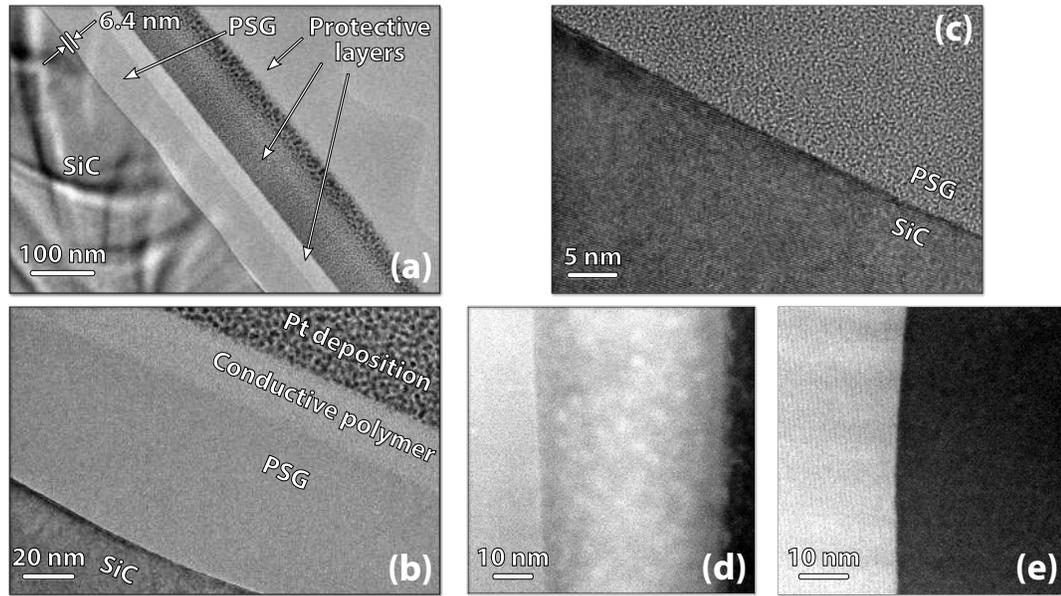
Figure 3.24: HRTEM and HAADF-STEM from a P-passivated SiC MOS device. (a) Low-magnification conventional TEM image of the semiconductor-oxide stack, showing (from left to right) the Si-face SiC substrate, the ≈60 to 65 nm PSG oxide layer, and three protective layers deposited prior to FIB lamella preparation. Longer range roughness is visible in this image. (b) Higher magnification TEM view of the PSG layer, showing subtle variations not observed in typical SiO_2 images. (c) HRTEM image of the SiC/PSG interface, showing many more atomic steps due to the significantly higher long-range roughness. (d-e) HAADF-STEM (Z-contrast) images of the SiC/PSG interface. In (d), the contrast is artificially enhanced to illustrate the presence of a bright spots distributed throughout the PSG, with a darker layer (lower mass) near the interface.

the substrate giving rise to a peak-to-valley height of about 6.4 nm. Rather than mirroring this undulation, the opposite surface of the PSG layer appears to be very planar. This indicates that the PSG film reflows at the high temperatures used in this work, in agreement with previous findings [234, 235]. This ability to reflow suggests that PSG likely reduces mechanical interfacial stresses, which may help explain its success as a passivating agent. In Fig. 3.24b, the PSG layer appears to contain some slight modulations in intensity (although very difficult to see in the image), indicating perhaps slightly different compositions (while retaining an

amorphous structure). Fig. 3.24c depicts the SiC/PSG interface in high resolution. Due to the large macro-scale roughness of the substrate, there is a high density of atomic steps at the interface, but besides this, no significant interfacial features are observed.

In Fig. 3.24d and e, the PSG layer is imaged in HAADF-STEM mode, rather than conventional TEM. In this mode, the intensity of the image is (to a first order) proportional to the atomic number of the atoms being sampled (giving rise to the term "Z-contrast" to describe the image). Fig. 3.24d shows the entire oxide layer with enhanced contrast, illustrating a non-uniform darker region 5 to 10 nm in thickness, suggesting a lower atomic mass in this area compared to the rest of the oxide. In the remainder of the PSG, there are bright clusters throughout, which are evidence of a heterogeneous elemental distribution.

TEM-EELS results

To explain the features observed in the HRTEM and STEM images, an EELS spectrum imaging analysis was performed, using the hyperspectral decomposition methods introduced in Sec. 2.1.2.2. This technique is especially well-suited to investigations of PSG, due to the severe overlap of the Si-$L_{2,3}$ (99 eV), Si-L_1 (149 eV), and P-$L_{2,3}$ (132 eV) edges. The P-$L_{2,3}$ edge cannot be reliably identified in typical analyses due to the effect of ELNES oscillations of the Si-$L_{2,3}$ edge. Spectral unmixing however, clearly reveals the locations of phosphorus within the collected data. Typically, a power-law background subtraction would be performed prior to unmixing. This method can introduce substantial variation in the resulting signal

depending on the pre-edge fitting window used however, especially at energies far beyond the immediate ELNES [236]. To mitigate this potential error, unmixing was performed without an initial background subtractions routine.

The results of the STEM-EELS acquisition are shown in Fig. 3.25. The data was collected over a 100 eV range, wide enough to include both Si and the P edge, while maintaining sufficiently high energy resolution. Due to the overlap of multiple signals, five components were necessary in the decomposition to fully describe the data (more than any other interface analyzed to this point). The first two components (blue and green) capture most of the inelastic scattering background and SiC-like signal, respectively. The remaining three signals all have a Si-$L_{2,3}$ edge similar to SiO$_2$.
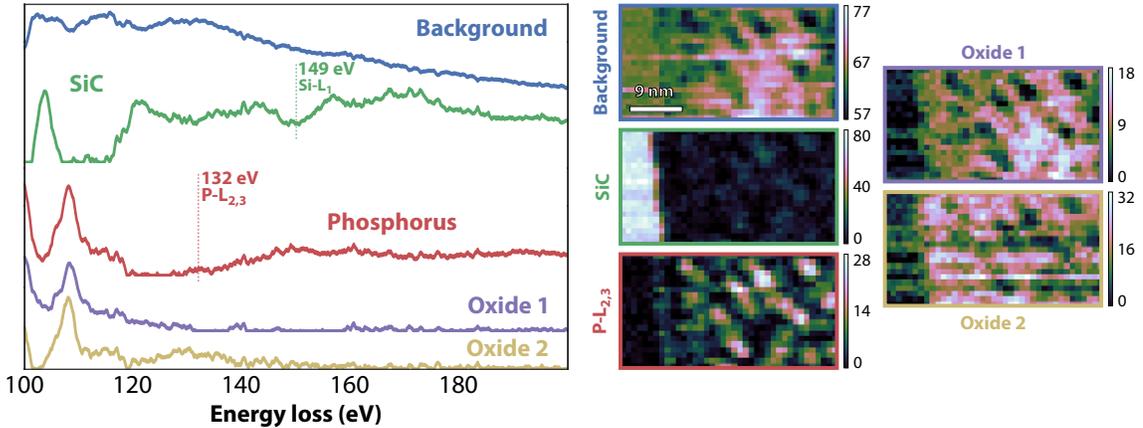
Figure 3.25: Hyperspectral unmixing analysis of the SiC/PSG interface at the Si-$L_{2,3}$ (99 eV) and P-$L_{2,3}$ (132 eV) edges (without background subtraction). Significant overlap between the ELNES of the Si-$L_{2,3}$/Si-L_1 edges with the P-$L_{2,3}$ edge make detection of phosphorus very difficult without the use of MVA techniques. Decomposition reveals five components, with the most interesting being the third, representing the onset of the P-$L_{2,3}$ edge. The loading maps reveal this component to be heavily clustered throughout the oxide, correlating with observed clusters in the HRTEM and STEM images in Fig. 3.24.

Among these oxide-like signals however, the first (red) can be definitively at-

tributed to a phosphorus-silicon-oxide complex due to the emergence of an edge onset at 132 eV. Analyzing the loading map of this component, it is clear that the clusters of phosphorus correlate very well with the bright spots observed in the HAADF-STEM image of Fig. 3.24d. This shows with great certainty that in this sample P is not at all distributed "homogeneously" at the nanoscale, as might be expected from previous works [234]. Instead, it is clustered in nano-globules with approximate diameters of (3.6 ± 0.8) nm. There is also a distinct decrease in the intensity of the phosphorus component within about 5 nm of the interface, correlating well with the uneven darker layer observed in the STEM images in Fig. 3.24. It would appear that this layer is more SiO_2-like, while the remainder of the oxide has more PSG character. It is expected that due to the polarizability of P, these globules will have a significant impact on the electrical performance of devices, potentially creating small clusters of fixed charge within the oxide layer during operation.

Analyzing the ELNES of the phosphorus component can reveal slightly more information about the arrangement of P atoms within the PSG layer. As can be seen in Fig. 3.25, the onset of the phosphorus appears to start at a few eV below the elemental energy of 132 eV. A pure P_2O_5 P-$L_{2,3}$ edge would be expected to have an onset exactly at 132 eV, with distinct peaks at 136 and 144 eV [237]. Neither of these features are seen in the present phosphorus component. Instead, there is a reduced edge-onset energy, and a general lack of peaks, which points towards a P^{3-} valence state, arising from substitution of P onto O lattice sites [237, 238]. Thus, the EELS evidence suggests that the phosphorus is not incorporated as a $P_2O_5 - SiO_2$ solid solution, and instead is more chemically combined, while segregating into P-rich

147

clusters, as previously described.

The other interesting result of the EELS decomposition was the splitting necessary to fully describe the oxide signal, resulting in the fourth and fifth components of Fig. 3.25 (purple and yellow). The two components are spectrally similar, but have important differences. The first *Oxide 1* signal (purple) has a slightly higher onset energy of 105 eV, compared to 103 eV for the second *Oxide 2* (yellow). The 105 eV feature of *Oxide 1* is strongly indicative of the excitonic transition in SiO_4 tetrahedral bonding units, while the ramp of intensity to an onset at lower energy (as seen in *Oxide 2*) suggests reduced oxygen coordination, typical in SiO_x substoichiometric oxides [239]. In the SiC system, the introduction of C to the bonding unit may be a possibility as well in this "sub-oxide" feature, but is not clearly resolved in the present data. *Oxide 1* is primarily located farther from the interface, while the *Oxide 2* signal is more localized at the material boundary, suggesting a reduction in oxidation state of Si towards the interface.

The non-homogeneous distribution of phosphorus throughout the PSG is particularly surprising, and is believed to be the first recorded evidence of such a phenomenon. The impacts of such a distribution on the electrical properties of the resulting devices in presently unclear, although it is easy to imagine how such nonuniformity could give rise to polarization instabilities or fixed charge within the PSG layer, which would be expected to negatively impact performance. The presence of these clusters raises the interesting possibility of trying to eliminate (or control) them, and may provide another means by which to engineer the channel response of SiC MOSFETs.

3.4.2 Boron passivation

Introduction

While phosphorus treatments have garnered significant research interest since their introduction in 2010 [240], boron passivation has been recently reported as another potential improvement beyond the NO process. In the only existing published work on the subject, Okamoto *et al.* [58] reported high μ_{FE} values using a PDS consisting of BN and B_2O_3. Mobilities were measured to be about 25% higher than those obtained from a P-anneal, breaking the $100\,\mathrm{cm^2/V\,s}$ mobility plateau with Si-face substrates.

As a dopant or passivation agent, boron stands in stark contrast to phosphorus and nitrogen. Both P and N are Group V elements, while B is Group III, meaning it acts as an acceptor within SiC and cannot provide *n*-type counter-doping like P and N do [60]. Nevertheless, B has been found to reduce D_{it} and improve mobilities beyond either of those methods. Furthermore, the polarization instabilities witnessed with phosphorus have not been observed for B, although more work is needed in this regard [241]. In the work of Okamoto *et al.* [58], the only compositional characterization of the oxide reported was a SIMS profile, indicating a uniform concentration of $2.5 \times 10^{20}\,\mathrm{cm^{-3}}$ B atoms throughout the majority of the oxide layer, with an asymmetric pileup localized within 5 to $10\,\mathrm{nm}$ of the interface, peaking at $6.8 \times 10^{20}\,\mathrm{cm^{-3}}$ (2.7 times the "bulk" concentration).

The samples used in the present work were grown via a standard thermal oxidation on Si-face SiC substrates, in a process nearly identical to that used for

the PSG. To incorporate boron into the oxide layer, the sample was additionally annealed under Ar for 30 min in the presence of a B_2O_3 ceramic planar diffusion source. Following the diffusion anneal, an additional "drive-in" anneal was performed for 2 h at 950 °C. SIMS profiles from the sample indicate an average boron concentration throughout the BSG of about 10 at.% [241]. Electrical measurements from this sample by collaborators at Auburn indicated a high μ_{FE} of approximately 115 cm^2/V s, with D_{it} similar to that observed in NO-annealed oxides. This indicates the improved mobility is not just a result of the reduced traps (or else μ_{FE} would be expected to be similar to the NO values) [241]. Previous reports have suggested that a structural change in SiO_2 near the interface due to stress relaxation may result in the higher observed μ_{FE}, although the authors admit little evidence supported this claim, making it more of an operating theory than definitive explanation [58]. Detailed microscopic investigation of this interface is urgently needed to aid in understanding the origins of high mobility in SiC/BSG MOS devices.

TEM imaging results

A TEM lamella was fabricated from the BSG sample following the procedures of Sec. 2.2.1 and 3.1.1. The provided sample had a polycrystalline deposited aluminum gate, which served as a protective layer during the FIB preparation.. High-resolution and HAADF-STEM images of the SiC/BSG interface are shown in Fig. 3.26. A number of differences (compared to the native SiO_2 and the PSG data) are noticeable in the images.

The first observation obvious from Fig. 3.26a is the lack of undulations in
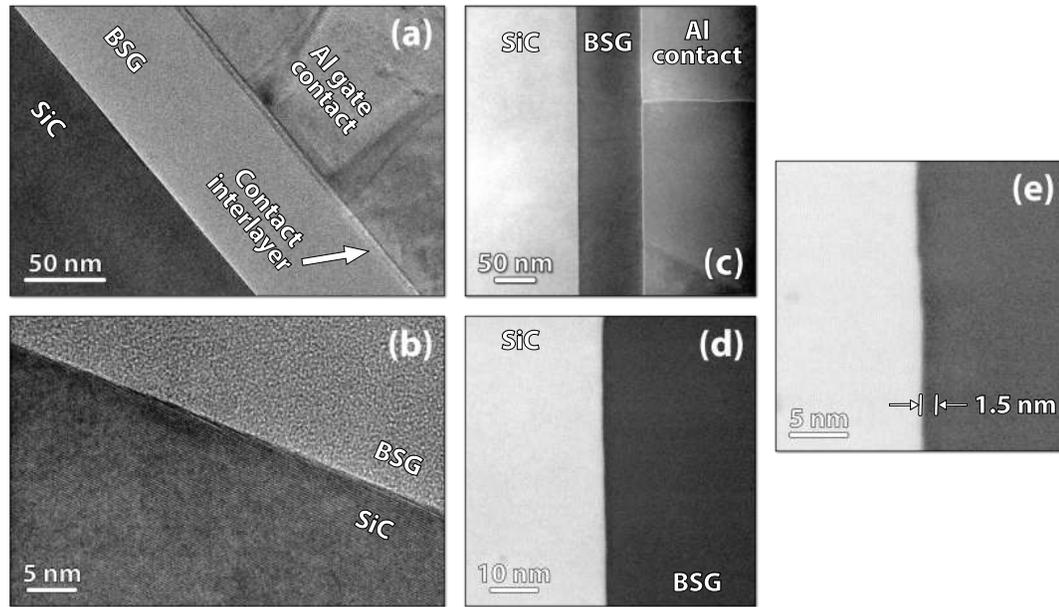
Figure 3.26: HRTEM and STEM from a B-passivated SiC MOS device. (a) Low-magnification conventional TEM image of the MOS stack, showing (from left to right) the Si-face SiC substrate, the ≈73 nm BSG oxide layer, a 4 nm amorphous interlayer, and the polycrystalline Al gate contact. (b) HRTEM image of the SiC/BSG interface, showing low roughness and little variation from previously observed oxidized and NO POA samples. (c-e) HAADF-STEM (Z-contrast) images of the SiC/BSG interface at progressively increasing magnifications. In (e), the contrast is artificially enhanced to illustrate the presence of a dark (lower atomic mass) layer approximately 1.5 nm wide at the interface.

the underlying substrate compared to the PSG interface. It is unclear if this is an effect of the B-passivation, or purely a substrate effect, requiring analysis of further samples to be certain. Regardless, the BSG layer is observed to be completely planar, suggesting an ability to reflow during the anneal, similar to observed for PSG. The BSG layer is uniformly about 73 nm thick, approximately 10 nm thicker than the PSG layer analyzed in Sec. 3.4.1, suggesting additional oxidation during the anneal process.

Between the Al gate and the BSG, a uniformly 5 nm thick amorphous layer

was observed, distinct from the bulk of the BSG. Fourier analysis of the HRTEM images (not shown) indicated a smaller average interatomic distance in this layer than within the BSG, and HAADF-STEM images (also not shown) suggest a lower average atomic mass within the layer. Given the known shorter bond length for B–O compared to Si–O (1.375 Å vs. 1.625 Å, respectively) [242], together with the lower atomic mass of B compared to Si, it is assumed that this 5 nm layer represents a B-rich surface state, distinct from the BSG. It is also possible that this layer could be an amorphous interphase formed from contact with the aluminum gate, but given the longer Al–O bond length of 1.7 Å in amorphous Al_2O_3 [243], and the layer's darker appearance in HAADF-STEM (not shown), this is very unlikely.

Fig. 3.26b depicts the SiC/BSG interface in high resolution. Overall interfacial quality appears similar to that observed for NO-annealed samples, with no significant structural changes immediately apparent near the interface. Fig. 3.26c shows a lower magnification HAADF-STEM image of the MOS stack. While there are some slight variations in intensity within the BSG layer, there are no significant clusters like those observed for the PSG. At higher magnifications (Fig. 3.26d and e), a thin darker layer of approximately 1.5 nm is clearly visible at the interface, suggesting a lower atomic mass within this area (likely due to B enrichment near the interface).

TEM-EELS results

Similar to the PSG sample, a detailed STEM-EELS experiment was performed on the SiC/BSG interface to learn more about the chemical states and elemental

distributions throughout the oxide. The separation between the Si-$L_{2,3}$ (99 eV) and B-K (188 eV) edges is greater than between the Si-$L_{2,3}$ and P-$L_{2,3}$ edges in the PSG sample, enabling easier evaluation of the distinct contributions of each element. The B-K edge immediately follows the fine structure of the Si-L_1 edge however, meaning that a power-law fit of the pre-edge background intensity will not suitably remove the background (and preventing a reliable simultaneous quantification of the relative Si/B composition). Nevertheless, individual analysis of each edge reveals some interesting results.
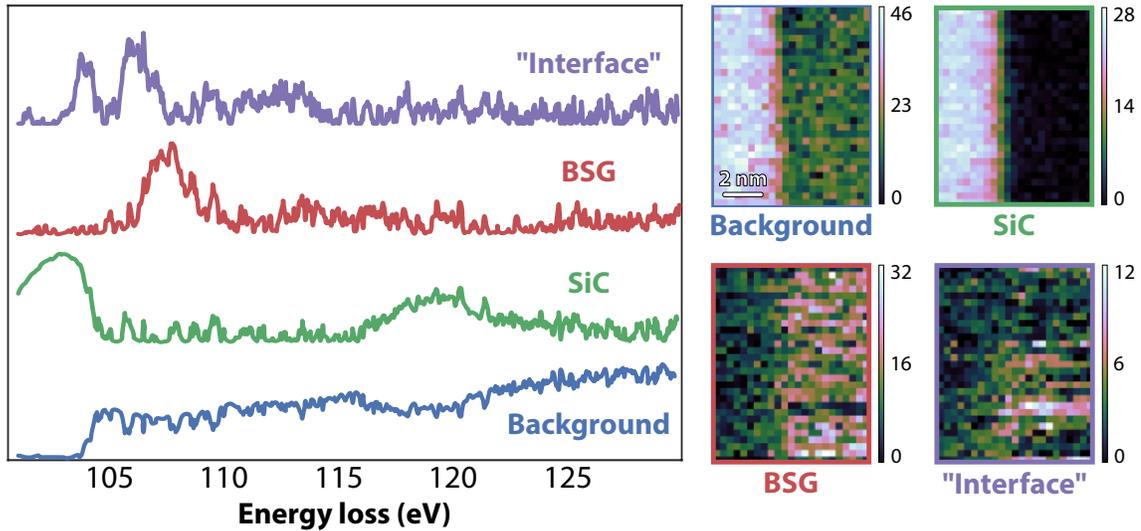
Figure 3.27: Hyperspectral unmixing analysis of the SiC/BSG interface at the Si-$L_{2,3}$ edge. Four components (left) were needed to sufficiently describe the dataset. The loading maps of these components are shown on the right, with a resolution of 0.5 nm/pixel. The oxide component does not appear significantly different than oxidized or NO samples. The fourth component (with energy onset between SiC and the oxide) does not appear to uniformly distribute at the interface, as was observed for NO annealed devices.

Fig. 3.27 presents results from an analysis of the Si-$L_{2,3}$ edge in the interfacial area, in a similar manner to that used for the samples in Sec. 3.3. Decomposition of the edge was performed using NMF after subtraction of the inelastic background

signal. Overall, four components were necessary to sufficiently describe the signal, and the spectral signatures of the components were very similar to those observed for NO-annealed samples in Sec. 3.3 (and very much *unlike* those for PSG). The first three components matched typical observations of the background, SiC, and oxide layers, respectively. The last component, containing a distinct doublet peak at an onset energy between SiC and SiO_2 was labeled "interface" due to its similarity to the NO-annealed interfacial components previously measured. Inspection of the signal's loading map (Fig. 3.27) reveals however, that it is not uniformly located at the interface. Instead, the signal appears to cluster in an area about 3 nm wide, near to the interface. The origins of this signal (and its similarity to the NO) are not immediately clear, but it is possible that the presence of boron at the interface (see Fig. 3.28) may cause bonding states in Si similar to nitrogen, albeit in a less uniform distribution.

Detailed analysis of the B-K edge is presented in Fig. 3.28a. This spectrum image was collected with a larger pixel size (1.0 nm) to enable a profile of the boron edge throughout almost the entire BSG layer. Due to the overlap of the Si-L_1 fine structure with the pre-edge region of the B-K edge, decomposition of the SI was performed without background subtraction. The unmixing process resulted in three components, the first of which (blue) almost perfectly represented the overall background intensity. The second (green) component is attributed to some residual signal from the Si-L_1 edge, and is strongest within the SiC (see the loading map in Fig. 3.28). Together, these two components represent the *non-boron* contributions to the signal.
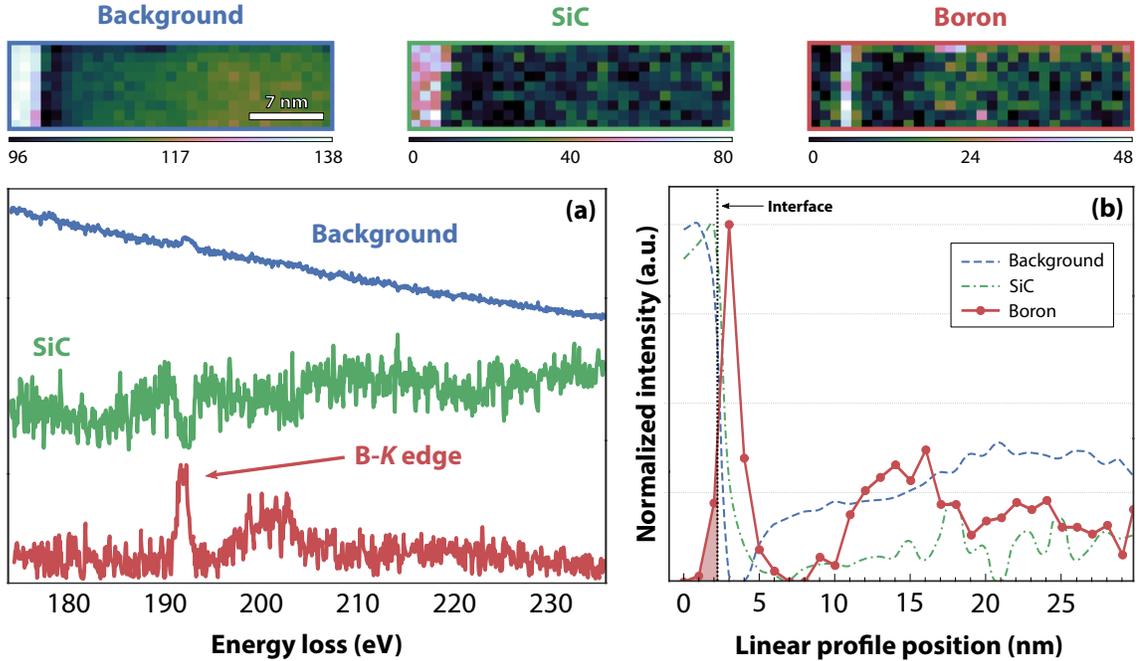
Figure 3.28: Hyperspectral unmixing analysis of the SiC/BSG interface at the B-K edge (without background subtraction). Although quantification via standard methods was not possible due to the weak B-K signal, decomposition of the data clearly isolates the boron contribution. (a) Three components described the dataset, attributed to the inelastic background, SiC, and boron. The loading maps of these components are shown above, with a resolution of $1.0\,\mathrm{nm/pixel}$. (b) Horizontal profile (perpendicular to the interface) for each component, obtained by summing the loading maps along the vertical axis. The interface is indicated by the dotted black line, defined as the inflection point of the background component profile. The boron contribution has a clear peak adjacent to the interface between SiC and BSG. The shaded area of the boron profile represents $\approx 1.0\,\mathrm{nm}$ of diffusion into the SiC substrate.

The third component (red) is at the expected onset energy and matches the shape of the B-K edge, confirming that boron is detected with certainty in the oxide layer. Observing the loading map shows a bright column of pixels localized to the interface between the SiC and BSG. The intensity of the B-K signal is directly proportional to the number of boron atoms present, meaning there is a peak in concentration at the interface. Fig. 3.28b shows a linear profile of the loading maps perpendicular to the SiC/BSG interface (through the oxide layer), summed

155

in the vertical direction and normalized for easier comparison. As expected, the background and SiC components drop sharply across the interface. The boron profile exhibits a distinct peak 0.8 nm from the SiC/BSG interface, followed by a layer of depleted intensity before returning to a moderate value and slowly decaying throughout the remainder of the BSG layer.

As with the PSG sample, a careful comparison of the observed B-K signal to known references enables some insight as to the configuration of the boron atoms within the BSG layer. The primary peak of the observed boron signal is located at 191.8 eV, matching exactly to the previously reported energy of the π^* antibonding orbital, which is indicative of boron in a BO_3 trigonal-planar sp^2 hybridized state [244]. No characteristics of tetrahedrally coordinated boron are observed in the signal, either [245], suggesting a fully trigonal configuration. Furthermore, the primary peak better matches a BN-like configuration than B_2O_3-like [244], implying that (like for P in the PSG) boron is not in a simple mixture of B_2O_3 and SiO_2, but instead more intimately involved in chemical bonding within the oxide.

With regards to the spatial distribution of boron in the oxide layer, comparisons of this result to the SIMS profiles by Okamoto *et al.* [58] provide some similarities and distinct differences between the two boron-passivated interfaces. Similar to the other work, a peak is observed in B concentration near the interface. The EELS results suggest greater segregation however, with the peak intensity 3.0 to 5.6 times that of the bulk BSG, compared to a 2.7 times enhancement in the SIMS profile. Furthermore, a depletion zone is observed that was not reported in the SIMS results. Also, rather than a uniform concentration throughout the BSG layer, the

EELS result suggests a B concentration that decreases slowly towards the surface of the oxide (and at the interface).

Spatially, the distribution of the boron peak in this work appears to be much narrower than that of Okamoto. The full width at half maximum (FWHM) of the EELS signal is 1.5 nm, compared to 6.3 nm in the SIMS profile. This width is exactly the same as measured for the dark layer observed in the HAADF-STEM images of Fig. 3.26, providing further confidence in the result. While SIMS suffers from great difficulty profiling composition across interfaces (due to knock-on effects and changes in sputter yields), the cross-sectional TEM used in this work provides a clear picture of B diffusion into the SiC. As shown in Fig. 3.28b, there is a finite signal from the boron signal that extends beyond the interface by about 1 nm, suggesting a limit to the boron diffusion of about one unit cell into the SiC. This 1 nm value was confirmed with a much higher resolution spectrum image (not shown), indicating it is not simply an artifact of the profile measurement, but instead a true measure of B diffusing into SiC.

The distribution of boron throughout the BSG layer is likely to have strong impacts on device performance. Structurally, boron acts as a glass former, but does not form direct bonding configurations with Si (unless in the presence of metal oxides such as Al_2O_3 or Na_2O) [246]. This likely explains the lack of any uniform interfacial boron-related features observed in the Si-$L_{2,3}$ EELS results of Fig. 3.27. B-containing glasses have weaker bonds, and are softer and more fluid than SiO_2. The enhanced concentration of boron at the interface means that the layer is likely more capable of relieving interfacial stresses than pure SiO_2, suggesting the stress-reliving argument

157

presented by Okamoto *et al.* [58] may be a correct one. Definitive evidence of this stress relief remains elusive however, and further work is needed to confirm this interpretation. Furthermore, the uniform nature of the boron distribution (parallel to the interface) may explain the lack of instabilities observed compared to the highly heterogeneous PSG oxide layer.

3.4.3 Conclusions

In this portion of the thesis, initial investigations into next-generation SiC passivation techniques were performed. Phosphosilicate and borosilicate glass oxide layers were analyzed using detailed TEM and EELS experiments. Contrary to the NO-annealed samples, bulk oxide effects were found to be dominant in the PSG samples. Phosphorus was observed to be distributed non-uniformly throughout the PSG layer and the chemical signature of the SiO_2 signal varied as a function of distance from the SiC/PSG interface. In the BSG sample, boron was determined to accumulate within a narrow layer at the interface and diffuse slightly into the SiC substrate, although with a much narrower distribution than had been observed in prior works. The boron concentration decreased throughout the thickness of the oxide, likely affecting the distribution of electronic traps and impacting performance. Further work analyzing the stress and strain at these interfaces is needed, to confirm initial assumptions that it is the improved stress relief provided by BSG that leads to such high mobilities.

3.5 Bias temperature stress of SiC MOSFETs

To this point, the majority of the characterization efforts in this thesis have focused on studying the origins of enhanced mobility in SiC MOSFETs. Another key issue facing SiC MOSFETs however is their overall reliability. A key component of this reliability is bias and temperature-induced instability (BTI), introduced by bias and temperature stressing (BTS). Typically BTI results in a shift in the threshold voltage (V_{th}) of the MOSFET, increasing V_{th} when stressed by a positive bias (PBTI) and decreasing it with a negative one (NBTI). If uncontrolled, NBTI can cause a shift of V_{th} to below $0\,V$, causing a normally off MOSFET to turn on, introducing a catastrophic mode of failure that must be prevented in power devices [231].

NO-annealing (and nitridation in general) has been shown to dramatically improve SiC PBTI, but degrades NBTI when compared to as-oxidized devices, meaning that electron trapping is decreased, but hole trapping is increased [182, 184, 247]. While the electronic origins and impacts of BTI are fairly well understood [248], their effects on the structure and composition of the interfacial region are not. Recent XPS results have suggested that C may migrate from the SiC 1 to 2 nm into the SiO_2 during high applied biases [249].

To investigate the effects of BTS on the interface, a number of SiC/SiO_2 devices were fabricated by collaborators at Rutgers and stressed at $150\,°C$ using a field of $5.2\,MV\,cm^{-1}$ for $1\,h$. Devices with and without NO annealing were tested, so comparisons between the two could be made. It is important to note that the

work in this section represents initial investigations into the effects of BTS at the interface, and is by no means exhaustive. Instead, it is presented as an introduction to the effects of stress observed by TEM, with the goal of informing future work in the area.

3.5.1 TEM-EELS Results

Expanding upon the details above, the samples investigated in this work were fabricated on Si-face substrates with $10\,\mu m$ n-type epilayers. The epilayers were oxidized following standard procedures, resulting in $\approx 48\,nm$ oxide layers. One of the samples was subjected to a $2\,h$ post-oxidation NO anneal, the details of which are provided in Sec. 3.1. An aluminum source was sputtered onto the surface to form the top gate contact pads. Multiple devices were formed in this manner on each $1\,cm \times 1\,cm$ substrate. The devices were stressed using the conditions above for $1\,h$, and C-V measurements were obtained from each sample both before and after the BTS, enabling a precise determination of the magnitude of the V_{th} shift (ΔV_{th}).

In the case of the oxidized sample, all eight tested devices experienced catastrophic breakdown during the BTS. Failures occurred between 4 to $33\,min$, with a mean time to failure of $16.9\,min$. The fastest breakdown device was chosen for TEM analysis, in hopes of observing the largest difference compared to the pristine interfaces measured previously. Of the eight NO-annealed samples, none broke down over the course of the hour-long BTS, but all experienced a ΔV_{th} ranging from 1.41

to 3.31 V. The device with the largest shift of 3.31 V was chosen for TEM analysis.

Oxidized

The results from the TEM-EELS analysis of the broken-down oxidized sample are presented in Fig. 3.29. In general, the results appeared to be very similar to those of non-stressed devices investigated in Sec. 3.3. The HRTEM image reveals a typical interfacial structure with the miscut steps evident, but no damage to the oxide layer, as may be expected from a broken down sample. Likewise, there appears to be no significant interfacial structure in the HRTEM image.

The results of a hyperspectral unmixing of the Si-$L_{2,3}$ edge are also presented in Fig. 3.29. As with the TEM images, there is little apparent difference in the overall decomposition results (compare with Fig. 3.17). The only slight modification is the slightly more intense excitonic peak at 105 eV in the SiO_2 component, although there is little reason to expect more tetrahedral SiO_4 bonding units in the broken-down oxide. Thus, this difference is most likely due to individual sample variation, rather than a pronounced breakdown effect.

Comparison to TEM work studying the breakdown of the Si/SiO_2 interface provides some insight into the lack of differences observed. In a thorough study by Li *et al.* [250], the primary evidence of dielectric breakdown was observed to be the presence of a hillock of Si atoms protruding into the SiO_2 from the Si, the product of dielectric breakdown induced epitaxial growth (DBIE). These hillocks were measured to be approximately 15 nm in diameter, and were only located for TEM analysis through the use of an intentionally nano-scale transistor for electrical
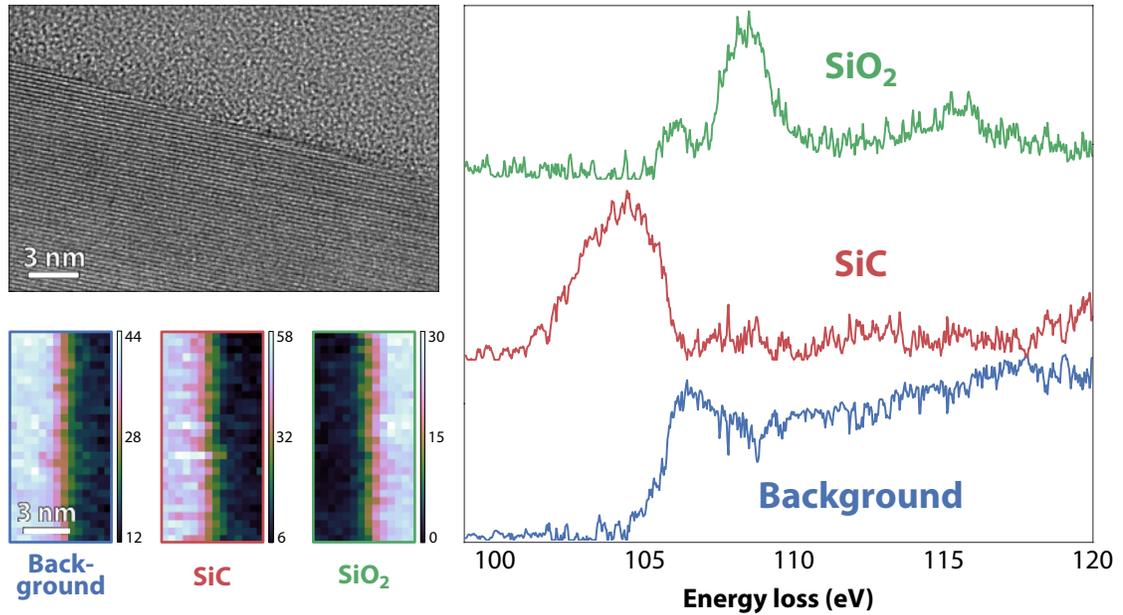
Figure 3.29:   HRTEM image of the SiC/SiO$_2$ interface in the oxidized sample, after BTS testing until device breakdown, together with the results from the hyperspectral unmixing of the Si-$L_{2,3}$ edge. Overall, this sample appeared very similar to those not experiencing dielectric breakdown.

measurements. Given the large gate metal pads (400 µm diameter) used in this work, locating a single nanometer-scale point of dielectric failure is likely to be exceedingly unlikely, without some way of locating this point in advance (which is noted to be particularly difficult [250]). It is most probable that the lamella examined in Fig. 3.29 is simply from an area not experiencing any sort of breakdown, explaining its similarity to prior observations. More precise fabrication of the initial devices is likely required in order to observe the effects of breakdown with any certainty.

NO-annealed

Compared to the oxidized sample, the NO-annealed BTS device did manifest some slight differences from the pristine samples measured in Sec. 3.3. As men-

tioned above, the NO sample experienced a ΔV_{th} of 3.3 V, measured after stressing. Unfortunately however, it is generally well-known that V_{th} can recover most of its shift upon resting in an unbiased condition for even just a few hours [248]. Because of this, large irreversible changes in the oxide character are not expected to be observed.

The results of an analysis on the NO-annealed sample analogous to that in the previous section are presented in Fig. 3.30 As with the oxidized sample, the HRTEM image does not reveal any unexpected features at the interface, and the atomic steps originating from the miscut are clearly visible. As with prior NO-annealed samples (Fig. 3.15), no effects of the NO process are observable within the HRTEM images.
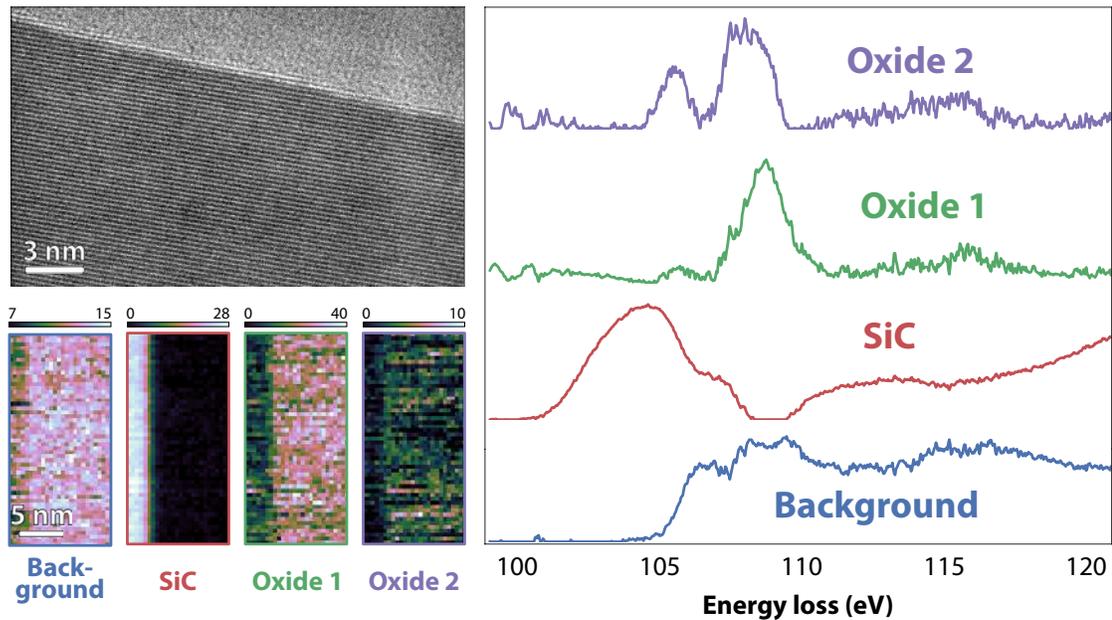
Figure 3.30: HRTEM image of the SiC/SiO$_2$ interface in the NO-annealed sample, after BTS testing (3.31 V shift in flatband voltage), together with the results from the hyperspectral unmixing of the Si-$L_{2,3}$ edge. While no distinct interfacial components were observed, an additional signal (compared to prior results) was observed to be evenly distributed throughout the oxide layer.

The results of the Si-$L_{2,3}$ EELS edge hyperspectral unmixing are also shown in Fig. 3.30. As with the non-BTS NO samples, four components were identified, with the extra containing a doublet peak very similar to those witnessed in Fig. 3.18. Examining the loading maps, there does appear to be a slight difference in the distribution of the doublet component. In the un-stressed Si-face samples, this component was highly localized to the interface. In the stressed sample however, it appears that the signal is more evenly distributed throughout the oxide. Summing the loading map vertically into a perpendicular profile (not shown) reveals a slight enrichment of this component at the interface, but a substantial presence through the remainder of the oxide as well.

It is proposed that the modified distribution of the "sub-oxide" Si-bonding states (which have been attributed to Si–N bonding) suggests BTS may mobilize the N and its bonding configurations from the interface into the oxide layer. These states clearly have a positive net effect, as they prevent the device from breaking down, but it is certainly possible that they may have deleterious effects as well. Further investigations of the stressed oxides identifying the distribution of N after BTS would help clarify this result (perhaps using SIMS profiles).

3.5.2   Conclusions and future work

While only an initial investigation of BTS effects on the quality of SiC/SiO$_2$ interfaces, the results from this section raise some interesting questions regarding the effects of NO during device stressing. In the case of the oxidized sample, no changes

were observed compared to pristine samples, likely because the specific location of the dielectric breakdown was not located. Closer examination of the precise breakdown point would be necessary to gain insights as to the failure mechanisms in SiC/SiO$_2$ MOSFETs. In the NO-annealed sample, the Si-$L_{2,3}$ edge revealed a bonding state very similar to that observed at the interface in the pristine samples, but it was dispersed throughout the oxide layer instead, with only a slight increase in intensity at the interface. This result implies that BTS may convert the NO passivation layer into a more diffuse state, with potentially significant impacts on device performance. A great deal more work is necessary to better explain these devices, for which the results presented here provide an impetus.

3.6   Summary of SiC experiments

Overall, the results presented in this chapter encompass a wide and thorough analysis of the interfacial characteristics in multiple SiC/SiO$_2$ devices. In particular, the work has focused on the impacts of the various techniques used to improve mobility and reliability, with the goal of understanding the physical and chemical impacts of these methods, perhaps informing future device engineering. In the first study (Sec. 3.1), a clear transition layer was measured at the SiC/SiO$_2$ interface using the chemical shift of the Si-$L_{2,3}$ EELS edge. The width of this layer was found to decrease with increased NO annealing time and nitrogen coverage at the interface. These results also correlated with mobility measurements. Namely, the devices with highest mobilities showed the narrowest w_{TL}. In the second portion of the work

(Sec. 3.2), a spin-etch technique was refined to enable precise angle-resolved XPS measurements of the interfacial region. These measurements confirmed an interfacial bonding state for the Si atoms that changes slightly upon NO annealing. N was observed to form at least four distinct configurations at the interface, and the angle resolved measurements confirmed a transition layer on the same order of width as the EELS results.

Later studies made use of advanced MVA techniques to enable closer inspection of the unknown interfacial states obtained in EELS measurements. The third experiment (Sec. 3.3) explored the impacts of substrate orientation and miscut on the states observed at the interface, with and without NO-annealing. Distinct interfacial configurations were observed in all NO-annealed samples in the Si-$L_{2,3}$ edge, attributable to nitrogen bonding configurations localized within a few nanometers of the interface. Similarly, the NO-annealed samples revealed interfacial states in the C-K edge, with substantial sp^2 character, and was strongest in the a-face sample due to the higher activity of the surface and availability of C for bonding. The a-face also exhibited a strong interfacial component in the O-K edge when NO annealed, suggesting a reduced bandgap at the interface, and potentially explaining the origins of the drastic mobility enhancement in NO-annealed a-face MOSFETs.

In the fourth experiment (Sec. 3.4), the "Beyond NO" passivation techniques of phosphorus and boron passivation were explored. In the PSG oxide, phosphorus was found to be distributed heterogeneously, forming P-rich clusters approximately 3.6 nm in diameter. The oxide spectral signature also varied throughout the oxide layer. In the borosilicate layer, a substantial accumulation of boron was observed

at the interface, with limited diffusion into the SiC substrate. It is argued that the B-enriched layer will reduce stress at the interface better than the NO-annealed SiO_2, leading to improved mobilities in devices with BSG oxide layers.

Finally, in Sec. 3.5 an initial investigation into the effects of bias-temperature stressing was performed. While little changes were observed in the oxidized sample (likely due to missing the critical area of analysis where breakdown occurred), some slight differences were observed in the NO-annealed sample. Primarily, the previously observed NO interfacial state appeared to be distributed more evenly throughout the oxide layer, potentially indicating a redistribution of N away from the interface during device operation.

Chapter 4:   Quantitative microstructural characterization of SOFC composite cathodes

As presented in Sec. 1.2, solid oxide fuel cells are uniquely positioned to transform the global energy landscape using efficient and inexpensive fuels. Durability concerns limit their immediate success in the marketplace however. SOFCs are also a particularly interesting system for microstructural characterization, given their complex internal structure and multiphase composition. In the remaining portion of this thesis, the development of FIB/SEM data collection and analysis methods used to quantify the microstructure of SOFCs is described (Sec. 4.1), as well as the application of these methods to analyze the degradation of two different types of fuel cell cathodes (Sec. 4.2 and 4.3).

4.1   Improvements in FIB-nt microstructural quantification

The first successful research implementation of FIB-nt was reported nearly 15 years ago [109]. The technique has become much more common as the adoption of combined focused ion beam – scanning electron microscopy (FIB/SEM) systems has increased, such that commercial vendors now typically advertise and sell software packages specifically used to acquire 3D data (some common packages are: *Auto*

Slice and View [251], *Atlas 5* [252], *Mill and Monitor* [253], and *3D Acquisition Wizard* [254]). Generally, the 3D data acquisition process proceeds as follows [255]:

1. To acquire a stack of SEM images, the sample is tilted to an inclined angle, usually the same as the angular offset between the electron and ion beams.

2. Using the FIB, a large trench is milled around an area of interest to expose a "data cube" to be acquired, which is then placed at the coincidence point of the two beams (see Figure 4.1).

3. Slices of the sample are milled in the z direction, and after each mill, an image is taken with the electron beam in the xy plane (at an angle).

   a) If desired, chemical and/or structural information can also be obtained at each slice by collecting X-ray EDS spectrum images (EDS) or electron backscatter diffraction (EBSD) patterns as well [256, 257].

4. The slice and image process is repeated using automation software supplied with the microscope in order to build up a 3D volume of data.

FIB-nt has been successfully used on a broad variety of sample types, beyond solely SOFC investigations. Inkson *et al.* [109] initially developed the FIB-nt methodology for examining FeAl nanocomposites, but it has since been used for 3D chemical analysis of alloys [258], microstructural characterization of Li-ion battery electrodes [259], and pore structure characterization in shale gas samples [260]. FIB-nt has seen extensive use in the microstructural investigation of solid oxide fuel cell cathodes and anodes [106, 107, 110–112, 114, 115, 170, 171, 261–269], and
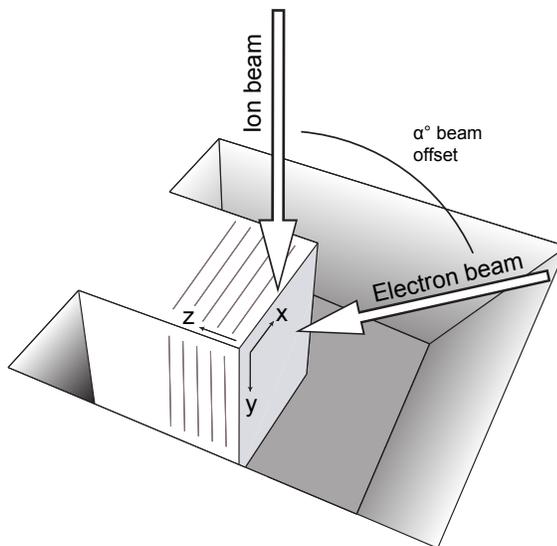
Figure 4.1: Schematic of FIB-*nt* experimental geometry. The sample is positioned at the intersection of the electron and ion beams for simultaneous imaging and milling. α is typically in the range of $[50 - 55]°$. Figure adapted from Holzer *et al.* [110].

in the characterization of many other materials (see Holzer *et al.* [255] for a thorough review). These works feature exciting findings in a range of materials, but the majority are published with a focus on samples and applications, rather than on microscopic methodology. As such, there are often only scant descriptions of methodology, and a lack of details about specific methods and their implementations. In this thesis, a number of techniques to improve the quality of acquired FIB-*nt* data are outlined. The specific implementations are also published in a freely available repository to assist other researchers in the use and improvement of the methods presented here [116].

As explained in Sec. 1.2.4, many quantifiable microstructural parameters such as overall porosity, tortuosity (τ), and connectivity of the pore network have specific impacts on the total polarization resistance observed in SOFC cathodes. Other

parameters such as surface area and volume of each phase change the available sites for gas adsorption within the cathode, while the triple phase boundary length controls overall charge transfer. Many of these parameters can be directly quantified using a FIB/SEM. The simplest parameters, such as porosity, phase surface area and volume, particle size, *etc.* were some of the first to be investigated using this method [110, 112, 262, 263]. Wilson *et al.* [113] and Gostovic *et al.* [106] followed with detailed descriptions of phase and three-dimensional topological connectivity, respectively. Many authors have explored the concepts of phase tortuosity with various approaches, ranging from relatively simple center of mass considerations to more complex finite element modeling [106, 111, 113, 114, 264, 270, 271]. A natural extension of these methods was to examine the three dimensional interface between all phases (the TPB), and to quantify the total triple phase boundary lengths (L_{TPB}), as well as the fraction of these that were expected to be electrochemically active [106, 111, 113, 115, 267, 270]. In the SOFC literature (and in other fields as well), there is little consensus regarding the methods used to measure many of these parameters. Even among works from the same research group, the specific techniques used to calculate L_{TPB} or τ can vary widely (and the implementations are rarely publicly available), leading to difficulty comparing results between reports.

This section of the thesis describes the specific techniques used to acquire a high resolution image stacks composite SOFC cathodes. Image acquisition and post-processing strategies are demonstrated and discussed, followed by a detailed review of computational methods that can be used to calculate various morphological and microstructural properties from a three-dimensional dataset. In the following

171

sections, implementation of these procedures is demonstrated on LSM-YSZ and LSCF-GDC cathode samples.

4.1.1 Experimental procedures

4.1.1.1 Sample fabrication

In this work, composite cathode layers were fabricated by collaborators in the Wachsman group (University of Maryland) using standard screen printing techniques on a pre-sintered YSZ or GDC bulk electrolyte supports, yielding SOFC "half-cells". For the supports, YSZ or GDC powder (TOSOH Corp.) was uniaxially pressed in a 10 mm diameter die and sintered at 1450 °C for 6 h. The sintered electrolyte pellets were then polished to 5 mm thickness. Slurries of composite cathode material (Fuel Cell Materials), were screen printed onto the electrolyte supports, resulting in a cathode layers of approximately 30 to 50 μm thickness. The LSM cathodes (together with the pre-sintered electrolyte) were sintered at 1100 °C for 2 h to remove the pore-forming material and generate a composite cathode layer with porous structure. The same process was used for the LSCF cathodes, only at 950 °C. Pt paste was painted inside a previously cut groove and a Pt wire wrapped around the pellet to act as a reference electrode. The Pt paste was dried at 900 °C for 30 min. Finally, a thin layer of Au paste was painted on both the working and counter electrodes and dried at room temperature for 1 h. The cells were then loaded into a custom built single-environment reactor and heated to 875 °C for 15 min to finish drying the Au paste before being cooled to the temperature of interest to

begin testing. A photograph of a completed cell is shown in Figure 4.2a.

4.1.1.2 FIB/SEM sample preparation

The quality of a volume reconstruction can be only as high as each individual image that is acquired during the FIB-nt process. Many artifacts common to FIB/SEM can complicate the segmentation and reconstruction process, including (but not limited to): "pore-back" imaging, FIB curtaining, and local sample charging. As such, a number of steps taken prior to SEM observation can significantly enhance the fidelity of the resulting volumetric representation, while other artifacts can be corrected through post-acquisition image processing.

(a)   (b)
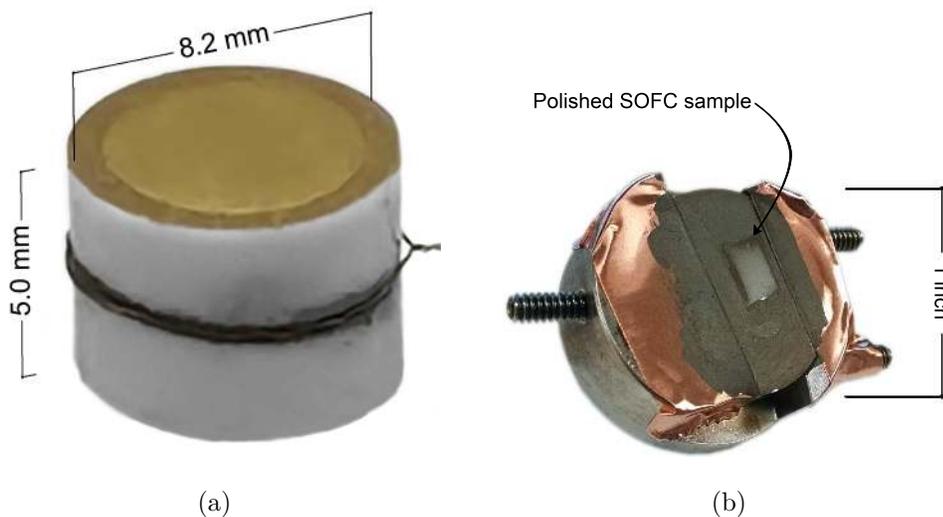
Figure 4.2: (a) Photograph of half-cell SOFC stack. A Pt wire (for electrical measurements) is wrapped around the center of the (white) YSZ electrolyte support. The 30 µm cathode layer is visible on the top of the support, and the entire top surface is coated with an Au contact. (b) Photograph of the SOFC mounted in cross section after epoxy impregnation, ready for FIB/SEM examination. The sample is mechanically clamped on the sides with three set screws.

Figure 4.3 illustrates a few of the more critical artifacts encountered during
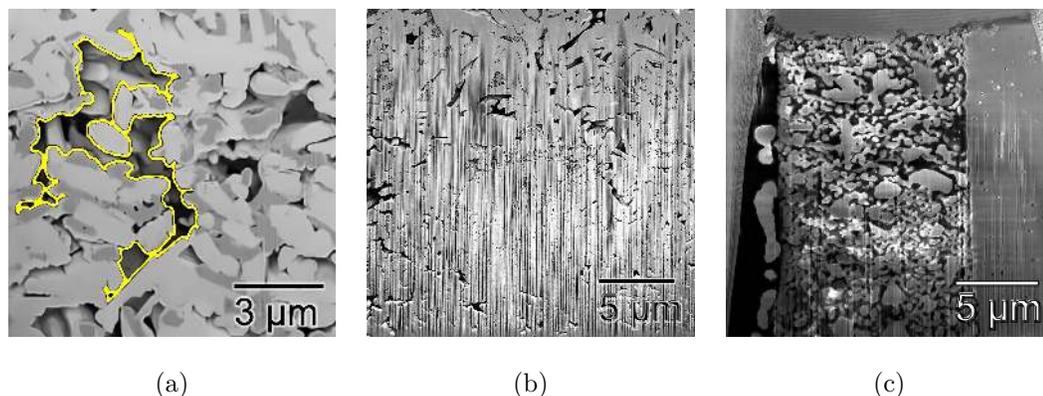
Figure 4.3: Examples of common artifacts that can occur during a FIB/SEM nanotomographic acquisition. (a) The "pore-back" effect is the imaging of material that is not on the current plane of interest, which appears due to electrons escaping from the back of a pore through the open vacuum; (b) Curtaining artifacts arise from ion channeling during the milling process and appear as vertical striations; (c) Electron image ($V_{acc} = 5\,kV$) showing sample charging (bright regions) on a LSM-YSZ cathode that is typical when imaging poorly conducting materials.

an automated FIB-nt acquisition. The "pore-back" effect is shown in Fig. 4.3a and is highlighted by the pore outlined in yellow. Within this region there is non-negligible contrast visible, arising from electrons emitted from behind the current face of interest that reach the electron detector through the open pore. While this feature is relatively easy to manually distinguish, this contrast causes significant challenges for automated segmentation routines, and is best avoided if at all possible. Additionally, inhomogeneity in both surface and subsurface structure can result in ion channeling during milling, which causes vertical striations on the cut face (so-called "curtaining," see Fig. 4.3b), preventing a clear view of the true structure at each slice. While any inhomogeneity can cause this effect, it is especially pronounced when there is open pore space, as the pores funnel the milling ions into specific channels. These artifacts can be somewhat mitigated by wavelet and Fourier image

post-processing techniques [272], but initial avoidance is very beneficial for high-fidelity reconstructions. Finally, electrical charging artifacts, which are common in all SEM investigations of insulating samples (see Fig. 4.3c) [273], need to be mitigated as much as possible, especially in systems where subtle contrast changes are important (such as the LSM-YSZ composite imaged in this work).

Sufficient sample preparation and careful control of imaging conditions can alleviate many of the listed concerns. Both the "pore-back" and curtaining artifacts can be significantly reduced by impregnating the porous structure with a low viscosity epoxy. This makes the structure more homogeneous (reducing curtaining) and also prevents imaging of the pore-backs. Another option that achieves a similar effect with the benefit of added conductivity, is a Wood's metal intrusion [274], although sensitive microstructures can be adversely modified by the pressure required to fill the pores. Careful consideration of specific sample requirements will determine the best procedure. Furthermore, these intrusion/impregnation strategies are only of use in samples with majority open pore networks, which provide a percolation pathway for the filling material.

In this work, a vacuum infiltrator (Allied VacuPrep) was used to fully encase the samples. The sample was placed in a 1 inch mounting cup such that the cathode-electrolyte interface was normal to the bottom surface. Samples were then degassed under vacuum for 5 min, at which point a low viscosity epoxy (Allied EpoxySet) was flowed slowly over each cup, allowing ample time for the epoxy to fully permeate the porous structure. The epoxy was introduced using a ¼" *ID* flexible tube, allowing approximately 1 drip (roughly 0.5 mL) per second. Once the samples were

175

fully covered with epoxy, they were held under vacuum for 1 min and returned to atmospheric pressure, at which point they were left to cure overnight. Once cured, the samples were planarized using a low grit SiC abrasive paper (LECO). An automated polishing machine (LECO GPX-200) was used to grind the sample using 320 - 1200 grit papers, and then polished with a 3 µm diamond suspension. To prevent charging, a thin layer (few nm) of carbon was sputtered (Balzers) onto the polished surface, and the sample was mounted with conductive graphite paint and Cu tape onto an epoxy mount SEM holder (Ted Pella, Inc.) (see Fig. 4.2b). Mechanical clamping of the sample is preferred over conductive adhesive mounting to maximize long-term acquisition stability and minimize physical specimen drift.

4.1.1.3   FIB/SEM observation

In this work, images for the three-dimensional reconstructions were obtained using the two Ga^+-ion FIB/SEM systems described in Sec. 2.2. Once an area of interest was located, the surrounding area was prepared to maximize the imaging signal and structural fidelity. First, a layer of protective Pt (or another material) was deposited on the sample surface using the ion beam. Next, two angled lines were milled into the deposited platinum, such that the thickness of each slice can be verified after acquisition[1] [275], on top of which a thick layer of protective carbon was similarly deposited. Different deposition materials were used to provide visual contrast between the layers, assisting the fiducial pattern tracking. Slightly above the area of interest, a fiducial pad (of carbon) was deposited, and a mark milled

---

[1]See the `FIB-SEM/fibtracking` module of Ref. [116].

into it as a reference for the ion beam during the automated tomography process. Finally, a large "C-trench" was milled using the highest current to reveal the face of the desired data cube (see Fig. 4.4a). Using the Xe$^+$ plasma-FIB (Sec. 2.2) greatly accelerated this portion of the preparation.

(a)   (b)
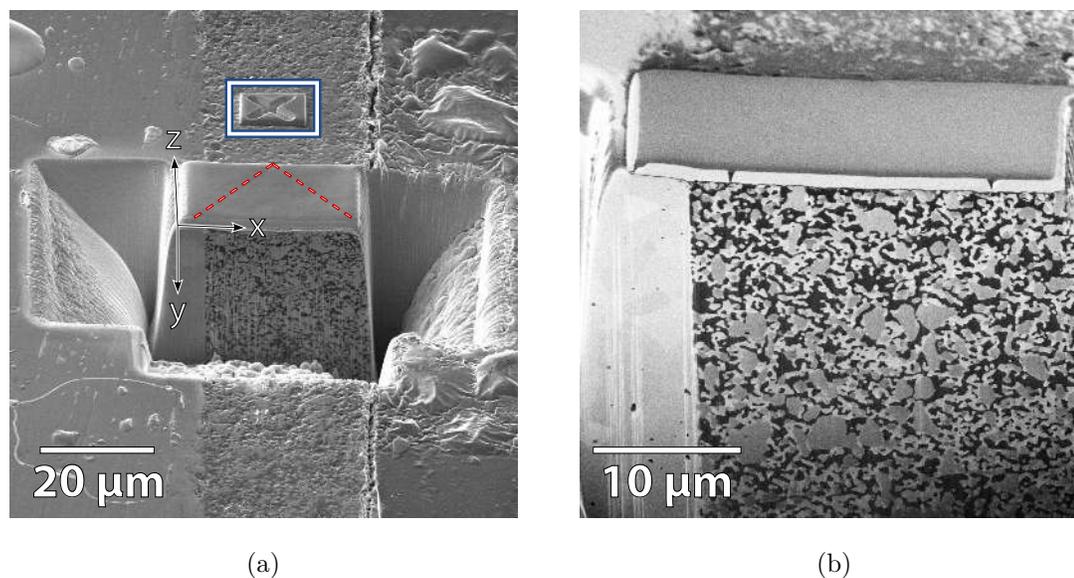
Figure 4.4: (a) Overview of data acquisition site after initial preparation (trenching and fiducial milling). Referenced directions are as shown in the figure, such that each image is taken of an *xy* plane, and slices progress in the *z* direction (following the convention of Holzer *et al.* [110]). The dashed lines highlight the position of the lines milled into the protective layer to track slice thickness, and the outlined box is the fiducial mark that has been milled for ion beam positioning during the automated process. (b) Example raw image that is acquired during the FIB-*nt* process. The bulk YSZ electrolyte is visible on the left, while the three phases (Pore - dark, LSM - intermediate, YSZ - bright) are all clearly distinguished in the composite cathode. The fiducials milled to measure slice thickness are visible in the FIB-deposited Pt at the sample surface.

In the composite cathodes investigated in this work, the LSM and YSZ (as well as LSCF and GDC) phases are often very difficult to distinguish owing to the similarity between and relatively poor room temperature conductivity of the materials. Because of this, careful consideration of imaging parameters was necessary in

order to optimize the contrast between the phases of interest, requiring the balancing of electron yield, interaction volume, and sample charging. Previous work on this system has revealed sufficient contrast can be extracted from these materials using low energy-loss backscattered electrons (BSE), collected using an energy filtered backscatter detector [270]. While this configuration was not available on the FEI tool (used for the LSM-YSZ studies), adequate (if not quite ideal) conditions were found using secondary electron imaging. The primary beam was low-energy, with an accelerating voltage (V_{acc}) of 750 V, and was operated in the magnetic immersion mode. Detection utilized the "through the lens" detector (TLD) with a 600 V collection grid bias. For the LSCF-GDC samples, use of the Tescan FIB/SEM enabled low-loss BSE collection, greatly enhancing the contrast of the collected images.

In addition to improving contrast between phases, using low V_{acc} improves spatial resolution and reduces the total interaction volume, enhancing the contrast within the epoxy-filled pores and providing sharper contrast at material edges. To prevent buildup of charge within the specimen, images were taken using full frame integration of 16 images with a short (100 ns) dwell time per pixel. To improve the reliability of later quantifications, the field of view and resolution of the electron images were selected to result in approximately isometric voxel sizes. Auto-focus and auto-contrast/brightness routines were performed before every image, resulting in raw images as shown in Fig. 4.4b. The assignment of particular intensity levels to each phase was confirmed prior to the full data acquisition using energy dispersive X-ray spectroscopy (EDS) scans (Oxford Instruments).

Once the site preparations were completed, the FIB-*nt* process was begun using

the Auto Slice and View software on the FEI tool, or the 3D Acquisition Wizard on the Tescan instrument. The prepared site was selected as the area of interest and the slice thickness was nominally set between 20 to 35 nm (depending on the material) to provide at least 10 slices per particle for faithful reconstruction [110]. Through post-acquisition analysis of the thickness tracking fiducials, the true slice thickness was determined vary from the nominal value with a standard deviation of 0.3 nm. In a typical acquisition, each slice required a total of approximately 2 to 3 min for milling and imaging. In the static geometry used here, no stage motion is necessary during the FIB-nt collection. For the datasets collected in this work, slice totals ranged from 211 to 1112, with total acquisition times ranging from 10.5 to 90 h (local use of the Tescan machine enabled longer data acquisition times for the LSCF-GDC samples, resulting in correspondingly larger reconstructions).

4.1.1.4 Data pre-processing

In addition to the methods used to acquire the image data, the processing steps that are taken can greatly affect the quality and fidelity of the resulting reconstruction. These processing steps are taken prior to image segmentation in order to facilitate the image labeling process and minimize the number of errors in the resulting output. In this work, these steps were implemented using a variety of software, including *Avizo Fire* (FEI Company), *Fiji* (open-source) [276], and Python libraries such as `NumPy` [277], `OpenCV` [278], and `scikit-image` (open-source) [279]. Where possible, other open-source libraries with similar functionality are recommended,

179

although may not be specifically implemented in this work.

Collected images first required a shearing correction (in the y direction) to account for anisotropic voxel sizes in the x and y directions. This anisotropy is due to the foreshortening caused by the 52° angle of electron beam illumination. Additionally, although each image was acquired relative to a predefined fiducial marker, final alignment using a least-squares optimization (using the 'Align Slices' module in *Avizo Fire*, or the 'StackReg' plugin in *Fiji* [280]) removed any residual artifacts from errant drift correction. Following alignment, the volume was then cropped to the area of interest within the acquired data.

Additionally, an intensity gradient was often observed on the acquired slices, due to the shadowing (lower detection efficiency) of electrons originating from the bottom of the sample face (see Fig. 4.5a). This artifact was more prevalent when imaging with secondary electrons on the FEI system, than in the BSE images acquired by the Tescan. The shadowing artifact derives from the geometry of the system, and is a common issue in FIB-*nt* acquisitions that can complicate analysis [171]. Previous researchers have attempted to remove this artifact by changing the sample geometry. One method in particular, the block lift-out technique, has been demonstrated to be very successful, but requires a great deal of time (6 h to prepare a 20 x 20 x 20 μm^3 volume prior to any data acquisition) [255, 281]. The shadowing in Fig. 4.5a causes an overlap within the global histogram between the brightest and moderate-intensity phases. Bright pixels towards the bottom will be incorrectly grouped with the moderate pixels towards the top, which greatly hinders the segmentation procedure. While the darker portions at the bottom of the

images could be cropped to remove the artifact (at the expense of the total reconstructed volume), a correction mechanism is preferred to quickly enable full use of the acquired data.

A unique method to correct the intensity gradient observed in the images is presented in Fig. 4.5. The technique relies on the fact that the intensity gradient is relatively constant on successive slices in the z-direction and is only present in the y-direction. By "reslicing" the image data onto an orthogonal set of xz-planes, the gradient was easily corrected through image stack normalization. The original (xy) images will have a gradient, but xz images will have uniform illumination on each slice and get progressively darker as the stack progresses in the y-direction (Fig. 4.5b). Each successive xz image was be normalized to the first by matching the first and second order statistics of the images' probability distribution functions [282]. This normalization along the y dimension effectively removed the intensity gradient once the data was resliced to its original orientation (compare Fig. 4.5a and 4.5c). While surprisingly simple, this method greatly improved the segmentation results by reducing the amount of pixel-intensity overlap between adjacent phases (Fig. 4.5d) [116].

Finally, after all corrections were made, the images were filtered using a two-dimensional, edge-preserving non-local means filter implemented within *Avizo Fire* [283]. This filter is extremely effective at removing the noise present in FIB/SEM images while retaining the fidelity of edges between particles. Various open-source implementations of this algorithm are additionally available [284, 285].
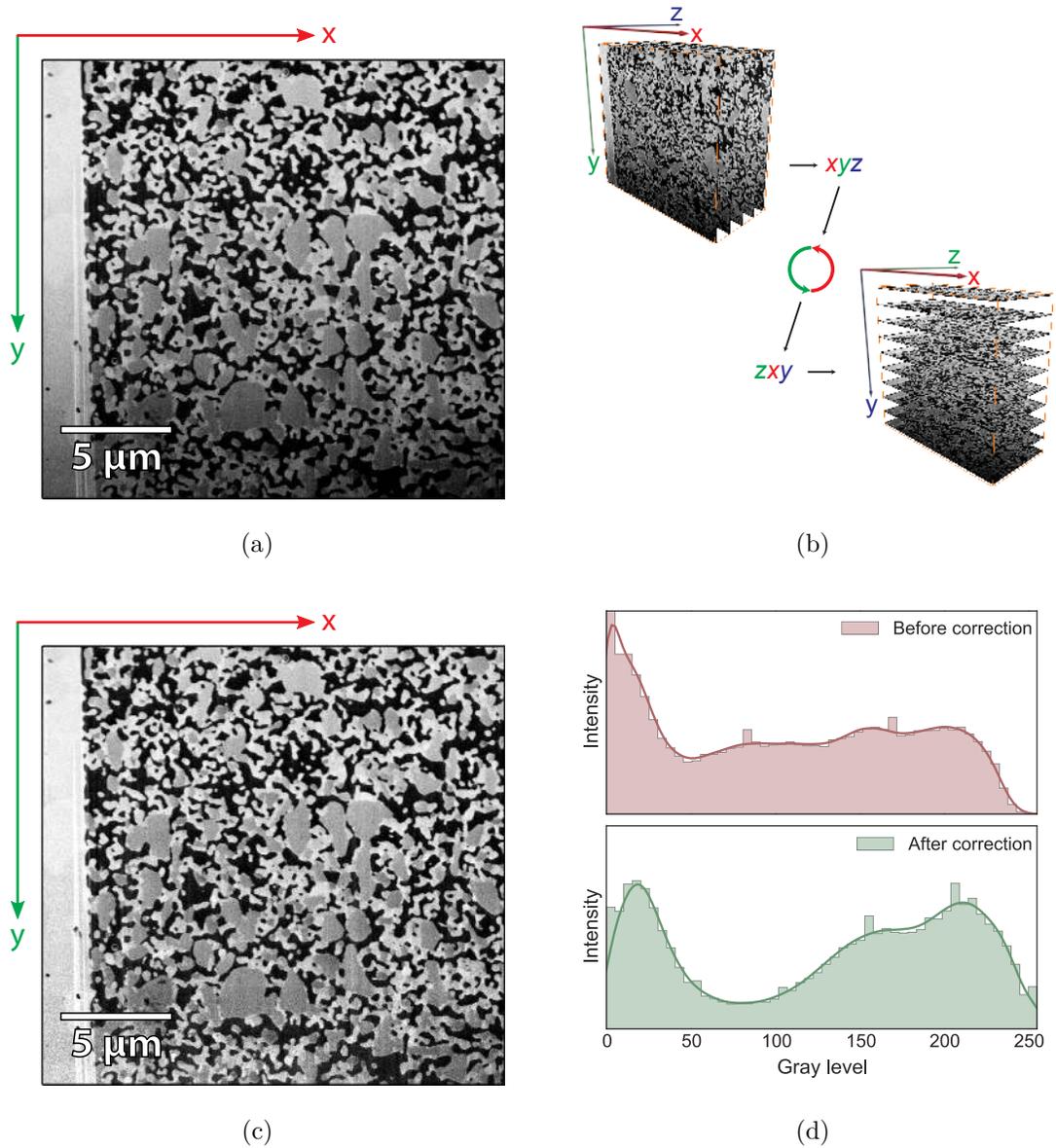
Figure 4.5: Example of an acquired image (a) before and (c) after FIB trench shading normalization. (b) shows the "reslicing" of the sample volume that enables the normalization. (d) Histogram and kernel density estimate for each image. After shading correction, the image is no longer undersaturated, and there is greatly improved contrast between the three phases, evidenced by the emergence of clearer intensity peaks (although still overlapping). In particular, much of the illumination in the $[50-100]$ range (top, red) has been corrected into the pore and LSM peaks at 20 and 160, respectively (bottom, green). All images are displayed on the same brightness/contrast scale.

4.1.1.5   Image segmentation

As the number of phases present in a sample is increased, so to is the complexity of an automated segmentation strategy. For a three-component system such as those studied in this work, simple thresholding did not suffice to accurately label the particles contained within the volume. It was also preferable to keep manual intervention to a minimum, for the sake of reproducibility as well as throughput. In this work, a marker-based watershed algorithm was used [286], implemented within *Avizo Fire*. The markers were set by using a conservative thresholding, such that only a fraction of the total volume was assigned to a phase. Each catchment basin was then filled according to the local gradient of illumination. This technique allowed for a mostly automated process, requiring limited manual intervention to ensure that particularly challenging particles are correctly segmented. Final processing of the dataset involved restricted smoothing of the labels to reduce unphysically sharp corners, and the removal of small "island" particles, which were formed by the presence of spurious single or few voxel labels. These segmented (binarized) datasets then formed the bases of the following quantitative analysis.

It should be noted that beyond the methods presented in this thesis, there is significant opportunity for advancement in the area of automated image segmentation. Current commercial solutions typically rely on simple thresholding (with *Avizo Fire's* watershed implementation a notable exception) to label images into a segmented volume, often requiring extensive human interaction. A number of more advanced segmentation algorithms utilizing modern research in the machine learning

and computer vision fields have been presented in the literature (see [287–290]). Application of these methods to FIB-nt data could greatly facilitate the reconstruction process, and would improve one of the most difficult and time-consuming aspects of the technique.

4.1.2   Computational procedures

Once a segmented volume has been acquired, various microstructural parameters can be measured and calculated. In SOFCs, these values can then be directly related to cell performance. A number of these parameters have been well described in prior works [106, 110, 113], and are only be briefly reviewed here. A more detailed discussion is provided for the calculation of phase connectivity, phase tortuosity (τ), and triple phase boundary density (ρ_{TPB}), as novel methods for these calculations were developed specifically during this work.

4.1.2.1   Volume quantifications

Phase volume fractions (η)

The volume and surface area of each phase were calculated by generating a surface representation of each phase within *Avizo Fire* (analogous functionality is available using the *Blender* [291] or *VTK* [292] open-source software packages). Such routines create a network of triangles (mesh) to represent a particular phase with a three dimensional surface. Once the meshes were obtained, basic statistics for each phase were calculated, including the total volume and surface area (in *Avizo*, this

184

was accomplished with the 'Surface Area Volume' module), as well as the surface area to volume ratio (SA:V). The volume fraction (η) for each phase was obtained by dividing the volume of each phase by the total sample volume. This method of using a surface mesh is more accurate than a simple counting of voxels (used in prior works [112]), particularly for area calculations. This is because a voxel counting algorithm will overestimate the total surface area due to the discrete nature of the rectilinear voxel edges. Solid fractions for each cathode phase (η_{solid}) were computed as the fractional volume for each solid phase (e.g. LSM and YSZ) relative to the total solid phase volume:

$$\eta_{\mathrm{solid,LSM}} = \frac{V_{\mathrm{LSM}}}{V_{\mathrm{LSM}} + V_{\mathrm{YSZ}}} \tag{4.1}$$

Comparing these ratios to those of the source materials enabled an analysis of potential mass transfer from one phase to another during cell operation.

Particle size ($\bar{d}$)

From the surface area and volume measurements, a global average of particle sizes was determined through the use of a formula common in the Brunauer, Emmett, and Teller (BET) method, which measures powder sizes using gas adsorption techniques: $D = 6 \times V/S$, where D is the average particle diameter and V and S are the total phase volume and surface area, respectively [110, 293]. This method assumes a spherical particle geometry, which is generally an invalid assumption for these types of particles, but it provided a simple means by which to compare the particle size magnitude of the various phases, and has been used in numerous prior FIB/SEM reconstruction studies [107, 110, 112, 264, 266, 294]. If desired, further

detail regarding the distribution of these parameters can be calculated as well, provided that individual particles can be suitably separated (when needed, this was performed using the 'Separate Objects' module in *Avizo Fire*).

Phase distribution

Phase distributions throughout each sample volume was computed by examining profiles of the distribution in each orthogonal direction (*x*, *y*, and *z*). Such profiles were useful for investigating whether or not any anisotropic ordering was present within the phases. In this work, the distribution was calculated as the fraction of each plane that was occupied by each material along the profile direction. Within *Avizo*, this was accomplished using the 'Volume per slice' calculation available in the 'Material Statistics' module, but such a calculation would be relatively simple to implement in any other computing environment (*e.g.*, *Python* and `NumPy`). In addition to viewing the phase distribution, the slope obtained by fitting a linear function to this profile allows for a measure of the magnitude of the change in η ($\nabla\eta$), which was compared between directions and samples. Variations in the phase distribution would imply migration of phases within the volume, and could have significant impacts on transport kinetics.

4.1.2.2 Phase connectivity

The interconnectivity of different phases in a sample is a critical parameter in determining the bulk transport properties and possible kinetic pathways of various reactions that may take place within it. A common technique to analyze this

connectivity is to "skeletonize" the structure, making use of any number of possible algorithms [295]. The goal of these methods is to represent each phase by a graph that is homotopic (representative), thin (single voxel), and medial (at the center of the phase) [296, 297]. In this work, *Avizo Fire* was used to calculate the skeletons (in particular, the 'Distance Map,' 'Distance-Ordered Thinner,' 'Trace Lines,' and 'Evaluate on Lines' modules). Using a these individual modules (rather than the supplied "Auto Skeleton" feature) allowed for careful tailoring of module inputs to obtain a skeleton free of "starburst" artifacts, which are often produced using the default settings, especially in areas with large particles. Similar functionality is available in the *ITK* [298, 299] and *CGAL* [300, 301] libraries.

Using these techniques, the skeleton network for each phase was calculated, and each network consisted of one or more discrete *graphs*. Each graph in turn was comprised of a series of *nodes*, connected by *edges*. A number of useful statistics regarding the network were figured, many of which were first introduced in the SOFC literature by Gostovic *et al.* [106]. A brief overview of these metrics is provided here, and a simple illustration of each is given in Figure 4.6 for reference. Useful among the quantifiable parameters are the number of edges (E) and nodes (N) within the skeleton network of each phase, as well as their volumetric density, relative to total sample volume (ρ_E and ρ_N, respectively). From these values, the degree of each node (k_i) was calculated by counting the number of edges coinciding at each node: $k_i = E_i/N_i$. The mean of these values ($\bar{k}$) gave a measure of the amount of self-connectivity in each phase [106]. Finally, the mean topological length ($\overline{L}$) defines the average distance throughout the network that can be traveled between

187

branching nodes. Physically, this property can be interpreted as a sort of mean free path for particles traversing the network. $\overline{L}$ was calculated by summing the lengths of each edge within the network (l_i) and dividing by the number of nodes present:

$$\overline{L} = \frac{1}{N} \sum_i l_i. \tag{4.2}$$

In addition to these metrics from previous works, another useful measurement that was obtained from the skeleton model was the degree of percolation for a phase (p). This parameter aims to quantify the fraction of the overall skeleton network length that is interconnected (percolated), and should relate to the ease of carrier transport within the phase. Each phase network (with total length L and mean topological length $\overline{L}$) consisted of a finite number of individual graphs (with lengths $\mathcal{L}_i$), and each graph represented a portion of the total network that was discontinuous with the remainder of the network (see Fig. 4.6a and 4.6b for a simple example). If a phase was particularly discontinuous, its network consisted of many smaller graphs. A fully percolated phase on the other hand was represented by one large graph. The degree of percolation (p) was defined in this work by finding the point at which the cumulative network length changes by less than 1% as follows: The individual graphs (with lengths $\mathcal{L}_i$) were sorted in decreasing order and their cumulative sum (L_{cum}) calculated. If the total length of the network is L, the value of p was taken to be the value of L_{cum}/L at the point where adding successive terms to L_{cum} caused a change (ΔL_{cum}) of less than 1%. Formally, p was defined as:

$$p = \frac{\sum_n \mathcal{L}_n}{L} \quad \text{s.t.} \quad \frac{\mathcal{L}_{n+1}}{L} < 1\% \tag{4.3}$$

A p near unity represented a phase that was fully percolated throughout the sampled

(a)   (b)   (c)
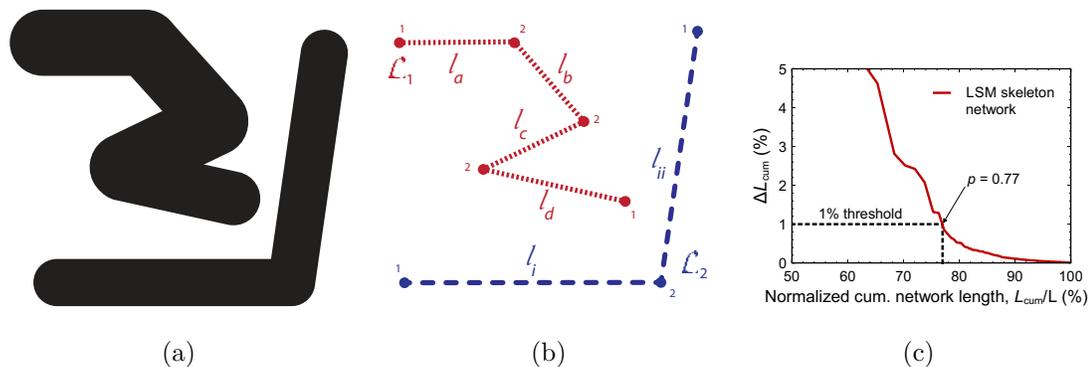
Figure 4.6: (a) Artificial simulation of a 2D phase, consisting of two discontinuous components. (b) Theoretical skeletonization of the phase presented in (a). This total network consists of two graphs, with lengths $\mathcal{L}_1 = l_a + l_b + l_c + l_d$ and $\mathcal{L}_2 = l_i + l_{ii}$. In this simple example, $N = 8$, $E = 6$, $\overline{L} = (\mathcal{L}_1 + \mathcal{L}_2)/8$, and k for each node is represented by a small number adjacent to each node. (c) Example determination of the degree of percolation, p, for the LSM phase within the SOFC sample characterized in this work. The percentage change in cumulative network length ΔL_{cum} is calculated, and the value of L_{cum}/L where $\Delta L_{\mathrm{cum}} < 1\%$ is taken as p.

volume, while significant deviations corresponded to poorly connected phases. An example determination of p is shown in Fig. 4.6c.

4.1.2.3   Tortuosity (τ)

Another useful microstructural measure in these systems is the amount of tortuosity in each phase. In general, "tortuosity" (τ) is a rather poorly defined parameter [169], and is frequently determined differently for each particular case in question. At its essence however, tortuosity represents the added difficulty that a particle traveling through a phase experiences due to the complexity of the available physical paths (such as a gas molecule through the pore space). Among other properties, the degree of tortuosity can affect the ease of molecular diffusion and both electrical and ionic conductivity through a material [271]. As such, it is an

189

important parameter to accurately quantify in any system potentially limited by species transport, especially in SOFC cathodes and anodes.

Within the literature specific to SOFC electrode reconstructions, various methods have been used to calculate τ. Generally, τ can be calculated on a geometric, hydraulic, electrical, or diffusion basis [169], leading to disparate methods being used throughout prior works. Some of the earliest techniques were based on a Monte Carlo method, approximating molecular flux through a finite element model of the pore volume in an SOFC anode [111]. Vivet *et al.* [170] further expanded upon this method with a finite difference solution to the diffusive transport equation. Joos *et al.* [171] used a similar method to calculate electrical tortuosity, solving Ohm's law on a finite element model to compare effective conductivities, the ratio of which was defined as the tortuosity.

Besides these application specific techniques, another set of methods are those based on purely geometric (*a.k.a.* geodesic) considerations. These methods are much simpler to calculate, and aim to describe purely the physical tortuousness of the microstructure. Because they do not rely on a material's diffusivity or conductivity, the values obtained can be easily compared between different phases, materials, and samples, at the expense of a direct physical interpretation of the results. In short, the geometric tortuosity between two points is simply the ratio of the geodesic distance (L_{G}) and the euclidean distance (L_{E}) between them. L_{G} is the shortest path that is possible given the presence of any interfering structure (such as another phase), and L_{E} is what the shortest distance would be if there were no hindering structure (the "straight-line" distance or sample thickness).

Some of the first methods used to calculate the geometric tortuosity relied on tracking the center of mass of each phase on each slice, and comparing the length of this path to the straight line distance through the sampled volume in the same direction [106, 107]. This technique has since been made available in *Avizo* as the 'Centroid Path Tortuosity' module. While simple to implement, this method has significant limitations in that it calculates the geodesic distance globally, rather than at every point within the volume. This results in the method being generally insensitive to local variations in structure, such as can arise from bottlenecks and phase discontinuities. Furthermore, the center of mass calculation is problematic for a well dispersed, but fairly tortuous phase (like observed in YSZ in this work), since the center of mass does not move very much, leading to an underestimation of τ. Another approach to calculating the geometric tortuosity based on a diffusion-simulating random walk method has been used in the literature as well [115, 302], providing both local and global information about tortuosity, but requiring significant computational effort.

In this work, a geometric approach to calculating tortuosity was implemented. Unlike prior methods, it does not depend on computationally-intensive simulation, and τ was calculated at every point within the volume, rather than on a global basis. Specifically, the definition of τ used in this thesis is that provided by Gommes *et al.* [271], which has gained traction in recent literature (e.g. [303–305]):

$$\tau = \lim_{L_\mathrm{G}, L_\mathrm{E} \to \infty} \frac{L_\mathrm{G}}{L_\mathrm{E}} \tag{4.4}$$

where L_G and L_E are the geodesic and euclidean distances, respectively. Figure 4.7
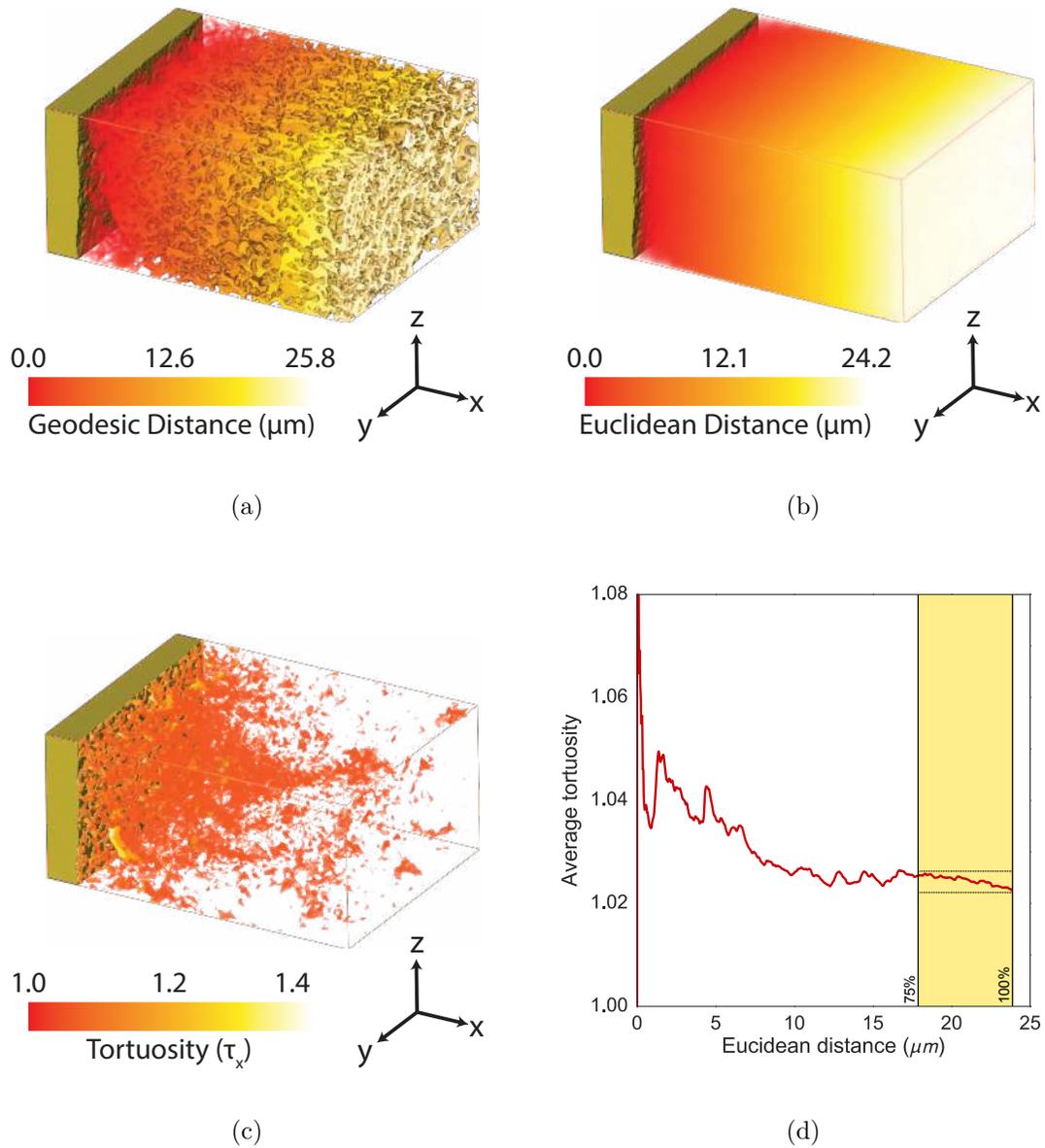
Figure 4.7: Example of tortuosity calculation (in the x direction) for the pore space in an SOFC cathode sample. The (a) geodesic and (b) euclidean distances from the electrolyte/cathode interface are calculated for every voxel within the cathode volume. Dividing these values at every point yields (c) the tortuosity at every voxel. This data can be averaged into (d) a profile along any direction, in this case x, which is perpendicular to the interface of interest. The error of the measurement depends on the convergence (as a function of sampled volume), and is estimated as $\pm$ one standard deviation of the data contained within the final 25% of the profile (as shaded above).

illustrates the method for a pore phase τ calculation in the LSM-YSZ composite cathode. The geodesic distance (Fig. 4.7a) was calculated at every point throughout the volume using a 'Fast Marching' algorithm [306, 307]. The euclidean distance (Fig. 4.7b) was calculated as a simple "straight-line" measurement, parallel to the particular direction of interest. In the x direction, the euclidean distance (Fig. 4.7b) was calculated as the distance between the current point and the electrolyte/cathode interface. For the y and z directions, the distance to the planar boundary of the sampled volume was used rather than the interface. The tortuosity (Fig. 4.7c) at each point was then figured by dividing L_G by L_E. While the true $L_G \to \infty$ limit of τ cannot be explicitly calculated due to the limited sampling volume, a representative average value for each direction can be obtained by computing the tortuosity profile (Fig. 4.7d) along each dimension. To reduce the impact of local oscillations in the profile, the mean and standard deviation of τ within the last 25% of the profile (as highlighted in Fig. 4.7d) was reported as the value and error for τ. This technique correctly indicated significantly higher error in the measurements of τ for phases with a large degree of discontinuity.

Of further interest in the specific application of τ to SOFC samples is the ratio of volume phase fraction to tortuosity, η/τ. This parameter is a determining factor for the effective diffusivity of gaseous molecules through the porous structure an electrode. The effective diffusivity due to the tortuous porous structure has been defined as

$$D_{\text{eff}} = \frac{\eta}{\tau} D \tag{4.5}$$

where D is the Knudsen diffusivity without the effects of porosity and tortuosity [308]. Using this ratio, relationships between the expected D_{eff} can be examined by measuring only two relatively simple microstructural properties.

4.1.2.4 Triple phase boundary density

In multiphase systems like SOFCs, the distribution of the common boundaries between materials is critical in controlling the reactions that take place within a device, and contributes significantly to its overall performance. In a composite SOFC cathode, the triple phase boundaries (TPB) are locations where all three phases (cathode, electrolyte, and pore space) meet, and the three necessary reactants (electrons, ions, and gaseous oxygen) enable the ORR (Eq. 1.3). A direct relationship between the volumetric density of TPB points (ρ_{TPB}) and SOFC performance has been previously observed [107, 309], making the accurate quantification of this parameter of utmost importance. A brief review (and evaluation) of some common methods, as well as a description of an improved implementation for the calculation of L_{TPB} are presented here.

Existing methods

L_{TPB} (and ρ_{TPB}) have been quantified using numerous techniques, leading to some discrepancy between reported values, even for similar materials [270, 310]. Among the techniques that have been used are phase change analysis, [107], intersection point analysis [106], theoretical simulation [310], stereology [172], voxel edge-counting [113], centroid smoothed edge-counting [114], and the volume expan-

sion method [115, 302]. As expected, the values produced by each of these methods vary based on differences in the underlying techniques. Some of these methods (in particular the edge-counting methods) overestimate TPB lengths due to improper handling of the discrete nature of a three-dimensional voxel representation. The centroid smoothing algorithm, essentially a three-dimensional box filter, improves upon edge-counting by simulating a more physically realistic TPB path through the volume [114].

Implementation of a centroid edge counting method

In this work, a centroid smoothed edge-counting technique to measure TPB networks was developed in collaboration with researchers from the Information Technology Laboratory at NIST. This method extends and improves the implementation presented by Shikazono *et al.* [114], and has been made publicly available.[2] An overview of the algorithm is presented in Figure 4.8. Briefly, the algorithm operates on a segmented volume by finding the voxel edges (i.e. the edges of a cube) where the four neighboring voxels contain all three phases. The edges are joined into TPB paths to form a TPB network for each volume, which is then smoothed by a centroid box filtering process. Within the TPB path, the centroid of the triangles formed by voxel edge midpoints is used to determine the overall path. The filter is clamped at endpoints of a TPB path (such as A in Fig. 4.8a), such that the endpoint is used to fill the neighborhood where a midpoint is missing.

Additionally, the algorithm presented in this work has been optimized to in-

---

[2]See the `TPB scripts` module of [116]
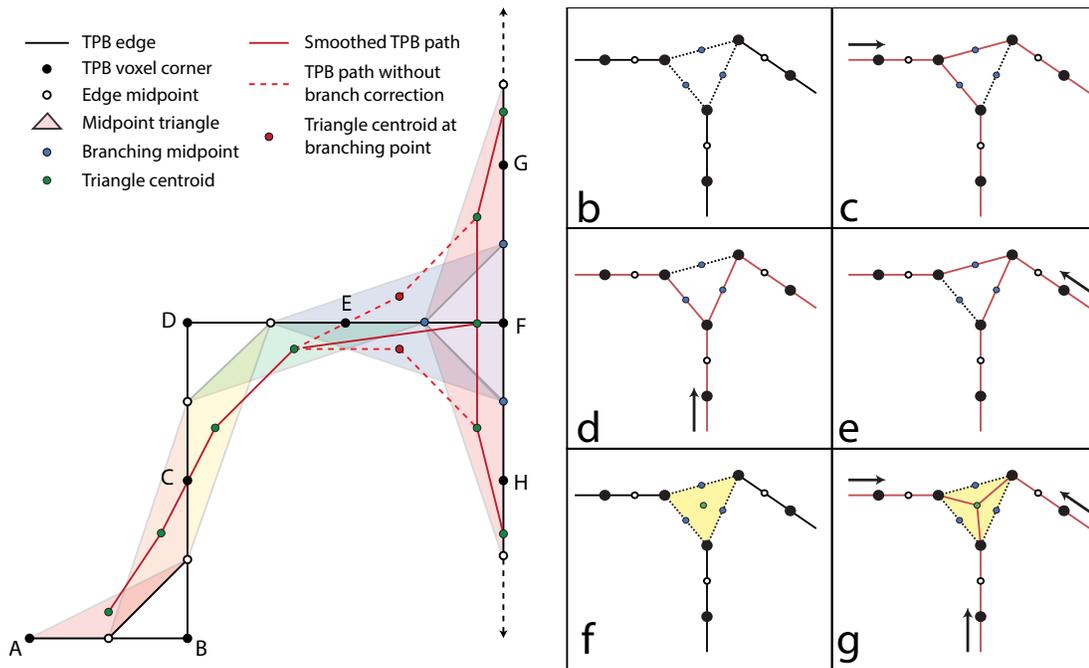
Figure 4.8: (a) Schematic diagram of the centroid smoothing algorithm used to calculate the TPB network. The diagram is shown in two dimensions, but the concepts are easily extended to three. The black path $(\overline{ABCD}\ldots)$ depicts a theoretical path of TPB edges with a branch occurring at point F. The centroids of subsequent edges (green dots) are connected, and a new point is created at all branching points in order to preserve the topology of the original TPB network. The centroid smoothed network is represented by the solid red lines. The dashed lines represent how the network would be figured without correction of branching points. (b-e) Example of a branching TPB path and how the total length calculated will vary depending on the direction of approach when counting TPB edge lengths. (f) Addition of centroid at branching point; (g) TPB path determined using additional centroid. The total path length remains consistent regardless of direction of approach during the calculation.

clude homotopic network descriptions at branching TPB points. Because of the branching points, the network could fail a self-consistency test if calculated multiple times starting from different points within the structure, as shown in Fig 4.8c-e. A simple solution to this problem is to add an additional point at the center of each branch within the path. The center is determined by finding the centroid of the voxel edge midpoints surrounding each branch (Fig. 4.8f). Once this has been done at all branching locations, the TPB network is built by connecting the TPB paths as shown in Figure 4.8g. This technique ensures that the total TPB length will be measured the same regardless of the direction from which the length is measured, and that the topology of the true TPB network is preserved.

Comparison to volume expansion method

Recently, a "volume expansion" method has gained favor within the literature as an alternative means by which to calculate the TPB network due to its computational simplicity. This method uses global morphological operations on each phase and does not require the traversal of the entire volume [115]. The volume expansion method consists of three steps: a morphological dilation of the three phases that are present, a logical operation to find where the three phases overlap, and the thinning of the resulting volume to yield a three-dimensional network. While this method is more computationally efficient than an edge-counting algorithm, it relies on a number of configurable parameters that can significantly affect the resulting network. The direction, dimensionality and magnitude of the dilation all affect the morphology of the resulting overlapping volume, in addition to the parameters used

in the algorithm to skeletonize the volume.
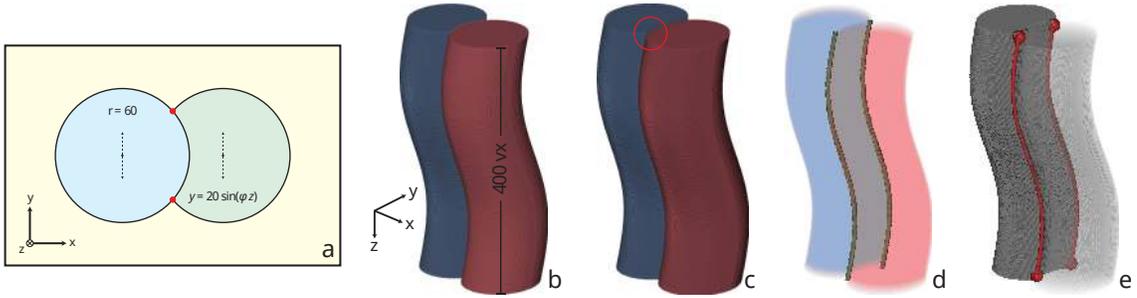
Figure 4.9: Example of TPB test volume and volume expansion calculation method. (a) 2D template used to create test volume. The red dots highlight the TPB points in two dimensions. The positions of the two circles were oscillated together in the y-direction to generate (b), a 3D volume extruded in the z-direction. In this example, $\varphi = \frac{2\pi}{400}$, such that one period of the sine function was completed over the 400 z voxels. (c) The original surfaces are dilated by four voxels in each of the six neighboring directions, causing the two cylinders to overlap one another by a small amount. Evidence of the overlap is visible in the area circled in red. (d) The overlapping volume of the dilated data is located at the interface between the two phases, as expected. (e) This volume is then skeletonized using typical thinning algorithms to yield the TPB network (shown in red).

To examine these effects and compare the performance of the TPB algorithm developed in this work, a test volume was created as shown in Figure 4.9. While simplistic, the model is effective in demonstrating some of the most important limitations inherent in the volume expansion method. It consists of two overlapping circles (with radii of 60 voxels) in the xy plane that have been extruded in the z dimension. The vertical position of the circles (y) is determined by the arbitrary sinusoidal function $y = 20\sin\left(\frac{2\pi}{400}z\right)$, resulting in an S-shaped volume (Fig. 4.9b). Each circle and the surrounding volume are considered a distinct phase, such that there are two TPB paths within the volume, each with a full period sine wave path with length 409.7 linear voxel units (*lvu*), calculated by integrating the arc length of $y(z)$ over one period. Summing the lengths of the two paths gives a ground

Table 4.1: Comparison of the centroid edge-counting and volume expansion methods used to calculate L_{TPB} for the sample volume of Figure 4.9. Units of each value are *lvu*; the percentage provided represents the degree of error compared to the true L_{TPB} value. For the volume expansion method, the minimum, mean, and maximum values obtained for a range of algorithm input parameters are reported.

Ground truth L_{TPB}	Centroid Edge Counting		Volume Expansion
		min:	814.5 (-1.2%)
819.4	820.9 (0.2%)	mean:	834.6 (1.9%)
		max:	880.4 (7.5%)

truth theoretical L_{TPB} of 819.4 *lvu*. The volume expansion method was tested by repeating the TPB measurement on this theoretical volume using various dilation and skeletonization settings (Fig. 4.9c - 4.9e). Depending on the settings used, the length of the resulting TPB network was found to vary by up to 8% (see Table 4.1). By contrast, the implementation of the centroid method presented in this work (which does not use any "tunable" parameters) obtained almost the exact correct result, within 0.2% of the true value.

A detailed comparison of TPB paths obtained with both the volume expansion and centroid edge-counting method is shown in Figure 4.10. In Fig. 4.10c, the difference between the two methods can be clearly seen. When used with the "best-case" parameters, the volume expansion method was able to approximate the theoretical L_{TPB} in this simple example, but it is clear that this is due to two distinct errors counteracting one another. First, the location of the TPB endpoints is incorrectly placed, as can be observed by the displacement of the red sphere from the top edge of the cylindrical volume in Fig. 4.10c. Due to the volume dilation and then erosion, the phase microstructure is intentionally modified, and the exact
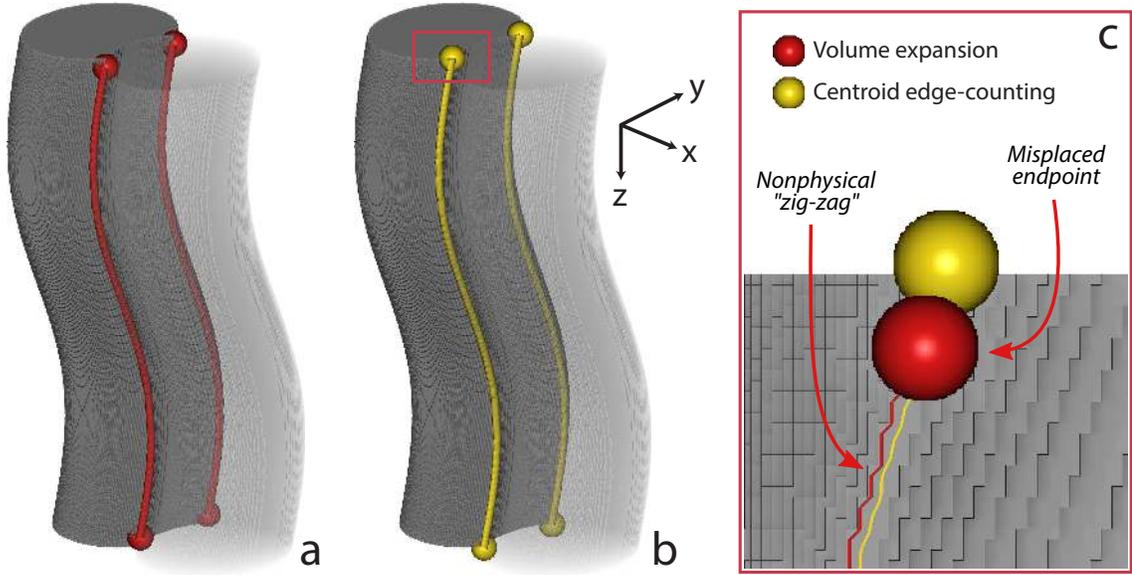
Figure 4.10: Comparison of the two methods used to determine TPB network on the test volume described in Fig. 4.9. (a) TPB network measured using the volume expansion method (red). Note, the "best-case" parameters were used in this figure, resulting in a measurement of 823.2 *lvu* (0.5% error). (b) TPB network measured using the centroid edge-counting method (yellow) gives a measurement of 820.9 *lvu* (0.2% error). The outlined region is shown in detail in (c), demonstrating the differences between the two methods. Notice that for the centroid algorithm introduced in this work, the TPB path endpoint is properly located at the edge of the volume ensuring an accurate calculation of the total L_{TPB}.

position of the TPB path edge is lost. As such, the node at the end of the TPB path is not explicitly preserved at the phase boundary. This error serves to shorten the overall measured L_{TPB}, but is counteracted by insufficient smoothing of the TPB network generated by volume expansion. The nonphysical "zig-zag" pattern that arises from the discrete nature of the voxel representation is clearly visible in Fig. 4.10c. This results in a wide range of possible values for the measurement, depending on the specific settings used for the morphological operations. In a real dataset, these small errors will be greatly magnified due to the large number of discrete TPB paths within the overall network. In fact, the range of L_{TPB} values

obtained for one experimental dataset varied $\pm 30\%$ depending on the settings used for dilation and skeletonization, indicating that while the volume expansion method may be suitable for simple structures, it is likely less appropriate for complex ones such as those observed in composite SOFC electrodes due to the convolution of multiple sources of error.

Estimation of electrochemical activity

Of particular interest in the electrochemical applications of FIB-*nt* is a measurement of the expected "activity" of the different parts of the TPB network. Within a composite cathode, a certain proportion of the TPB network is expected to be isolated from any larger percolated phase network, and because of this will not contribute to useful ionic, electronic, or gas conduction. Thus, it is prudent to determine the active vs. inactive L_{TPB}, in addition to the total length. The present techniques and definitions used to determine TPB activity have been proposed in prior works [113, 270], and have been incorporated into the L_{TPB} algorithm presented earlier in this section.

Briefly, once the overall TPB network was calculated, it was analyzed for activity by examining the connectivity of the phases (referred to as *connected components* or *CC*) to which it is connected. The connectivity of adjacent voxels was restricted to only those that share at least one face, meaning each voxel had a possibility of six nearest neighbors. Each *CC* was classified as either *percolated*, *isolated*, or *dead-end*, depending on which boundaries of the volume it intersected. A *percolated CC* was one that extended to two or more of the sampled volume's faces. This approxima-
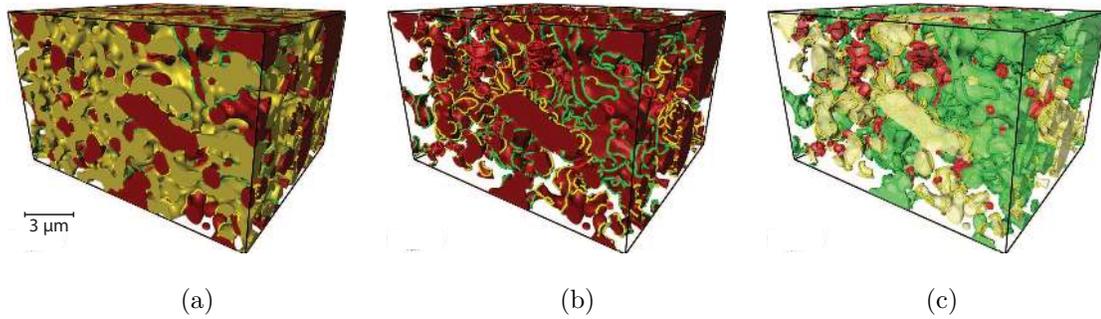
Figure 4.11: Example classification of triple phase boundary network shown with an example LSM-YSZ composite cathode sample. (a) The LSM (electronic conductor) and YSZ (ionic conductor) volume models are displayed (red and yellow, respectively;) with the TPB network visible at the boundaries; (b) the YSZ volume model has been removed, leaving just the LSM and the TPB network colored by their electrochemical classifications: active (green), inactive (red), and unknown (yellow) (c) volume model of LSM network, colored by connected component activity, revealing how the connectivity of the LSM components determines the TPB activity due to its limited percolation in this sample. The displayed volume is a limited sub-sample of an overall FIB-nt acquisition (sub-volume is approximately $6 \times 10 \times 9$ µm).

tion is necessary since only a limited volume of the total sample can be examined through FIB-nt, and a *percolated CC* was assumed to be well-connected to the overall sample volume. A *dead-end CC* was one that borders just one face of and ended within the sampled volume. An *isolated CC* was one that was completely contained within the sampled volume, and had no intersections with the volume boundaries. An example of this classification process is shown in Figure 4.11 for a sample SOFC cathode volume. In this sample, the pore and YSZ phases were almost completely percolated, meaning the performance of the sample was limited by electronic conduction and the LSM phase determined the overall activity of the TPB network. Figure 4.11c shows the *CC* evaluation for the LSM phase, with green, yellow, and red representing active, unknown, and inactive classifications, respectively.

Once the *CC* were classified, each TPB edge was categorized based on the

classes of the four voxels that it connects. An *inactive* TPB edge was one that contacts any voxel of an isolated *CC*. A TPB edge was *unknown* if it did not contact any isolated *CC*, but was connected to at least one dead-end CC, and an *active* TPB edge was one that contacted only percolated *CC*. The total TPB networks comprised multiple TPB paths that each were sets of connected TPB edges. Each TPB path was classified based upon the edges it contains. Again, a path was *active* if all edges were active, *unknown* if all edges were either active or unknown, and *inactive* if any edges were inactive. Finally, since the ratio between the active and inactive L_{TPB} is assumed to be accurate even with the presence of unknown TPBs, the final active L_{TPB} was figured as:

$$L_{\mathrm{TPB,A}} = A \left(1 + \frac{U}{A + I} \right) \tag{4.6}$$

where A, U, and I are the active, unknown, and inactive L_{TPB} values initially calculated, respectively. Dividing L_{TPB} by the sample volume gives the triple phase boundary density (ρ_{TPB}), which can be compared between samples regardless of collected volume. Finally, the fractions of the TPB network that were active and inactive ($f_{a,\mathrm{TPB}}$ and $f_{i,\mathrm{TPB}}$) can be compared. All L_{TPB} values reported in this work were corrected using Equation 4.6.

4.1.3 Conclusions

FIB-*nt* is a remarkably powerful technique for measuring material microstructures, and is applicable to wide range of sample types. Analyses of "advanced" microstructural properties such as tortuosity and triple phase boundary length are of

great interest when it comes to determining the behavior of many material systems, but are difficult to quantify with currently available commercial and open-source tools. Additionally, specific implementations from research are rarely made available to the community, leading to severe discrepancies between reported methods.

This section introduced and provided an overview of a number of techniques that can be used to process FIB-nt data and quantify the microstructural properties of a reconstructed volume. Significant advancements have been presented in the correction of the common FIB-shading artifact, allowing for improved segmentations. Additional improvements in the calculation of microstructural parameters have been presented, in particular for tortuosity and triple phase boundaries. These methods are used in the following sections to model the degradation of two types of composite SOFC cathodes, demonstrating their practical implementation. The algorithms and techniques introduced here have been made freely available for public use in an online code repository, with the intent of allowing peer-review of not only results, but methodology as well [116].

4.2 Quantification of LSM-YSZ composite cathode microstructure

To analyze the mechanisms of degradation in high-temperature SOFC cathodes, the LSM-YSZ system was chosen. (see Sec. 1.2.2 for a review of the SOFC materials used in this work). Half-cell stacks were fabricated according to the procedure in Sec. 4.1.1.1, and electrochemically tested by collaborators in the Wachsman laboratory. Impedance spectroscopy measurements were performed using a 1400 Frequency Response Analyzer and a 1470 Cell Test System (Solartron Analytical). During aging tests, cells were held at a constant temperature, in a constant gas environment, and EIS spectra measured throughout the aging process. A thermocouple was placed inside the reactor, near the cell to ensure accurate temperature measurements. Gas flow rates and mixtures were controlled using a set of mass flow controllers (MKS) [311].

Measurements were taken for cells aged for $500\,\mathrm{h}$ under dry and humid environments, both with and without applied polarization. Specifically, synthetic air (N_2–O_2 mixture) was introduced at a flow rate of $100\,\mathrm{sccm}$. To generate a humid environment, the synthetic air was bubbled through water ($25\,^{\circ}\mathrm{C}$) using a quartz impinger, resulting in 3% H_2O moisture. Cathodic polarization was applied via a $-0.7\,\mathrm{V}$ potential applied across the cell from the working electrode (WE) to the counter electrode (CE), driving O^{2-} across the electrolyte. Four samples were chosen for detailed microstructural analysis to analyze the effects of humidity and polarization on the composition of the cell. For the sake of simplicity, these cells will be referred to by simpler labels throughout this section, based on the aging environment

and applied polarization: *Air*, *Air-Cathodic*, *H$_2$O-Anodic*, and *H$_2$O-Cathodic*.

4.2.1   LSM-YSZ FIB-*nt* reconstruction results

Representative volumes from the four LSM-YSZ composite cathode samples were reconstructed using FIB/SEM nanotomography. Of the four samples, two were aged in dry air and two in a humid environment, while under no load, anodic, or cathodic polarization. After data post-processing and segmentation, the resulting segmented volumes were analyzed using the methods presented in Sec. 4.1. Each of these sample volumes is shown in Figure 4.12. As can be seen in this figure, the aspect ratio and amount of data varied somewhat between samples due to experimental limitations. As such, efforts were made to ensure that comparisons are made between intrinsic measures that are insensitive to the sample volumes. Where unavoidable, the dependence of a measure on the sampled volume is discussed.

Further specifics of the reconstructions are presented in Table 4.2. The composite cathodes were sliced at a nominal z resolution of 20 nm. Given a smallest average particle diameter of 574 nm (YSZ particles in *H$_2$O-Anodic*; see Fig. 4.13c), this slice thickness well exceeds the minimum 10 slice per particle standard proposed for FIB/SEM reconstructions [110]. To reduce the error in slice thicknesses, extremely high resolution ion images (4096 x 3536 pixels) were used to localize the ion milling fiducial. The slice thicknesses were verified after acquisition through geometric analysis of fiducial markers [275], and were found to remain within approximately 5% of the nominal value. As such, uniform thicknesses in the z direction
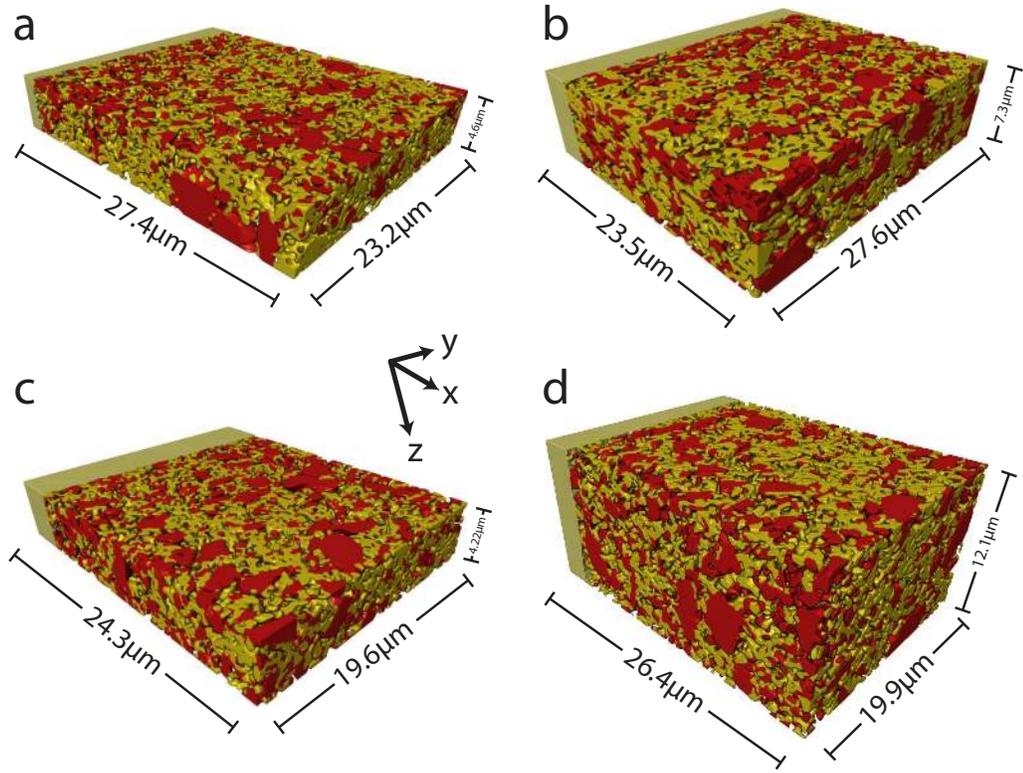
Figure 4.12: Representative visualizations of the four LSM-YSZ composite cathodes reconstructed by FIB-nt. Phases are distinguished by color: LSM in red, YSZ in yellow and the pore phase omitted for clarity. A portion of the bulk YSZ electrolyte is visible at the rear of each figure. The samples are (a) *Air*, (b) *Air-Cathodic*, (c) *H_2O-Anodic*, (d) *H_2O-Cathodic*.

were assumed for subsequent calculations. Typical *x-y* pixel resolutions were around

15 to 30 nm.

To gain an understanding of the statistical significance of the microstructural

quantifications, a subsampling technique was used to measure the variance of each

parameter throughout the collected volume. For all four samples, each quantification

was repeated at least 400 times on smaller (4 x 4 x 4 µm) volumes extracted from

random locations within each cathode. Based on these data populations, a percentile

bootstrap algorithm was used to estimate the 95% confidence intervals of their

means [312, 313], providing a measure of the error inherent in each microstructural

Table 4.2: Detailed LSM-YSZ reconstruction parameters of the composite cathode models shown in Fig. 4.12. Dimensions and volumes listed are those used for analysis after all relevant cropping of the acquired data.

Sample	Total vol. (μm^3)	Voxel resolution (nm)			Bounding box (μm)		
		x	y	z	x	y	z
Air	2951.5	13.9	17.6	20.0	27.4	23.2	4.6
Air-Cathodic	4729.1	33.9	43.0	20.0	23.5	27.6	7.3
H_2O-Anodic	2011.7	16.2	20.5	20.0	24.3	19.6	4.2
H_2O-Cathodic	6359.3	19.5	24.7	20.0	26.4	19.9	12.1

quantification, and it is this value that is used as the error bar in the subsequent plots.

4.2.1.1 Volume and surface quantifications

Figure 4.13 reports a number of volumetric and surface quantifications for each sample. The volumetric phase fractions, as well as the overall porosity were determined and are shown in Fig. 4.13a. The cathodes in all samples are majority porous, and there is very little difference between the phase fractions of *Air* and *Air-Cathodic*, indicating that polarization alone does not significantly affect the phase distribution. The H_2O samples show differences however, primarily with lower porosity and an enhanced fraction of YSZ, particularly in the *H_2O-Cathodic* sample.

This effect is further pronounced in Figure 4.13b, which shows the solid phase fraction. All samples except for *H_2O-Cathodic* have solid fractions identical (within error) to what is expected from the source materials. In *H_2O-Cathodic*, the ratio of YSZ to LSM is significantly higher. It is important to note that because phase
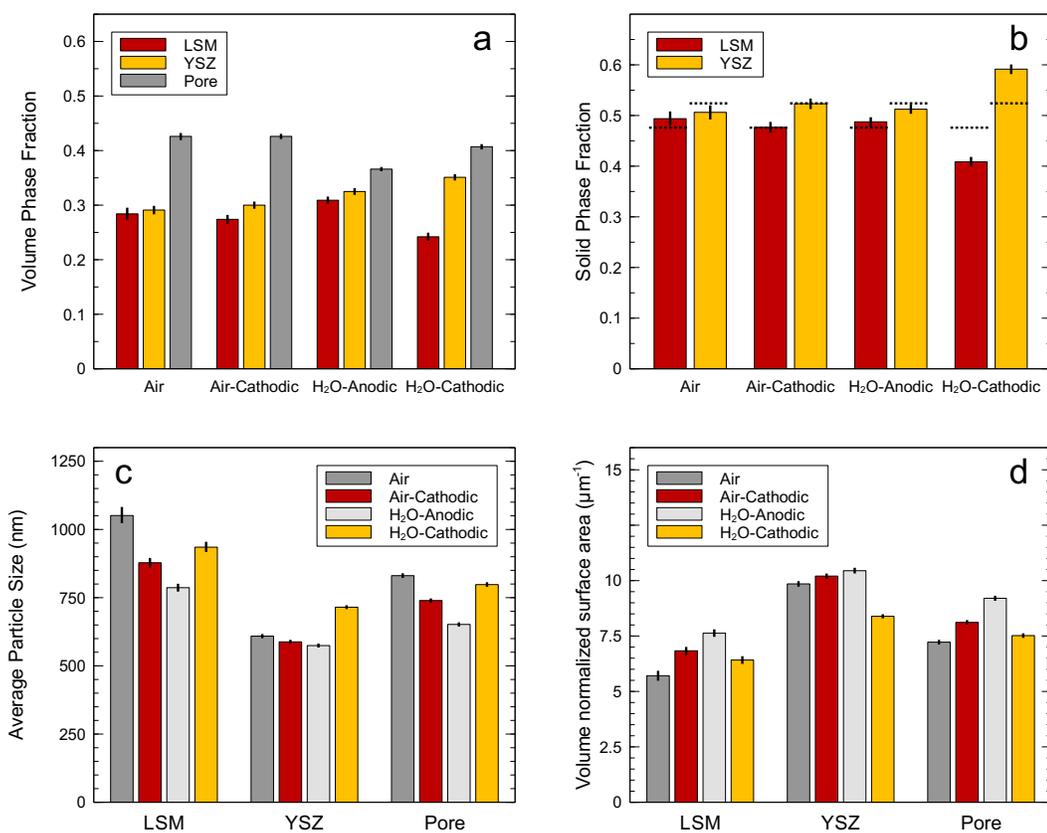
Figure 4.13: Comparisons of various phase properties measured from the reconstructed volumes. (a) Volume phase fraction of each phase within the volume, (b) Solid phase fraction (percentage of solid phase that is LSM vs. YSZ); the expected ratio is indicated on each bar by the dotted line, (c) Average particle size as calculated by the BET method, (d) Volume normalized surface area. In each plot, the solid vertical lines are the 95% confidence intervals for the mean, calculated with a percentile bootstrap algorithm using 100,000 bootstrap samples.

segmentation is based solely off of image contrast, other phases or cation diffusion that causes a particle to appear brighter could cause it to be attributed to the YSZ phase. Regardless, there is a significant change in the solid volume fractions of this sample after cathodic polarization in a humid environment.

Figure 4.13c-d report quantifications derived from a surface generation of each phase. The average particle diameter (as calculated using the BET method) is shown in Fig. 4.13c and confirms that the LSM particles in all samples are much larger than YSZ. Across samples, there does not appear to be a correlation between particle or pore size and either polarization or humidity. This finding is mirrored in the volume normalized surface area calculated for each phase (Fig. 4.13d). Again, no clear trend is observed in this result.

Beyond an analysis of bulk parameters, it is illustrative to examine how the phases present are distributed throughout the cathode layer. Non-uniform distributions in phases and porosity would have substantial implications on the number of accessible sites for the ORR, and have indeed been previously observed in SOFC cathodes [112]. Intentionally creating these sorts of distributions has also been proposed as a more efficient means of distributing the active area within composite cathodes [314]. The phase fraction of each material is plotted as a function of distance from the electrolyte-cathode interface in Figure 4.14. The dashed line in each plot represents the average value throughout the volume, reported in Figure 4.13a. As can be seen, there is no significant evolution in phase fraction as a function of distance in any of the samples. The small deviation observed in Figure 4.14a at 22 μm is due to the presence of two larger LSM particles that happened to coincide,
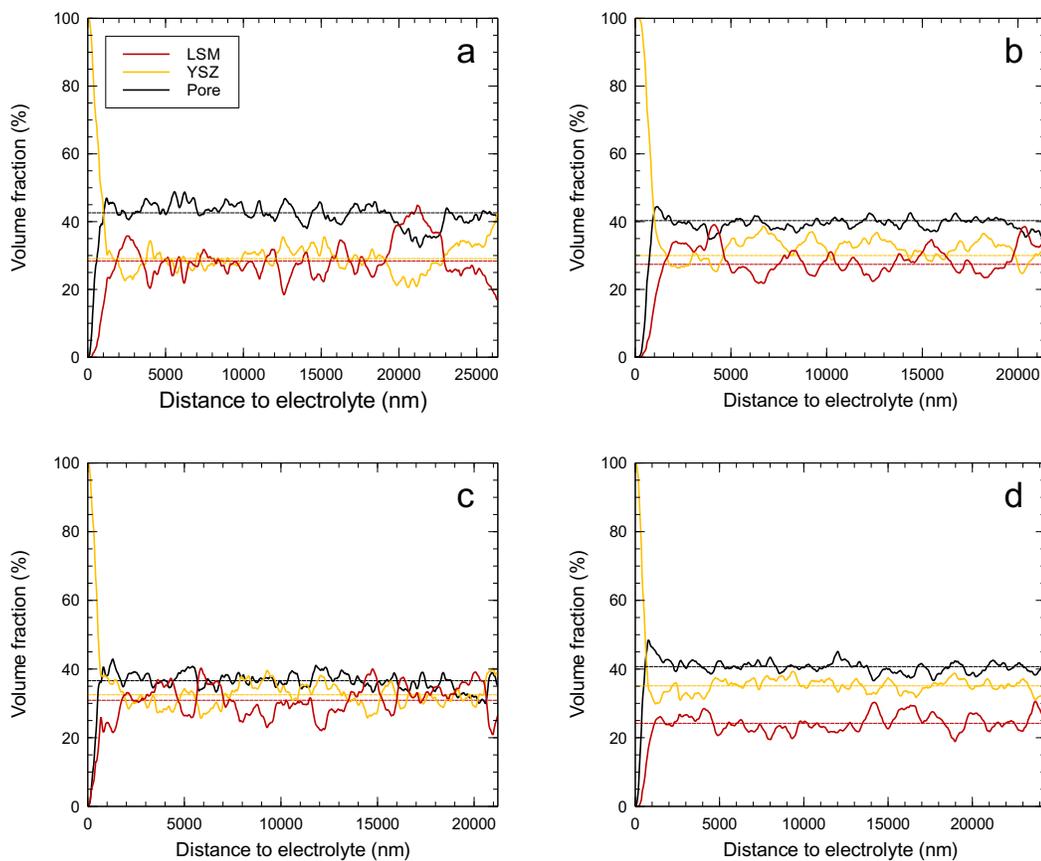
Figure 4.14: Graded phase fraction plots. These plots show the volume fraction as a function of distance through the cathode, normal to the electrolyte-cathode interface. The "bulk" phase fraction (Fig. 4.13a) is represented for each material by a dashed line. Red represents LSM, yellow is YSZ, and black is pore. The samples are (a) *Air*, (b) *Air-Cathodic*, (c) H_2O-*Anodic*, and (d) H_2O-*Cathodic*.
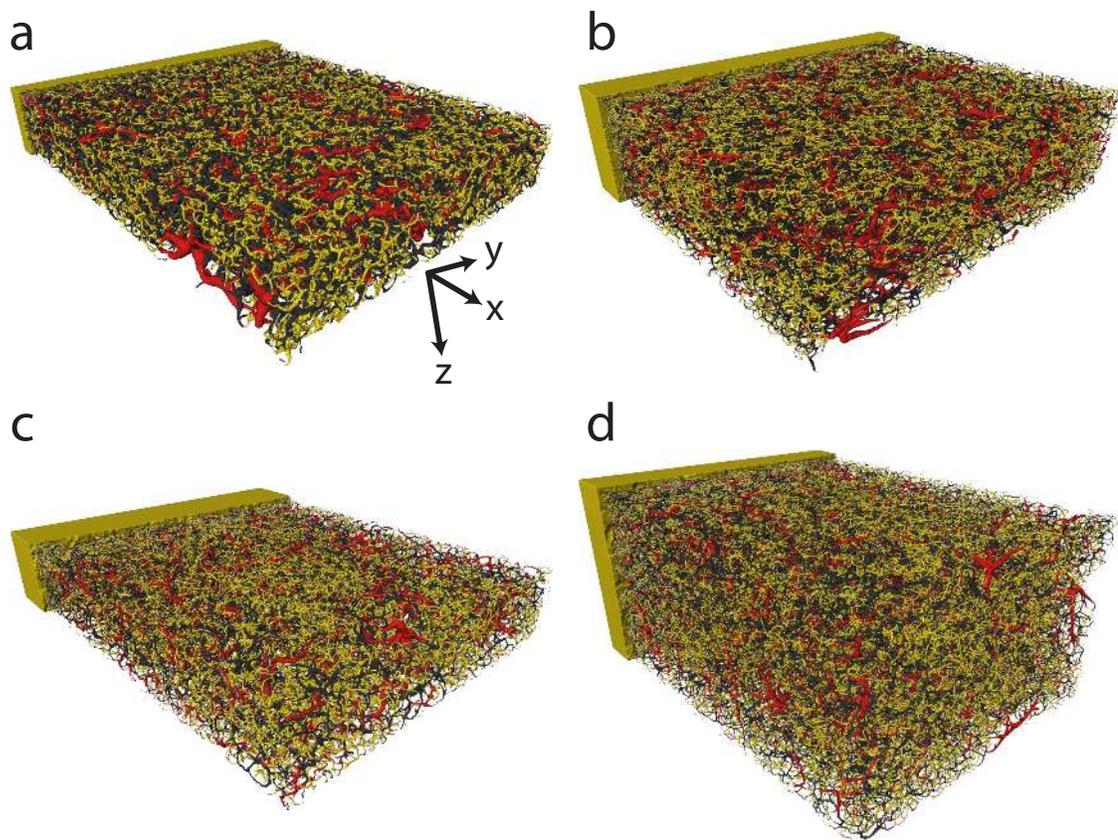
Figure 4.15: Representative visualizations of four LSM-YSZ composite cathodes, after reduction into skeletonized networks. Colors and scale are the same as Fig. 4.12. Networks were calculated in *Avizo Fire* by thinning each phase until a connected path with single voxel thickness is obtained. The thicknesses displayed in the figure are a visualization of the centerline distance map (*i.e.* the amount of material removed to obtain the thinned network). The samples are (a) *Air*, (b) *Air-Cathodic*, (c) H_2O-*Anodic*, (d) H_2O-*Cathodic*.

and the phase fraction quickly reverts back to the mean. This indicates that on the

time scales of this study, polarization and humid environments have little effect on

the distribution of phases throughout the cathode layer.

4.2.1.2   Phase connectivity and network analysis

From the three-dimensional volume reconstructions, skeletonized phase networks were calculated using thinning algorithms available within *Avizo Fire*, result-
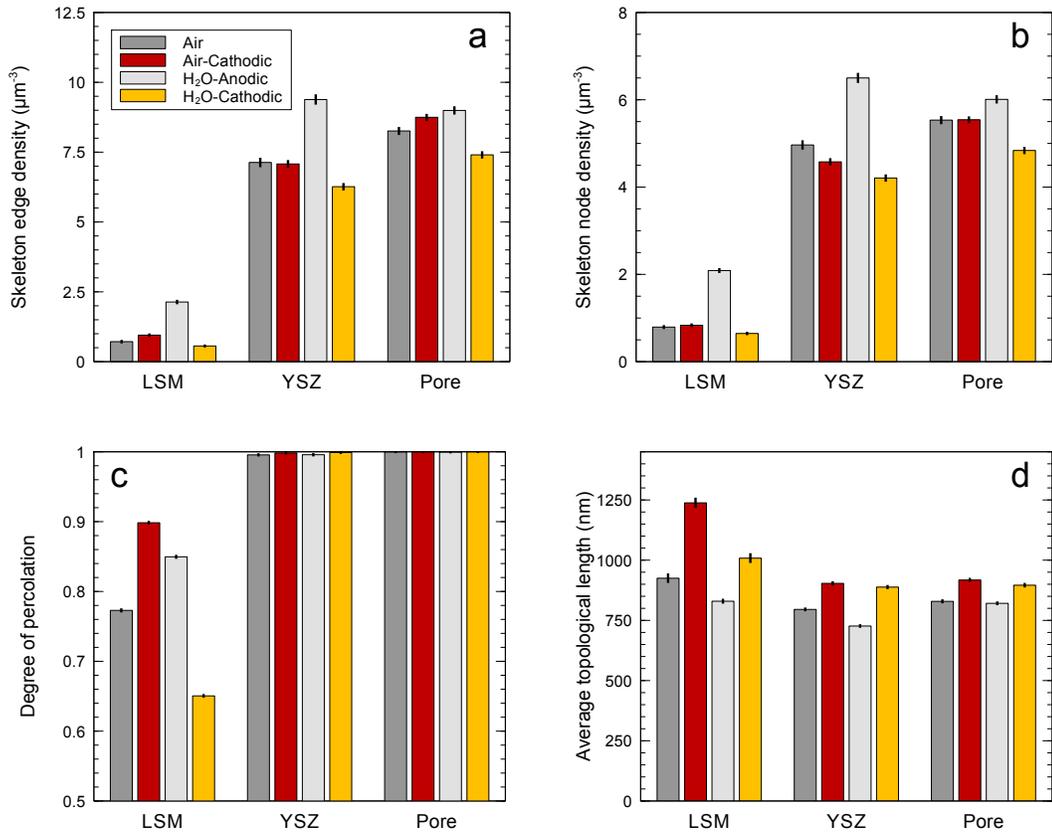
Figure 4.16: Comparisons of connectivity parameters, derived from the skeleton models of the composite cathodes. (a) The density of skeleton edges (E/V) and (b) nodes (N/V) provide insight into the complexity of each individual phase network. (c) The percolation degree (p) represents how well percolated each phase is throughout the volume. (d) Average topological length ($\overline{L}$) gives an indication of the average uninterrupted length an ion or gas molecule might be able to travel throughout a phase (similar to a mean free path).

ing in a single voxel network that represents the connectivity of each phase. A distance map is also calculated at every point of the skeleton, giving a measure of the thickness of the phase at every location in the phase network. This value can be used to generate a visualization of the skeleton networks, as shown in Figure 4.15.

A number of useful statistics from these networks can be easily calculated by examining the length of the discrete paths that comprise each network, as well as

their interconnectedness, as described in Section 4.1.2.2. The calculated parameters are reported in Figure 4.16. It is clear from Fig. 4.16a-b that the LSM networks in all samples consist of significantly fewer nodes and edges than the other phases, even though the LSM volume fraction is near to that of YSZ (Fig. 4.13). This result, combined with the finding of much lower surface area for LSM confirms that overall the LSM network is comprised of larger particles with simpler geometry than those of the pore and YSZ networks. This agrees with a dynamic light scattering inspection of the source material, which found the LSM and YSZ particles to be in a bimodal distribution with average LSM and YSZ particle diameters of approximately 800 and 150 nm, respectively. The smaller YSZ particles agglomerate into a more complex interconnected network, while many of the larger LSM particles remain isolated. This result further agrees with the connectivity analysis of Fig. 4.16c.

Between samples, an obvious trend in node or edge density is not apparent. All phases in the *H₂O-Anodic* sample have higher densities, but this may be an artifact of the smaller volume acquired for this sample. Because nodes (and edges) will inevitably exist at the boundaries of the volume, a higher overall surface area to volume ratio of the acquired volume's bounding box will artificially inflate volumetric measures, which appears to be the case for *H₂O-Anodic*. Besides this sample, there appears to be little difference in edge or node density between *Air*, and *Air-Cathodic*, again indicating little impact on this measure from polarization alone. For all phases, *H₂O-Cathodic* has values of *E/V* and *N/V* close to, but slightly lower than the samples aged in dry air, indicating that humid cathodic polarization *may* lower the complexity of the phase networks by reducing the number of edges and nodes needed

to describe the network.

Figure 4.16c shows the degree of percolation for each sample and phase. In all samples, both the YSZ electrolyte and pore structure are completely percolated, meaning that almost all the material of these phases is interconnected. Sample aging environment or polarization had little to no effect on this parameter. The LSM electronic conducting phase is much more poorly connected, with a p_{LSM} value significantly lower than unity in all samples. This indicates many disjointed graphs within the phase network, which has negative implications for the activity of the triple phase boundaries due to the limited distance electrons are able to travel within the LSM phase. Variation between samples in p_{LSM} is attributed to the specific volumes analyzed containing variously sized LSM particles, rather than a difference due to sample aging environment or polarization. Larger reconstructed volumes would be expected to reveal similar p_{LSM} values for all four conditions tested.

The average topological length ($\overline{L}$) for all conditions and phases is shown in Figure 4.16d. This is an averaged parameter that gives an indication of the mean "straight-line" distance that exists between nodes of a given phase. In a basic sense, it can be interpreted as a geometric mean free path, (i.e. without taking into account material properties) the average distance a particle or molecule would be able to travel before reaching an obstruction such as the end or branching of a path. A lower value for $\overline{L}$ would indicate a more complex connectivity for a phase, with more branching (and likely more potential sites for the ORR). While the values of $\overline{L}$ are similar amongst all conditions, the values are consistently higher for all phases in the samples receiving cathodic polarization, when compared with their counterpart

215

(*e.g. Air* vs. *Air-Cathodic*).

In particular, the $\overline{L}$ of LSM in the *Air-Cathodic* sample was significantly higher than the others. Recalling the definition of $\overline{L}$ (Eq. 4.2), and considering that this sample's node density (Fig. 4.16b) is not significantly different than the others, it can be determined that the increase in $\overline{L}$ corresponds to longer individual paths for the LSM within *Air-Cathodic*, even though average particle size is not substantially larger (Fig. 4.13c). This suggests a "simpler" LSM network that is not as well interconnected, which would serve to limit electronic transport in the cathode. Values for the topological length have not been reported previously on LSM-YSZ cathodes, but the values found here are on the same order as those measured for different SOFC material systems ($\overline{L}$ has been reported to range from 0.20 to 0.28 µm in lanthanum strontium cobalt ferrite (LSCF) samples [315], and from 1.50 to 2.67 µm in Ca-doped lanthanum manganite(LCM) samples [106]).

4.2.1.3 Tortuosity analysis

The tortuosity (τ) of the various phases within the cathode layer can significantly impact the transport of both gaseous and ionic species. By comparing the geodesic and euclidean distances for each sample, phase, and direction, the relative difficulty of a molecule, ion, or electron moving through the convoluted porous structure can be estimated (see Fig. 4.7). The results of the tortuosity calculations are shown in Figure 4.17. Fig. 4.17a reports the results of the raw tortuosity, while Fig. 4.17b is the tortuosity ratio (proportional to D_{eff}), as defined in Section 4.1.2.3.

216
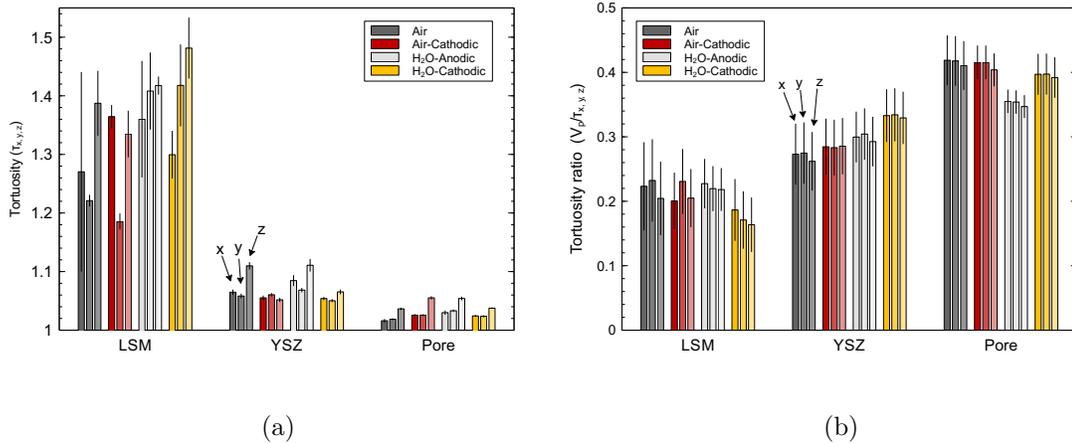
Figure 4.17: Tortuosity (a) and tortuosity ratios (b) for each phase, sample, and direction. The tortuosity ratio is related to the expected effective diffusivity (conductivity, etc.) for each phase. For each sample and phase, the values are plotted as $[x, y, z]$ in similar colors. Besides LSM, there is little variation in tortuosity and ratio in all directions, indicating that this is likely an isotropic property in these cathodes. The specified error bars are $\pm$ one standard deviation of the data within the final 25% of each τ profile.

Immediately it is clear from Fig.4.17a that the LSM phase has much higher τ values in all samples and in all directions than the YSZ and pore networks. This is primarily due to the poor connectivity of the overall LSM network, leading to exceedingly long (and in some cases, abruptly terminated) geodesic pathways through the volume. This effect is also made apparent by the large anisotropic variation of τ for LSM. Large and isolated particles, as were observed in the reconstruction, will cause significant deviations in the tortuosity depending on their orientation, leading to substantial variation in τ_x vs. τ_y vs. τ_z. In both YSZ and the pore space, the τ values are very similar between samples and in every direction. Generally in these two phases, it appears that $\tau_x \approx \tau_y \approx \tau_z$. τ_z is in all cases slightly larger than the other dimensions, due to the limited sampling size in that dimension. Comparing the overall τ profiles (as in Fig. 4.18), reveals that the τ values for each dimension

217

are approximately equal at similar L_E magnitudes. The tortuosities of the YSZ and pore phases are very isotropic, and for the time scales and environments used in this work, there appears to be no significant impact of H_2O or polarization on tortuosity.

The tortuosity ratio is derived from the raw tortuosity values and is plotted in Fig. 4.17b. Due to the similarity of the raw values, the variation in tortuosity ratio is primarily a function of the volume phase fraction measurements. η/τ follows the general trends that would be expected, with very low values for LSM. Because of the larger volume fraction, η/τ is larger for YSZ in the *H$_2$O-Cathodic* sample than all the others. In the pore network, *Air* and *Air-Cathodic* are practically identical while *H$_2$O-Anodic* and *H$_2$O-Cathodic* follow the same trend as the volume fraction previously reported. Within error, there appears to be little significant variation in these values as a function of H_2O or polarization.

To illustrate the differences in the nature of τ for each phase, the tortuosity profiles for each phase and direction of the *H$_2$O-Cathodic* sample are plotted in Figure 4.18. The pore and YSZ profiles follow the expected nature of increased τ at very small L_E values, that decreases as the distance is increased. The profiles for each of the phases are very isotropic, and all reach a stable value within the sampled volume. The LSM profiles reveal the origin of the significantly higher values reported in Fig. 4.17. Because this phase is poorly connected, the shortest pathway available to a mobile species (electron) is extremely tortuous. The impact of a poorly connected large particle is particularly evident in the y direction profile at $L_E \approx 12\,\mu m$, giving rise to a sudden spike in τ_y. Additionally, beyond a certain L_E, there is no continuous pathway for the LSM within the sampled volume. These

218
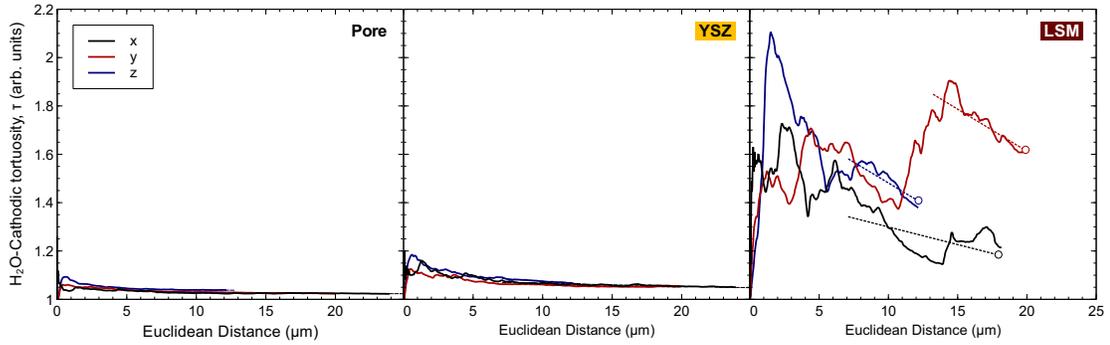
Figure 4.18: Examples of the tortuosity profiles in the x, y and z directions for each phase in the H_2O-*Cathodic* sample. The plots are all shown on the same scale to facilitate comparison between the phases. The LSM profiles end at a considerably smaller L_E than the others because this phase lacks a continuous pathway through the whole volume, causing τ to become infinite at these points due to the limited sample volume (physically, it is likely just extremely high). The pore and YSZ phases are observed to have isotropic tortuosity profiles of expected shape, given their high degree of percolation throughout the volume. The dashed lines (clearest in the LSM plot) represent the linear fit used to determine the average τ value at the end of each profile. The hollow circle is the τ value reported in Fig. 4.7c.

profiles definitively show that in these cells, LSM is the limiting factor for charge transfer.

4.2.1.4   Triple phase boundary calculations

The TPB points within these composite cathodes allow for the ORR (Eq. 1.3) to take place. In order for this reaction to occur however, the phases surrounding the TPB must be well connected and percolated throughout the entire cathode, allowing for conduction of electrons from the electrode, O_2 from the air, and oxygen ions through the electrolyte. Without these conditions, the TPB point will be electrochemically inactive and will not contribute to the overall performance of the cell. The volumetric density of the TPB network and its activity fraction within

each sample provide critical insight into how the microstructure of each cathode is expected to impact the efficiency and operation of the cell. These measurements have been made using the methods introduced in Section 4.1.2.4.

In each of the cathodes tested, the LSM phase again was the limiting material due to its poor connectivity. Analysis of the connected components revealed the pore and YSZ phase networks to be almost completely percolated (predominantly consisting of one large connected component), while the LSM network had a significantly larger fraction of isolated components. For example, the LSM phase in *H₂O-Cathodic* had 23/61/16 vol.% isolated, percolated, and dead-end components, respectively. The results for other samples were similar, with a smaller fraction of isolated components classified as percolated due to the smaller z dimension in these particular reconstructions (see Table 4.2).

The results of the ρ_{TPB} and TPB activity calculations are shown in Figure 4.19. The error bars on these plots were obtained using a bootstrapping algorithm, as discussed previously. The TPB networks were cropped using 500 random sub-volumes of $64\,\mu\mathrm{m}^3$, and both ρ_{TPB} and the activity fraction were calculated independently for each volume. Based on these results, the 95% confidence interval of the mean was calculated, and is displayed as the error bars in Fig 4.19. The most striking observation is the similarity between the *Air* and *Air-Cathodic* samples in both Fig. 4.19a and 4.19b. *Air-Cathodic* has very similar ρ_{TPB} and active fraction values to *Air*, indicating little dependence of the TPB density or activity on polarization alone. This suggests it is the presence of environmental contaminants that will significantly alter the TPB microstructure in these LSM-YSZ cathodes. The presence of 3% H_2O
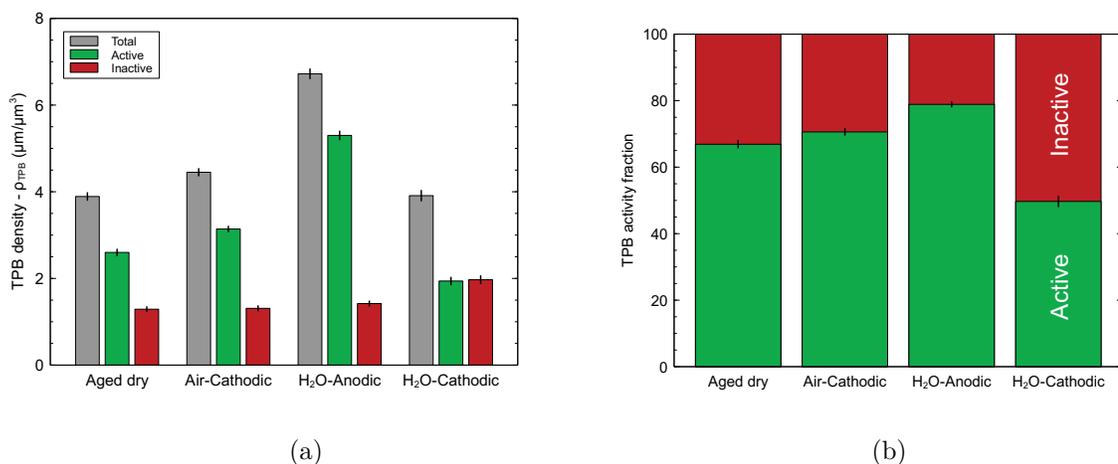
Figure 4.19: Triple phase boundary (TPB) calculations. (a) Total, active, and inactive ρ_{TPB} for each sample. Density is relative to total cathode phase volume (including pore). (b) Active vs. inactive TPB fractions, comparing relative activity of TPB networks between samples.

reveals a significant impact on the both the density and activity of the triple phase network. Under humidified anodic polarization, the total ρ_{TPB} and activity increase slightly in comparison to the samples aged in dry air. With cathodic polarization however, a significant change is observed in the active fraction of TPB path lengths, dropping to approximately 50% (with a relatively unchanged total ρ_{TPB}).

To ensure accurate interpretation of the data, it is important to consider how the methodology used to measure TPB activity may unintentionally bias the results. Due to the limited sampling volume available with the FIB/SEM technique, the definition of activity used in this work (and many others) is an estimate that relies upon the degree to which the three intersecting phases are connected to the volume boundaries. Consider the two limiting scenarios for the cathode volume reconstructions: At the lower limit, a sufficiently small sampled volume would be expected to result in a TPB network that is 100% active, because even a very dis-

221

continuous phase could appear to be well connected if the sampled volume is small enough. At the higher limit, it is easy to imagine a case where a poorly connected phase could result in no paths being considered "active," if the sampled volume is very large. Thus, it is clear that the magnitude of the sampled volume can have a substantial impact on the measurement of activity, and it is critical to separate the true microstructural variations from those changes that are induced solely by volume effects.

In this work, the reconstructed cathode volumes ranged from 2012 to 6359 μm^3 (Table 4.2). *H_2O-Cathodic*, the largest volume acquired, was found to have the lowest TPB activity as well, raising suspicions that the observed difference may originate from the larger volume sampled, rather than a true microstructural difference. To analyze this, the *H_2O-Cathodic* dataset was split into smaller volumes, and each was reanalyzed for TPB activity independently. In the full dataset, the z direction (slicing direction) bounding box length was 12.10 μm. To better match the other samples, the overall volume was split into two sub-volumes (each with $z \approx 8\,\mu m$), and then again into three sub-volumes (with $z \approx 4\,\mu m$), resulting in a total of six "subsamples" with varying total volume. A connected components analysis was conducted to determine the activity fraction for LSM (since it was the limiting phase) for each subsample, which was plotted as a function of the total cathode bounding box volume.

The results of this analysis are presented in Figure 4.20. In Fig. 4.20a, volume renderings of the LSM phase in three of the subsampled volumes are shown, each with a z dimension one-third that of the original volume. The connected compo-
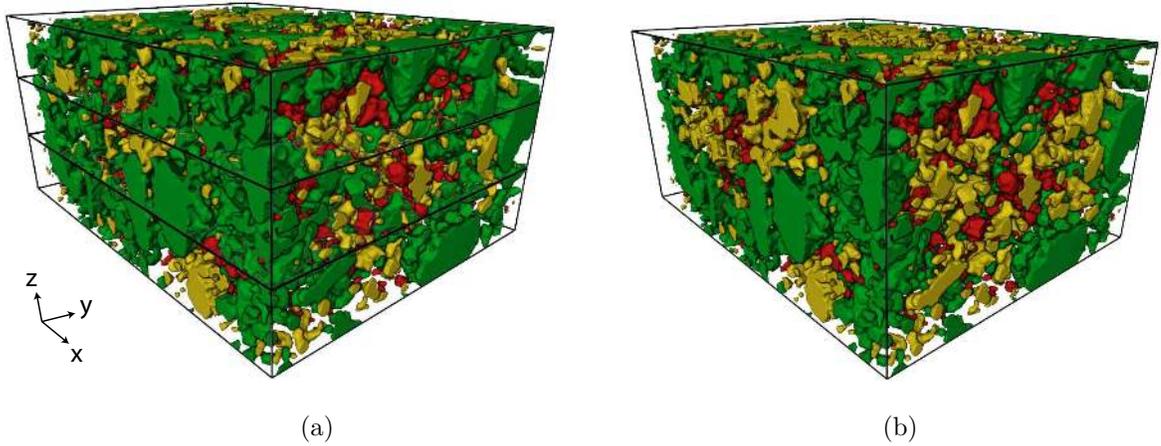
Figure 4.20: Volume renderings of LSM phase in the H_2O-*Cathodic* sample, colored by their connectivity (similar to Figure 4.11c). In (a), the total volume ($z = 12\,\mu m$) was split into three smaller volumes ($z = 4\,\mu m$), and the LSM activity was calculated independently for each volume. In (b), the whole volume was used to determine LSM connected component activity. In both figures, the color of the phase represents the expected activity: green – *active*, yellow – *unknown*, and red – *inactive*.

nent analysis from the whole volume is shown in Fig. 4.20b. In these figures, the LSM particles are colored by their expected activity, determined as described in Section 4.1.2.4. As should be expected, there are substantially more particles determined to be active (green) in the subsampled data (Fig. 4.20a) due to the decreased aspect ratio between the z and x-y dimensions, which raises the probability that a given particle will intercept a face of the bounding box. This increase in active LSM particles demonstrates the significant impact that a reduced volume can have on the overall activity measurement.

Figure 4.21 investigates the results of the sub-volume analysis in more detail. In Fig. 4.21a, the active volume fraction for LSM (f_a) (i.e., what fraction is green, in Fig. 4.20a) of each sub-volume is plotted against the total bounding box volume for the sub-volume (V_{BB}). The point at $x = 6359\,\mu m^3$ represents the full sampled
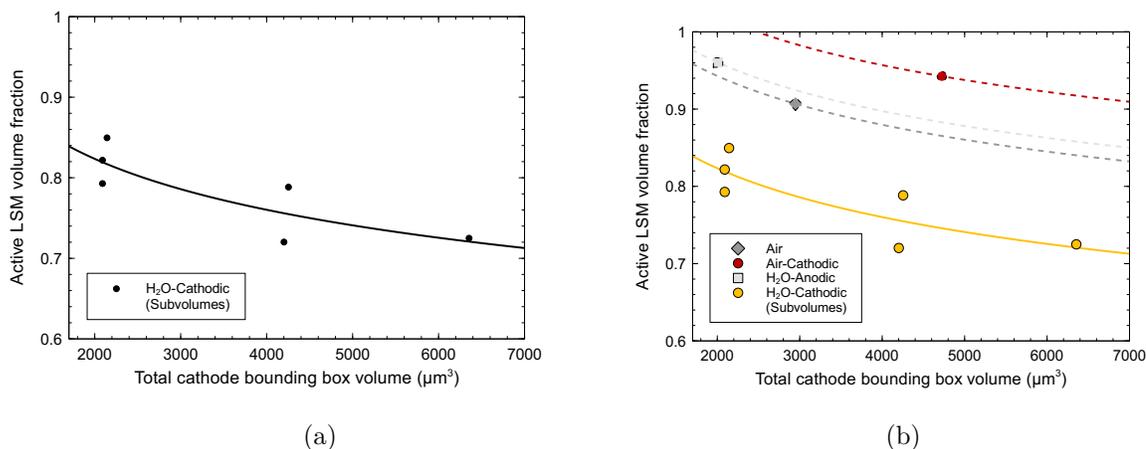
Figure 4.21: (a) Active LSM volume fraction (f_a) measured as a function of total cathode bounding box volume (V_{BB}). As the bounding box volume decreases, activity of the LSM increases due to the definition used for "activity." An empirical relationship of $f_a = 1.98\,V_{BB}^{-0.12}$ was measured for this trend. (b) A reproduction of the data in (a), together with the (V_{BB}, f_a) data for the full volumes of the other three samples measured in this work. The same empirical relationship is plotted through each of the additional points to demonstrate how their f_a values would be expected to be higher than that of H_2O-Cathodic, regardless of volume sampled.

volume. As suggested by Fig. 4.20, as the V_{BB} decreases, the volume fraction of LSM connected components determined to be active increases. From this data, an empirical relationship can be determined to predict how the magnitude of an acquired volume will affect its measured activity (Fig. 4.21a). With this relationship, the difference in activity between samples of varying volume can be more easily compared. Figure 4.21b shows the H_2O-Cathodic data, along with the same sort of measurement obtained for the three remaining samples. This plot shows that even at volumes comparable to those acquired for *Air*, *Air-Cathodic*, and *H_2O-Anodic*, the *H_2O-Cathodic* sample had significantly lower activity, indicating that the lower TPB activity observed in Figure 4.19b is due to true microstructural differences, and not to volume sampling artifacts.

4.2.1.5 Quantification summary

Overall, the vast majority of the microstructural parameters analyzed in these samples revealed little change with respect to humidification and applied polarization bias. A few particular parameters however, showed some distinct differences. In all samples, the LSM was determined to be the transport limiting phase on account of its poor connectivity and high tortuosity. In the H_2O-*Cathodic* sample, the solid phase fraction of YSZ was observed to be unexpectedly higher than normal, which in turn led to a higher value of η/τ. Finally, the $f_{a,\mathrm{TPB}}$ (active ρ_{TPB} fraction) was significantly lower in the H_2O-*Cathodic* sample as well, suggesting fewer well-connected sites for the ORR in this cathode.

4.2.2 Relationship to cell performance

While the specifics of the electrochemical measurements from these samples are not provided in this thesis, a few of the general findings are mentioned to enable a comparison to the microstructural results. These results were obtained by a collaborator in the Wachsman laboratory (C. Pellegrinelli), whose thesis should be consulted for further detail.

Generally speaking, as with the microstructural findings of this work, few dramatic changes were observed in the electrical measurements of these four samples. In all samples, the series resistance of the cell was observed to increase monotonically over time, regardless of applied bias or environmental condition. This indicates that changes in the electrolyte resistance can not generally be expected to be a function

of the testing conditions, further implying that the LSM and the TPB sites will likely be the source of accelerated performance degradation.

Measurements of the total polarization resistance (R_p) in these samples indicated that R_p decreased over time for both the *Air* and *H$_2$O-Cathodic* samples, while increasing for *Air-Cathodic* during the test duration, suggesting that the presence of H$_2$O modifies (in a positive way) the manner in which oxygen is reduced at the cathode. Unfortunately however (for this study), the vast majority of the changes measured via EIS were observed to be reversible upon the removal of the bias or the H$_2$O environment. Since the FIB-*nt* characterization occurs *ex-situ* post-EIS testing, reversible changes would not be expected to be captured in the results presented here.

With respect to the microstructural results, there is fairly little evidence to explain the decreased R_p (increased performance) observed for the *Air* and *H$_2$O-Cathodic* samples. This is perhaps to be expected given the reversible nature of the performance changes. Throughout all the tests performed, *H$_2$O-Cathodic* consistently had the lowest R_p values, even though this sample had the lowest activity fraction for TPBs. This would suggest potentially a lower threshold value for TPB activity (lower than the 50% value measured here), which must be reached for adverse effects to be observed.

Regardless, the comparison of the microstructural parameters to the electrochemical performance indicate that at the conditions used in this work, little significant permanent degradation occurred. This is the case for both electrochemical behavior and microstructure as well. To definitively characterize the impact of water

on the microstructure, further degradation testing that shows irreversible changes in the impedance characteristics of the cell would be necessary.

4.2.3   Analytical TEM analysis of LSM-YSZ cathodes

While the FIB/SEM characterization of the previous section provides a thorough quantification of the overall microstructure of the cathode layer, it cannot supply a detailed picture of elemental distributions or fine changes in chemistry. To obtain this sort of information, a chemical analysis was performed using TEM-EELS and EDS.

The first such analysis was performed on a sample aged under the H_2O environment, but not subject to polarization bias. EDS data was collected from a YSZ-YSZ grain boundary within the composite cathode using an ChemiSTEM instrument, provided courtesy of FEI Company (Hillsboro, OR). The results of this data collection are presented in Fig 4.22. Elemental maps for each constituent element are shown, with the Mn, La, and Y distributions providing the most interesting information. A clear enhancement of the Mn and La signals is evident at the YSZ grain boundary and (to a lesser degree) at the YSZ surfaces. This indicates that La and Mn form mobile species during the operation of the cathode, and preferentially deposit at the surfaces of the YSZ (and do not appear to diffuse into the particles). Such mobility is not observed for the Sr cations, which appear to remain within the LSM grain the top left corner of the maps.

Also of interest is the apparent reduction in Y concentration in the upper-
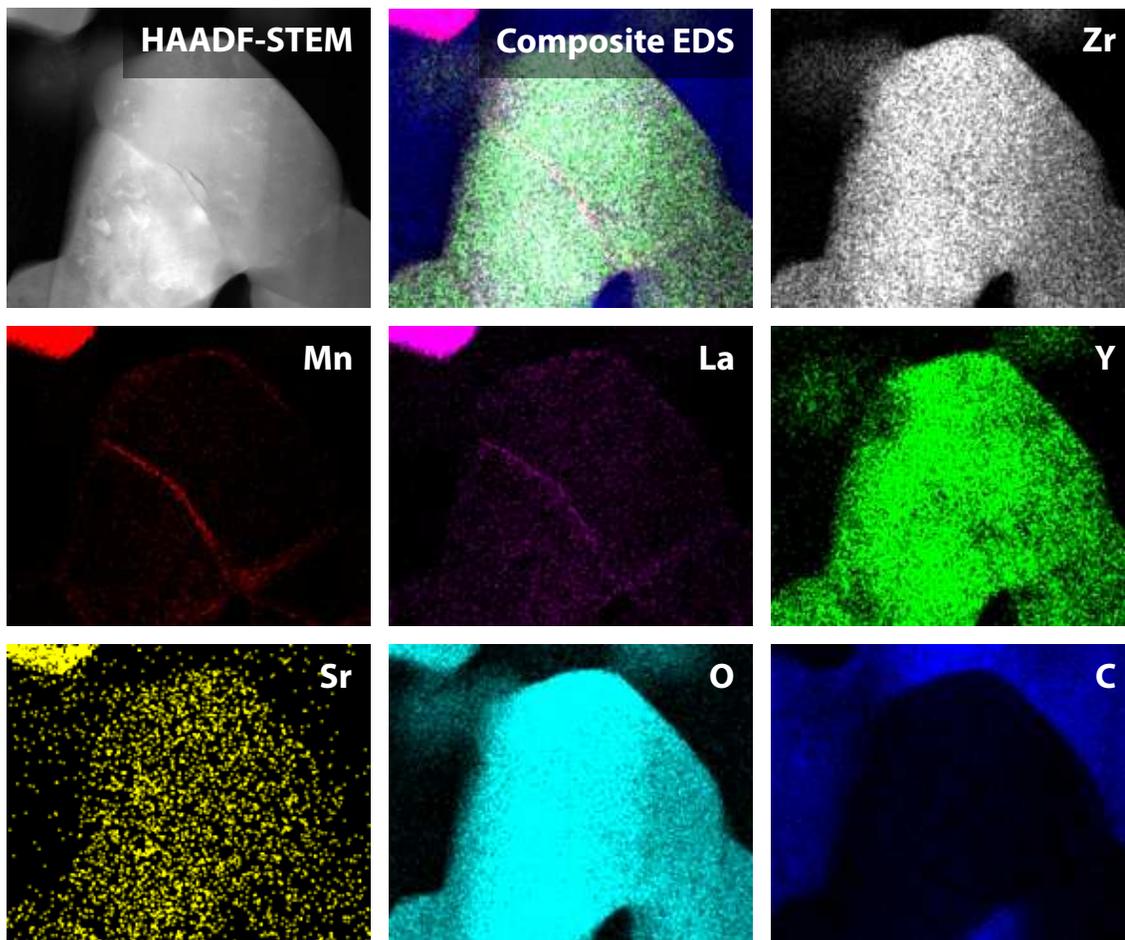
Figure 4.22: TEM-EDS of a YSZ grain boundary in an H_2O aged composite cathode (no bias applied). A small piece of an LSM particle is visible in the top-left of each image. The HAADF-STEM signal from the area is shown in the top-left, and the composite color map of the whole sample (excluding the O map) is shown in the top center. Each subsequent map is a single elemental map showing the relative strength of the X-ray signal. La and Mn are clearly visible at the YSZ grain boundary, and parts of the YSZ grain are Y-deficient. The collected data was acquired from an area with width and height of 300 nm. Data acquired using an *FEI ChemiSTEM* courtesy of FEI Company (Hillsboro, OR).

left of the central YSZ grain. Compared with the Zr map, there is a significantly reduced signal in this area, demonstrating that Y ions can also be mobile within the cathode layer. The Y ions are not observed to preferentially redeposit in any particularly unexpected locations, however. Segregation of Mn cations has been previously observed under humidification, but the migration of La ions was not reported [92]. Such migration of La and Mn was not observed in the *Air* aged sample, confirming previous arguments in the literature that H_2O provides a pathway for cation migration in LSM-YSZ cathodes. The removal of Mn and La from the LSM is likely to have significant effects on the active contact area between LSM and YSZ, as well as on the gas adsorption kinetics. Of note is the fact that none of the commonly found secondary phases (such as $SrZrO_3$ or $La_2Zr_2O_7$) were observed in these cathodes, suggesting distribution of the cations in a solid solution, as opposed to distinct secondary phases.

Further chemical analysis of the *H_2O-Cathodic* sample was achieved through the use of TEM-EELS, which enabled investigations of chemical state and cation valency. In Fig 4.23, a detailed probe of the O-*K* edge at the boundary between LSM and YSZ is shown. The O-*K* edge (and its fine structure) reflects the atomic projection of the unoccupied density of states onto the sampled oxygen atoms. Previous studies on this system have revealed a triplet structure for the O-*K* edge in LSM, and an asymmetric doublet (at higher onset energy) for YSZ [316]. These features are reproduced exactly in the data presented in Fig. 4.23, confirming the bulk compositions of LSM and YSZ using only the O-*K* signal.

Using the spectral unmixing methodologies introduced in Sec. 2.1.2.2, a third
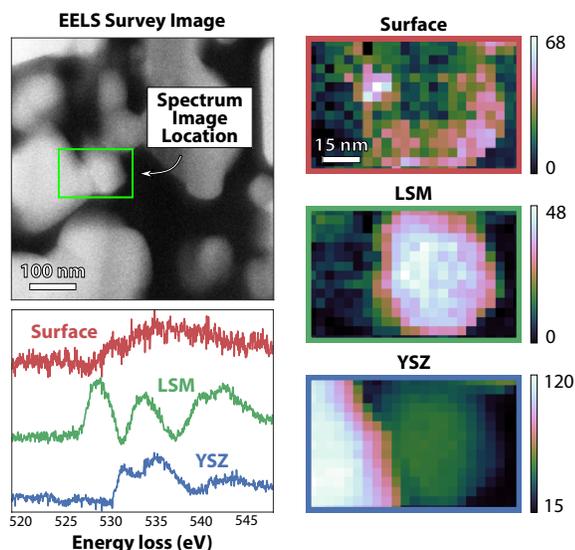
Figure 4.23: EELS spectral unmixing analysis of the O-K edge at a triple phase boundary in the H_2O-*Cathodic* sample. LSM and YSZ are identified by their distinct oxygen spectral signatures (green and blue, respectively). A third component to the signal was identified at the surfaces of the LSM and boundary with the YSZ, associated with oxygen vacancies [222].

component (red) was identified in the data that was preferentially localized to the surface of the LSM and its boundary with YSZ. The spectral signature of this component is characterized by its generally broad character and lack of distinctive peaks above the edge onset. Such features indicate a lack of scattering from $O-O$ second nearest neighbor interactions, and typically result from oxygen-deficient environments [222]. The shape of this signal, as well as its location at the particle surfaces, strongly hint at an abundance of oxygen vacancies ($V_O^{\bullet\bullet}$) at the surface of the perovskite LSM. High concentrations of $V_O^{\bullet\bullet}$ would serve to encourage oxygen incorporation at the electrolyte/cathode interfaces, and their presence may help explain the increased performance (lowered R_p) observed during aging of the H_2O-*Cathodic* sample.

In addition to the H$_2$O non-biased sample (Fig. 4.22), segregation of Mn and
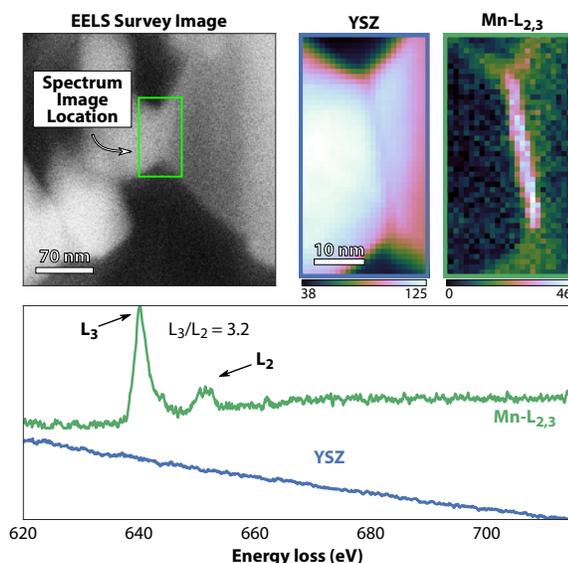
Figure 4.24: EELS unmixing of the Mn-$L_{2,3}$ edge at a YSZ grain boundary in the H_2O-*Cathodic* sample. The decomposition produces two definitive components attributable to the YSZ background and the Mn-$L_{2,3}$ edge (blue and green, respectively). The ratio of the Mn-$L_{2,3}$ edge peaks is 3.2, indicating Mn is in an average $Mn^{2.5+}$ valence state at the grain boundary [317].

La to the YSZ grain boundaries was observed in the H_2O-*Cathodic* sample as well, indicating that such cation migration occurs regardless of polarization applied to the cell. A detailed analysis of the fine structure of the Mn-$L_{2,3}$ edge is presented in Fig. 4.24 (for the sake of brevity, the La signal is omitted from this section). This EELS spectrum image was acquired from the region surrounding the boundary between two YSZ grains.

Spectral decomposition of the data revealed a background component and a single Mn contribution, which is prototypical of the Mn-$L_{2,3}$ edge. The Mn was entirely localized at the interface of the YSZ grains, with some slight intensity extending onto the outer surfaces of the particles. The lack of Mn signal within the YSZ grains indicates a surface-mediated transport mechanism, rather than a bulk

diffusion of the foreign cations.

Analysis of the relative intensities of the Mn-L_2 and Mn-L_3 edges enables an inspection of the average cation valency. In a typical perovskite Mn coordination, the L_3/L_2 ratio is expected to be approximately 2, reflecting a $Mn^{3+/4+}$ configuration [316, 317]. The interfacial Mn measured in Fig. 4.24 reveals an L_3/L_2 ratio of 3.2, indicating an average Mn valency of $\approx Mn^{2.5+}$. Such a configuration should necessitate a correspondingly higher concentration of $V_O^{\bullet\bullet}$, which was indeed observed in the O-K signal from the same area, similar to Fig. 4.23 (not shown).

Furthermore, using EIS data, Nielsen *et al.* [92] proposed the formation of a volatile Mn^{2+} species via decomposition of LSM at the LSM-YSZ interface in humid environments. No chemical evidence was given for such a species, but its presence explained the electrochemical behavior of the system, and it was expected that the presence of H_2O would enable fast diffusion pathways for Mn^{2+} across the YSZ surfaces. It would appear that the EELS and EDS results from this thesis confirm the presence of such a species located at the surfaces and grain boundaries of the YSZ particles. This process appears to promote the formation of vacancies at the cathode and electrolyte interfaces, which should enhance adsorption and charge transfer in these devices. Such a decomposition of LSM into volatile Mn^{2+} species is eventually expected to deplete the TPB regions of Mn however, meaning that prolonged aging experiments of the samples studied in this thesis might eventually experience performance degradation, even if there is an enhancement during initial cell operation [92].

4.2.4 Conclusions

In this portion of the thesis, the three dimensional reconstruction of four LSM-YSZ composite cathodes aged under polarization and humidification was reported. Generally, most microstructural parameters exhibited little change regardless of the aging conditions, while LSM was found to limit transport in all samples. The H_2O-$Cathodic$ sample had a higher than expected YSZ phase fraction, and a lower active TPB fraction than the other samples, even though its electrical performance was observed to improve during aging in a humid environment. Most of these electrical changes were reversible however, meaning little effect of them would be expected to be observed in post-aging FIB/SEM studies.

Compositional and chemical analysis of the cathode layers revealed some insight as to the origins of the improved performance in the H_2O-$Cathodic$ sample. Regardless of polarization, the perovskite cations (Mn and La) were observed to migrate to the YSZ and its boundaries in the humidified samples. The Mn valency and fine structure of the oxygen EELS signals revealed a high concentration of oxygen vacancies at the triple phase boundaries and the particle surfaces, which would be expected to enhance oxygen incorporation into the electrolyte. Generally however, the conditions used in this work did not induce significant performance or microstructural degradation, and further studies in more extreme environments would be needed to gain a thorough understanding of the mechanisms of degradation in LSM-YSZ cathodes.

4.3   Quantification of LSCF-GDC composite cathode microstructure

To analyze the mechanisms of degradation in intermediate temperature SOFC cathodes, the LSCF-GDC system was chosen (Sec. 1.2.2). Half-cell stacks were fabricated according to the procedure in Sec. 4.1.1.1, and again electrochemically tested by collaborators in the Wachsman laboratory. EIS measurements were performed using the techniques from the previous section. FIB-nt measurements were taken for seven different LSCF-GDC cathode stacks that were aged at $750\,°C$ for $500\,h$ under various conditions. The effects of H_2O, CO_2, and Cr vapor were analyzed, together with the impacts of cathodic cell polarization.

During the aging tests, the SOFC symmetric half-cells were held at a constant temperature and gas environment. The H_2O environment was formed in the same manner as for the LSM-YSZ SOFC cathode in the previous section, with room temperature air bubbled through water, creating a 3% H_2O ambient. The CO_2 ambient was created by introducing the gas at a 5% concentration, controlled via a mass flow controller, with the remaining fraction consisting of dry synthetic air (as in Sec. 4.2). Throughout this section, the cells will be referenced by their ambient aging environment, and a suffix of -P if they were aged under a polarization bias (e.g. CO_2-P for the CO_2 environment aged under bias, or H_2O for the H_2O environment with no bias).

The samples used to analyze Cr degradation underwent a slightly modified preparation and aging process. The primary goal for these samples was to determine the transport mechanism for Cr into the cathode layers. As such, a range of cathodes

were created, sintered for 3 h at temperatures ranging from 950 to 1080 °C, which was expected to have a strong influence on the microstructure. Cr contamination was introduced by placing a layer of Crofer 22 APU (a stainless steel SOFC interconnect material) directly between the working electrode and the electrical contact layer during aging, to simulate a real SOFC stack environment. Crofer 22 contains a nominal Cr concentration of 22 wt.%, and is commonly considered the primary source of Cr poisoning during SOFC operation [95]. The Cr samples were aged at 750 °C for 200 h under open circuit conditions (no applied bias). The samples subjected to the highest and lowest sintering temperatures were chosen for FIB-*nt* investigation (referred to in this work as *Cr-1080°*C and *Cr-950°*C, respectively).

4.3.1   LSCF-GDC FIB-*nt* reconstruction results

Representative volumes from the seven LSCF-GDC composite cathode samples described previously were reconstructed using FIB-*nt*. As with the LSM samples, the data acquisition and analysis was performed according to the methods presented in Sec. 4.1. Due to the timing of the samples' preparation, the FIB-*nt* process for the LSCF samples was able to be performed on the Tescan *Gaia* FIB/SEM recently acquired by the University of Maryland. While the results from the LSM analysis in the previous section are believed to be representative, having local access to the FIB/SEM enabled drastically longer experimental running times, and consequently larger sampled volumes, providing strong assurance that the results collected are representative of the entire cathode layer (compare the order of magnitude difference

in volumes from Table 4.2 to those in Table 4.3). Furthermore, the long runtime enabled collection of data from the entire thickness of the cathode layer (generally 30 to 50 µm), providing a complete picture of phase distribution throughout the electrode stack. Each of the sample volumes is shown in Figure 4.25 (pg. 238). As can be seen in this figure, the collected volumes are much closer to cubic than for the LSM-YSZ cathodes, generally alleviating the concerns of artifacts arising from the aspect ratios of the data.

Specifics of the reconstructions are given in Table 4.3. The LSCF cathodes were sliced at a nominal z resolution of 35 nm, again well above the threshold of 10 slices per particle. By measuring the slice thicknesses post-acquisition, the average value was found to never deviate more than 1.2 nm from the nominal value. As with the data from the previous section, usually the first 20 slices (approximately) were cropped due to non-equilibrium milling. Uniform values were assumed for slice thicknesses based on the average measured value, which is generally a safe assumption after the initial non-equilibrium behavior has been passed [269]. Error values for each parameter were calculated using a bootstrap of subsampled data, as in the LSM-YSZ experiment. Finally, it is noted that comparisons to literature for this portion of the work will be difficult, as no other detailed FIB/SEM studies of LSCF-GDC composite cathodes were found in the literature. Where possible, values will be compared to similar materials (such as single-phase LSCF cathode layers).

Table 4.3: Detailed LSCF-GDC reconstruction parameters of the composite cathode models shown in Fig. 4.25. Dimensions and volumes listed are those used for analysis after all relevant cropping of the acquired data.

Sample	Total vol. (μm^3)	Voxel resolution (nm)			Bounding box (μm)		
		x	y	z	x	y	z
Air	18,874	26.0	26.0	34.6	51.8	27.6	13.2
CO$_2$	16,167	17.0	17.0	35.0	38.9	23.4	17.8
CO$_2$-P	37,069	24.0	24.0	35.0	50.0	35.3	21.0
H$_2$O	70,450	22.0	22.0	36.0	49.8	36.6	38.7
H$_2$O-P	68,158	24.0	24.0	34.9	51.8	38.1	34.6
*Cr-950°*C	50,321	24.0	24.0	33.8	40.8	37.9	32.6
*Cr-1080°*C	70,244	24.0	24.0	35.0	51.9	34.8	38.9

4.3.1.1   Volume and surface quantifications

Volumetric representations of the collected data are shown for each sample in Fig. 4.25 (pg. 238). Generally, four intensity levels were visible in each image, which could fairly easily be segmented into corresponding phases. In the backscatter images, the brightest intensity originated from the electrolyte (GDC), the cathode material (LSCF) was a moderate intensity, and the epoxy-filled pore space was the absolute darkest. In all samples, dark particles with an intensity between that of the pore and LSCF were observed, and were included in the segmentation. EDS analysis of these particles (in multiple samples) revealed them to be Co and Fe-rich (or alternatively, Sr and La-deficient) oxides. This phase was very minor however, never totaling more than 0.5% of the total sampled volume. In the Cr-exposed samples, an additional phase was evident, at an intensity slightly below that of the

LSCF (for a total of five segmented phases).

The results of the surface and volume quantifications are presented in Fig. 4.26. Fig. 4.26a shows the overall volume phase fractions (η) for each sample. Porosity in these samples varied from 39 to 45.2 %, although there does not appear to be a consistent effect on this value from polarization or gas exposure, meaning it is likely individual sample variation causing the differences. These porosity values are slightly higher than those reported for a single phase LSCF cathode, although since the volume examined here is orders of magnitude larger the presently reported value is believed to be more accurate [112]. As expected, the Cr sample sintered at higher temperature had slightly lower porosity than the other. Both Cr samples had an appreciable amount of Cr-containing contaminant phase, although *Cr-950°C* had significantly more (6.4 % vs. 1.9 %). Further differences between the two Cr-aged samples are discussed in Sec. 4.3.1.5.

The relationships between LSCF and GDC composition are best observed in Fig. 4.26b, which shows the ratio of LSCF to GDC volume in the samples. This calculation does not take into account any secondary phases that were observed in the cathode layer. The source material for these cathodes was a 50/50 wt. % mixture of LSCF and GDC, corresponding to a 52.4/47.6 vol. %, giving an expected volume ratio of 1.101. All samples (except for *CO_2*) were found to have a larger

Figure 4.25: (*Following page*) Representative visualizations of the seven LSCF-GDC composite cathodes reconstructed by FIB-nt. Phases are distinguished by color: LSCF in red, GDC in yellow and the pore phase omitted for clarity. A portion of the bulk GDC electrolyte is visible in a lighter yellow at the rear of each figure. The small blue particles are a Co/Fe-rich secondary phase that was present in all samples examined, while the pink are Cr-containing particles observed only in the Cr-aged samples.

Air
18,874 μm^3

51.8 μm

y

x

z

CO$_2$
16,167 μm^3

38.9 μm

CO$_2$-P
37,069 μm^3

50.0 μm

H$_2$O
70,450 μm^3

49.8 μm

H$_2$O-P
68,158 μm^3

51.8 μm

Cr-950
50,321 μm^3

40.8 μm

Cr-1080
70,244 μm^3

51.9 μm
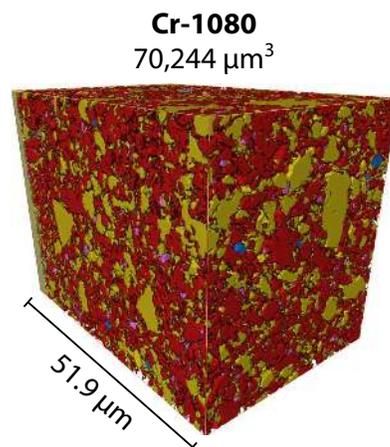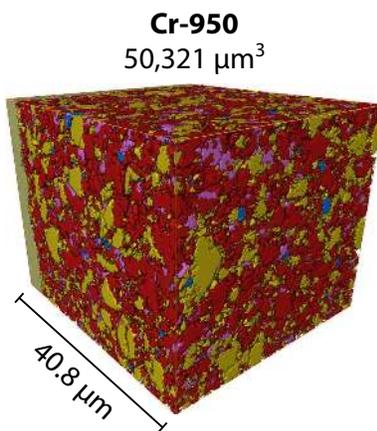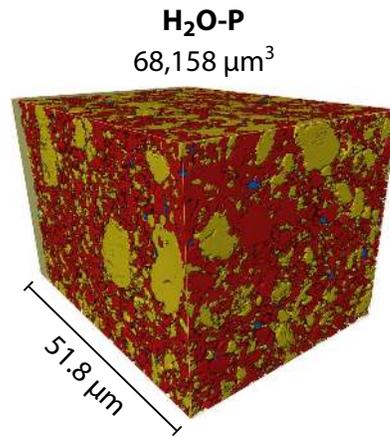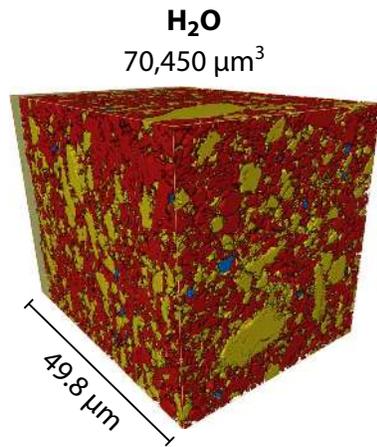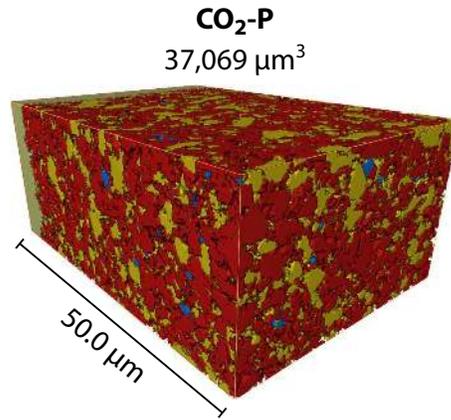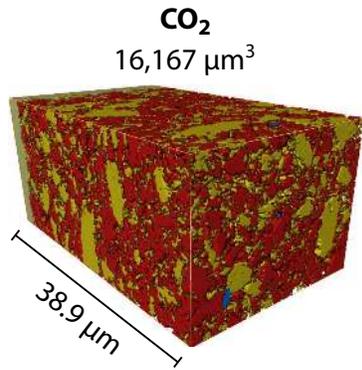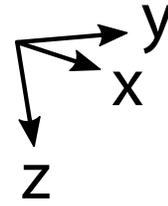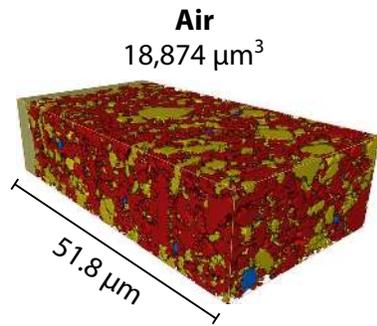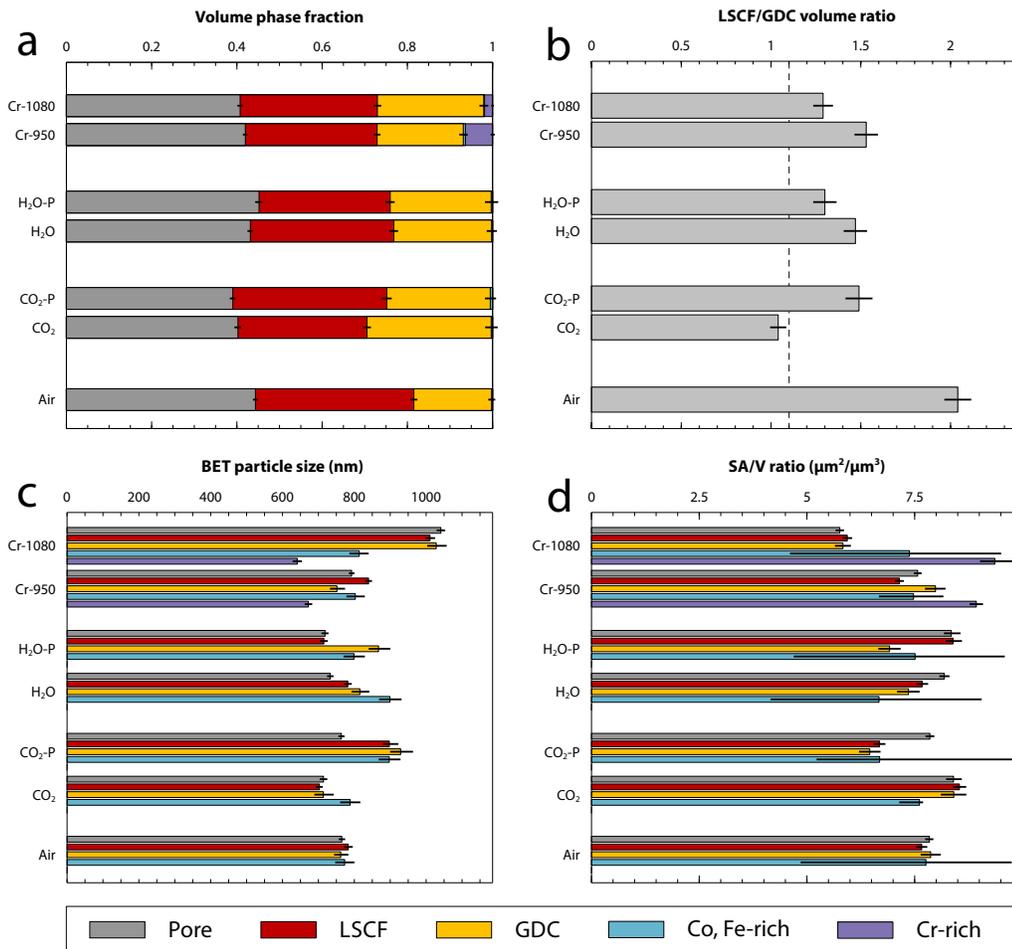
Figure 4.26: Comparisons of various phase properties measured from the reconstructed volumes. (a) Volume phase fraction (η) of each phase within the volume, (b) Solid phase fraction ratio ($\eta_{\mathrm{LSCF}}/\eta_{\mathrm{GDC}}$); the ratio of the source materials is indicated by the dashed line, (c) Average particle size as calculated by the BET method, (d) Volume normalized surface area. In each plot, the error bars are the bootstrapped 95% confidence intervals for the mean, calculated from 500 randomly sampled subvolumes.

than expected ratio, indicating either that there is a generally preferred increase in LSCF content (or loss of GDC) during aging (somewhat unlikely) or that the source materials may not have been as evenly distributed as advertised. Again, no consistent effect of polarization on this quantity is observed, although all six contaminated samples have significantly lower ratios than the pristine reference.

The average particle sizes for each sample are reported in Fig. 4.26c. Generally, these values are most sensitive to sintering temperature, as is clearly seen in the Cr-exposed samples, with the majority phases nearly 200 nm larger (on average) for the cell sintered at higher temperature. Overall, the particle sizes are much more uniformly distributed than in the LSM-YSZ cathodes from the previous section. In almost all samples, the LSCF and GDC have nearly identical average sizes, except for the H_2O-P sample, which has substantially larger electrolyte particles. This suggest that these conditions may encourage additional sintering of the electrolyte phase during aging. Similar increases in GDC size compared to the Air control are observed in the CO_2-P sample as well, further hinting at added sintering. These effects appear to be less uniform for the LSCF however.

Next, the surface area to volume (SA:V) ratios of the various phases are presented in Fig. 4.26d. Most values were around $7.5\,\mu m^{-1}$, slightly less than the value of $8.8\,\mu m^{-1}$ measured in the literature for a purely LSCF cathode [112], although this is to be expected, given that the cells in that work had a much finer overall microstructures, leading to more surface area. As it is an MIEC, the surface area of the LSCF phase is generally the most important. The SA:V ratio for LSCF decreased significantly in the Cr-aged samples (compared to the Air control), likely reduced

by the formation of the Cr/Fe/Sr impurity phase. The results for the other contaminants were more mixed. CO_2 caused an increase in the LSCF SA:V, but then a decrease with polarization, while the H_2O and H_2O-P samples had an opposite effect, making the overall impacts of polarization on this parameter unclear.

Finally, from the volumetric data, the overall spatial distribution of phases was determined through the analysis of graded phase plots (not shown), as described in Sec. 4.1.2.1. Overall, no preferential ordering or uneven distribution of the phases was observed (similar to the LSM-YSZ data). This reveals that on the 500 h (200 h for the Cr-contaminated samples) time scale of these aging experiments, massive migration or segregation of phases does not occur, and should not be a factor in cell degradation, as has been observed during long term operation of Ni-YSZ SOFC anodes [318].

4.3.1.2 Phase connectivity and network analysis

Using the volume reconstructions, skeletonization of each phase into a representative network was performed in *Avizo Fire*. As the visualizations of the networks are not particularly revealing, they are not shown here and just the quantifications from the results are presented. The overall data for each phase are shown in Fig. 4.27.

Fig. 4.27a and b show the edge and node densities for the skeleton network of each phase, respectively. These quantities reflect the "complexity" of the phases, in that higher densities of edges and nodes indicates the necessity of more kinks and bends to describe the topology of the phase. Compared to the *Air* sample, the pres-

ence of H_2O appears to significantly enhance the complexity of the pore network. Both the *H_2O* and *H_2O-P* samples have higher densities of nodes and edges for the pore phase, perhaps indicating a more tortuous pathway with more opportunity for gas-phase reactions. This generally agrees with the higher SA:V ratio observed for the pore phase in these samples in Fig. 4.26d. H_2O has a comparatively small influence on the LSCF network, although with polarization, the network is slightly more complex. In both H_2O samples the YSZ network is also more complex, suggesting an overall more intricate phase network under the effects of H_2O, which may serve to enhance cell performance by providing a greater density of reaction sites within the cathode (assuming the complexity of the networks causes a greater degree of TPB formation).

In contrast, the effect of polarization appears to be opposite in the CO_2-aged samples. For each phase, the density of network components was significantly less in the *CO_2-P* sample than *CO_2*, indicating a "simpler" phase network that may offer fewer reaction sites (but easier diffusive transport through the phases). For the Cr-aged samples, the network densities were substantially less for *Cr-1080°C* than *Cr-950°C*. This is an intuitive result, as the additional sintering at higher temperature results in larger average particle sizes (Fig. 4.26c), which should be simpler to describe with a skeletonization. Such an effect should enable easier bulk transport of species through each phase in the higher temperature sample (although may adversely impact ohmic resistances by decreasing contact area between the cathode and electrolyte phases).

The overall degree of percolation (p) for each phase is reported in Fig. 4.27c.
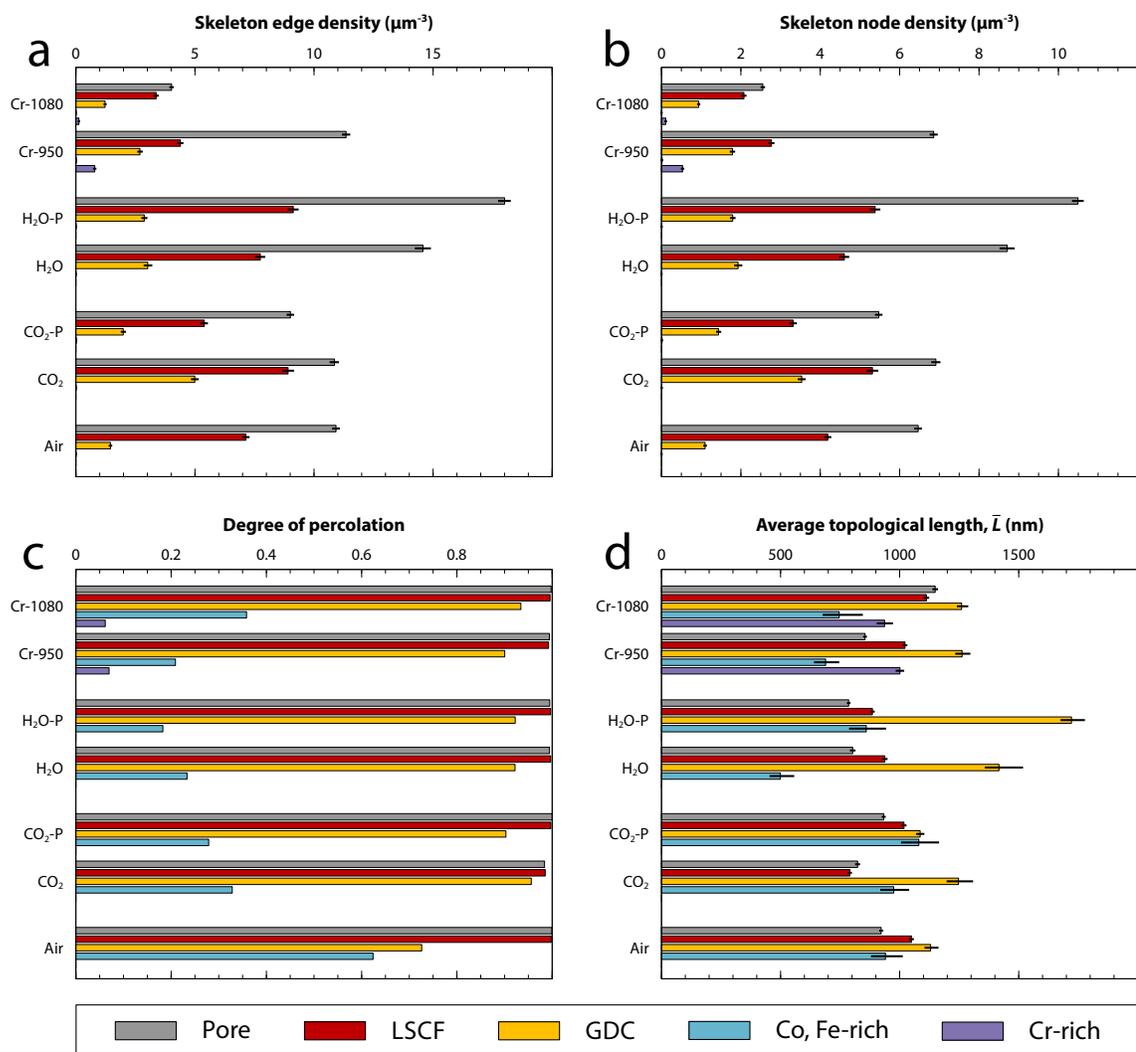
Figure 4.27: Comparisons of connectivity parameters, derived from the skeleton models of the LSCF-GDC composite cathodes. (a) The density of skeleton edges (E/V) and (b) nodes (N/V) provide insight into the complexity of each individual phase network. (c) The percolation degree (p) represents how well percolated each phase is throughout the volume. (d) Average topological length ($\overline{L}$) gives an indication of the average uninterrupted length an ion or gas molecule might be able to travel throughout a phase (similar to a mean free path). The error bars are 95% confidence intervals obtained by subsampling.

In contrast to the LSM-YSZ cathodes, there is not an easily identified phase that severely limits bulk conduction, as all three primary phases (LSCF, GDC, and pore) are fairly well percolated throughout the reconstructed volumes. In general, the GDC electrolyte appears to be slightly less connected in each sample than the LSCF and pore, although $p > 0.9$ for each (except the *Air* sample), meaning that this effect is not likely to have a severe impact. Interestingly, the *Air* sample had a significantly lower p_{GDC} than the others, while the LSCF and pore phases stayed completely percolated. While this could be individual sample variation, it is assumed that this is due to the significantly lower volume fraction of GDC (compared to LSCF) in this sample (see Fig. 4.26a and b), and this feature would be expected to negatively affect ohmic resistances within the cell.

Fig. 4.27d shows the average topological length, which is related to a geometric mean free path for conduction throughout each phase. In general, the results appear to be quite scattered, but a few interesting trends are observed. First, in the H_2O-aged samples, the GDC has markedly larger $\overline{L}$. These samples also had a higher density of nodes and edges, indicating that the total network length is also longer in these samples. Indeed, a comparison of GDC total network length (normalized by cathode volume) revealed the H_2O samples to have a value nearly twice that of the *Air* sample. The reasons for this increase are unclear, but indicate that a humid aging environment (regardless of applied bias) has a profound impact on the electrolyte network topology.

Besides this effect, there were few clear impacts of aging conditions on $\overline{L}$. Between phases, the topological lengths were generally similar in value, again indi-

245

cating that there is not a particular phase that likely limits conduction (in contrast to the LSM-limited conduction of the previous section). In the Cr-aged samples, the Cr contamination phases are poorly connected, but are otherwise of similar size and topology to the primary phases, illustrating a dependence of the secondary phase growth on the existing microstructure. Further discussion of this effect is given in Sec. 4.3.1.5.

4.3.1.3 Tortuosity analysis

The tortuosity (τ) of the various phases should have substantial impacts on the transport of both gaseous and ionic species. The results of the tortuosity calculations for the LSCF-GDC composite cathodes are presented in Figure 4.28. Fig. 4.28a reports the results of the raw tortuosity, while Fig. 4.28b is the tortuosity ratio (proportional to D_{eff}), as defined in Section 4.1.2.3. Only the values in the direction perpendicular to the cathode/bulk electrolyte interface (through the thickness of th cathode layer) are shown, as this direction should have the largest influence on performance (and the values were generally isotropic, similar to observations in the LSM-YSZ cathodes).

Generally, the tortuosity values for the pore and LSCF phases are fairly close to unity, as would be expected by their fully percolated phase networks. The values for LSCF ($\tau \approx 1.1$) are lower than have been previously measured for single-phase LSCF cathode layers ($\tau = 1.6$) [319], although the volumes sampled in the present data are more than 100 times that of the previous work. Since tortuosity generally

246
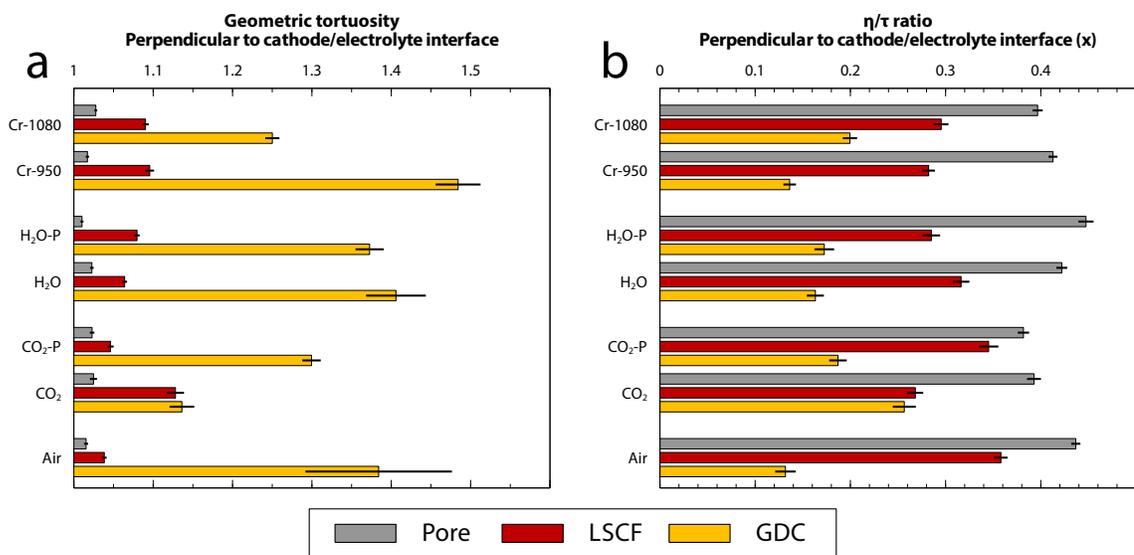
Figure 4.28: Tortuosity (a) and tortuosity ratios (b) for each phase and sample, measured perpendicular to the bulk electrolyte/cathode interface (through the thickness of the cathode layer). The specified error bars for τ are $\pm$ one standard deviation of the data within the final 25% of each τ profile (as in Fig. 4.7).

decreases as a function of distance throughout the cathode (see Fig. 4.18), the values reported in this thesis are expected to be much more representative of the true value.

Compared to LSCF and the pores, the GDC tortuosity values are generally higher, ranging from 1.14 to 1.48. While there was always at least one continuous pathway from the bulk electrolyte to the cathode surface, it was generally very tortuous, which is expected to have negative impacts on bulk ionic conduction. There does not appear to be a consistent effect for polarization, but some changes with respect to aging environment are observed. H_2O-aged samples appeared generally similar to the *Air* sample, while the CO_2 samples had lower GDC tortuosity, but higher LSCF tortuosity. Differences in the pore τ values for all samples were nearly negligible. The varied temperature Cr-exposed samples had roughly identical pore and LSCF τ, but the increased particle sizes from additional sintering decreased the

GDC tortuosity significantly.

4.3.1.4 Triple phase boundary calculations

In a MIEC such as LSCF, some conduction of ionic species through the cathode material extends the active area for the ORR to occur, but generally speaking the density and distribution of TPB points in the cathode layer are still expected to have a substantial impact on overall device performance. As previously described, these TPB points must be connected to a greater overall network in order to usefully contribute to electrochemical activity. As such, measurements of the TPB density (ρ_{TPB}) and the relative fraction of active vs. inactive TPB points were carried out according to the methods of Section 4.1.2.4. The results for each of these quantities are reported in Fig. 4.29a and b, respectively.

Overall the total ρ_{TPB} (Fig. 4.29a) for the five non- Cr samples are similar (around 3.5 to 4 $\mathrm{\mu m}/\mathrm{\mu m}^3$), with CO_2 being a notable exception. Coincidentally, the CO_2 sample had the lowest sampled volume of all the reconstructions. While ρ_{TPB} should be intrinsic property insensitive to the total sampled volume, it is possible that some of the increased density could be an artifact of measurement size. Otherwise, for the H_2O, H_2O-P, and CO_2-P samples, there does not appear to be a strong effect of aging environment on total ρ_{TPB}. Comparing the polarized samples to the open-circuit ones, there does appear to be a reduction in ρ_{TPB} upon polarization regardless of environment, suggesting a possible mechanism for performance degradation in these cells. In the Cr-aged specimens, the *Cr-1080°C* sample has the
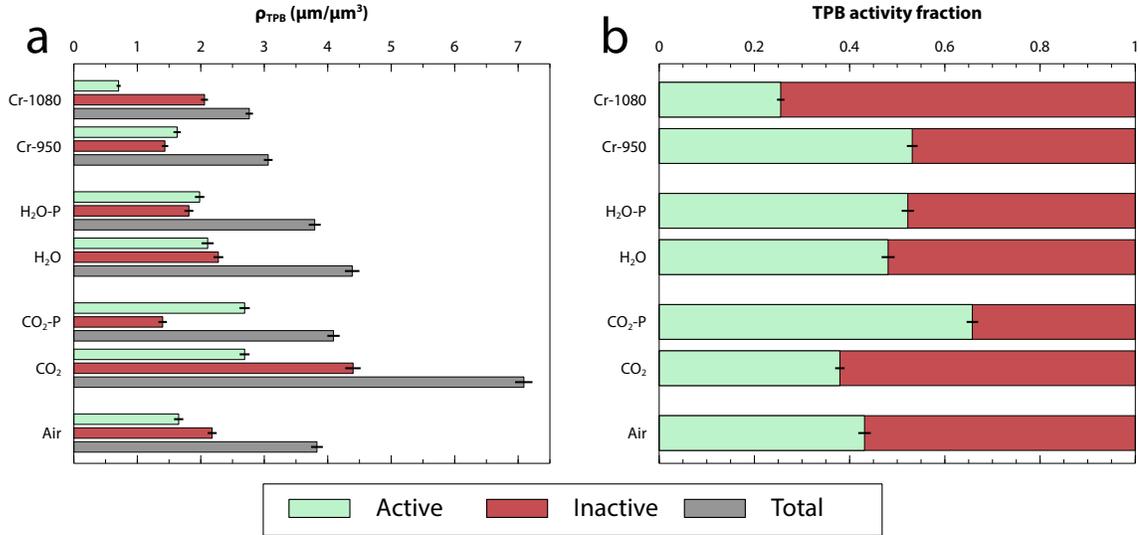
Figure 4.29: Triple phase boundary (TPB) calculations. (a) Total, active, and inactive ρ_{TPB} for each sample. Density is relative to total cathode phase volume (including pore). (b) Active vs. inactive TPB fractions, comparing relative activity of TPB networks between samples. Boundaries adjacent to contaminant phases are not counted as part of this total.

lower of the ρ_{TPB} values, matching expectations due to the larger particle sizes that will cause fewer intersections between phases.

Comparison of the present findings to literature is difficult, due to the relatively few studies published on LSCF-GDC composite cathode layers. One such study by Kim *et al.* [320] reported a total ρ_{TPB} of $1.66\,\mathrm{\mu m}/\mathrm{\mu m}^3$, significantly lower than the values obtained in this work, but this difference can be attributed to the much higher cathode sintering temperature used in their study ($1150\,^{\circ}\mathrm{C}$). Due to the lack of comparable results in the literature, this work is likely to serve as one of the first such references for the microstructural parameters of LSCF-GDC composite cathodes.

To analyze the activity of the TPB networks, it is more useful to compare the fraction of active vs. inactive ρ_{TPB}, as displayed in Fig. 4.29b. For the samples

sintered at 950 °C, the average TPB network activity (as defined in Sec. 4.1) was 50%. Deviations were observed from sample to sample however. Both of the H_2O-aged samples had higher activity than the *Air* sample. The CO_2 samples had varying activities depending on the applied polarization bias. Interestingly, while the *CO_2* sample had much higher total ρ_{TPB}, its active fraction was relatively unchanged (if not a bit lower) than the *Air* reference, while the *CO_2-P* sample had significantly higher activity. This implies a varying effect of polarization bias dependent on aging environment. Interestingly, comparing the "raw" active ρ_{TPB} values (green bars in Fig. 4.29a), it is clear that for each environment, the active ρ_{TPB} does not change as a function of polarization, and instead it is the inactive ρ_{TPB} that is changed. The origins (and implications) of this behavior are unclear, but it is a curious phenomenon worthy of further investigation.

The Cr-aged samples show slightly different trends in TPB activity fraction. As might be expected for the larger particles, the active fraction at higher sintering temperatures (*Cr-1080°C*) is reduced compared to the lower temperature sample. Perhaps surprising is that for *Cr-950°C*, there is not a significant reduction in active TPB fraction or ρ_{TPB} compared to the reference *Air* sample. Significant increases were observed in the ohmic and polarization resistances in this sample (see Sec. 4.3.1.5 for further discussion), and the Cr-containing phases were found to comprise 6.4% of the total cathode volume. Furthermore, *Cr-950°C* had worse performance than *Cr-1080°C*, even though it had significantly higher active TPB density. Thus, it appears that performance reduction is irrespective of the TPB microstructure, and depends more critically on overall Cr content within the cathode.

4.3.1.5   Detailed chromium analysis

As they were the samples to show the most signs of degradation, a more detailed analysis of the two Cr-aged samples is provided here. In EIS studies of these samples (by Wachsman laboratory collaborators), the performance of the cells was found to degrade significantly over the 200 h of aging. Both ohmic resistance and polarization resistances increased as a function of aging time, and the rate of cell degradation was inversely related to the cathode sintering temperature. More specifically, over the 200 h of aging, R_Ω and R_P increased 7 and 5 times greater for *Cr-950*°C than *Cr-1080*°C, respectively. X-ray diffraction (XRD) spectra from the two Cr-aged samples indicate the presence of $SrCrO_4$, revealing the formation of distinct phases, rather than just substitutional incorporation of Cr into the existing phases [321]. Preliminary TEM-EELS studies of the secondary phases (not shown) suggest that additional Cr-containing phases beyond $SrCrO_4$ form in these cells, as well.

As reported previously, a significantly higher fraction of Cr-rich phase was observed in the *Cr-950*°C sample. The contaminants comprised 6.4% of the total cathode volume for *Cr-950*°C compared to 1.9% for *Cr-1080*°C (3.4× increase). An example of the contamination phase distribution in the two samples is illustrated in Fig. 4.30. In this figure, the top row of data is for *Cr-950*°C while the bottom row is for *Cr-1080*°C. Fig. 4.30(a and d) show images that are representative of each sample (after non-local means filtering). Fig. 4.30(b and e) illustrate how these images were segmented into a labeled image, with each contrast level of the images

assigned to a particular phase. The Cr-containing phases were slightly darker than the LSCF, and are labeled with purple in the segmented images. As is clear for both samples, the Cr-phase appears to be relatively evenly distributed throughout the width of the images.
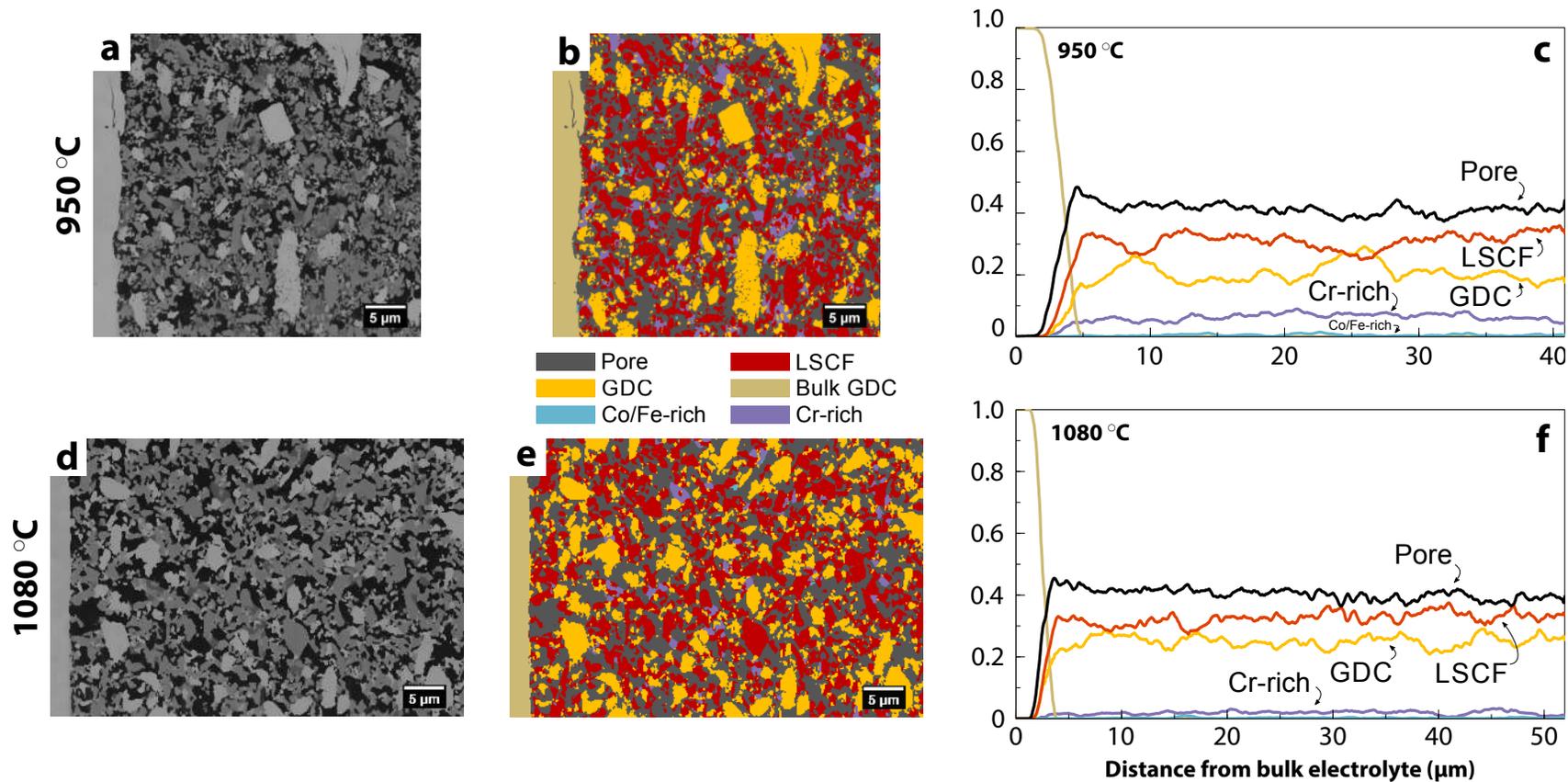
Figure 4.30: Illustration of Cr contamination phase distribution through the thickness of the cathode. (a, d) Representative SEM images from the *Cr-950°C* and *Cr-1080°C* samples, respectively. (b, e) Segmented versions of the images in (a) and (d), respectively. The phases were assigned by grayscale intensity, and are indicated by color in the key. (c, f) Graded average volume fraction profiles of each phase through the thickness of the cathode. In each sample, the entire cathode thickness was reconstructed, providing a picture of phase distribution inclusively from the bulk electrolyte to the cathode surface. The plots illustrate the relatively uniform distribution of each phase as a function of distance through the cathode layer.

To gain further insight regarding the distribution of the phases throughout these two cathodes, average phase fraction profiles were calculated using the methods from Sec. 4.1.2.1. These profiles are shown in Fig. 4.30(c and f), and demonstrate how the concentration of each phase changes as a function of distance throughout the cathode thickness (normal to the interface with the bulk electrolyte). It is important to note in these plots that the entire thickness of the cathode layer is included in these profiles, thus any distinctive layers of a particular phase (either at the electrolyte boundary or at the surface) would be apparent. The profiles reveal no features such as these, and each phase has a generally constant volume fraction throughout the cathode layer.

This result informs an important revelation regarding Cr transport throughout the cathode layer. Even though the Crofer interconnect material is placed in direct contact with the cathode layer, the reaction does not appear to take place in the solid phase, and is instead mediated by gaseous transport through the cathode. Were it to be a solid-phase process, a gradient of Cr content would be expected, with a maximum at the surface of the cathode, but there is no evidence of such features. Indeed, a gaseous process transporting Cr to the interfaces between LSCF and GDC would explain the near instantaneous increase of R_P observed in the EIS results [321]. To confirm this assumption, shortened aging experiments would need to be performed, to ensure that any diffusive processes do not reach equilibrium. A uniform distribution of Cr in such experiments would more definitively indicate a gas-phase reaction.

Further evidence for this reaction mode can be found by investigating the

particle sizes and interfacial areas within the cathode, measurements of which are easily obtained from the FIB-*nt* data. Fig. 4.31a shows a histogram of the individual pore sizes within each cathode layer (obtained using the 'Separate Objects' module in *Avizo Fire*). Both samples have a bimodal distribution of pore sizes. The smaller diameter pores in the first distribution arise from small gaps between and at the edges of particles, as well as any small closed pores that sometimes are present within the electrolyte phase. The larger pore distribution (centered around 700 to 900 nm) represents the primary gas conduction pores, and it is these larger pores that form the bulk of the percolated pore network. It is clear that the lower sintering temperature sample is skewed to smaller pore sizes when compared with *Cr-1080°C*. Although not shown, similar trends in particle size were observed for the LSCF and GDC phases as well. Such smaller average particles will lead to an increase in the total surface area between phases (as observed in Fig. 4.26d), providing more sites for Cr deposition and contamination phase. Indeed, the amount of Cr-phase formation appears to be proportional to available surface area within the cathode, additionally suggesting a gaseous reaction.

Additional inferences can be made about the Cr reaction kinetics by analyzing the interfacial areas of the contaminant phase in the FIB/SEM data. The common interfacial area between phases was obtained by performing a volumetric dilation of each phase, and finding the overlap of the resulting volumes. The dilation was performed with a single voxel element, so dividing the resultant overlapping volume by the average edge length of a voxel (approximately 30 nm) provides a very reasonable estimate of the interfacial area between the two phases. This process was
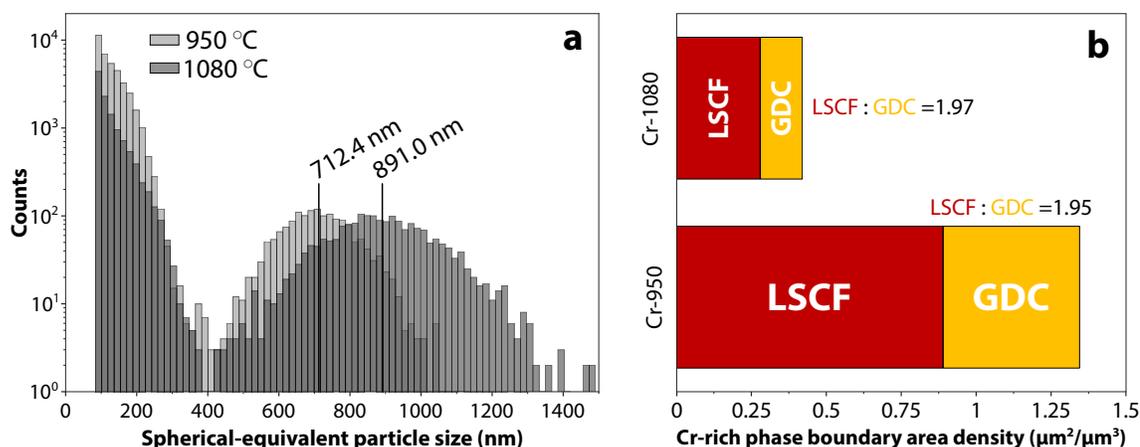
Figure 4.31: (a) Histogram showing the distribution of individual pore sizes for the *Cr-950°C* and *Cr-1080°C* samples. The sample sintered at 1080 °C has a larger average pore size, as expected from the additional coarsening that occurs at higher temperatures. The mean of the larger portion of the bimodal distribution is indicated for each sample in the figure. (b) Comparison of interfacial area (normalized by total cathode volume) between the Cr contamination and both LSCF and GDC for the two Cr-aged samples. Both samples have an identical ratio of Cr/LSCF to Cr/GDC intersection area of approximately 2.

performed for both Cr samples to find the interfacial area between Cr-LSCF and Cr-GDC. For comparison between samples, these areas were normalized by the total cathode volume, and the results are reported in Fig. 4.31b.

As shown in that figure, the Cr-phase interfacial area to both LSCF and GDC was significantly larger in *Cr-950°C* than in *Cr-1080°C*, which matches intuition, given the larger volume fraction in the lower temperature sample. For both phases, *Cr-950°C* forms approximately 3.2× the interfacial area when compared with *Cr-1080°C*. Comparing the LSCF area to GDC in each sample reveals that the Cr consistently forms double the interfacial area with LSCF than with GDC. This implies that the majority of the reaction is with the LSCF phase, which is not unexpected, given the strong evidence from XRD for the presence of $SrCrO_4$ [321]. The constant LSCF:GDC ratio is surprising, given the significant differences in

particle sizes and surface area between the two different temperature samples. The consistent ratio possibly suggests that both LSCF and GDC actively contribute to the formation of the Cr-containing contaminant phases. Analysis of samples containing varying proportions of LSCF and GDC would be useful in testing the relative contributions of each phase to the contamination product.

4.3.1.6   Quantification summary

When compared with the LSM-YSZ cathodes from the previous section, the LSCF-GDC cathode layers produced much greater changes in almost all the microstructural parameters investigated. Unfortunately however, there appeared to be little systematic change for most of the reconstructed samples. In general, the samples exposed to CO_2 had greater variation in their microstructural parameters compared to the sample aged in dry air, while the H_2O-exposed samples changed very little in most aspects. The effect of polarization was not uniform, often having an apparent opposite effect in CO_2 vs. H_2O. Part of the difficulty in interpreting the results arises from the "on/off" nature of the variables tested (e.g. polarization). To gain a more thorough understanding of the effects of each variable, a systematic variation (in contamination amount, polarization bias magnitude, etc.) in aging parameters is likely necessary.

Regardless, some interesting microstructural features were observed. The presence of H_2O appeared to lead to a more complex phase network as measured by density of the skeletonized nodes and edges. Furthermore, the GDC phase was found to

have particularly high tortuosity in each sample, perhaps related to the increase in R_Ω described in the next section. Given the dearth of existing reports regarding the microstructure of composite LSCF-GDC cathodes, the results obtained in this thesis will serve as a worthwhile reference for future studies, especially as intermediate temperature SOFCs become more prevalent.

4.3.2   Relationship to H_2O/CO_2 cell performance

Similar to the LSM-YSZ system, EIS measurements were performed on the analyzed cells by collaborators in the Wachsman laboratory. Measurements of the impedance response throughout the aging process enables the determination of the ohmic and various polarization resistances over time. The primary findings from these experiments are reported in Ref. [322], and form the basis for comparison to the microstructural parameters. Results were only reported for samples aged under open-circuit conditions, meaning the effects of polarization cannot be compared (although publication of the results from those samples will be forthcoming).

The primary findings of Ref. [322] reveal that similar to the LSM-YSZ cathodes, the changes observed during operation in the contaminant environments were for the most part reversible, meaning that those effects would not be expected to be observed in the FIB-nt results. Of the irreversible changes observed, the most significant was an increase in R_Ω (the ohmic series resistance) that was greater under humidification than under the CO_2 ambient. This effect was primarily attributed to additional sintering of the electrolyte phase, and it was suggested that an H_2O

258

environment helps promote this effect.

Examining the average particle size quantification from H_2O and CO_2, there appears to be microstructural evidence for this phenomenon. As shown in Fig 4.26c, the spherical equivalent particle sizes were $(815 \pm 22)\,\text{nm}$ and $(714 \pm 24)\,\text{nm}$ for the H_2O and CO_2 samples, respectively. This difference is larger than the calculated 95% confidence intervals indicating that it is a significant change in average particle size, suggesting that the 3% H_2O environment does enhance GDC sintering.

Compared to the ohmic effects, changes in the polarization resistances were found to be almost completely reversible in the H_2O-aged sample. This could help explain the general lack of any change (compared to the *Air* sample) observed in τ and ρ_{TPB} for the H_2O samples. R_P changes in the CO_2 sample were smaller during operation, but not completely reversible, correlating with the greater changes observed in the microstructure of the two CO_2-aged samples reconstructed. The primary impact of CO_2 was a small irreversible increase in the low-frequency polarization resistance, which is generally attributed to a combination of reaction steps related to the ORR within the cathode. This correlates well with the slight decrease in active ρ_{TPB} fraction for the CO_2 sample, suggesting a decrease in the available active sites at which the ORR can take place.

4.3.3 Conclusions

In this portion of the thesis, seven different LSCF-GDC composite cathodes aged in various environment were reconstructed using FIB-*nt*. Greater changes in

microstructural parameters were observed for the LSCF-GDC system than in the similarly analyzed LSM-YSZ materials. Generally, most microstructural parameters exhibited some sort of modification as a function of aging environment or polarization, but the effects were not very consistent. As with LSM-YSZ, many of the electrical effects of the contamination environments were found to be reversible upon removal of the foreign species, meaning little effect of them would be expected to be observed in post-aging FIB/SEM studies.

The Cr-aged samples revealed particularly interesting results related to the mechanisms of Cr poisoning, which was revealed to be primarily a gas-phase process. Growth of Cr-containing secondary phases did not appear to significantly reduce the total or active fraction of ρ_{TPB} for samples sintered at the same temperature, even though it caused extreme performance degradation. This result implies that Cr poisoning of SOFC cells is not primarily a microstructural effect, and likely instead impacts the kinetics of oxygen adsorption within the cathode, given the relationship between degradation of performance and the total Cr-phase surface area.

4.4 Summary of SOFC studies

In this chapter of the thesis, FIB-*nt* was demonstrated as a very capable technique for the reconstruction of microstructural data from moderately sized volumes. The method was used to reconstruct a range of composite SOFC cathode samples spanning two material systems: the high-temperature LSM-YSZ cathode and the intermediate-temperature LSCF-GDC system.

In Sec. 4.1, the FIB-*nt* process was introduced, and a number of methodological enhancements were presented over the methods used in existing literature. Among these was a shading correction algorithm that enables the quantification of greater volumes by intelligently correcting image intensity in areas that would typically be cropped out of a reconstruction. This algorithm also improves the fidelity of image segmentation by removing overlapping grayscale intensity values from adjacent phases. Also presented was an efficient and accurate means of calculating the geometric tortuosity of a fuel cell (or any sinuous) three-dimensional structure. Finally, a novel algorithm for calculating a precise and homotopic representation of the triple phase boundary network was developed. In addition to the development of these algorithms, the specific implementations have been well documented and are provided to the scientific community under an open-source license to further development in the 3D reconstruction field.

Using the methods of Sec. 4.1, a detailed study of the effects of H_2O contamination and polarization bias on LSM-YSZ composite cathodes was performed in Sec. 4.2. Most microstructural parameters exhibited little change regardless of the

aging conditions, and LSM determined to be the transport limiting phase. TEM compositional and chemical analysis of the LSM-YSZ provided insight into the origins of the performance enhancement observed for the H_2O sample aged under cathodic polarization. Mn and La cations were observed to migrate to the YSZ grain boundaries, and EELS analysis revealed a high concentration of oxygen vacancies at the triple phase boundaries, promoting oxygen incorporation into the electrolyte. Overall however, the conditions used in this work did not induce significant performance degradation, which correlated with the general lack of microstructural degradation observed in the reconstructions.

Finally, in Sec. 4.3, the FIB-nt method was used to analyze a range of intermediate-temperature LSCF-GDC composite cathode layers, exposed to H_2O, CO_2, and Cr-vapor contamination. Volume and connectivity statistics were reported for each sample, contributing valuable reference points to the literature where none previously existed. The impacts of H_2O and CO_2 on microstructure were subtle, but generally agreed with the changes observed in the electrochemical performance of the cells. Greater changes were observed in the sample aged in CO_2 under polarization bias, but electrical results were not available for comparison. Cr-contamination was found to have a significant effect on cell performance, as well as cathodic microstructure. The cathode sintered at lower temperature had a significantly higher Cr content, attributed to the increased surface area available for reaction with the vapor-phase Cr during cell operation. Analysis of the interfacial areas between the LSCF, GDC, and Cr-rich phases revealed that the Cr preferentially reacts with LSCF. Performance degradation in Cr-exposed cells was attributed to kinetic effects

262

of the Cr, and while there was not an overall reduction in active ρ_{TPB} fraction, the total ρ_{TPB} was reduced approximately 20% in the *Cr-950°C* sample due to the additional presence of the Cr-containing phases at the triple phase points, suggesting a microstructural degradation as well.

Overall, this chapter provides a wide-ranging and thorough investigation of the methods and applications of SOFC three-dimensional reconstruction. The novel methods introduced were developed for analysis of SOFC data, but their generality means they are applicable in a much wider range of fields. Implementation of these methods was demonstrated on multiple material systems, using various microscopy equipment, illustrating the generality and adaptability of the techniques for future studies.

Chapter 5:   Conclusions and future outlooks

The research presented in this thesis has explored two distinct material systems with a range of chemical, physical, and microstructural characterization techniques. Throughout this process, a number of novel and improved methods were developed for sample processing and data analysis, which are general enough to be applied in many fields. The results of this work illustrate the importance of obtaining a thorough picture of a system through a multifaceted characterization approach in order to explain observed behaviors. A summary of the most important findings is presented here, together with suggestions for future work informed by the remaining unanswered questions for each system.

5.1   Summary of research findings

5.1.1   SiC/SiO$_2$ interfaces

This thesis explored a number of aspects of the interface between *4H*-SiC and SiO$_2$ in SiC MOSFET devices. In the first study, a method to measure the transition layer between SiC and SiO$_2$ was introduced, drastically improving upon the methods currently used in the literature. Comparisons to existing techniques

were demonstrated, and the "chemical shift" technique was found to be by far the most reliable metric. Using this method, the width of the transition layer (w_{TL}) was measured for an array of interfaces annealed for varying amounts of time in a NO ambient. w_{TL} was discovered to correlate inversely with the measured mobility of the devices, suggesting an intimate connection between interfacial structure and device performance. Profiles of elemental composition across the interfaces revealed no excess carbon at the interface, as had been observed in prior works.

Following this w_{TL} study was an investigation of the transition layer using XPS. The combination of methods provided a similar picture of the interfacial structure, increasing confidence in the given interpretation of the TEM results. A relatively uncommon spin-etch technique was adapted from the Si literature, which enabled careful angle resolved and depth-sensitive XPS studies of the transition layer at the SiC/SiO$_2$ interface. This study revealed one primary interfacial Si-bonding configuration that changes slightly in energy upon NO annealing of the device. Analysis of the nitrogen signal in NO annealed devices revealed at least four distinct bonding configurations for N at the interface, suggesting a complex incorporation of the passivating element. Attenuation model calculations from the angle resolved XPS measurements resulted in a w_{TL} calculation of about 1.8 to 3 nm, very close to the values measured by STEM-EELS, confirming the presence of a distinct interfacial transition region.

To gain a better understanding of the effects of NO annealing and substrate orientation on the interfacial structure, a more detailed study of the subtle changes in ELNES features was performed. This study made extensive use of spectral unmixing

methodologies adapted from the machine learning community. Doing so uncovered evidence of a distinct layer of Si−N bonding at the interface in NO-annealed devices within the Si-$L_{2,3}$ EELS edge. On a-face devices, this feature was shifted to lower energies due to the additional contributions of carbon bonding at the interface. The NO-annealed samples also revealed C−N bonding at the interface, regardless of orientation, but apparently strongest in the a-face sample. Analysis of the O-K edge in these samples resulted in a significant interfacial state only in the a-face NO-annealed device, signaling an electrically modified oxynitride layer at the interface that is proposed as the origin of the drastically enhanced mobility in the a-face devices.

With the techniques refined in the previous studies, an analysis of newer "Beyond NO" techniques was performed to inspect the effects of phosphorus and boron anneals on the interfacial structure. Compared to NO, the phosphorus anneal had a far greater impact throughout the oxide than at the interface. P was observed to be non-uniformly distributed throughout the oxide layer, gathering in P-rich clusters approximately 4 nm in diameter, in direct contradiction to the previously understood model for P distribution in such phosphosilicate glass layers. Boron on the other hand, was determined to accumulate within a uniform layer of approximately 1.5 nm at the interface, with a much narrower distribution than suggested by prior works. The B atoms were also observed to diffuse approximately 1 nm into the SiC, where it is expected to act as a p-type dopant.

Finally, an initial investigation into the interfacial effects of bias and temperature stressing was performed (with and without NO annealing). In the non-NO

266

sample, no changes compared to pristine interfaces were observed, even though the devices had experienced dielectric breakdown during operation. This was attributed to insufficiently locating the precise location of breakdown for TEM analysis. In the NO-annealed device, a Si-$L_{2,3}$ feature very similar to the previously-observed interfacial states was detected, but was found to be distributed throughout the oxide layer, rather than pinned at the interface as measured in the non-stressed samples. This finding raises important questions about the impacts of device operation bonding configurations at the SiC/SiO$_2$ interface.

5.1.2   Solid oxide fuel cell microstructure

Compared to the SiC studies, the investigations of SOFC materials performed in this thesis made extensive use of the FIB/SEM platform as a characterization tool, beyond its primary role as a sample preparation instrument. In order to better quantify the microstructures of the materials studied in this work, a number of novel methods were developed. Primary among these was an algorithm to allow correction of the often-present FIB shading artifact, allowing for a substantial increase in the volumes that can be successfully segmented for microstructural analysis. Also introduced were improvements to the calculations of tortuosity and triple phase boundary networks. These methods have been made freely available under an open-source license, enabling their use (and further development) by the scientific community.

The first system explored for FIB-nt reconstruction was the high-temperature

LSM-YSZ composite cathode. Microstructural parameters were calculated for cathode layers aged under polarization and with H_2O contamination, with the goal of demonstrating which parameters correlate best with performance degradation. For the conditions tested, relatively little irreversible performance loss was observed, which correlated with little overall change in the microstructural parameters. For the one sample that showed a decrease in active TPB density (*H_2O-Cathodic*), performance was actually found to be slightly enhanced, indicating that the kinetic effects of H_2O within the cathode (at these conditions) are likely to dominate over microstructural ones.

More interesting results were obtained for LSM-YSZ samples analyzed using STEM-EELS and EDS techniques, providing insight into the origins of the observed H_2O performance enhancement. In both H_2O samples analyzed, Mn and La were observed to segregate to the YSZ grain boundaries and surfaces. Measurements of the Mn cation valency and the O-K EELS signal indicated a high concentration of oxygen vacancies in these areas. This would be expected to promote oxygen incorporation into the electrolyte, potentially explaining the reversible performance enhancement.

The second SOFC system studied was the intermediate-temperature and mixed conducting LSCF-GDC composite cathode. Seven different samples were reconstructed, with total volumes over an order of magnitude larger than typically reported in literature. Among these samples were cathodes aged in H_2O-, CO_2-, and Cr-contaminated environments. Generally, few changes were observed for the H_2O-aged samples, correlating with limited LSCF-H_2O interaction observed by collabo-

rators at the aging temperature used in this work. The CO_2-aged devices exhibited greater changes compared to the control sample, and applied polarization bias during operation appeared to significantly affect these changes.

Compared to the H_2O and CO_2 samples, the cathode layers aged in the presence of Cr-containing material demonstrated vastly more significant changes to their microstructures. Substantial formation of Cr-containing secondary phases was observed, with a stronger effect for the sample sintered at lower temperatures. The Cr incorporation was determined to be a gaseous process due to its dependence on total cathode surface area. The Cr-aged samples experienced severe performance degradation, which correlated with changes in the phase fractions and particle surface areas in the cathodes. The active ρ_{TPB} value did not change substantially however, indicating that Cr-poisoning is most likely a kinetic effect, as well as a microstructural one.

5.2   Recommendations for future work

While this work has contributed significantly to the better understanding of the material systems investigated, it also raises a number of important questions that could form the basis of future studies.

With respect to methodology, the extensive use of spectral unmixing methods in this work has clearly demonstrated the power of the technique in identifying weak and previously unknown signal sources within a spectrum image. As previously mentioned however, the number of EELS studies published using these techniques

is still remarkably low. This is likely due to uncertainty regarding the physical justification for using these sorts of techniques to represent physical phenomena such as EELS excitations. A detailed comparison of the various algorithms, applied to theoretical and experimental data, should be performed to quantify the efficacy of the different methods for EELS data. Such a study could also identify potential pitfalls in these sorts of analyses that are still unclear.

Within the SiC field, there are a number of interesting remaining questions originating from the last two studies presented. As the SiC market develops, further improvements in performance will be necessary, and it appears that processing techniques other than NO-annealing will lead the way. The results from phospho- and borosilicate glass layers analyzed in this work represent some of the very first nanoscale characterization of such oxides in the SiC MOSFET field. The effects of the observed P-rich clusters on device performance are completely unknown, as is their dependence on device processing conditions. Analysis of varying P concentrations should be performed to observe how such changes affect the oxide layer. Similarly, the findings related to boron distribution in the BSG layers are the first report of such sharp compositional profiles. The specific impacts of boron at the interface are still unclear, as the passivation process is still under development. Investigation of varying boron concentration, as well as changing oxide thickness would help to explain whether it is the interfacial or oxide layer boron that gives rise to the performance enhancements.

With regards to the SOFC studies, there are still a number of remaining questions related to specific degradation mechanisms in both LSM-YSZ and LSCF-

270

GDC composite cathodes. Unfortunately, many of the aging conditions used in this work did not result in the sort of significant irreversible performance degradations that could be analyzed via FIB/SEM. Furthermore, the on/off type of cell testing performed complicated the interpretation of the microstructural changes that were observed. To gain a better understanding of the degradation modes, a more systematic investigation of increasingly extreme contamination environments should be performed (this would be useful for both LSM and LSCF cathodes). Additionally, there is uncertainty regarding the contamination products of Cr exposure within the LSCF-GDC system. XRD experiments revealed the presence of $SrCrO_4$ within the poisoned cathodes, but initial STEM-EELS results suggest a much larger range of contaminant phases formed within the cathode. Further experimentation and analysis of these phases should be performed to better explain the many Cr reactions that occur during cathode poisoning.

Bibliography

[1] J. Rozen, "Tailoring oxide/silicon carbide interfaces: NO annealing and beyond," in *Physics and Technology of Silicon Carbide Devices*, Y. Hijikata, Ed., InTech, 2012, ch. 10, pp. 251–278.

[2] Advanced Manufacturing Office, "Wide bandgap semiconductors: pursuing the promise," U.S. Department of Energy, Washington, DC, Tech. Rep., 2013.

[3] A. J. Lelis, R. Green, and D. Habersat, "High-temperature reliability of SiC power MOSFETs," *Materials Science Forum*, vol. 679-680, pp. 599–602, Mar. 2011.

[4] B. Burger, D. Kranzer, and O. Stalter, "Cost reduction of PV-inverters with SiC-DMOSFETs," in *5th International Conference on Integrated Power Systems*, VDE, 2008.

[5] J. Rozen, "Energy efficiency in high power electronics: role and challenges of silicon carbide interface," in *Human Photonics International Forum, Saitama University*, 2012.

[6] The Noun Project, *Application icons used under the creative commons license*, 2016.

[7] J. Cooper, M. Melloch, R. Singh, A. Agarwal, and J. Palmour, "Status and prospects for SiC power MOSFETs," *IEEE Transactions on Electron Devices*, vol. 49, no. 4, pp. 658–664, 2002.

[8] A. Bauer, P. Reischauer, J. Kräusslich, N. Schell, W. Matz, and K. Goetz, "Structure refinement of the silicon carbide polytypes 4H and 6H: unambiguous determination of the refinement parameters," *Acta Crystallographica Section A Foundations of Crystallography*, vol. 57, no. 1, pp. 60–67, Jan. 2001.

[9] G. R. Fisher and P. Barnes, "Towards a unified view of polytypism in silicon carbide," *Philosophical Magazine Part B*, vol. 61, no. 2, pp. 217–236, Feb. 1990.

[10] U. Starke, "Atomic structure of hexagonal SiC surfaces," *Physica Status Solidi (B)*, vol. 202, pp. 475–499, 1997.

[11] S. Dhar, "Nitrogen and hydrogen induced trap passivation at the SiO_2/4H-SiC interface," PhD thesis, Vanderbilt University, 2005, p. 147.

[12] Y. Goldberg, M. Levinshtein, and S. Rumyantsev, *Properties of Advanced Semiconductor Materials: GaN, AlN, InN, BN, SiC, SiGe*, M. Levinshtein, S. Rumyantsev, and M. Shur, Eds. John Wiley and Sons, Inc., 2001.

[13] V. Siklitsky, *NSM archive - Physical properties of semiconductors*, http://www.ioffe.ru/SVA/NSM/Semicond/, (Accessed on 06/23/2016).

[14] M. Golio, *RF and microwave semiconductor device handbook*. CRC Press, 2002.

[15] S. Vitanov and V. Palankovski, "Electron mobility models for III-Nitrides," *Annual Journal of Electronics*, pp. 18–21, 2010.

[16] T. L. Biggerstaff, "Atomic scale characterization of the origin of mobility loss at the SiC/SiO_2 interface," PhD thesis, North Carolina State University, 2008, p. 150.

[17] Cree Inc., "Cree silicon carbide substrates and epitaxy," Tech. Rep., 2014.

[18] MTI Corporation, http://www.mtixtl.com/SiC-4H-z-76D04-C2.aspx, May 2016.

[19] A. Schöner, "New development in hot wall vapor phase epitaxial growth of silicon carbide," in *Silicon Carbide: Recent Major Advances*, W. J. Choyke, H. Matsunami, and G. Pensl, Eds., Berlin, Germany: Springer Berlin Heidelberg, 2004, pp. 229–250.

[20] T. Kimoto, A. Itoh, and H. Matsunami, "Step-controlled epitaxial growth of high-quality SiC layers," *Physica Status Solidi (B)*, vol. 202, pp. 247–262, 1997.

[21] C. Raynaud, "Silica films on silicon carbide: a review of electrical properties and device applications," *Journal of Non-Crystalline Solids*, vol. 280, pp. 1–31, 2001.

[22] S. Salemi, "Electronic structure of SiC/SiO_2 by density functional theory," PhD Thesis, University of Maryland, 2012.

[23] J. Rozen, C. A. Ahyi, X. Zhu, J. R. Williams, and L. C. Feldman, "Scaling between channel mobility and interface state density in SiC MOSFETs," *IEEE Transactions on Electron Devices*, vol. 58, no. 11, pp. 3808–3811, Nov. 2011.

[24] R. Schörner, P. Friedrichs, D. Peters, and D. Stephani, "Significantly improved performance of MOSFETs on silicon carbide using the 15R-SiC polytype," *IEEE Electron Device Letters*, vol. 20, no. 5, pp. 241–244, May 1999.

[25] J. Rozen, "Electronic properties and reliability of the SiO_2/SiC interface," PhD thesis, Vanderbilt University, 2008.

[26] C. R. Helms and E. H. Poindexter, "The silicon-silicon-dioxide system: its microstructure and imperfections," *Reports on Progress in Physics*, vol. 57, pp. 791–852, 1994.

[27] P. M. Lenahan and P. V. Dressendorfer, "Hole traps and trivalent silicon centers in metal/oxide/silicon devices," *Journal of Applied Physics*, vol. 55, no. May, pp. 3495–3499, 1984.

[28] V. V. Afanas'ev and A. Stesmans, "Interfacial defects in SiO_2 revealed by photon stimulated tunneling of electrons," *Physical Review Letters*, vol. 78, pp. 2437–2440, 1997.

[29] C. Radtke and I. J. R. Baumvol, "Effects of ion irradiation in the thermal oxidation of SiC," *Physical Review B*, vol. 66, no. 15, pp. 1–7, 2002.

[30] H.-f. Li, S. Dimitrijev, D. Sweatman, H. B. Harrison, P. Tanner, and B. Feil, "Investigation of nitric oxide and Ar annealed SiO_2/SiC interfaces by x-ray photoelectron spectroscopy," *Journal of Applied Physics*, vol. 86, no. 8, p. 4316, 1999.

[31] A. Ekoué, O. Renault, T. Billon, L. Di Cioccio, and G. Guillot, "Study of the wet re-oxidation annealing of SiO_2/4H-SiC (0001) interface properties by AR-XPS measurements," *Materials Science Forum*, vol. 433-436, pp. 555–558, 2003.

[32] C. Virojanadara and L. Johansson, "Photoemission study of Si-rich 4H-SiC surfaces and initial SiO_2SiC interface formation," *Physical Review B*, vol. 71, no. 19, p. 195 335, May 2005.

[33] B. Hornetz, H.-J. Michel, and J. Halbritter, "ARXPS studies of SiO_2-SiC interfaces and oxidation of 6H SiC single crystal Si-(001) and C-(001) surfaces," *Journal of Materials Research*, vol. 9, no. 12, pp. 3088–3094, Dec. 1994.

[34] K. C. Chang, N. T. Nuhfer, L. M. Porter, and Q. Wahab, "High-carbon concentrations at the silicon dioxide – silicon carbide interface identified by electron energy loss spectroscopy identified by electron energy loss spectroscopy," *Applied Physics Letters*, vol. 77, p. 2186, 2000.

[35] K. C. Chang, L. M. Porter, J. Bentley, C. Y. Lu, and J. Cooper Jr., "Electrical, structural, and chemical analysis of silicon carbide-based metal-oxide-semiconductor field-effect-transistors," *Journal of Applied Physics*, vol. 95, no. 12, p. 8252, 2004.

[36] W. Lu, L. C. Feldman, Y. Song, S. Dhar, W. E. Collins, W. C. Mitchel, and J. R. Williams, "Graphitic features on SiC surface following oxidation and etching using surface enhanced Raman spectroscopy," *Applied Physics Letters*, vol. 85, no. 16, pp. 3495–3497, 2004.

[37] T. Iida, Y. Tomioka, K. Yoshimoto, M. Midorikawa, H. Tukada, M. Orihara, Y. Hijikata, H. Yaguchi, M. Yoshikawa, H. Itoh, Y. Ishida, and S. Yoshida, "Measurements of the depth profile of the refractive indices in oxide films on SiC by spectroscopic ellipsometry," *Japanese Journal of Applied Physics, Part 1*, vol. 41, no. 2 A, pp. 800–804, 2002.

[38] P. Liu, G. Li, G. Duscher, Y. K. Sharma, A. C. Ahyi, T. Isaacs-Smith, J. R. Williams, and S. Dhar, "Roughness of the SiC/SiO_2 vicinal interface and atomic structure of the transition layers," *Journal of Vacuum Science and Technology*, vol. 32, no. 6, p. 060 603, 2014.

[39] T. Hatakeyama, H. Matsuhata, T. Suzuki, T. Shinohe, and H. Okumura, "Microscopic examination of SiO_2/4H-SiC interfaces," *Materials Science Forum*, vol. 679-680, pp. 330–333, Mar. 2011.

[40] C. Strenger, V. Häublein, T. Erlbacher, A. J. Bauer, H. Ryssel, A. M. Beltran, S. Schamm-Chardon, V. Mortet, E. Bedel-Pereira, M. Lefebvre, and F. Cristiano, "Comparative study of electrical and microstructural properties of 4H-SiC MOSFETs," *Materials Science Forum*, vol. 717-720, pp. 437–440, May 2012.

[41] V. V. Afanas'ev, F. Ciobanu, G. Pensl, and A. Stesmans, "Contributions to the density of interface states in SiC MOS structures," in *Silicon Carbide: Recent Major Advances*, Berlin, Germany: Springer Berlin Heidelberg, 2004, pp. 343–371.

[42] K. L. Brower, "Kinetics of H_2 passivation of P_b centers at the (111) Si-SiO_2 interface," *Physical Review B*, vol. 38, no. 14, pp. 9657–9666, 1988.

[43] ——, "Dissociation kinetics of hydrogen-passivated (111) Si-SiO_2 interface defects," *Physical Review B*, vol. 42, no. 6, pp. 3444–3453, 1990.

[44] S.-R. Wang, S. Dhar, C. A. Ahyi, A. Franceschetti, J. R. Williams, L. C. Feldman, and S. T. Pantelides, "Bonding at the SiC-SiO_2 interface and the effects of nitrogen and hydrogen," *Physical Review Letters*, vol. 98, no. 2, pp. 10–13, Jan. 2007.

[45] V. V. Afanasev, M. Bassler, G. Pensl, and M. Schulz, "Intrinsic sic/sio2 interface states," *Physica Status Solidi (a)*, vol. 162, pp. 321–337, 1997.

[46] H.-F. Li, S. Dimitrijev, H. Harrison, and D. Sweatman, "Interfacial characteristics of N_2O and NO nitrided SiO_2 grown on SiC by rapid thermal processing," *Applied Physics Letters*, vol. 70, no. 15, p. 2028, 1997.

[47] G. Y. Chung, C. C. Tin, J. R. Williams, K. McDonald, M. Di Ventra, S. T. Pantelides, L. C. Feldman, and R. A. Weller, "Effect of nitric oxide annealing on the interface trap densities near the band edges in the 4H polytype of silicon carbide," *Applied Physics Letters*, vol. 76, no. 13, p. 1713, 2000.

[48] S. Dhar, S. Wang, A. Ahyi, T. Isaacs-Smith, S. T. Pantelides, J. R. Williams, and L. C. Feldman, "Nitrogen and hydrogen induced trap passivation at the SiO_2/4H-SiC interface," *Materials Science Forum*, vol. 527-529, pp. 949–954, 2006.

[49] Semiconductor Today. (2016). SiC & GaN power semiconductors market to grow 17-fold to \$2.5bn in 2023, [Online]. Available: http://web.archive.org/web/20150906134350/http://www.semiconductor-today.com/news_items/2015/apr/ihs2_010415.shtml (visited on 05/23/2016).

[50] K. McDonald, R. A. Weller, S. T. Pantelides, L. C. Feldman, G. Y. Chung, C. C. Tin, and J. R. Williams, "Characterization and modeling of the nitrogen passivation of interface traps in SiO_2/4H-SiC," *Journal of Applied Physics*, vol. 93, no. May, pp. 2719–2722, 2003.

[51] K. C. Chang, Y. Cao, L. M. Porter, J. Bentley, S. Dhar, L. C. Feldman, and J. R. Williams, "High-resolution elemental profiles of the silicon dioxide/ 4H-silicon carbide interface," *Journal of Applied Physics*, vol. 97, p. 104 920, 2005.

[52] P. Tanner, S. Dimitrijev, H.-F. Li, D. Sweatman, K. Prince, and H. B. Harrison, "SIMS analysis of nitrided oxides grown on 4H-SiC," *Journal of Electronic Materials*, vol. 28, no. 2, pp. 109–111, Feb. 1999.

[53] S. Salemi, N. Goldsman, D. P. Ettisserry, A. Akturk, and A. J. Lelis, "The effect of defects and their passivation on the density of states of the 4H-silicon-carbide/silicon-dioxide interface," *Journal of Applied Physics*, vol. 113, no. 5, p. 053 703, 2013.

[54] D. P. Ettisserry, N. Goldsman, A. Akturk, and A. J. Lelis, "Structure, bonding, and passivation of single carbon-related oxide hole traps near 4H-SiC/SiO_2 interfaces," *Journal of Applied Physics*, vol. 116, no. May 2016, p. 174 502, 2014.

[55] J. Rozen, X. Zhu, C. A. Ahyi, J. R. Williams, and L. C. Feldman, "The limits of post oxidation annealing in NO," *Materials Science Forum*, vol. 645-648, pp. 693–696, Apr. 2010.

[56] A. Modic, Y. Sharma, Y. Xu, G. Liu, A. Ahyi, J. Williams, L. Feldman, and S. Dhar, "Nitrogen plasma processing of SiO_2/4H-SiC interfaces," *Journal of Electronic Materials*, vol. 43, no. 4, pp. 857–862, Apr. 2014.

[57] Y. K. Sharma, C. A. Ahyi, T. Isaacs-Smith, X. Shen, S. T. Pantelides, X. Zhu, L. C. Feldman, J. Rozen, and J. R. Williams, "Phosphorous passivation of the SiO_2/4H-SiC interface," *Solid-State Electronics*, vol. 68, pp. 103–107, 2012.

[58] D. Okamoto, M. Sometani, S. Harada, R. Kosugi, Y. Yonezawa, and H. Yano, "Improved channel mobility in 4H-SiC MOSFETs by boron passivation," *IEEE Electron Device Letters*, vol. 35, no. 12, pp. 1176–1178, 2014.

[59] M. Okamoto, Y. Makifuchi, M. Iijima, Y. Sakai, N. Iwamuro, H. Kimura, K. Fukuda, and H. Okumura, "Coexistence of small threshold voltage instability and high channel mobility in 4H-SiC(000$\bar{1}$) metal-oxide-semiconductor field-effect transistors," *Applied Physics Express*, vol. 5, no. 4, pp. 3–6, 2012.

[60] G. Liu, A. C. Ahyi, Y. Xu, T. Isaacs-Smith, Y. K. Sharma, J. R. Williams, L. C. Feldman, and S. Dhar, "Enhanced inversion mobility on 4H-SiC (11$\bar{2}$0) using phosphorus and nitrogen interface passivation," *IEEE Electron Device Letters*, vol. 34, no. 2, pp. 181–183, Feb. 2013.

[61] O. L. Krivanek, D. Tsui, T. Sheng, and A. Kamgar, "A high resolution electron microscopy study of the Si-SiO$_2$ interface," in *Proceedings of the International Topical Conference on the Physics of SiO$_2$ and its Interfaces*, S. T. Pantelides, Ed., Yorktown Heights, NY: Pergamon Press, 1978, pp. 356–361.

[62] K. C. Chang, J. Bentley, and L. M. Porter, "Nanoscale characterization of the silicon dioxide-silicon carbide interface using elemental mapping by energy-filtered transmission electron microscopy," *Journal of Electronic Materials*, vol. 32, no. 5, pp. 464–469, May 2003.

[63] T. S. Zheleva, A. J. Lelis, G. Duscher, F. Liu, I. Levin, and M. K. Das, "Transition layers at the SiO$_2$/SiC interface," *Applied Physics Letters*, vol. 93, no. 2, p. 022108, 2008.

[64] T. L. Biggerstaff, C. L. Reynolds, T. S. Zheleva, A. J. Lelis, D. Habersat, S. Haney, S.-H. Ryu, A. K. Agarwal, and G. Duscher, "Relationship between 4H-SiC/SiO$_2$ transition layer thickness and mobility," *Applied Physics Letters*, vol. 95, no. 3, p. 032108, 2009.

[65] P. Liu, "Supporting user-oriented analysis for multi-view domain-specific visual languages," PhD thesis, University of Tennessee, Knoxville, 2014, p. 123.

[66] J. Houston Dycus, W. Xu, D. J. Lichtenwalner, B. Hull, J. W. Palmour, J. M. Lebeau, and J. M. Lebeau, "Structure and chemistry of passivated SiC/SiO$_2$ interfaces," *Applied Physics Letters*, vol. 108, p. 201607, 2016.

[67] H. Watanabe, T. Hosoi, T. Kirino, Y. Kagei, Y. Uenishi, A. Chanthaphan, A. Yoshigoe, Y. Teraoka, and T. Shimura, "Synchrotron x-ray photoelectron spectroscopy study on thermally grown SiO$_2$/4H-SiC(0001) interface and its correlation with electrical properties," *Applied Physics Letters*, vol. 99, no. 2, p. 021907, 2011.

[68] L. I. Johansson, C. Virojanadara, T. Eickhoff, and W. Drube, "Properties of the SiO$_2$/SiC interface investigated by angle resolved studies of the Si 2p and Si 1s levels and the Si KLL Auger transitions," *Surface Science*, vol. 529, no. 3, pp. 515–526, 2003.

[69] X. Zhu, H. D. Lee, T. Feng, C. A. Ahyi, D. Mastrogiovanni, A. Wan, E. C. Garnett, J. R. Williams, T. Gustafsson, and L. C. Feldman, "Structure and stoichiometry of (0001) 4H-SiC/oxide interface," *Applied Physics Letters*, vol. 97, no. 7, p. 071908, 2010.

[70] J. Cook, D. Nuccitelli, S. A. Green, M. Richardson, B. Winkler, R. Painting, R. Way, P. Jacobs, and A. Skuce, "Quantifying the consensus on anthropogenic global warming in the scientific literature," *Environ. Res. Lett.*, vol. 8, no. 2, p. 024024, May 2013.

[71] R. A. Rohde and R. A. Muller, "Air pollution in China: Mapping of concentrations and sources," *PLOS ONE*, vol. 10, no. 8, A. Ding, Ed., e0135749, Aug. 2015.

[72] H. Guo and K. Kliesen, "Oil price volatility and U.S. macroeconomic activity," *Federal Reserve Bank of St. Louis Review*, no. Nov, pp. 669–84, 2005.

[73] B. Steele, "Oxygen ion conductors and their technological applications," *Materials Science and Engineering: B*, vol. 13, no. 2, pp. 79–87, 1992.

[74] N. Q. Minh, "Ceramic fuel cells," *Journal of the American Ceramic Society*, vol. 76, pp. 563–588, 1993.

[75] E. D. Wachsman and K. T. Lee, "Lowering the temperature of solid oxide fuel cells," *Science*, vol. 334, no. 6058, pp. 935–939, 2011.

[76] N. Q. Minh and T. Takahashi, *Science and Technology of Ceramic Fuel Cells*. Amsterdam: Elsevier, 1995, pp. 1–14.

[77] S. C. Singhal and K. Kendall, "Introduction to SOFCs," in *High Temperature and Solid Oxide Fuel Cells*, S. C. Singhal and K. Kendal, Eds., Oxford: Elsevier, 2003, ch. 1, pp. 1–22.

[78] E. D. Wachsman, C. A. Marlowe, and K. T. Lee, "Role of solid oxide fuel cells in a balanced energy strategy," *Energy & Environmental Science*, vol. 5, no. 2, pp. 5498–5509, 2012.

[79] Y.-L. Huang, "Fundamental understanding of SOFC cathode durability; a kinetics and catalysis study," PhD thesis, University of Maryland, 2015.

[80] I. Pilatowsky, R. Romero, C. Isaza, S. Gamboa, P. Sebastian, and W. Rivera, "Thermodynamics of fuel cells," in *Modeling Solid Oxide Fuel Cells*, 2011, pp. 25–36.

[81] A.-S. Feiner and A. J. McEvoy, "The Nernst equation," *Journal of Chemical Education*, vol. 71, no. 6, p. 493, Jun. 1994.

[82] S. B. Adler, "Factors governing oxygen reduction in solid oxide fuel cell cathodes," *Chemical Reviews*, vol. 104, no. 10, pp. 4791–4844, Oct. 2004.

[83] R. J. H. Voorhoeve, J. P. Remeika, and L. E. Trimble, "Defect chemistry and catalysis in oxidation and reduction over perovskite-type oxides," *Annals of the New York Academy of Sciences*, vol. 272, pp. 3–21, 1976.

[84] T. Nitadori, S. Kurihara, and M. Misono, "Catalytic properties of $La_{1-x}A'_xMnO_3$ (A' = Sr, Ce, Hf)," *Journal of Catalysis*, vol. 98, no. 1, pp. 221–228, Mar. 1986.

[85] S. Carter, A. Selcuk, R. J. Chater, J. Kajda, J. A. Kilner, and B. C. H. Steele, "Oxygen transport in selected nonstoichiometric perovskite-structure oxides," *Solid State Ionics*, vol. 53-56, pp. 597–605, 1992.

[86] M. C. Williams, J. P. Strakey, W. A. Surdoval, and L. C. Wilson, "Solid oxide fuel cell technology development in the U.S.," *Solid State Ionics*, vol. 177, pp. 2039–2044, 2006.

[87] H.-H. Möbius, "On the history of solid electrolyte fuel cells," *Journal of Solid State Electrochemistry*, vol. 1, pp. 2–16, 1997.

[88] A. J. Mcevoy, "Materials for high-temperature oxygen reduction in solid oxide fuel cells," *Journal of Materials Science*, vol. 36, pp. 1087–1091, 2001.

[89] J. Richter, P. Holtappels, T. Graule, T. Nakamura, and L. J. Gauckler, "Materials design for perovskite SOFC cathodes," *Monatshefte für Chemie - Chemical Monthly*, vol. 140, no. 9, pp. 985–999, May 2009.

[90] Y. Liu, A. Hagen, R. Barfod, M. Chen, H. Wang, F. Poulsen, and P. Hendriksen, "Microstructural studies on degradation of interface between LSM–YSZ cathode and YSZ electrolyte in SOFCs," *Solid State Ionics*, vol. 180, no. 23-25, pp. 1298–1304, Oct. 2009.

[91] J. Nielsen, A. Hagen, and Y. L. Liu, "Effect of cathode gas humidification on performance and durability of solid oxide fuel cells," *Solid State Ionics*, vol. 181, no. 11-12, pp. 517–524, 2010.

[92] J. Nielsen and M. Mogensen, "SOFC LSM:YSZ cathode degradation induced by moisture: an impedance spectroscopy study," *Solid State Ionics*, vol. 189, no. 1, pp. 74–81, 2011.

[93] Y. Teraoka, T. Nobunaga, K. Okamoto, N. Miura, and N. Yamazoe, "Influence of constituent metal cations in substituted $LaCoO_3$ on mixed conductivity and oxygen permeability," *Solid State Ionics*, vol. 48, pp. 207–212, 1991.

[94] A. Virkar, J. Chen, C. W. Tanner, and J.-W. Kim, "The role of electrode microstructure on activation and concentration polarizations in solid oxide fuel cells," *Solid State Ionics*, vol. 131, no. 1-2, pp. 189–198, Jun. 2000.

[95] C. Sun, R. Hui, and J. Roller, "Cathode materials for solid oxide fuel cells: a review," *Journal of Solid State Electrochemistry*, vol. 14, no. 7, pp. 1125–1144, Oct. 2010.

[96] Y.-L. Huang, C. Pellegrinelli, and E. D. Wachsman, "Fundamental impact of humidity on SOFC cathode degradation," *Journal of Electrochemical Society*, vol. 163, no. 3, F171–F182, 2016.

[97] Z. Zhao, L. Liu, X. Zhang, W. Wu, B. Tu, D. Ou, and M. Cheng, "A comparison on effects of CO_2 on $La_{0.8}Sr_{0.2}MnO_{3+\delta}$ and $La_{0.6}Sr_{0.4}CoO_{3-\delta}$ cathodes," *Journal of Power Sources*, vol. 222, pp. 542–553, 2013.

[98] Y. Hsiao and J. Selman, "The degradation of SOFC electrodes," *Solid State Ionics*, vol. 98, no. January, pp. 33–38, 1997.

[99] S. P. Simner, M. D. Anderson, M. H. Engelhard, and J. W. Stevenson, *Electrochemical and Solid-State Letters*, vol. 9, A478, 2006.

[100] H. Yokokawa, H. Tu, B. Iwanschitz, and A. Mai, "Fundamental mechanisms limiting solid oxide fuel cell durability," *Journal of Power Sources*, vol. 182, pp. 400–412, 2008.

[101] S. J. Benson, D. Waller, and J. A. Kilner, "Degradation of $La_{0.6}Sr_{0.4}Fe_{0.8}Co_{0.2}O_{3-\delta}$ in carbon dioxide and water atmospheres," *Journal of The Electrochemical Society*, vol. 146, no. 4, pp. 1305–1309, 2000.

[102] S. Raz, K. Sasaki, J. Maier, and I. Riess, *Solid State Ionics*, vol. 143, pp. 181–204, 2001.

[103] N. Sakai, K. Yamaji, T. Horita, Y. P. Xiong, H. Kishimoto, and H. Yokokawa, "Effect of water on oxygen transport properties on electrolyte surface in SOFCs," *Journal of The Electrochemical Society*, vol. 150, A689–A694, 2003.

[104] H. Yokokawa, "Thermodynamic and SIMS analyses on the role of proton/water in oxygen reduction process and related degradations in solid oxide fuel cells," *Solid State Ionics*, vol. 225, pp. 6–17, 2012.

[105] Y. Matsuzaki and I. Yasuda, "Dependence of SOFC cathode degradation by chromium-containing alloy on compositions of electrodes and electrolytes," *Journal of The Electrochemical Society*, vol. 148, no. 2, A126, 2001.

[106] D. Gostovic, N. J. Vito, K. A. O'Hara, K. S. Jones, and E. D. Wachsman, "Microstructure and connectivity quantification of complex composite solid oxide fuel cell electrode three-dimensional networks," *Journal of the American Ceramic Society*, vol. 94, no. 2, pp. 620–627, Feb. 2011.

[107] J. R. Smith, A. Chen, D. Gostovic, D. Hickey, D. P. Kundinger, K. Duncan, R. DeHoff, K. S. Jones, and E. D. Wachsman, "Evaluation of the relationship between cathode microstructure and electrochemical behavior for SOFCs," *Solid State Ionics*, vol. 180, no. 1, pp. 90–98, Feb. 2009.

[108] E. Wachsman, "Deconvolution of SOFC cathode polarization," in *ECS Transactions*, vol. 7, ECS, 2007, pp. 1051–1054.

[109] B. J. Inkson, M. Mulvihill, and G. Möbus, "3D determination of grain shape in a FeAl-based nanocomposite by 3D FIB tomography," *Scripta Materialia*, vol. 45, pp. 753–758, 2001.

[110] L. Holzer, F. Indutnyi, P. H. Gasser, B. Münch, and M. Wegmann, "Three-dimensional analysis of porous $BaTiO_3$ ceramics using FIB nanotomography.," *Journal of Microscopy*, vol. 216, no. Pt 1, pp. 84–95, Oct. 2004.

[111] J. R. Wilson, W. Kobsiriphat, R. Mendoza, H.-Y. Chen, J. M. Hiller, D. J. Miller, K. Thornton, P. W. Voorhees, S. B. Adler, and S. A. Barnett, "Three-dimensional reconstruction of a solid-oxide fuel-cell anode," *Nature Materials*, vol. 5, no. 7, pp. 541–4, Jul. 2006.

[112] D. Gostovic, J. R. Smith, D. P. Kundinger, K. S. Jones, and E. D. Wachsman, "Three-dimensional reconstruction of porous LSCF cathodes," *Electrochemical and Solid-State Letters*, vol. 10, no. 12, B214, 2007.

[113] J. R. Wilson, M. Gameiro, K. Mischaikow, W. Kalies, P. W. Voorhees, and S. A. Barnett, "Three-dimensional analysis of solid oxide fuel cell Ni-YSZ anode interconnectivity," *Microscopy and Microanalysis*, vol. 15, no. 1, pp. 71–7, Feb. 2009.

[114] N. Shikazono, D. Kanno, K. Matsuzaki, H. Teshima, S. Sumino, and N. Kasagi, "Numerical assessment of SOFC anode polarization based on three-dimensional model microstructure reconstructed from FIB-SEM images," *Journal of The Electrochemical Society*, vol. 157, no. 5, B665, 2010.

[115] H. Iwai, *Journal of Power Sources*, vol. 195, no. 4, pp. 955–961, Feb. 2010.

[116] J. A. Taillon, *FIB*-nt *code repository*, https://bitbucket.org/jat255/jat255-python-modules, 2016.

[117] Lord Rayleigh F.R.S., "XXXI. investigations in optics, with special reference to the spectroscope," *Philosophical Magazine Series 5*, vol. 8, no. 49, pp. 261–274, 1879.

[118] D. Williams and C. Carter, *Transmission Electron Microscopy*, 2nd ed. New York, NY: Springer Science, 2009, p. 760.

[119] B. Fultz and J. Howe, *Transmission Electron Microscopy and Diffractometry of Materials*, ser. Graduate Texts in Physics. Berlin, Heidelberg: Springer Berlin Heidelberg, 2013.

[120] M. Haider, P. Hartel, H. Müller, S. Uhlemann, and J. Zach, "Information transfer in a TEM corrected for spherical and chromatic aberration," *Microscopy and Microanalysis*, vol. 16, pp. 393–408, 2010.

[121] P. W. Hawkes and J. C. H. Spence, Eds., *Science of Microscopy*. Springer, 2007, vol. 1, p. 385.

[122] N. Tanaka, Ed., *Scanning Transmission Electron Microscopy of Nanomaterials*. London: Imperial College Press, 2014, p. 616.

[123] FEI Company, *An Introduction to Electron Microscopy*. Hillsboro, OR, 2010, p. 40.

[124] R. F. Egerton, "Electron energy-loss spectroscopy in the TEM," *Reports on Progress in Physics*, vol. 72, p. 16 502, 2009.

[125] R. Egerton, *Electron Energy-Loss Spectroscopy in the Electron Microscope*, 3rd ed. Boston, MA: Springer US, 2011, p. 491.

[126] C. C. Ahn, Ed., *Transmission Electron Energy Loss Spectrometry in Materials Science and The EELS Atlas*, 2nd. Weinheim, FRG: Wiley-VCH Verlag GmbH & Co. KGaA, Sep. 2004, vol. 40, pp. 69–87.

[127] K. Masek, "Reflection high-energy electron loss spectroscopy (RHEELS): a new approach in the investigation of epitaxial thin film growth by reflection high-energy electron diffraction (RHEED)," *Vacuum*, vol. 71, no. 1-2, pp. 59–64, May 2003.

[128] R. F. Egerton, "Prospects for vibrational-mode EELS with high spatial resolution," *Microscopy and Microanalysis*, pp. 1–6, 2014.

[129] T. Malis, S. C. Cheng, and R. F. Egerton, "EELS log-ratio technique for specimen-thickness measurement in the TEM," *Journal of Electron Microscopy Technique*, vol. 8, no. 2, pp. 193–200, Feb. 1988.

[130] R. Brydson, "Interpretation of near-edge structure in the electron energy-loss spectrum," *EMSA Bulletin*, vol. 21, no. 2, pp. 57–67, 1991.

[131] L. A. J. Garvie and P. R. Buseck, "Bonding in silicates: investigation of the Si $L_{2,3}$ edge by parallel electron energy-loss spectroscopy," *American Mineralogist*, vol. 84, no. 5-6, pp. 946–964, 1999.

[132] P. Rez, "Cross-sections for energy loss spectrometry," *Ultramicroscopy*, vol. 9, pp. 283–287, 1982.

[133] G. Bertoni and J. Verbeeck, "Accuracy and precision in model based EELS quantification," *Ultramicroscopy*, vol. 108, pp. 782–790, 2008.

[134] R. D. Leapman and C. R. Swyt, "Separation of overlapping core edges in electron energy loss spectra by multiple-least-squares fitting," *Ultramicroscopy*, vol. 26, pp. 393–403, 1988.

[135] E. R. Malinowski, *Factor Analysis in Chemistry*. Wiley, 2002.

[136] P. Potapov, "Why principal component analysis of STEM spectrum-images results in "abstract", uninterpretable loadings?" *Ultramicroscopy*, vol. 160, pp. 197–212, Jan. 2016.

[137] N. Keshava, "A survey of spectral unmixing algorithms," *Lincoln Laboratory Journal*, vol. 14, no. 1, pp. 55–78, 2003.

[138] C. G. Puntonet and A. Prieto, Eds., *Independent Component Analysis and Blind Signal Separation*. New York: Springer Berlin Heidelberg, 2004.

[139] A. F. Goetz, G. Vane, J. E. Solomon, and B. N. Rock, "Imaging spectrometry for Earth remote sensing," *Science*, vol. 228, no. 4704, pp. 1147–1153, 1985.

[140] S. Beauchemin, D. Hesterberg, and M. Beauchemin, "Principal component analysis approach for modeling sulfur K-XANES spectra of humic acids," *Soil Science Society of America Journal*, vol. 66, pp. 83–91, 2002.

[141] K. M. Horn, B. S. Swartzentruber, G. C. Osbourn, A. Bouchard, and J. W. Bartholomew, "Electronic structure classifications using scanning tunneling microscopy conductance imaging," *Journal of Applied Physics*, vol. 84, no. 1998, pp. 2487–2496, 1998.

[142] P. Trebbia and N. Bonnet, "EELS elemental mapping with unconventional methods I. theoretical basis: image analysis with multivariate statistics and entropy concepts," *Ultramicroscopy*, vol. 34, pp. 165–178, 1990.

[143] D. Nuzillard and N. Bonnet, "BSS for series of electron energy loss spectra," in *Proceedings of the Fifth International Conference, ICA*, C. G. Puntonet and A. Prieto, Eds., New York: Springer Berlin Heidelberg, 2004, pp. 1150–1157.

[144] M. Bosman, M. Watanabe, D. T. L. Alexander, and V. J. Keast, "Mapping chemical and bonding information using multivariate analysis of electron energy-loss spectrum images.," *Ultramicroscopy*, vol. 106, no. 11-12, pp. 1024–32, 2006.

[145]   C. Witte, N. J. Zaluzec, and L. J. Allen, "Extracting physically interpretable data from electron energy-loss spectra.," *Ultramicroscopy*, vol. 110, no. 11, pp. 1390–6, Oct. 2010.

[146]   F. de la Peña, M.-H. Berger, J.-F. Hochepied, F. Dynys, O. Stephan, and M. Walls, "Mapping titanium and tin oxide phases using EELS: an application of independent component analysis," *Ultramicroscopy*, vol. 111, no. 2, pp. 169–76, Jan. 2011.

[147]   N. Dobigeon and N. Brun, "Spectral mixture analysis of EELS spectrum-images," *Ultramicroscopy*, vol. 120, pp. 25–34, 2012.

[148]   O. Nicoletti, F. de la Peña, R. K. Leary, D. J. Holland, C. Ducati, and P. A. Midgley, "Three-dimensional imaging of localized surface plasmon resonances of metal nanoparticles," *Nature*, vol. 502, pp. 80–4, 2013.

[149]   S. Lichtert and J. Verbeeck, "Statistical consequences of applying a PCA noise filter on EELS spectrum images.," *Ultramicroscopy*, vol. 125, pp. 35–42, Feb. 2013.

[150]   A. Eljarrat, L. López-Conesa, J. López-Vidrier, S. Hernández, B. Garrido, C. Magén, F. Peiró, and S. Estradé, "Retrieving the electronic properties of silicon nanocrystals embedded in a dielectric matrix by low-loss EELS," *Nanoscale*, vol. 6, pp. 14 971–83, 2014.

[151]   I. T. Jolliffe, *Principal Component Analysis*, ser. Springer Series in Statistics. New York: Springer, 2002.

[152]   L. Albera, M. Amin, M. Babaie-Zadeh, R. Bro, J.-F. Cardoso, M. Castella, P. Chevalier, A. Chevreuil, A. Cichocki, P. Comon, L. D. Lathauwer, A. Mohammad-Djafari, Y. Deville, R. Gribonval, A. Hyvarinen, C. Jutten, A. Kachenoura, A. Karfoul, J. Jarhunen, K. H. Knuth, E. Moreau, L. C. Parra, J.-C. Pesquet, M. D. Plumbley, D.-T. Pham, L. Senhadji, D. Slock, N. Thirion-Moreau, R. Vigario, E. Vincent, A. Yeredor, V. Zarzoso, and M. Zibulevsky, *Handbook of Blind Source Separation: Indepenent Component Analysis and Applications*, 1st ed., P. Comon and C. Jutten, Eds. Oxford: Academic Press, 2010, pp. 107–154.

[153]   J.-F. Cardoso, "High-order contrasts for independent component analysis," *Neural Computation*, vol. 11, pp. 157–192, 1999.

[154]   N. Bonnet and D. Nuzillard, "Independent component analysis: a new possibility for analysing series of electron energy loss spectra.," *Ultramicroscopy*, vol. 102, no. 4, pp. 327–37, Mar. 2005.

[155]   A. Hyvärinen and E. Oja, "Independent component analysis: algorithms and applications," *Neural networks*, vol. 13, pp. 411–430, 2000.

[156]   D. D. Lee and H. S. Seung, "Learning the parts of objects by non-negative matrix factorization," *Nature*, vol. 401, no. October 1999, pp. 788–791, Oct. 1999.

[157] R. Leary, F. de la Peña, J. S. Barnard, Y. Luo, M. Armbr uster, J. M. Thomas, and P. A. Midgley, "Revealing the atomic structure of intermetallic GaPd$_2$ nanocatalysts by using aberration-corrected scanning transmission electron microscopy," *ChemCatChem*, vol. 5, no. 9, pp. 2599–2609, 2013.

[158] S. M. Collins, O. Nicoletti, D. Rossouw, T. Ostasevicius, and P. A. Midgley, "Excitation dependent Fano-like interference effects in plasmonic silver nanorods," *Physical Review B*, vol. 90, no. 15, p. 155 419, 2014.

[159] S. M. Collins, E. Ringe, M. Duchamp, Z. Saghi, R. E. Dunin-Borkowski, and P. A. Midgley, "Eigenmode tomography of surface charge oscillations of plasmonic nanoparticles by electron energy loss spectroscopy," *ACS Photonics*, vol. 2, no. 11, pp. 1628–1635, 2015.

[160] E. Ringe, C. J. DeSantis, S. M. Collins, M. Duchamp, R. E. Dunin-Borkowski, S. E. Skrabalak, and P. A. Midgley, "Resonances of nanoparticles with poor plasmonic metal tips," *Scientific Reports*, vol. 5, p. 17 431, 2015.

[161] R. K. Leary, A. Kumar, P. J. Straney, S. M. Collins, S. Yazdi, R. E. Dunin-Borkowski, P. A. Midgley, J. E. Millstone, and E. Ringe, "Structural and optical properties of discrete dendritic Pt nanoparticles on colloidal Au nanoprisms," *The Journal of Physical Chemistry C*, May 2016.

[162] J. Zečević, K. P. de Jong, and P. E. de Jongh, "Progress in electron tomography to assess the 3D nanostructure of catalysts," *Current Opinion in Solid State and Materials Science*, vol. 17, no. 3, pp. 115–125, 2013, Electron Tomography.

[163] F. de la Peña, V. T. Fauske, P. Burdet, T. Ostasevicius, M. Sarahan, M. Nord, J. A. Taillon, D. Johnstone, K. E. MacArthur, A. Eljarrat, S. Mazzucco, J. Caron, T. Furnival, M. Walls, E. Prestat, G. Donval, Ben, L. F. Zagonel, Petras, T. Aarholt, A. Garmannslund, and I. Iyengar, *Hyperspy: A multi-dimensional data analysis toolbox*, Jun. 2016.

[164] J. Orloff, L. W. Swanson, and M. Utlaut, *High resolution focused ion beams: FIB and its applications*, 1st. New York: Springer Science+Business Media, 2003.

[165] L. A. Giannuzzi and F. A. Stevie, Eds., *Introduction to Focused Ion Beams: Instrumentation, Theory, Techniques and Practice*. New York, NY: Springer Science+Business Media, Inc., 2005.

[166] M. Schaffer, B. Schaffer, and Q. Ramasse, "Sample preparation for atomic-resolution STEM at low voltages by FIB," *Ultramicroscopy*, vol. 114, pp. 62–71, Mar. 2012.

[167] B. Arnold, D. Lohse, H.-D. Bauer, T. Gemming, K. Wetzig, and K. Binder, "Surface damages on FIB prepared TEM-specimens: possibilities of avoidance and removal," *Microscopy and Microanalysis*, vol. 9, no. S03, pp. 140–141, 2003.

[168] T. Ishitani, "Improvements in performance of focused ion beam cross-sectioning: aspects of ion-sample interaction," *Journal of Electron Microscopy*, vol. 53, no. 5, pp. 443–449, Oct. 2004.

[169] M. B. Clennell, "Tortuosity: a guide through the maze," *Geological Society, London, Special Publications*, vol. 122, no. 1, pp. 299–344, Jan. 1997.

[170] N. Vivet, S. Chupin, E. Estrade, T. Piquero, P. Pommier, D. Rochais, and E. Bruneton, "3D microstructural characterization of a solid oxide fuel cell anode reconstructed by focused ion beam tomography," *Journal of Power Sources*, vol. 196, no. 18, pp. 7541–7549, Sep. 2011.

[171] J. Joos, T. Carraro, A. Weber, and E. Ivers-Tiffée, "Reconstruction of porous electrodes by FIB/SEM for detailed microstructure modeling," *Journal of Power Sources*, vol. 196, no. 17, pp. 7302–7307, Sep. 2011.

[172] J. R. Wilson and S. A. Barnett, "Solid oxide fuel cell Ni-YSZ anodes: effect of composition on microstructure and performance," *Electrochemical and Solid-State Letters*, vol. 11, no. 10, B181, 2008.

[173] J. F. Watts and J. Wolstenholme, *An Introduction to Surface Analysis by XPS and AES*. West Sussex: John Wiley & Sons, 2003.

[174] N. Fairley and Casa Software Ltd, *CasaXPS manual 2.3.15 - Intro to XPS and AES (Yellow Book)*, 2009.

[175] ——, *CasaXPS Manual 2.3.15 - XPS, AES, ToF-SIMS, Dynamic SIMS (Blue Book)*. 2009.

[176] ——, *CasaXPS Manual 2.3.15 - Spectroscopy (Orange Book)*. 2009.

[177] Elettra Sincrotrone Trieste, *X-ray photoelectron spectroscopy*, https://www.elettra.trieste.it/lightsources/labs-and-services/surface-lab/x-ray-photoelectron-spectroscopy.html, (Accessed on 06/02/2016).

[178] X. Shen, M. P. Oxley, Y. Puzyrev, B. R. Tuttle, G. Duscher, and S. T. Pantelides, "Excess carbon in silicon carbide," *Journal of Applied Physics*, vol. 108, no. 12, p. 123 705, 2010.

[179] M. Di Ventra and S. T. Pantelides, "Oxygen stability, diffusion, and precipitation in SiC: implications for thin-film oxidation," *Journal of Electronic Materials*, vol. 29, no. 3, pp. 353–358, Mar. 2000.

[180] C. J. Cochrane, P. M. Lenahan, and A. J. Lelis, "Identification of a silicon vacancy as an important defect in 4H SiC metal oxide semiconducting field effect transistor using spin dependent recombination," *Applied Physics Letters*, vol. 100, no. 2, p. 023 509, 2012.

[181] G. Y. Chung, C. C. Tin, J. R. Williams, K. McDonald, R. K. Chanana, R. A. Weller, S. T. Pantelides, L. C. Feldman, O. W. Holland, M. K. Das, and J. W. Palmour, "Improved inversion channel mobility for 4H-SiC MOSFETs following high temperature anneals in nitric oxide," *IEEE Electron Device Letters*, vol. 22, no. 4, pp. 176–178, Apr. 2001.

[182] J. Rozen, S. Dhar, S. K. Dixit, V. V. Afanas'ev, F. O. Roberts, H. L. Dang, S.-R. Wang, S. T. Pantelides, J. R. Williams, and L. C. Feldman, "Increase in oxide hole trap density associated with nitrogen incorporation at the SiO_2/SiC interface," *Journal of Applied Physics*, vol. 103, no. 12, p. 124 513, 2008.

[183] S. A. Correa, C. Radtke, G. V. Soares, L. Miotti, I. J. R. Baumvol, S. Dimitrijev, J. Han, L. Hold, F. Kong, and F. C. Stedile, "Effects of nitrogen incorporation on the interfacial layer between thermally grown dielectric films and SiC," *Applied Physics Letters*, vol. 94, no. 25, p. 251 909, 2009.

[184] J. Rozen, S. Dhar, M. E. Zvanut, J. R. Williams, and L. C. Feldman, "Density of interface states, electron traps, and hole traps as a function of the nitrogen density in SiO_2 on SiC," *Journal of Applied Physics*, vol. 105, no. 12, p. 124 506, 2009.

[185] C. Jeanguillaume and C. Colliex, "Spectrum-image: the next step in EELS digital acquisition and processing," *Ultramicroscopy*, vol. 28, no. 1-4, pp. 252–257, Apr. 1989.

[186] P. Fiorenza, F. Giannazzo, A. Frazzetto, and F. Roccaforte, "Influence of the surface morphology on the channel mobility of lateral implanted 4H-SiC(0001) metal-oxide-semiconductor field-effect transistors," *Journal of Applied Physics*, vol. 112, no. 8, p. 084 501, 2012.

[187] D. A. Muller, "Why changes in bond lengths and cohesion lead to core-level shifts in metals, and consequences for the spatial difference method," *Ultramicroscopy*, vol. 78, no. 1-4, pp. 163–174, Jun. 1999.

[188] R. Brydson and Royal Microscopical Society (UK), *Electron Energy Loss Spectroscopy*, ser. Microscopy Handbooks. Bios, 2001.

[189] D. R. McKenzie, S. Berger, and L. Brown, "Bonding in a-$Si_{1-x}C_x$:H films studied by electron energy loss near edge structure," *Solid State Communications*, vol. 59, no. 5, pp. 325–329, Aug. 1986.

[190] D. A. Muller, P. Batson, and J. Silcox, "Measurement and models of electron-energy-loss spectroscopy core-level shifts in nickel aluminum intermetallics," *Physical Review B*, vol. 58, no. 18, pp. 11 970–11 981, Nov. 1998.

[191] E. M. Cherry and D. E. Hooper, *Amplifying Devices and Low-Pass Amplifier Design*. New York: John Wiley & Sons, 1968.

[192] P. Jamet, S. Dimitrijev, and P. Tanner, "Effects of nitridation in gate oxides grown on 4H-SiC," *Journal of Applied Physics*, vol. 90, no. 10, p. 5058, 2001.

[193] E. Pippel, J. Woltersdorf, H. Ö. Ólafsson, and E. Ö. Sveinbjörnsson, "Interfaces between 4H-SiC and SiO_2: microstructure, nanochemistry, and near-interface traps," *Journal of Applied Physics*, vol. 97, no. 3, p. 034 302, 2005.

[194] D. Williams, J. Michael, J. Goldstein, and A. Romig, "Definition of the spatial resolution of X-ray microanalysis in thin foils," *Ultramicroscopy*, vol. 47, no. 1-3, pp. 121–132, Nov. 1992.

[195] N. Mottu, M. Vayer, R. Benoit, and R. Erre, "Is XPS combined with argon ion sputtering pertinent for depth profiling molybdenum-implanted stainless-steel layers?" *Surface and Interface Analysis*, vol. 34, pp. 276–279, 2002.

[196] Y. Xu, X. Zhu, H. D. Lee, C. Xu, S. M. Shubeita, a. C. Ahyi, Y. Sharma, J. R. Williams, W. Lu, S. Ceesay, B. R. Tuttle, a. Wan, S. T. Pantelides, T. Gustafsson, E. L. Garfunkel, and L. C. Feldman, "Atomic state and characterization of nitrogen at the SiC/SiO$_2$ interface," *Journal of Applied Physics*, vol. 115, no. 3, p. 033 502, Jan. 2014.

[197] F. J. Grunthaner and J. Maserjian, "Experimental observations of the chemistry of the SiO$_2$/Si interface," *IEEE Transactions on Nuclear Science*, vol. 24, no. 6, pp. 2108–2112, 1977.

[198] F. J. Grunthaner, P. J. Grunthaner, R. P. Vasquez, B. F. Lewis, J. Maserjian, and A. Madhukar, "Local atomic and electronic structure of oxide/GaAs and SiO$_2$/Si interfaces using high-resolution XPS," *Journal of Vacuum Science and Technology*, vol. 16, no. 5, p. 1443, Sep. 1979.

[199] ——, "High-resolution X-ray photoelectron spectroscopy as a probe of local atomic structure: application to amorphous SiO and the Si-SiO$_2$ interface," *Physical Review Letters*, vol. 43, no. 22, pp. 1683–1686, Nov. 1979.

[200] R. P. Vasquez and F. J. Grunthaner, "Chemical composition of the SiO$_2$/InSb interface as determined by x-ray photoelectron spectroscopy," *Journal of Applied Physics*, vol. 52, no. 5, p. 3509, 1981.

[201] R. P. Vasquez, M. H. Hecht, F. J. Grunthaner, and M. L. Naiman, "X-ray photoelectron spectroscopy study of the chemical structure of thermally nitrided SiO$_2$," *Applied Physics Letters*, vol. 44, no. 10, p. 969, 1984.

[202] D. B. Fenner, D. K. Biegelsen, and R. D. Bringans, "Silicon surface passivation by hydrogen termination: a comparative study of preparation methods," *Journal of Applied Physics*, vol. 66, no. 1, p. 419, 1989.

[203] A. Witvrouw, B. Du Bois, P. De Moor, A. Verbist, C. Van Hoof, H. Bender, and K. Baert, "A comparison between wet HF etching and vapor HF etching for sacrificial oxide removal," *Micromachining and Microfabrication Process Technology VI*, vol. 4174, pp. 130–141, 2000.

[204] P. Swift, "Adventitious carbon: the panacea for energy referencing?" *Surface and Interface Analysis*, vol. 4, no. 2, pp. 47–51, 1982.

[205] *NIST XPS database, selected element search result*, http://srdata.nist.gov/xps/, (Accessed on 06/09/2016).

[206] C. Virojanadara and L. I. Johansson, "Interfacial investigation of in situ oxidation of 4H-SiC," *Surface Science*, vol. 472, pp. L145–L149, 2001.

[207] C. Virojanadara and L. Johansson, "Oxidation studies of 4H–SiC(0001) and (000$\bar{1}$)," *Surface Science*, vol. 505, pp. 358–366, May 2002.

[208] L. C. Feldman, Personal communication, Aug. 2014.

[209] C. Önneby and C. G. Pantano, "Silicon oxycarbide formation on SiC surfaces and at the SiC/SiO$_2$ interface," *Journal of Vacuum Science & Technology A: Vacuum, Surfaces, and Films*, vol. 15, no. 3, p. 1597, May 1997.

[210] K. Yamamoto, Y. Koga, and S. Fujiwara, "XPS studies of amorphous SiCN thin films prepared by nitrogen ion-assisted pulsed-laser deposition of SiC target," *Diamond and Related Materials*, vol. 10, pp. 1921–1926, 2001.

[211] G. Rignanese, A. Pasquarello, J. Charlier, X. Gonze, and R. Car, "Nitrogen incorporation at Si(001)-SiO$_2$ interfaces: relation between N 1s core-level shifts and microscopic structure," *Phys. Rev. Lett.*, vol. 79, no. 25, pp. 5174–5177, 1997.

[212] J. R. Shallenberger, D. A. Cole, and S. W. Novak, "Characterization of silicon oxynitride thin films by x-ray photoelectron spectroscopy," *Journal of Vacuum Science & Technology A: Vacuum, Surfaces, and Films*, vol. 17, no. 1999, p. 1086, 1999.

[213] Thermo Scientific, *Angle resolved XPS; application note 31014*, 2008.

[214] C. Powell, *NIST Standard Reference Database 82*, Surface and Microanalysis Science Division (837), Gaithersburg MD, 2011.

[215] H. Yano, T. Hirao, T. Kimoto, H. Matsunami, K. Asano, and Y. Sugawara, "High channel mobility in inversion layers of 4H-SiC MOSFETs by utilizing (11$\bar{2}$0) face," *IEEE Electron Device Letters*, vol. 20, no. 12, pp. 611–613, Dec. 1999.

[216] J. Senzaki, K. Kojima, S. Harada, R. Kosugi, S. Suzuki, T. Suzuki, and K. Fukuda, "Excellent effects of hydrogen postoxidation annealing on inversion channel mobility of 4H-SiC MOSFET fabricated on (11$\bar{2}$0) face," *IEEE Electron Device Letters*, vol. 23, no. 1, pp. 13–15, Jan. 2002.

[217] T. Kimoto, Y. Kanzaki, M. Noborio, H. Kawano, and H. Matsunami, "Interface properties of metal–oxide–semiconductor structures on 4H-SiC{0001} and (11$\bar{2}$0) formed by N$_2$O oxidation," *Japanese Journal of Applied Physics*, vol. 44, no. 3, pp. 1213–1218, Mar. 2005.

[218] M. Yoshikawa, K. Inoue, H. Seki, Y. Nanen, M. Kato, and T. Kimoto, "Characterization of silicon dioxide films on 4H-SiC (0001) Si, (1$\bar{1}$00) M, and (11$\bar{2}$0) A faces by cathodoluminescence spectroscopy," *Applied Physics Letters*, vol. 102, no. 5, p. 051 612, 2013.

[219] Y. Negoro, N. Miyamoto, T. Kimoto, and H. Matsunami, "Remarkable lattice recovery and low sheet resistance of phosphorus-implanted 4H-SiC (11$\bar{2}$0)," *Applied Physics Letters*, vol. 80, no. 2, pp. 240–242, 2002.

[220] C. T. Koch, "A flux-preserving non-linear inline holography reconstruction algorithm for partially coherent electrons.," *Ultramicroscopy*, vol. 108, no. 2, pp. 141–50, Jan. 2008.

[221] J. A. Taillon, J. H. Yang, C. A. Ahyi, J. Rozen, J. R. Williams, L. C. Feldman, T. S. Zheleva, A. J. Lelis, and L. G. Salamanca-Riba, "Systematic structural and chemical characterization of the transition layer at the interface of NO-annealed 4H-SiC / SiO_2 metal-oxide-semiconductor field-effect transistors," *Journal of Applied Physics*, vol. 113, no. 4, p. 044 517, 2013.

[222] D. A. Muller, T. Sorsch, S. Moccio, F. H. Baumann, K. Evans-Lutterodt, and G. Timp, "The electronic structure at the atomic scale of ultrathin gate oxides," *Nature*, vol. 399, no. June, 758–761w, 1999.

[223] W. M. Skiff, R. W. Carpenter, and S. H. Lin, "Near-edge fine-structure analysis of core-shell electronic absorption edges in silicon and its refractory compounds with the use of electron-energy-loss microspectroscopy," *Journal of Applied Physics*, vol. 62, no. 1987, pp. 2439–2449, 1987.

[224] G. J. Auchterlonie, D. R. McKenzie, and D. J. H. Cockayne, "Using ELNES with parallel EELS for differentiating between a-Si:X thin films," *Ultramicroscopy*, vol. 31, no. 2, pp. 217–222, Oct. 1989.

[225] H. K. Schmid, "Phase identification in carbon and BN systems by EELS," *Microscopy Microanalysis Microstructures*, vol. 6, pp. 99–111, 1995.

[226] J. Hu, P. Yang, and C. Lieber, "Nitrogen-driven sp^3 to sp^2 transformation in carbon nitride materials," *Physical Review B*, vol. 57, no. 6, R3185–R3188, 1998.

[227] N. Nakagawa, H. Y. Hwang, and D. A. Muller, "Why some interfaces cannot be sharp," *Nature Materials*, vol. 5, no. March, pp. 204–209, 2006.

[228] W. Czaja and I. Granacher, "A relation between gap energy and dielectric constant in semiconductors of diamond structure," *Helvetica Physica Acta*, vol. 36, p. 1073, 1963.

[229] S. Dhar, Y. W. Song, L. C. Feldman, T. Isaacs-Smith, C. C. Tin, J. R. Williams, G. Y. Chung, T. Nishimura, D. Starodub, T. Gustafsson, and E. C. Garnett, "Effect of nitric oxide annealing on the interface trap density near the conduction bandedge of 4H–SiC at the oxide/(11$\bar{2}$0) 4H–SiC interface," *Applied Physics Letters*, vol. 84, no. 9, p. 1498, 2004.

[230] K. Ueno and T. Oikawa, "Counter-doped MOSFETs of 4H-SiC," *IEEE Electron Device Letters*, vol. 20, no. 12, pp. 624–626, 1999.

[231] G. Liu, B. R. Tuttle, and S. Dhar, "Silicon carbide: a unique platform for metal-oxide-semiconductor physics," *Applied Physics Reviews*, p. 021 307, 2 2015.

[232] C. Jiao, A. C. Ahyi, C. Xu, D. Morisette, L. C. Feldman, and S. Dhar, "Phospho-silicate glass gated 4H-SiC metal-oxide-semiconductor devices: Phosphorus concentration dependence," *Journal of Applied Physics*, vol. 119, p. 155 705, 2016.

[233] Y. K. Sharma, A. C. Ahyi, T. Isaacs-Smith, A. Modic, M. Park, Y. Xu, E. L. Garfunkel, S. Dhar, L. C. Feldman, and J. R. Williams, "High-mobility stable 4H-SiC MOSFETs using a thin PSG interfacial passivation layer," *IEEE Electron Device Letters*, vol. 34, no. 2, pp. 175–177, Feb. 2013.

[234] P. Fiorenza, L. K. Swanson, M. Vivona, F. Giannazzo, C. Bongiorno, A. Frazzetto, and F. Roccaforte, "Comparative study of gate oxide in 4H-SiC lateral MOSFETs subjected to post-deposition-annealing in N_2O and $POCl_3$," *Applied Physics A: Materials Science and Processing*, vol. 115, pp. 333–339, 2014.

[235] O. K. T. Wu, "Effect of annealing on chemical state of phosphorus in SiO_2 films," *Journal of The Electrochemical Society*, vol. 132, p. 932, 1985.

[236] H. Tenailleau and J. M. Martin, "A new background subtraction for low-energy EELS core edges," *Journal of Microscopy*, vol. 166, no. 3, pp. 297–306, Jun. 1992.

[237] J. Gao, Q. Zhao, Y. Sun, G. Li, J. Zhang, and D. Yu, "A novel way for synthesizing phosphorus-doped ZnO nanowires," *Nanoscale Research Letters*, vol. 6, pp. 1–6, 2011.

[238] V. Vaithianathan, K. Asokan, J. Y. Park, and S. S. Kim, "Local electronic structure of phosphorus-doped ZnO films investigated by X-ray absorption near-edge spectroscopy," *Applied Physics A*, vol. 94, no. January, pp. 995–998, 2008.

[239] P. E. Batson, "Current trends for EELS studies in physics," *Microscopy Microanalysis Microstructures*, vol. 2, no. 2-3, pp. 395–402, 1991.

[240] D. Okamoto, H. Yano, K. Hirata, T. Hatayama, and T. Fuyuki, "Improved inversion channel mobility in 4H-SiC MOSFETs on Si face utilizing phosphorus-doped gate oxide," *IEEE Electron Device Letters*, vol. 31, no. 7, pp. 710–712, Jul. 2010.

[241] S. Dhar, Personal communication, Feb. 2016.

[242] I. D. Brown and R. D. Shannon, "Empirical bond-strength–bond-length curves for oxides," *Acta Crystallographica Section A*, vol. 29, no. 3, pp. 266–282, May 1973.

[243] H. Chang, Y. Choi, K. Kong, and B.-H. Ryu, "Atomic and electronic structures of amorphous Al_2O_3," *Chemical Physics Letters*, vol. 391, no. 4–6, pp. 293–296, 2004.

[244] R. Arenal, F. de la Peña, O. Stéphan, M. Walls, M. Tencé, a. Loiseau, and C. Colliex, "Extending the analysis of EELS spectrum-imaging data, from elemental to bond mapping in complex nanostructures," *Ultramicroscopy*, vol. 109, no. 1, pp. 32–8, 2008.

[245] P. A. Bingham, G. Yang, R. J. Hand, and G. Mobus, "Boron environments and irradiation stability of iron borophosphate glasses analysed by EELS," *Solid State Sciences*, vol. 10, pp. 1194–1199, 2008.

[246] R. A. Smith, "Boron in glass and glass making," *Journal of Non-Crystalline Solids*, vol. 84, no. 1-3, pp. 421–432, 1986.

[247] A. J. Lelis, D. Habersat, R. Green, A. Ogunniyi, M. Gurfinkel, J. Suehle, and N. Goldsman, "Time dependence of bias-stress-induced SiC MOSFET threshold-voltage instability measurements," *IEEE Transactions on Electron Devices*, vol. 55, no. 8, pp. 1835–1840, Aug. 2008.

[248] A. J. Lelis, R. Green, D. B. Habersat, and M. El, "Basic mechanisms of threshold-voltage instability and implications for reliability testing of SiC MOSFETs," *IEEE Transactions on Electron Devices*, vol. 62, no. 2, pp. 316–323, Feb. 2015.

[249] A. Givon, H. Piao, J. McMahon, G. Zorn, and H. Cohen, "Contactless derivation of inner fields in gate-oxide layers: SiO_2 on SiC," *Applied Physics Letters*, vol. 107, no. 2015, p. 173 101, 2015.

[250] X. Li, C. H. Tung, and K. L. Pey, "The nature of dielectric breakdown," *Applied Physics Letters*, vol. 93, no. 7, pp. 2–5, 2008.

[251] FEI Company, *Auto slice & view, for automated acquisition of high resolution 3D images*, http://www.fei.com/software/auto-slice-and-view/, (Accessed on 06/03/2016), 2016.

[252] Zeiss, *Atlas 5 - large area imaging for ZEISS SEM, FE-SEM & FIB-SEM*, http://www.zeiss.com/microscopy/en_us/products/microscope-software/atlas-5.html, (Accessed on 06/03/2016), 2016.

[253] Hitachi High Technologies, *nanoDUE'T FIB-SEM NB5000*, http://www.hitachi-hightech.com/us/product_detail/?pn=em-nb5000, (Accessed on 06/03/2016), 2016.

[254] TESCAN, *3D tomography*, http://www.tescan.com/en/other-products/software/3d-tomography, (Accessed on 06/03/2016), 2016.

[255] L. Holzer and M. Cantoni, "Review of FIB tomography," in *Nanofabrication Using Focused Ion and Electron Beams: Principles and Applications*, 2012, pp. 410–435.

[256] M. Schaffer, J. Wagner, B. Schaffer, M. Schmied, and H. Mulders, "Automated three-dimensional X-ray analysis using a dual-beam FIB," *Ultramicroscopy*, vol. 107, pp. 587–597, 2007.

[257] J. Guyon, N. Gey, D. Goran, S. Chalal, and F. Pérez-Willard, "Advancing FIB assisted 3D EBSD using a static sample setup," *Ultramicroscopy*, vol. 161, pp. 161–167, 2016.

[258] P. Burdet, J. Vannod, A. Hessler-Wyser, M. Rappaz, and M. Cantoni, "Three-dimensional chemical analysis of laser-welded NiTi–stainless steel wires using a dual-beam FIB," *Acta Materialia*, vol. 61, no. 8, pp. 3090–3098, May 2013.

[259] T. Prill, K. Schladitz, D. Jeulin, M. Faessel, and C. Wieser, "Morphological segmentation of FIB-SEM data of highly porous media," *Journal of Microscopy*, vol. 250, no. 2, pp. 77–87, May 2013.

[260] B. Bai, M. Elgmati, H. Zhang, and M. Wei, "Rock characterization of Fayetteville shale gas plays," *Fuel*, vol. 105, pp. 645–652, Mar. 2013.

[261] J. A. Taillon, C. Pellegrinelli, Y. Huang, E. Wachsman, and L. Salamanca-Riba, "Three dimensional microstructural characterization of cathode degradation in SOFCs using FIB/SEM and TEM," *Microscopy and Microanalysis*, vol. 21, no. S3, pp. 2161–2162, 2015.

[262] L. Holzer, B. Münch, M. Wegmann, P. H. Gasser, and R. J. Flatt, "FIB-nanotomography of particulate systems—part I: particle shape and topology of interfaces," *Journal of the American Ceramic Society*, vol. 89, no. 8, pp. 2577–2585, Aug. 2006.

[263] R. K. Bansal, A. Kubis, R. Hull, and J. M. Fitz-Gerald, "High-resolution three-dimensional reconstruction: a combined scanning electron microscope and focused ion-beam approach," *Journal of Vacuum Science & Technology B*, vol. 24, no. 2, p. 554, 2006.

[264] D. Gostovic, K. A. O'Hara, N. J. Vito, E. D. Wachsman, and K. S. Jones, "Multiple length scale characterization of doped lanthanum manganate composite cathodes," *Electrochemical Society Transactions*, vol. 16, no. 51, pp. 83–93, 2009.

[265] G. A. Hughes, K. Yakal-Kremski, A. V. Call, and S. A. Barnett, "Durability testing of solid oxide cell electrodes with current switching," *Journal of The Electrochemical Society*, vol. 159, no. 12, F858–F863, 2012.

[266] K. T. Lee, N. J. Vito, and E. D. Wachsman, "Comprehensive quantification of $Ni–Gd_{0.1}Ce_{0.9}O_{1.95}$ anode functional layer microstructures by three-dimensional reconstruction using a FIB/SEM dual beam system," *Journal of Power Sources*, vol. 228, pp. 220–228, Apr. 2013.

[267] K. Yakal-Kremski, J. S. Cronin, Y.-C. K. Chen-Wiegart, J. Wang, and S. A. Barnett, "Studies of solid oxide fuel cell electrode evolution using 3D tomography," *Fuel Cells*, vol. 13, no. 4, pp. 449–454, 2013.

[268] J. Joos, M. Ender, I. Rotscholl, N. H. Menzler, and E. Ivers-Tiffée, "Quantification of double-layer Ni/YSZ fuel cell anodes from focused ion beam tomography data," *Journal of Power Sources*, vol. 246, pp. 819–830, Jan. 2014.

[269] H. Jones, K. Mingard, and D. Cox, "Investigation of slice thickness and shape milled by a focused ion beam for three-dimensional reconstruction of microstructures," *Ultramicroscopy*, vol. 139, pp. 20–28, Apr. 2014.

[270] J. R. Wilson, A. T. Duong, M. Gameiro, H.-Y. Chen, K. Thornton, D. R. Mumm, and S. A. Barnett, "Quantitative three-dimensional microstructure of a solid oxide fuel cell cathode," *Electrochemistry Communications*, vol. 11, no. 5, pp. 1052–1056, May 2009.

[271] C. J. Gommes, A. J. Bons, S. Blacher, J. H. Dunsmuir, and A. H. Tsou, "Practical methods for measuring the tortuosity of porous materials from binary or gray-tone tomographic reconstructions," *AIChE Journal*, vol. 55, no. 8, pp. 2000–2012, 2009.

[272] B. Münch, P. Trtik, F. Marone, and M. Stampanoni, "Stripe and ring artifact removal with combined wavelet—fourier filtering," *Optics Express*, vol. 17, no. 10, p. 8567, May 2009.

[273] D. C. Joy, "Control of charging in low-voltage SEM," *Scanning*, vol. 11, pp. 1–4, 1989.

[274] K. L. Willis, A. B. Abell, and D. A. Lange, "Image-based characterization of cement pore structure using Wood's metal intrusion," *Cement and Concrete Research*, vol. 28, no. 12, pp. 1695–1705, Dec. 1998.

[275] E. Principe, *Patent, US 8178838*, 2012.

[276] J. Schindelin, I. Arganda-Carreras, E. Frise, V. Kaynig, M. Longair, T. Pietzsch, S. Preibisch, C. Rueden, S. Saalfeld, B. Schmid, J.-Y. Tinevez, D. J. White, V. Hartenstein, K. Eliceiri, P. Tomancak, and A. Cardona, "Fiji: an open-source platform for biological-image analysis," *Nature Methods*, vol. 9, no. 7, pp. 676–682, 2012.

[277] S. van der Walt, S. C. Colbert, and G. Varoquaux, "The NumPy array: a structure for efficient numerical computation," *Comput. Sci. Eng.*, vol. 13, no. 2, pp. 22–30, Mar. 2011.

[278] G. Bradski, *Dr. Dobb's Journal of Software Tools*, 2000.

[279] S. van der Walt, J. L. Schönberger, J. Nunez-Iglesias, F. Boulogne, J. D. Warner, N. Yager, E. Gouillart, T. Yu, and the scikit-image contributors, "Scikit-image: Image processing in Python," *PeerJ*, vol. 2, e453, Jun. 2014.

[280] P. Thévenaz, U. Ruttimann, and M. Unser, "A pyramid approach to subpixel registration based on intensity," *IEEE Transactions on Image Processing*, vol. 7, no. 1, pp. 27–41, Jan. 1998.

[281] M. Schaffer and J. Wagner, "Block lift-out sample preparation for 3D experiments in a dual beam focused ion beam microscope," *Microchimica Acta*, vol. 161, no. 3-4, pp. 421–425, 2008.

[282] X. Dai, "The effects of image misregistration on the accuracy of remotely sensed change detection," *IEEE Transactions on Geoscience and Remote Sensing*, vol. 36, no. 5, pp. 1566–1577, 1998.

[283] A. Buades, B. Coll, and J.-M. Morel, "A non-local algorithm for image denoising," in *2005 IEEE Computer Society Conference on Computer Vision and Pattern Recognition (CVPR'05)*, vol. 2, IEEE, pp. 60–65.

[284] A. Buades, B. Coll, and J.-M. Morel, "Non-local means denoising," *Image Processing On Line*, vol. 1, pp. 490–530, 2011.

[285] OpenCV Developers, *Image denoising*, 2016.

[286] L. Vincent and P. Soille, "Watersheds in digital spaces: an efficient algorithm based on immersion simulations," *IEEE Transactions on Pattern Analysis and Machine Intelligence*, vol. 13, no. 6, pp. 583–598, Jun. 1991.

[287] Y. Chen and J. Z. Wang, "Image categorization by learning and reasoning with regions," *Journal of Machine Learning Research*, vol. 5, pp. 913–939, 2004. arXiv: arXiv:1003.0783v1.

[288] J. Shotton, M. Johnson, and R. Cipolla, "Semantic texton forests for image categorization and segmentation," *26th IEEE Conference on Computer Vision and Pattern Recognition, CVPR*, 2008.

[289] M. Rastgarpour and J. Shanbehzadeh, "Application of AI techniques in medical image segmentation and novel categorization of available methods and tools," *Proceedings of the International Multi Conference of Engineers and Computer Scientists (IMECS)2011, Hong Kon*, vol. 1, pp. 1–6, 2011.

[290] Y. Artan, "Interactive image segmentation using machine learning techniques," *Canadian Conference on Computer and Robot Vision*, pp. 264–269, 2011.

[291] Blender Online Community, *Blender - a 3D modeling and rendering package*, Blender Foundation, Blender Institute, Amsterdam, 2016.

[292] W. Schroeder, K. Martin, and B. Lorensen, *Visualization Toolkit: An Object-Oriented Approach to 3D Graphics, 4th Edition*. Kitware, 2006.

[293] S. Brunauer, P. H. Emmett, and E. Teller, "Adsorption of gases in multimolecular layers," *Journal of the American Chemical Society*, vol. 60, no. 2, pp. 309–319, 1938.

[294] J. A. Taillon, C. Pellegrinelli, Y. Huang, E. D. Wachsman, and L. G. Salamanca-Riba, "Three dimensional microstructural characterization of cathode degradation in SOFCs using focused ion beam and SEM," *ECS Transactions*, vol. 61, no. 1, pp. 109–120, 2014.

[295] P. K. Saha, G. Borgefors, and G. Sanniti di Baja, "A survey on skeletonization algorithms and their applications," *Pattern Recognition Letters*, vol. 000, pp. 1–10, 2015.

[296] C. Pudney, "Distance-ordered homotopic thinning: a skeletonization algorithm for 3D digital images," *Computer Vision and Image Understanding*, vol. 72, no. 3, pp. 404–413, Dec. 1998.

[297] C. Fouard, G. Malandain, S. Prohaska, M. Westerhoff, F. Cassot, C. Mazel, D. Asselot, and J. Marc-Vergnes, "Skeletonization by blocks for large 3D datasets: application to brain microcirculation," in *2004 2nd IEEE International Symposium on Biomedical Imaging: Macro to Nano (IEEE Cat No. 04EX821)*, vol. 2, IEEE, 2004, pp. 89–92.

[298] H. J. Johnson, M. McCormick, L. Ibáñez, and T. I. S. Consortium, *The ITK Software Guide*, Third, *In press*, Kitware, Inc., 2013.

[299] H. Homann, "Implementation of a 3D thinning algorithm," Oct. 2007.

[300] The CGAL Project, *CGAL User and Reference Manual*, 4.7. CGAL Editorial Board, 2015.

[301] X. Gao, S. Loriot, and A. Tagliasacchi, "Triangulated surface mesh skeletonization," in *CGAL User and Reference Manual*, 4.7, CGAL Editorial Board, 2015.

[302] G. Brus, K. Miyoshi, H. Iwai, M. Saito, and H. Yoshida, "Change of an anode's microstructure morphology during the fuel starvation of an anode-supported solid oxide fuel cell," *International Journal of Hydrogen Energy*, pp. 1–8, 2015.

[303] G. Gaiselmann, M. Neumann, V. Schmidt, O. Pecho, T. Hocker, and L. Holzer, "Quantitative relationships between microstructure and effective transport properties based on virtual materials testing," *AIChE Journal*, vol. 60, no. 6, pp. 1983–1999, 2014.

[304] L. Holzer, O. Stenzel, O. Pecho, T. Ott, G. Boiger, M. Gorbar, Y. De Hazan, D. Penner, I. Schneider, R. Cervera, and P. Gasser, "Fundamental relationships between 3D pore topology, electrolyte conduction and flow properties: towards knowledge-based design of ceramic diaphragms for sensor applications," *Materials and Design*, vol. 99, pp. 314–327, 2016.

[305] O. Stenzel, O. Pecho, L. Holzer, M. Neumann, and V. Schmidt, "Predicting effective conductivities based on geometric microstructure characteristics," *AIChE Journal*, vol. 62, in print, 2016.

[306] J. A. Sethian, "Fast marching methods," *SIAM Review*, vol. 41, no. 2, pp. 199–235, 1999.

[307] `scikit-fmm`, *Https://pypi.python.org/pypi/scikit-fmm*, 2015.

[308] J.-W. Kim, A. V. Virkar, K. Fung, K. Mehta, and S. C. Singhal, "Polarization effects in intermediate temperature, anode-supported solid oxide fuel cells," *Journal of The Electrochemical Society*, vol. 146, no. 1, p. 69, 1999.

[309] H. Fukunaga, M. Ihara, K. Sakaki, and K. Yamada, "The relationship between overpotential and the three phase boundary length," *Solid State Ionics*, vol. 86-88, no. PART 2, pp. 1179–1185, 1996.

[310] B. Kenney, M. Valdmanis, C. Baker, J. Pharoah, and K. Karan, "Computation of TPB length, surface area and pore size from numerical reconstruction of composite solid oxide fuel cell electrodes," *Journal of Power Sources*, vol. 189, no. 2, pp. 1051–1059, Apr. 2009.

[311] C. Pellegrinelli, Y.-L. Huang, J. A. Taillon, L. G. Salamanca-Riba, and E. D. Wachsman, "A study of SOFC cathode degradation in H_2O environments," *ECS Transactions*, vol. 64, no. 2, pp. 17–28, 2014.

[312] B. Efron and R. Tibshirani, *An Introduction to the Bootstrap (Chapman & Hall/CRC Monographs on Statistics & Applied Probability)*. Chapman and Hall/CRC, 1994.

[313] `scikits.bootstrap`, *Https://pypi.python.org/pypi/scikits.bootstrap*, 2016.

[314] J. Deseure, Y. Bultel, L. Dessemond, and E. Siebert, "Theoretical optimisation of a SOFC composite cathode," *Electrochimica Acta*, vol. 50, no. 10, pp. 2037–2046, 2005.

[315] D. Gostovic, "A multi-length scale approach to correlating solid oxide fuel cell porous cathode microstructure to electrochemical performance," PhD Thesis, University of Florida, 2009.

[316] M. Backhaus-Ricoult, "Interface chemistry in LSM-YSZ composite SOFC cathodes," *Solid State Ionics*, vol. 177, no. 19-25, pp. 2195–2200, Oct. 2006.

[317] S.-J. Shih, R. Sharghi-Moshtaghin, M. R. De Guire, R. Goettler, Z. Xing, Z. Liu, and A. H. Heuer, "Mn valence determination for lanthanum strontium manganite solid oxide fuel cell cathodes," *Journal of The Electrochemical Society*, vol. 158, no. 10, B1276, 2011.

[318] H. Parikh, "Microstructure changes in solid oxide fuel cell anodes after operation, observed using three-dimensional reconstruction and microchemical analysis," PhD Thesis, Case Western Reserve University, 2015.

[319] D. Gostovic, J. A. Taillon, J. R. Smith, N. J. Vito, K. A. O'Hara, K. S. Jones, and E. D. Wachsman, "Comprehensive quantification of porous LSCF cathode microstructure and electrochemical impedance," *Submitted to the Journal of the Electrochemical Society*, 2016.

[320] Y. T. Kim, A. Ohi, A. He, Z. Jiao, T. Shimura, D. Klotz, S. Hara, and N. Shikazono, "Microstructure and polarization characteristics of LSCF-GDC composite cathode with different volume fractions," *ECS Transactions*, vol. 68, no. 1, pp. 757–762, 2015.

[321] C. Xiong, C. Pellegrinelli, J. A. Taillon, Y.-L. Huang, L. G. Salamanca-Riba, B. Chi, L. Jian, J. Pu, and E. D. Wachsman, "Long-term Cr poisoning effect on LSCF-GDC composite cathodes sintered at different temperatures," *Submitted to the Journal of the Electrochemical Society*, 2016.

[322] C. Pellegrinelli, Y. Huang, J. A. Taillon, L. G. Salamanca-Riba, and E. D. Wachsman, "Effect of gas contaminants on LSCF-GDC composite cathodes," *In preparation*, 2016.